Self-assembly and optical properties of gold nanoparticle superlattices for surface-enhanced Raman spectroscopy

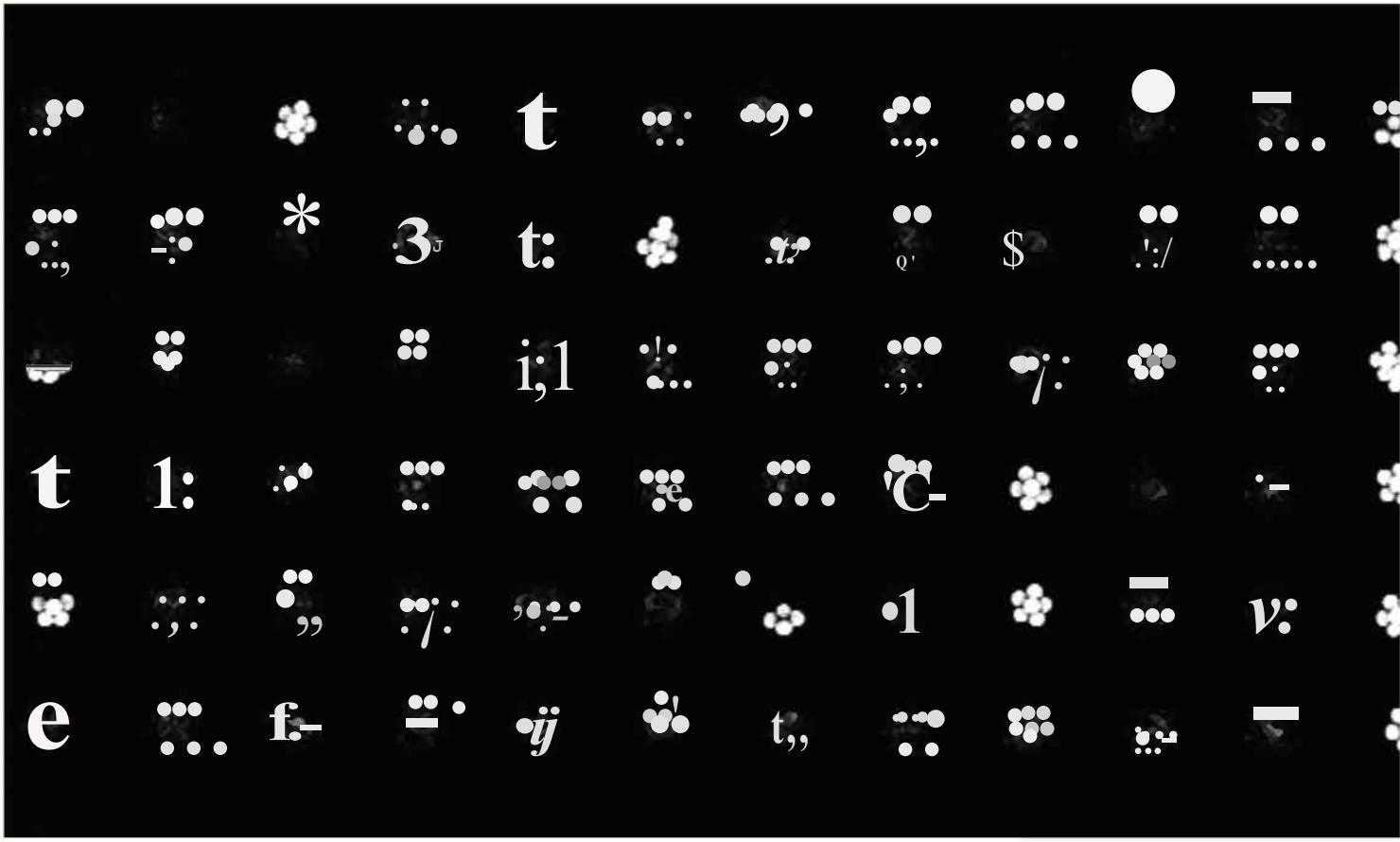

PhD thesis

Mathias Charconnet

Supervised by Andreos Seifert ond Luis M. Liz-Morzón

2021

Universidad del País Vasco

Euskal Herriko Unibertsitatea

Self-assembly and optical properties of gold nanoparticle superlattices for surface-enhanced Raman spectroscopy

a manuscript submitted to
the university of the basque country (UPV/EHU)

For the degree of
doctor in sciences

Presented by Mathias Charconnet

Under the supervision of
Andreas Seifert (Nanoengineering group / CIC nanoGUNE)
Luis M. Liz-Marzán (Bionanoplasmonics group / CIC biomaGUNE)

Donostia/San Sebastian
2021

CIC nanoGUNE
MEMBER OF BASQUE RESEARCH & TECHNOLOGY ALLIANCE

CIC biomaGUNE
MEMBER OF BASQUE RESEARCH & TECHNOLOGY ALLIANCE

eman ta zabal zazu
Universidad del País Vasco
Euskal Herriko Unibertsitatea

Contents

Glossary

4-MBA 4-Mercaptobenzoic acid.

AA Ascorbic acid.

AFM Atomic force microscopy.

BSPP Bis(p-sulfonatophenyl)phenylphosphine dihydrate dipotassium salt.

CTAC cethyl trimethyl ammonium chloride.

EBL electron beam lithography.

FDTD Finite-difference time-domain.

FEM Finite element method.

LSPR Localised surface plasmon resonance.

NPs nanoparticles.

NTP 4-nitrothiophenol.

PEG polyethylene glycol.

PEI polyethyleneimine.

PLGA poly-lactic-co-glycolic acid.

SEM Scanning electron microscopy.

SERS Surface-enhanced Raman spectroscopy.

SLR Surface lattice resonance.

VdW Van der Waals.

Acknowledgement

First of all, I would like to thank both my supervisors, Andreas Seifert and Luis M. Liz-Marzan, for giving me the amazing opportunity to make my PhD thesis in such a wonderful environment offered by CIC nanoGUNE and CIC biomaGUNE. Making the choice to do the thesis in San Sebastian has shaped my life forever, and for this reason I cannot thank you enough. To Andreas : I am grateful for your dedication, enthusiasm, and particularly for the time you spent explaining me all those writing and presentation tricks. Luis, agradezco mucho la libertad que me has dejado durante esta tesis y todos los consejos y explicaciones que me has dado, particularmente tengo que darte las gracias por dirigir un grupo de investigación con gente tan experta y agradable. I am also very grateful to Jost Adam for letting stay some weeks in the Southern University of Denmark, where I have learnt a lot on electromagnetic simulations. Jost, next time you come to the basque country we have to go for a surf !

Sans la détermination et l'insistance de ma mère, je ne serais pas là ou je suis aujourd'hui et pour cela je la remercie infiniment de m'avoir soutenu tout au long de mes études. Je te remercie également d'avoir pris le temps de relire ma thèse.

A mon père, je pense sincèrement que tu m'as donné le gout de la science et de la physique dans mon enfance en me donnant envie de faire la photographie et je pense que cela m'a fortement influencé dans mes choix tout au long de ma vie.

A Coralie, ta présence quotidienne tout au long de cette étape m'a énormément aidée, dans les hauts comme dans les bas, et sans toi je ne serais pas la même personne aujourd'hui. Bien qu'on aurait pu se rencontrer dans un festnoz quand j'habitais à Rennes (oui oui à 6 ans j'y allais déjà), le hasard a voulu que l'on se rencontre grâce à notre amour mutuel pour le pintxopote et je pense que c'est pour le mieux ! Merci pour tous les bons moments que l'on a passé pendant cette thèse et bien sûr pour tous ceux qui sont à venir.

During my PhD I have collaborated with different people from other institutes without whom some of the work I realized wouldn't have been possible, whether it has been actual contributions or insightful discussions. Particularly I have to thank Agustin Mihi, and his student Cristiano Matricardi for providing wonderful nanostructured templates. From the same research group, I have to thank Juan Luis Garcia Pomar for making such accurate electromag-

netic simulations. Because we always need more people making simulations when you are a nanophotonics researcher, I am very grateful to Matiyas Tsegay Korsa for helping me with the though electromagnetic simulations of different nanoparticles clusters.

Being a co-directed PhD student, I have met twice as much amazing people that helped me in so many different ways to fulfill my PhD thesis in a constant state of joy and motivation. I, will start to acknowledge the nanoGUNE people. Particularly, I have to acknowledge the members of the nanoengineering group for all the scientific conversations but also their willingness to listen and help (Ana, Maica, Jaione, Eneko, Ion, Laura, Constance, Leire, Olga, Stephen...). Tengo que agradecer a Eneko por ser el mejor técnico en que uno puede pensar, gracias por tu ayuda en el lab y tus intentos por comunicar conmigo en Francés. Ana, es una pena que te hayas ido tan temprano, pero has sido de buen consejo para temas del trabajo pero sobre todo de fuera del trabajo, espero que nos volveremos a ver en Zarrautz ! Auupa Yayo, estuvo muy contento de compartir la experiencia de este congreso tan lejos en Korea y sobre todo de compartir estos platos muy raros que comimos.

Outside of the nanoengineering group, I have to thank Nerea for being such a listenning neighbour and a good provider of snacks, Christopher Tollan for his help with taking beautiful SEM images, Itziar for facilitating the processes with the university, Maiara for helping me creating a safer environment for the PhDs through the PhD committee, Paolo for letting me use his laboratory and many more people (Inge, Francesco, Isabel, Iker, Juan Ma, Carmen, Patricia, Sara, Sarai, Giuseppe, ...)

I was always happy to come up to biomaGUNE thinking about the coffee break spent in the good company of the bionanoplasmonics crew and the equally nice presence of a nice pintxo de tortilla (special thanks to Fogon which helped quite a bit on Fridays...) ! Through the years many people have passed through the labs, and all of these people helped either with their scientific knowledge or good mood (most of the time both). During my PhD I have discovered the amazing world of self-assembly and colloids, and I am so glad to have started in the best hands possible. Christoph, I cannot thank you enough for all the scientific discussions we had and all the knowledge you transferred to me, it's a pity you left earlier than expected but I hope you are enjoying your actual position in Germany. David, ha estado un placer discutir de temas varios contigo pasando de anarchismo a tus vecinas de la talent, seguro que nos harás

girar nuestras cabezas con tus nanorods chirales. Adisssss, la verdad que tanto en nanoGUNE y biomaGUNE he contado con técnicos de laboratorios geniales ! Vished, thank you for letting me some nanos and helping me with synthesis, you're the boss. Ana portu, que risas nos hemos pegado cuando estabas mi vecina, recuerdo estos tiempos con mucha alegría. Elisa, Daiiiiiii, que bueno tenerte en este grupo que siempre hace falta una italiana loca. Rosalía, aunque solo has estado aquí poco tiempo, ha sido super guay disfrutar de este verano yendo a surfear contigo después del curro. Guilleee, craack, sintigo no disfrutaría de la misma manera mis tostadas con tomate, gracias por ensenarme estos pequenos trucos de la vida espanola. Christan K., you have taught me so much on how to present data in the best way possible, I also surely appreciated a lot the discussion we had on plasmonic and other topics, you truly deserve to keep on your scintific carreer in Germany. Ana S., gracias por todas la discusiones científicas que hemos tenido, me has aclarado muchas cosas de la ciencia de los coloides, el lab 1 ya estara con mas calma sinmigo (jejeje), la próxima vez que voy a Galicia ya me dirás donde está el verdadero pulpo Gallego ! Dorlee, gracias por las risas, espero que montaremos un buen fiestón cuando se acaba todo esto. Isa, gracias por ayudarnos con muchos aspectos de nuestro proyectos y por escucharnos siempre. Crissss, aunque me vaciles con mi acento francés, ha sido muy guay tenerte a nuestros lados para las pausas café. Carlito, ha sido un placer tener a otro físico que me entiendo en este grupo, sin ti no se a quien hubiera podido hablar de mis proyectos locos de fotoluminesciencia. I think i'm going to run out of space after thanking so many people of the bionanoplasmonics group, but there are still pleinty more I need to thank for creating such a good atmosphere in the group (Pablo, Oscar, Malou, Xiaolu, Yizhi, Clara, Bea, Anish, Jhoan, Govind, Marta Q, Jatish...)

The quarantine has been tough, but I couldn't have made it through without the installations offered by the cr@si and it's devoted members. To the scientific director, Stefan, I am very glad to have worked with you and particulatly enjoyed the coffee break accompanied by your lovely cinamon rolls or croissant, I hope cr@si will reach new heights after i'm graduating. A la recepcionista Cristian, ha sido un placer escucharte cantar en el cr@si con tu voz tan melódica. Al doctorando con mucha responsabilidad, Javi, agradezco mucho tu constante buen humor y positivismo, ha sido un placer colaborar contigo en esta tesis y estoy seguro que iras lejos si sigues en investigación, es un pena que ya no vayamos a escuchar mas a los black eyed peyes

en la sala del Raman !

I should also thank the zurriolab, which delivered varying working conditions during the whole thesis. Along with this, I have to acknowledge all my surfing budies who pumped me up waking at 7 am to go surfing at first light (TigerPaul, Anzu, Stefanizer, Luis el dentista, Alvabro, Mattezero, Joscha...). I have passed some amazing time with you guys, both in and out the water, I hope we can do some amazing trip together soon.

Les amitiés se font et se défont mais il y en a qui perdurent, je pense particulièrement à mes srabs du bureau du travail (BDD pour les intimes), avec qui on a écoulé beaucoup de cartouches lors des révisions du mercredi après-midi. Je ne pense pas vous imprimer ma thèse sinon je sais déjà en quoi ça va terminer... Sacha, malgré cette année de pandémie on s'est quand même fait bien plaisir et j'espère que ça n'annonce que le début de trips encore plus dingue ! Kiki, William, Etienne, trop hâte de vous recroiser, aux canaries inchallah. Je pense également à toutes mes potes de longue date de la copain crew, Ptit gros, James, Elf,Jo, Ludwig, William, Vignasse, Paquita,Lou... Je ne peux pas oublier le chaptal gang, particulièrement Clairou qui m'a épaulé tout au long de mes études et remis dans le droit chemin quand je n'écoutais pas en TP. Et bien sur, Caro qui m'a soutenu dans les moments difficiles à Toulouse.

Je souhaite également remercier la PNS et ses professeurs qui m'ont motivé pour continuer à faire un thèse, particulièrement à Quentin et JCT ! Merci également à Alice qui m'a donné de précieux conseil et a corrigé mes fautes d'orthographes présente dans ma thèse.

Of course I met tons of amazing people during my thesis in the research institutes I was working at, but I have also made frienships that I believe will be longlasting, particularly I am thinking of Theo and Floris. Théo, entre tous les trips qu'on s'est fait je crois bien qu'on a dépassé les 10000 km au compteur... avec un co-pilote hors-pair je tiens à le dire ! J'espère que tu vas te plaire aux states, mais t'inquiètes pas on viendra te voir. Floo, le hollandais volant, I'm so glad we met thanks to this crazy Plant biologist, let's hope that hutje mutje comes back even more confiné comme des sardines. But I am also thinking about my crazy group of pure blood donostiarran friends for the good nights out in and out of DBDB (Paul, Joscha, ZARA, Stefan, Alvaro, Virginia, Gabriele, Matteo, Sahsil, Yaiza, Emilie, Donato...).

Finalement j'aimerais remercier ma famille qui a toujours cru en moi. Je pense tout particulièrement à ma super sista Charlotte, qui m'a toujours motivé dans tout ce que j'ai entrepris.

Je tiens aussi à laisser une petite dédicace à Alma, qui rayonne de bonne humeur, qui sait peut être qu'un jour tu seras en train de lire cette thèse!

Summary

This thesis is oriented towards the fabrication and optical characterization of ordered clusters of gold nanoparticles, i.e. plasmonic superlattices, as substrates for surface-enhanced spectroscopy. Gold nanostructures have remarkable optical properties thanks to their plasmonic properties, which allow them to confine the electric field to nanosocale volumes. Particularly, the high near-field enhancement produced by gold nanostructures grant for a tremendous increase of the Raman signal of molecules present in its vicinity. Thanks to this effect, known as surface-enhanced Raman scattering, low amount of chemicals or biomarkers can be detected by SERS. In this context, the design and fabrication of new plasmonic substrates with optimized plasmonic properties would improve their SERS perfomance, and grant for the identification of lower analytes concentrations.

The nanofabrication of gold nanostructures is generally achieved through two main paths: (i) The fabrication of patterns through lithography followed by the deposition of bulk gold, (ii) the synthesis of gold nanoparticles, followed by their self-assembly into clusters or films with new optical properties. On the one hand, lithography techniques enable the acquisition of highly precise periodic structures, however they are slow and expensive. On the other hand, gold nanoparticle self-assembly is fast and relatively inexpensive, but the complexity of the attained nanostructures remains limited. To keep the advantages of both techniques a combination of lithography and self-assembly is used in this PhD to fabricate periodical arrays of gold nanoparticle clusters. For that purpose, colloidal nanoparticles are used as building blocks for their assembly into the wells of a nanostructured template, fabricated by lithography techniques. This approach, using capillary forces to trap nanoparticles in the wells of the template, results in the fabrication of periodical arrays of gold NP clusters.

Plasmonic superlattices exhibit remarkable plasmonic resonances, so-called surface lattice plasmon resonances, that arise from the coupling between plasmonic cluster modes and in-plane diffracted orders. Such far-field coupled resonances can be employed for ultrasensitive surface-enhanced Raman spectroscopy (SERS), provided they are spectrally matched to the excitation wavelength. Consequently, understanding coupling phenomena in arrays of self-assembled gold nanoparticles will help for the design of optimized plasmonic substrates for sensing applications,

using SERS for instance. Fabrication of new optimized plasmonic substrates for SERS is essential for reducing the SERS limit of detection but also its reproducibility. In this context, the overall goal of this thesis is to fabricate highly regular plasmonic superlattices and to study their optical properties with the aim of optimizing their SERS performance.

The first chapter of this thesis is dedicated to the development of a self-assembly process allowing for the homogeneous assembly of gold nanospheres into superlattices (i.e periodical arrays of gold nanoparticle clusters). Since the statistical error of SERS largely depends on the homogeneity of the sample, fabricating plasmonic substrates with a regular SERS enhancement over their surface motivated the fabrication of homogeneous superlattices. A systematic study of the optical properties of superlattices with different homogeneities is performed to show the influence of homogeneity on the surface lattice plasmon resonance of plasmonic superlattices. Particularly, the SERS signal of superlattices displaying different homogeneities is compared and the most homogeneous superlattice show the lowest standard deviation as well as the highest SERS signal on the account of a stronger far-field coupling.

In the second chapter, the self-assembly process developed in Chapter 1 is applied to the assembly of different nanoparticle shapes such as nanospheres, nanorods, and nanotriangles. The use of anisotropic nanoparticles was motivated by the fact that anisotropic nanoparticles provide higher near-field enhancement, therefore, their assemblies are expected to give a remarkable SERS signal. The aim of this chapter was therefore to optimize the SERS signal of plasmonic superlattices by changing the shape of the colloidal building blocks. In this sense, the universality of the templated self-assembly process is demonstrated by assembling the differently shaped nanoparticles, using the same assembly conditions, into superlattices of 400 and 500 nm period. Controlled assembly of gold nanoparticles into superlattices enables a comparative optical study of the different superlattices and a comparison of their SERS enhancement factor. At the same time, finite element method simulations were performed and enabled the identification of the nature of the different plasmonic mode involved in the optical properties of the plasmonic superlattices. Conversely to what was hypothesized, the gold nanosphere superlattices exhibit higher SERS enhancement factors than superlattices of nanorods and nanotriangles.

After optimization of the plasmonic superlattices SERS enhancement through the assembly of different nanoparticle shapes, chapter 3 discloses an optimization of the plasmonic superlat-

tices SERS enhancement through a systematic study of the lattice parameters. In this context, the templated self-assembly process was extended to flexible PDMS substrates. Since the main plasmon resonances of plasmonic superlattices depend on the lattice period, the optical properties of the flexible superlattices can be tailored through lattice period deformations by means of macroscopic mechanical strains. Finally, both unidirectional and bidirectional lattice deformations were used to adapt a single lattice structure to both red-shifted and blue-shifted excitation lines and find the optimal lattice parameters for SERS under both excitation wavelengths (633 and 785 nm).

In the last chapter, an application of SERS to the real-time sensing of dangerous analytes in microfluidic flows is exposed. SERS has proven to be a technique of choice for the detection of chemicals and biological markers, consequently real-time SERS would enable the monitoring of dynamic chemical and biological processes. However, SERS is affected by the so-called memory effect, which consists of the irreversible binding of molecules to the gold nanostructure and impedes successive detections with a single substrate. In this context, the last chapter presents a modification of the plasmonic superlattices, fabricated in the previous chapters, with a thermolabile polymer which protects the gold nanoparticles from analyte adsorption. Removal of the polymer in selected areas constitutes a way to perform a new SERS measurement at a given time, and consequently to monitor different chemicals flowing in a microfluidic channel by SERS. Furthermore, this method was transferred to simple plasmonic systems such as dried droplets of nanoparticles covered with the thermolabile polymer, which underlines the potential of the method to monitor dynamic chemical or biological processes by SERS.

Resumen

Esta tesis se centra en la fabricación y la caracterización óptica de clústeres de nanopartículas ordenados periódicamente, es decir super-redes plasmonicas, de cara a su uso como sustratos para espectroscopia Raman amplificada por superficies (SERS). La nanofabricación de dichas nanoestructuras de oro se suele realizar por medio de dos metodologías principales: (i) La fabricación de patrones por litografía seguido por la deposición de una capa de oro, usando generalmente técnicas de deposiciones físicas en fase de vapor y (ii) el ensamblaje de nanopartículas de oro (sintetizadas por métodos químicos en disolución) para la formación de agrupaciones que adquieren nuevas propiedades ópticas. Por un lado, las técnicas de litografía permiten fabricar nanoestructuras con una alta precisión, aunque estos procesos acaban resultando lentos y costosos. Por otra parte, el ensamblaje de nanopartículas es rápido y relativamente barato, sin embargo la complejidad de las estructuras que se pueden producir por esta vía es limitada. Con el objetivo de aunar las ventajas de estas dos técnicas, una combinación de procesos de litografía y de ensamblaje de nanopartículas se han empleado a lo largo de esta tesis para la fabricación de agrupaciones de nanopartículas ordenadas periódicamente. En este sentido, se han utilizado nanopartículas en forma de coloides como los bloques constituyentes del ensamblaje que se genera siguiendo los huecos de un patrón nanoestructurado fabricado por técnicas de litografía. Esta metodología, basada en las fuerzas capilares para la inmovilización de las nanopartículas en los huecos del patrón, permite fabricar agrupaciones de nanopartículas con una alta precisión, obteniendo estructuras organizadas periódicamente.

Las super-redes presentan resonancias plasmónicas con unas propiedades ópticas sobresalientes, que surgen del acoplamiento entre los modos plasmónicos de los clústeres y el orden de difracción en el plano de la red. Por otra parte, se ha demostrado (Matricardi et al) que este fenómeno puede ser aprovechado en la fabricación de sensores basados en espectroscopia Raman amplificada por superficies, obteniendo un incremento de la señal cuando la longitud de onda del plasmón de superficie coincide con la longitud de onda de la excitación Raman. En este sentido, la comprensión de los fenómenos de acoplamiento en las redes de clústeres de nanopartículas resulta crucial para optimizar del los sustratos plasmónicos de cara a sus aplicaciones en detección. Particularmente, un mayor control en los procesos de fabricación de

sustratos plasmonicos es imprescindible para mejorar la reproducibilidad de dicha tecnología, al mismo tiempo que se aumenta su sensibilidad. En este contexto, el reto principal de esta tesis ha sido fabricar super-redes plasmonicas altamente ordenadas y estudiar sus propriedades ópticas, con el fin de optimizar sus capacidades de amplificación SERS.

El primer capítulo de esta tesis esta dedicado al desarrollo de un procedimiento para el ensamblaje de nanopartículas en superredes de nanoesferas con alta homogeneidad a gran escala. De manera adicional, se realizó un estudio sistemático de las propriedades ópticas de dichas superredes con el fin de demostrar la influencia de la homogeneidad sobre la resonancia plasmonica de superficie. Finalmente, se comprobó que las superredes con alta homogeneidad mejoran la señal de SERS en intensidad y reproducibilidad.

En el segundo capitulo, el proceso de ensamblaje optimizado en el capítulo 1 se aplicó a nanopartículas de diferentes formas: nanoesferas, nanorods y nanotriángulos. El uso de dichas nanopartículas anisótropas estuvo motivado por el hecho de que proporcionan un mayor aumento del campo electromagnético en comparación con las nanosferas. En definitiva, este capítulo demostró la universalidad del proceso a través del ensamblaje nanopartículas con diferentes formas en super-redes de con periodos de 400 o 500 nm. El ensamblaje controlado de dichas nanopartículas permitió hacer un estudio óptico comparativo de las diferentes super-redes, al mismo tiempo que se comparaban los factores de aumento de la señal de SERS. Al contrario de lo esperado, se observó que las super-redes de nanoesferas proporcionan una mayor señal de SERS que super-redes formadas por nanorods y nanotriángulos.

Siguiendo con la optimización de la señal SERS, el capítulo 3 presenta un estudio sistemático sobre los efectos plasmónicos asociados a la modificación del periodo de red entre las nanopartículas. En este sentido, se adaptó el proceso de ensamblaje a sustratos flexibles de PDMS para modular de manera precisa la distancia entre las agrupaciones de nanopartículas. Dado que el plasmón de superficie de las super-redes depende principalmente del periodo de red, se ajustaron las propiedades ópticas a través del estiramiento mecánico del sustrato. Finalmente, estiramientos unidireccionales y bidireccionales permitieron adaptar las propiedades plasmónicas de la red inicial a múltiples longitudes de ondas, de mayor o menor energía. Esta técnica permite encontrar los parámetros de red óptimos para obtener un mayor incremento de SERS en función de la longitud de onda de excitación del laser empleado, 633 y 785 nm.

En el último capitulo, se presenta una aplicación de la tecnología de SERS para la detección en tiempo real de análitos de interés en dispositivos microflúidicos. El empleo de la técnica SERS se ha mostrado como una herramienta potente para la detección in situ de sustancias químicas y distintos biomarcadores. Sin embargo, las medidas de SERS suelen verse afectadas por un efecto de memoria, provocado por la unión irreversible de moléculas sobre la nanoestrucutra de oro, que impide la realización de detecciones sucesivas con un mismo sustrato. En este contexto, a lo largo del último capítulo se presenta una modificación de las super-redes plasmónicas, fabricadas en los capítulos previos, que consiste en la deposición de un polímero termolábil e impermeable que protege a las nanopartículas de la unión con las moléculas presentes en disolución. Gracias a las propiedades termoplasmónicas de las super-redes se ha podido retirar el polímero en zonas específicas tras una irradiación laser mas intensa, facilitando así la realización de una medida de SERS en el área desprotegida. De esta forma, la generación sucesiva de múltiples ventanas de medida posibilita la realización de medidas a diferentes tiempos para la monitorización de procesos dinámicos.

Chapter 1

General Introduction

1.1 General introduction on nanotechnology

At the beginning of the 21st century, nanotechnology was presented as the new technological revolution to come, Thomas Theis director of the IBM Watson research center said in 2008:"One way of defining nanotechnology is to talk about length scales. A different way is to see it as an upcoming economic, business, and social phenomenon. Nanoadvocates argue it will revolutionize the way we live, work, and communicate" [1]. Today, Nanotechnology can be considered an established field. Products coming to the market featuring nanotechnology are becoming more and more common, and according to Lux research nanotechnology, nano-enabled products generated 1.6 trillion in global revenues in 2014, and that figure is anticipated to increase to 3.5 trillion in 2018 following the so-called Moore law [2, 3]. Amongst the different technologies available on the market we can mention the implementation of solar cell farms around the world enabling for not only greener energies, but also the large scale widespread of faster and smaller computers and cellphones made possible by the development of transistors with lowered dimensions. At the same time, several studies sound out public opinion and the knowledge of people on nanotechnology. A European initiative for nanotechnology, Nanoopinion, interrogated European citizens to sound out their knowledge on nanotechnology through five different questions: (i) Are nanoparticles visible through X-rays, (ii) does nanotechnology allow scientists to rearrange molecules?, (iii) Is a nanometer about the width of the human hair?, (iv) Is it possible to find nanoparticles in nature?, (v) Have nanoproducts been on the market since a

long time?. In Europe, on average, people answered right to 3 or more questions [4]. More than 50 years after Richard Feynman's speech, considered to be the birth of nanotechnology, it seems that the global public is aware of the existence of nanotechnology and even has a moderate knowledge of what nanotechnology is. Those two social and economic indicators point out that the nanotechnology revolution is now taking place or that it has already happened.

Nanotechnology uses the physicochemical properties of matter at the nanoscale to create devices and materials possessing new abilities. By reducing dimensions to the nanometer physico-chemical properties of the material such as melting-point [5], electric conductivity [6], fluorescence [7] or chemical reactivity [8] change as compared to its bulk state. For instance, the synthesis of dielectric nanoparticles of different sizes, such as quantum dots made of cadmium selenide, granted tunable photoluminescence through the fine-tuning of the nanoparticle size (**Figure 1.1 a**). By changing the dimensions of cadmium selenide nanoparticles, electronic confinement can be changed leading to changes in the photoluminescence of quantum dots [9].

While understanding the effects of the nanoscale started just at the end of the 20th century, it has been used blindly for centuries by humanity. The use of new technologies such as electron microscopy made possible the finding of nanomaterials in objects dating from several centuries. For instance, the famous Lycurgus cup made in the 4th century in Rome presents glass embedded gold nanoparticles, allowing the cup to look opaque green when lit under normal illumination and glowing red when lit from inside the cup [10]. From the 6th century onwards gold nanoparticles were found in different artworks such as stained glass in European cathedrals but also ceramics in the Islamic world. Other materials such as carbon nanotubes, were found in other craftwork such as the "Damascus" blade. The steel of "Damascus" blades was used because of its excellent mechanical properties, and the finding of carbon nanotubes shines a light on why these blades were so resistant [11]. Even if certain processes were empirically giving specific properties to materials, the underlying phenomena controlling their properties were not known at the time.

In other ways, we can say that nature has also developed its own nanotechnology through evolution to confer special properties. For instance, Butterfly wings present bright colors that don't degrade over time as would a pigment (**Figure 1.1 b**). Indeed the color of butterfly wings is not due to pigments (i.e molecules absorbing light at specific wavelengths) but due to

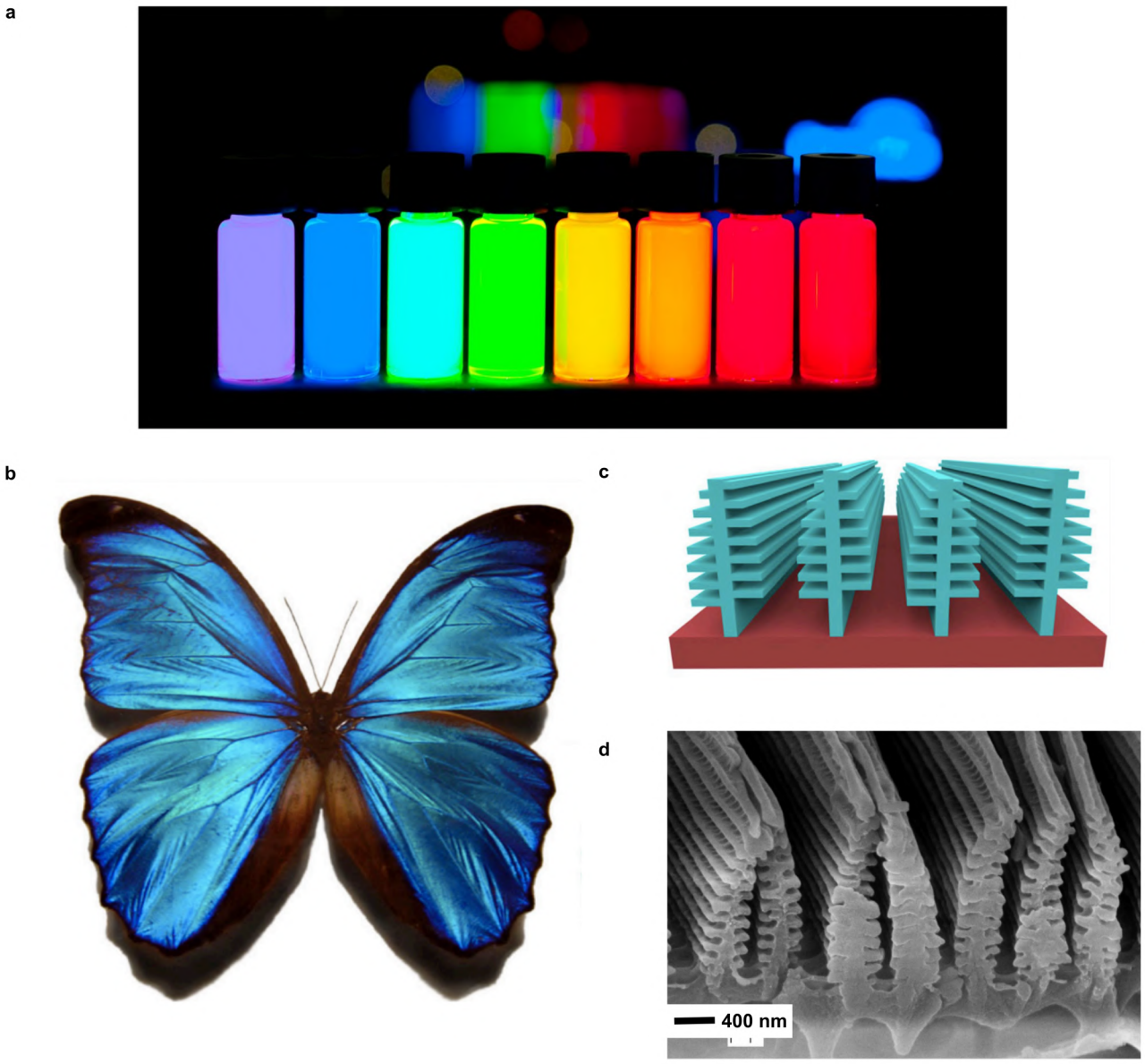

Figure 1.1: Examples of nanotechnology: a) Photoluminescence of cadmium selenide nanoparticles of different sizes. b) Photograph of a blue morpho butterfly displaying iridescent colors on its wings, by Gregory Phillips, under Creative commons BY-SA 3.0, via Wikimedia Commons. c)Scheme of the butterfly wings nanostructure, reproduced from [12] d) Scanning electron microscopy (SEM) image of a butterfly wing reproduced with permission from [13], Copyright 2013 American Physical Society.

nanostructures on their wings [13, 14]. Color formation due to specific nanostructures is known as structural coloring, and understanding the way they are created is today a whole field of research [15, 16]. Such designs developed by nature can be very insightful in order to create

new nanomaterials with interesting properties. For instance, by reproducing the nanostructure present on the hand of a gecko, researchers were able to produce a material that proportionate reversible binding without using any type of glue [17]. To go even further it is possible to use butterfly wings as biotemplates to create nanostructures with incredible optical properties [18].

While nature developed its own ways to use nanotechnology and former civilizations found processes to confer colors or specific mechanical properties to their material, researchers are now trying to synthesize and characterize various materials at the nanoscale. In this sense, today's approach is very different from fabricating stained glass, not only the study and synthesis of new materials is done in systematic ways but there exist new tools such as atomic force microscopy (AFM), electron microscopy, and scanning tunneling microscopy (SEM) that allow in effect to see the produced nanomaterials. Such instruments surely allowed the development of nanotechnology, but we should also mention the development of lithography, wet chemistry, and self-assembly that allowed the fabrication of complex materials with amazing electrical, mechanical, magnetic or optical properties. Finally, a lot of different technological advances made nanotechnology possible and it is now up to scientists and engineers to create useful applications for society.

1.2 Scope and objective of the thesis

This thesis is oriented towards the fabrication and optical characterization of ordered clusters of gold nanoparticles, i.e. plasmonic superlattices, as substrates for surface-enhanced spectroscopy. Due to their remarkable ability to confine light to the nanoscale, plasmonic nanostructures are ideal platforms for ultrasensitive spectroscopy techniques, such as surface-enhanced Raman scattering (SERS) spectroscopy [12, 13]. However, high and efficient SERS signals typically demands a match between the plasmon resonance wavelength and the Raman laser excitation wavelength [14, 19]. Plasmon resonances can be tailored through the nanostructure's shape or material, particularly, in periodically arranged nanoparticles, i.e. plasmonic superlattices, the plasmon resonance can be tuned through changes in the lattice period [9]. These lattice effects, known as surface lattice resonances, arise from the coupling between the plasmon resonance of the lattice sub-unit with an in-plane diffracted order. Such far-field coupled resonances can

be employed for ultrasensitive surface-enhanced Raman spectroscopy (SERS), provided they are spectrally matched to the excitation wavelength, as was shown by Matricardi et al [20]. Consequently, understanding coupling phenomena in arrays of self-assembled gold nanoparticles will help for the design of optimized plasmonic substrates for sensing applications, using SERS for instance. Fabrication of new optimized plasmonic substrates for SERS is primordial for lowering the SERS limit of detection but also its reproducibility. Generally, the fabrication of periodic plasmonic nanostructures follow lithography processes, but an increase interest is given to the self-assembly of colloidal gold nanoparticles into period superstructures due to its lower cost and its faster process [20, 21]. Particularly, capillary-assisted self-assembly has emerged as a versatile technique for the self-assembly of colloids into complex structures [22]. In this context, the overall goal of this thesis is to fabricate and study the plasmonic properties of highly regular gold nanoparticle superlattices made through self-assembly, with the aim of optimizing their SERS performances.

The synthesis and self-assembly of gold nanoparticles was performed in biomaGUNE in the bionanoplasmonics group, while the characterization of plasmonic superlattices was performed in nanoGUNE in the nanoengineering group. To complement some of the results with optical simulations (chapter 1 and chapter 2), a research stay was done in the Mads Clausen institute at the southern university of Denmark. Additional optical simulations results (chapter 3) were provided by the NANOPTO group from ICMAB (Barcelona).

The first chapter of this thesis is dedicated to the development of a self-assembly process allowing for the homogeneous assembly of gold nanospheres into superlattices (i.e periodical arrays of gold nanoparticle clusters). Since the statistical error of SERS largely depends on the homogeneity of the sample, fabricating plasmonic substrates with a regular SERS enhancement over their surface motivated the fabrication of homogeneous superlattices. To study the influence of homogeneity on the optical properties of periodically arranged clusters of nanoparticles, superlattices displaying different homogeneity were fabricated and characterized by UV-Vis and Raman spectroscopy. Particularly, the long-range order of plasmonic superlattices is expected to give rise to stronger far-field coupling, and consequently to increase the SERS enhancement of the plasmonic substrate.

In the second chapter, the self-assembly process developed in Chapter 1 is applied to the

assembly of different nanoparticle shapes such as nanospheres, nanorods, and nanotriangles. The use of anisotropic nanoparticles was motivated by the fact that anisotropic nanoparticles provide higher near-field enhancement, therefore, their assemblies are expected to give a remarkable SERS signal. The aim of this chapter was therefore to optimize the SERS signal of plasmonic superlattices by changing the shape of the colloidal building blocks. In this sense, the universality of the templated self-assembly process is demonstrated by assembling the differently shaped nanoparticles, using the same assembly conditions, into superlattices of 400, and 500 nm period. The controlled assembly of gold nanoparticles into superlattices enables a comparative optical study of the different superlattices and a comparison of their SERS enhancement factor.

After optimization of the plasmonic superlattices SERS enhancement through the assembly of different nanoparticle shapes, chapter 3 discloses an optimization of the plasmonic superlattices SERS enhancement through a systematic study of the lattice parameters. In this context, the templated self-assembly process is extended to flexible PDMS substrates. Since the main plasmon resonances of plasmonic superlattices depend on the lattice period, the optical properties of the flexible superlattices can be tailored through lattice period deformations by means of macroscopic mechanical strains. Finally, both unidirectional and bidirectional lattice deformations are used to adapt a single lattice structure to both red-shifted and blue-shifted excitation lines and find the optimal lattice parameters for SERS under both excitations (633 and 785 nm).

In the last chapter, an application of SERS to the real-time sensing of dangerous analytes in microfluidic flows is exposed. SERS has proven to be a technique of choice for the detection of chemicals and biological markers, consequently real-time SERS would enable the monitoring of dynamic chemical and biological processes. However, SERS is affected by the so-called memory effect, which consists of the irreversible binding of molecules to the gold nanostructure and impedes successive detections with a single substrate. In this context, the last chapter presents a modification of the plasmonic superlattices, fabricated in the previous chapters, with a thermolabile polymer which protects the gold nanoparticles from analytes adsorption. Removal of the polymer in selected areas constitutes a way to perform a new SERS measurement at a given time, and consequently to monitor different chemicals flowing in a microfluidic channel by SERS.

Bibliography

[1] Binks, P.; Ying, J. nan'o·tech·nol'o·gy n. *Nat. Nanotechnology* **2006**, *1*, 8–10.

[2] research, L. Nanotechnology Update: Corporations Up Their Spending as Revenues for Nano-enabled Products Increase. 2014.

[3] The Nanotech Report, 4th Edition. 2006.

[4] Marschalek, I.; Hofer, M. Nano and the public. *Nat. Nanotechnology* **2017**, *12*, 92.

[5] Aliofkhazraei, M. Handbook of nanoparticles. *Handbook of Nanoparticles* **2015**, 1–1426.

[6] Marinho, B.; Ghislandi, M.; Tkalya, E.; Koning, C. E.; de With, G. Electrical conductivity of compacts of graphene, multi-wall carbon nanotubes, carbon black, and graphite powder. *Powder Technol* **2012**, *221*, 351–358.

[7] Norris, D.; Efros, A. L.; Rosen, M. Size dependence of exciton fine structure in CdSe quantum dots. *Physical Review B - Condensed Matter and Materials Physics* **1996**, *53*, 16347–16354.

[8] Yaghmaee, M. S.; Shokri, B.; Rahimipour, M. R. Size dependence surface activity of metallic nanoparticles. *Plasma Process Polym* **2009**, *6*, 876–882.

[9] Norris, D.; Efros, A. L.; Rosen, M. Size dependence of exciton fine structure in CdSe quantum dots. *Physical Review B - Condensed Matter and Materials Physics* **1996**, *53*, 16347–16354.

[10] Ian Freestone, Nigel Meeks, Margaret Sax, C. H. Lycurgus cup a roman nanotechnology. *Gold Bull.* **2007**, *40*, 270–277.

[11] Reibold, M.; Paufler, P.; Levin, A. A.; Kochmann, W.; Pätzke, N.; Meyer, D. C. Materials: Carbon nanotubes in an ancient Damascus sabre. *Nature* **2006**, *444*, 286.

[12] Rayleigh, L. Note on the remarkable case of diffraction spectra. *The London, Edinburgh, and Dublin Philosophical Magazine and Journal of Science* **1907**, *14*, 60–65.

[13] Burg, S. L.; Parnell, A. J. Self-assembling structural colour in nature. *Journal of Physics Condensed Matter* **2018**, *30*.

[14] Mejdoubi, A.; Andraud, C.; Berthier, S.; Lafait, J.; Boulenguez, J.; Richalot, E. Finite element modeling of the radiative properties of Morpho butterfly wing scales. *Physical Review E - Statistical, Nonlinear, and Soft Matter Physics* **2013**, *87*.

[15] Zhang, C.; Jing, J.; Wu, Y.; Fan, Y.; Yang, W.; Wang, S.; Song, Q.; Xiao, S. Stretchable All-Dielectric Metasurfaces with Polarization-Insensitive and Full-Spectrum Response. *ACS Nano* **2020**, *14*, 1418–1426.

[16] Cheng, F.; Gao, J.; Luk, S. T.; Yang, X. Structural color printing based on plasmonic metasurfaces of perfect light absorption. *Sci. Rep.* **2015**, *5*, 1–10.

[17] Raut, H. K.; Baji, A.; Hariri, H. H.; Parveen, H.; Soh, G. S.; Low, H. Y.; Wood, K. L. Gecko-Inspired Dry Adhesive Based on Micro-Nanoscale Hierarchical Arrays for Application in Climbing Devices. *ACS Applied Materials and Interfaces* **2018**, *10*, 1288–1296.

[18] Wu, L.; Wang, W.; Zhang, W.; Su, H.; Liu, Q.; Gu, J.; Deng, T.; Zhang, D. Highly sensitive, reproducible and uniform SERS substrates with a high density of three-dimensionally distributed hotspots: gyroid-structured Au periodic metallic materials. *NPG Asia Mater.* **2018**, *10*, e462–e462.

[19] Graham, D. et al. Theory of SERS enhancement: General discussion. *Faraday Discuss.* **2017**, *205*, 173–211.

[20] Matricardi, C.; Hanske, C.; Garcia-Pomar, J. L.; Langer, J.; Mihi, A.; Liz-Marzán, L. M. Gold Nanoparticle Plasmonic Superlattices as Surface-Enhanced Raman Spectroscopy Substrates. *ACS Nano* **2018**, *12*, 8531–8539.

[21] García-Lojo, D.; Núñez-Sánchez, S.; Gómez-Graña, S.; Grzelczak, M.; Pastoriza-Santos, I.; Pérez-Juste, J.; Liz-Marzán, L. M. Plasmonic Supercrystals. *Accounts of chemical research* **2019**, *52*, 1855–1864.

[22] Kraus, T.; Malaquin, L.; Schmid, H.; Riess, W.; Spencer, N. D.; Wolf, H. Nanoparticle printing with single-particle resolution. *Nat. Nanotechnology* **2007**, *2*, 570–576.

Chapter 2

Background

2.1 Synthesis of gold nanoparticles

As we have seen in the previous section, the synthesis and use of gold nanoparticles preceded their scientific understanding. While gold nanoparticles were used for centuries as glass staining agents, the first scientific report on the synthesis of gold nanoparticles is published by Faraday in 1857 [1]. In his article, Faraday reports the synthesis of gold nanoparticles from chloroauric acid as a source of gold ions, with water as a solvent and the use of white phosphorous as a reducing agent. Faraday also accounts for the optical properties of such nanoparticles and attributes the production of a "ruby red" color to the reduction of gold to solid-state. Up to date this first synthesis of gold nanoparticles is still exposed in the Faraday museum located in the Royal Institution in London. Interestingly, the approach used nowadays to synthesize gold nanoparticles is not so different from the one Faraday used, although the reducing agent was replaced with less toxic chemicals than white phosphorous such as ascorbic acid. Still, a lot of progress has been made since then, amongst which the seed-mediated approach allowed for drastic improvement in the quality of nanoparticles. Separation of crystallization and growth of nanoparticles used in the seed-mediated synthesis enabled more control on the nanoparticle size and shape compared to the synthesis of gold nanoparticles in situ. Especially, the seed-mediated made possible the synthesis of nanoparticles of different shapes such as spheres [2], rods [3],triangles [4], nanostars [5] and more complex structures [6], as can be seen in **Figure 2.1**.

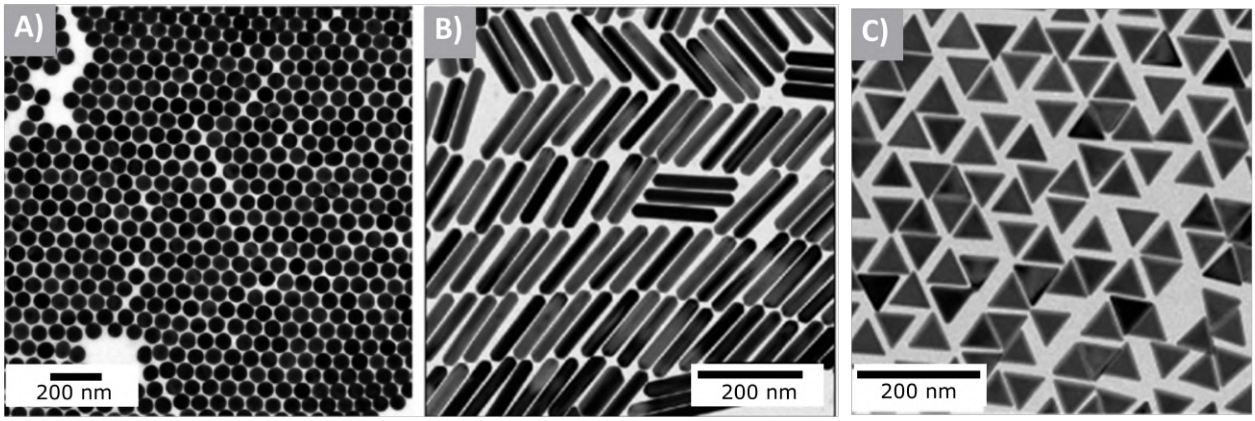

Figure 2.1: Gold nanoparticles of different shapes: a) Spheres reproduced with permission from [7], copyright 2017 American chemical society b) Rods reproduced with permission from [3], copyright 2015 American chemical society c) Triangles reproduced with permission from [4], copyright 2014 American chemical society.

To induce symmetry breaking in the growth of nanoparticles from seeds, the interaction of chemicals with particular crystalline facets of the growing seed is used. The most studied symmetry breaking mechanism is the one used for gold nanorods synthesis. In this case, the initial isotropic seed is overgrown in presence of CTAB and silver ions. Upon growth higher-index 110 and 250 facets are formed and stabilized through the adsorption of CTAB and silver ions [8, 9, 10]. The adsorption of the CTAB and silver ions slows down the growth on the 110 and 250 facets leading to the formation of gold nanorods.

2.2 Self-assembly of gold nanoparticles

Self-assembly is a process in which a disordered system of pre-existing components forms an organized structure or pattern as a consequence of specific local interactions among the components themselves, without external direction. Self-assembly is a powerful tool as it gives the possibility to create nanostructures by carefully designing the functionality of a colloid or the chemistry of its solvent. Especially, the fabrication of monodisperse gold colloids through the seeded growth method enabled the fabrication of complex nanostructures displaying new optical properties. This section gives an overview of the different forces acting on colloids. The

focus will then be put on external forces providing periodical self-assembly of colloids. The optical properties gained by self-assembled gold nanoparticles will be explained in **Section 2.4**

2.2.1 Forces in colloids

Colloidal solutions are prone to different forces that can attract nanoparticles(NPs) together or repel each other. These forces depend on the solvent, on their size, shape, and their material, as well as their surrounding ligand, polymer, or surfactant. By carefully designing the colloidal system, it is possible to induce reversible aggregation of gold nanoparticles, as we will see in this subsection.

Van der Waals forces

Van der Waals (vdW) forces are attractive or repulsive forces between atoms, molecules, and surfaces caused by dipole or induced dipole interactions. Different vdW interactions exist for different types of particles. Polar molecules interact through a permanent dipole - permanent dipole interaction known as the Keesom interaction. The potential of the Keesom force is written [11]

$$\frac{-m_1^2 m_2^2}{3(4\pi\epsilon_0)^2 kTr^6}. \tag{2.1}$$

m_1 and m_2 are the electric dipole moments of both molecules, k is the Boltzman constant, r is the distance between the molecules, T is the temperature and ϵ_0 is the vacuum permittivity. Keesom force is stronger with molecules having larger dipole moments. It is important here to differentiate this force from the Coulomb potential that quantifies the electrostatic interaction between charged particles. In a similar way, polar molecules can induce a dipole on non-polar molecules creating a force known as the Debye force with a potential of

$$\frac{-m_1^2 \alpha_2}{4\pi\epsilon_0^2 r^6}. \tag{2.2}$$

α represents the polarizability of the molecule.

Both Keesom and Debye forces imply the presence of at least one permanent dipole, in nanoparticle solutions the ligands are generally responsible for such interactions. Finally, all

apolar molecules interact together through an induced dipole - induced dipole force known as the London interaction. The combination of those three forces is known as the van der Walls potential and is a key indicator in the stability of a colloid solution. The London interaction has the following potential [12]:

$$U(x) = -\frac{3}{4}\frac{\alpha_1\alpha_2}{(4\pi\epsilon_0)^2 r^6}. \tag{2.3}$$

As we can see the potential of London interaction depends on the polarizability of both molecules. This means that such an interaction will be important in metal nanoparticles as their polarizability is high due to the free electrons of noble metals. Moreover, this potential is strictly negative and leads to an attraction between NPs. It has to be noted here that vdW forces do not include the repulsive force arising from Pauli exclusion principle, such a repulsive force is proportional to $1/r^{12}$ and therefore is stronger than vdW forces at very low distance preventing the collapse of molecules.

It is possible to calculate the vdW interaction of two spheres by integrating the contribution of all the vdW forces of all molecules from each nanoparticle, as Hamaker did in 1937 [13], by doing so we obtain

$$\frac{-A_{121}R}{12d}. \tag{2.4}$$

A is the Hamaker constant, it takes into account the material in between the nanoparticles, the subscript 121 represents the material of the nanoparticle and solvent we take into account, in this case, we consider the NP of material 2 to be in a uniform solvent 1. d is the distance between the nanoparticles and R the radius of the nanoparticle. The Hamaker constant is always positive, therefore the van der Waals interaction between two spheres is always attractive. However, by changing solvents, the Hamaker constant can change, which leads to stronger or weaker van der Waals interactions between nanoparticles. In view of the **Equation 2.4**, we see that bigger NPs are prone to higher van der Waals attraction which can become very important in large colloidal systems.

Electric double layer

Electrostatic forces are very important in self-assembly processes, they are quantified by the Coulomb potential

$$U(x) = \frac{Q_1 Q_2}{4\pi\epsilon_0 r^2}. \tag{2.5}$$

If the charges are of the same sign, which is generally the case in colloids, then the Coulomb will induce a repulsive forces. A typical example in colloids is the use of surfactant molecules that adsorb on the surface of nanoparticles and create a double layer of oppositely charged ions impeding nanoparticles to aggregate. The Derjaguin-Landau-Verwey-Overbeek (DLVO) theory describes the impact of van der Waals forces and electric double layer on two hard spheres. If the sum of the two potentials is negative, then the colloidal solution is not stable and the nanoparticles aggregate, and if the sum is positive, then the solution is stable and the nanoparticles are well dispersed in the solution. The electrical double layer repulsion energy can be written as [14]

$$E_{\text{el}} = C_{\text{el}} * e^{-\kappa * d}. \tag{2.6}$$

With κ the Debye constant proportionnal to temperature and C_{el} a constant depending on the geometry of the interaction entities, the solution condition and the charge of the surfactant of the surface of the interacting objects. The constant C_{el} can be calculated using the Poisson-Boltzmann equation in low potential case (also known as Debye-Hückel equation) [15] and the linear superposition approximation.

Steric repulsion

In colloidal solutions, steric repulsion arises due to the presence of polymer chains on the nanoparticle. The case where several polymer chains are attached to the NPs, covering its whole surface will be considered, each polymer has a length d. When two coated nanoparticles approach a separation distance of 2d the adsorbed polymer start to overlap, in such a situation either the polymer gets compressed either they get interdigitated. In the situation where the

polymer get interdigitated, the loss of solvent is thermodynamically favored if the polymer is in a bad solvent [16].

When the separation distance between the two nanoparticles is smaller than 2d, the spatial extension of the polymer is diminished by the presence of the opposing nanoparticles. This compression results in a loss of configurational entropy and hence creates a repulsion force in the form of an elastic restoring force [17]. This elastic force is always repulsive no matter if the polymer is in an appropriate solvent or not. Steric repulsion plays an important role in colloidal stability, by adding a polymer on the surface of the nanoparticle, it is possible to prevent the irreversible aggregation of NPs. Especially, such stabilization has been used extensively for the stability of inks and paints based on colloid particles [18]. Steric repulsion is also of great use to control interparticle distances in self-assembled clusters of NPs.

Hydrophobic attraction

In nanoparticle dispersions, polymer coatings are prone to hydrophobic interactions. Such interactions come from the interaction of solvent molecules with a polymer attached to the NP. For instance, in the case where nanoparticles are coated with a hydrophobic polymer and dispersed in water, the organization of water molecules around the hydrophobic polymer cost a lot of energy due to the spatial reorganization of water molecules. Therefore loss of surface contact between the polymer and the solvent by polymer interdigitation is entropically favored, causing an attraction force between two coated nanoparticles. In other words, in water, nanoparticles coated with a hydrophobic polymer undergo an attractive force due to hydrophobic interactions. There doesn't exist an accepted theory on hydrophobic interactions, however, an empirical law was proposed by Israelachvili [19]:

$$E_{hydro} = -\gamma(a - a_0)e^{-d/D_{\mathrm{hydro}}}. \tag{2.7}$$

γ is the interfacial energy of the polymer in a specific solvent composition, $(a - a_0)$ is a parameter representing the solubility of the polymer in the solvent and D_{hydro} is the hydrophobic length decay which represents the distance over which the hydrophobic force apply. Here we can see that the hydrophobic interaction highly depends on the interaction of the polymer with the solvent, if the polymer has a high interfacial energy the hydrophobic attraction will be

higher which makes sense as the polymer will tend to have less interaction with the solvent to minimize the energy of the system.

Assembly of gold nanoparticles in solution

By designing gold NP ligands or functionalization it is possible to control the aggregation state of nanoparticles in solution by an external trigger [19] such as temperature [20], solvent [21, 22] or pH [23]. Changing temperature mainly acts on electrostatic interaction, an increase of the temperature leads to higher electrostatic interaction as can be seen in the equation of the electric double layer (**Equation 2.6**). For instance, reversible assembly of gold nanospheres using Bis(p-sulfonatophenyl)phenylphosphine dihydrate dipotassium salt (BSPP) ligand and temperature as a trigger was shown. The assembly of BSPP coated gold nanoparticles was monitored by a color change of the nanoparticle solution due to plasmonic coupling between various nanoparticles (**Figure 2.2 a**). Calculations of the interaction potential between the nanoparticles explain the reversible assembly of the gold nanoparticles through a minimum in the interaction potential as can be seen in **Figure 2.2 b**.

It can be seen that the total potential energy between nanoparticles becomes positive with temperature increase and, especially the minimum of the interaction potential seen at low temperatures is disappearing, explaining the nanoparticles repulsion at high temperatures.

In another way, polystyrene coated nanospheres were reversibly aggregated by changing their solvent from tetrahydrofuran(THF) to water [22, 21]. Water is not an appropriate solvent for polystyrene, therefore the replacement of THF per water induces the aggregation of nanoparticles through the hydrophobic attraction. Polystyrene coated NPs were imaged in their aggregated and non-aggregated state by encapsulating nanoparticles in a silica capsule as can be seen in **Figure 2.2 d**.

2.2.2 External forces

This thesis focus on the fabrication of periodically arranged gold nanoparticles. The main strategy available for the self-assembly of periodical structure of colloidal nanoparticles is to use a nanostructured template. For that, nanoparticles are driven in the wells of a nanostructured template through different external forces. This subsection exposes the different external forces

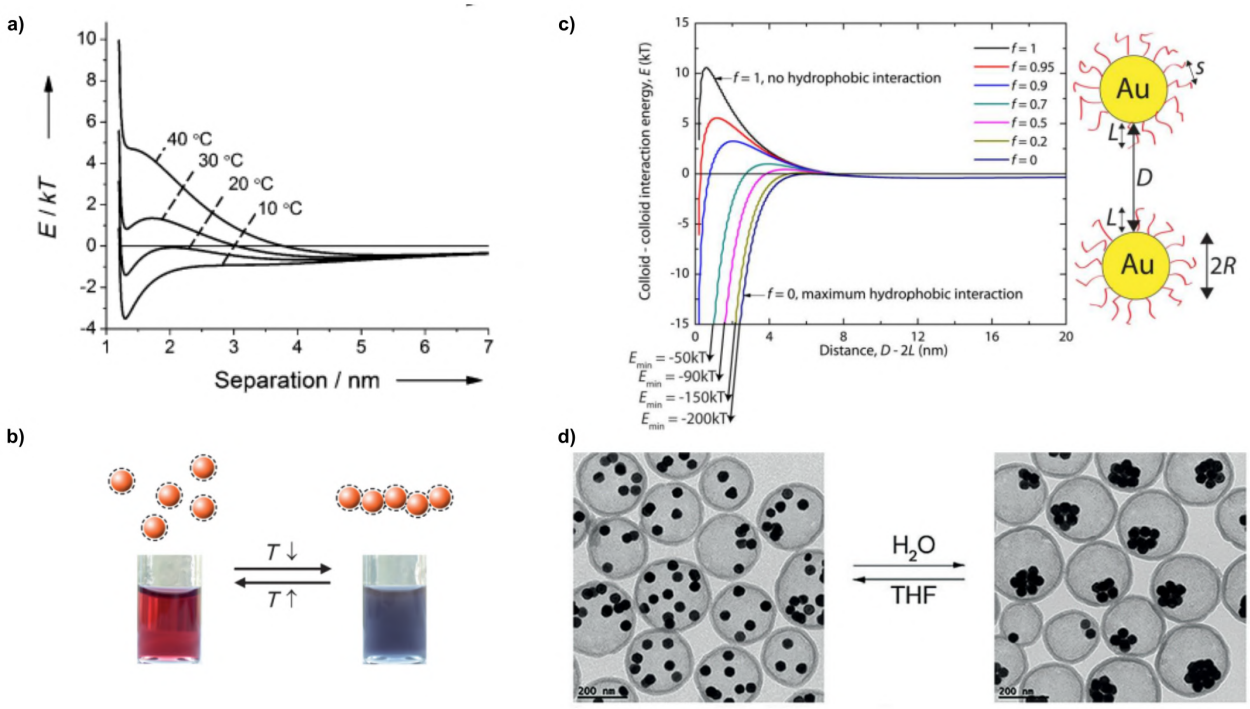

Figure 2.2: Reversible self-asembly of nanoparticles in solution using temperature or solvent change : a) Total interaction energy in function of distance at different temperatures for gold nanospheres coated with BSPP b) color change of the nanoparticle solution upon nanoparticle aggregation mediated by cooling reproduced with permission from [20], copyright 2012 Wiley c) Total interaction energy as a function of distance in different solvent for gold nanospheres coated with polystyrene reproduced with permission from [21], copyright 2012 American Chemical Society. d) SEM images of polystyrene coated gold nanospheres encapsulated into silica in an aggregated or non aggregated state reproduced from [22], licensed under CC BY-NC-ND 4.0.

that can be applied for the self assembly of single gold NPs into periodically arranged gold NP structures.

Electrostatic forces

As it was exposed in **Section 2.2.1**, nanoparticles can get polarized by a net charge from a surface through the Debye potential. Charged nanoparticles can also interact with a charged surface through the Coulomb potential. While most of the electrostatic self-assembly strategies use charged gold nanoparticles to interact with electrostatic potential, it is theoretically possible to attract bare gold NPs through VdW forces. One approach is to use positively charged

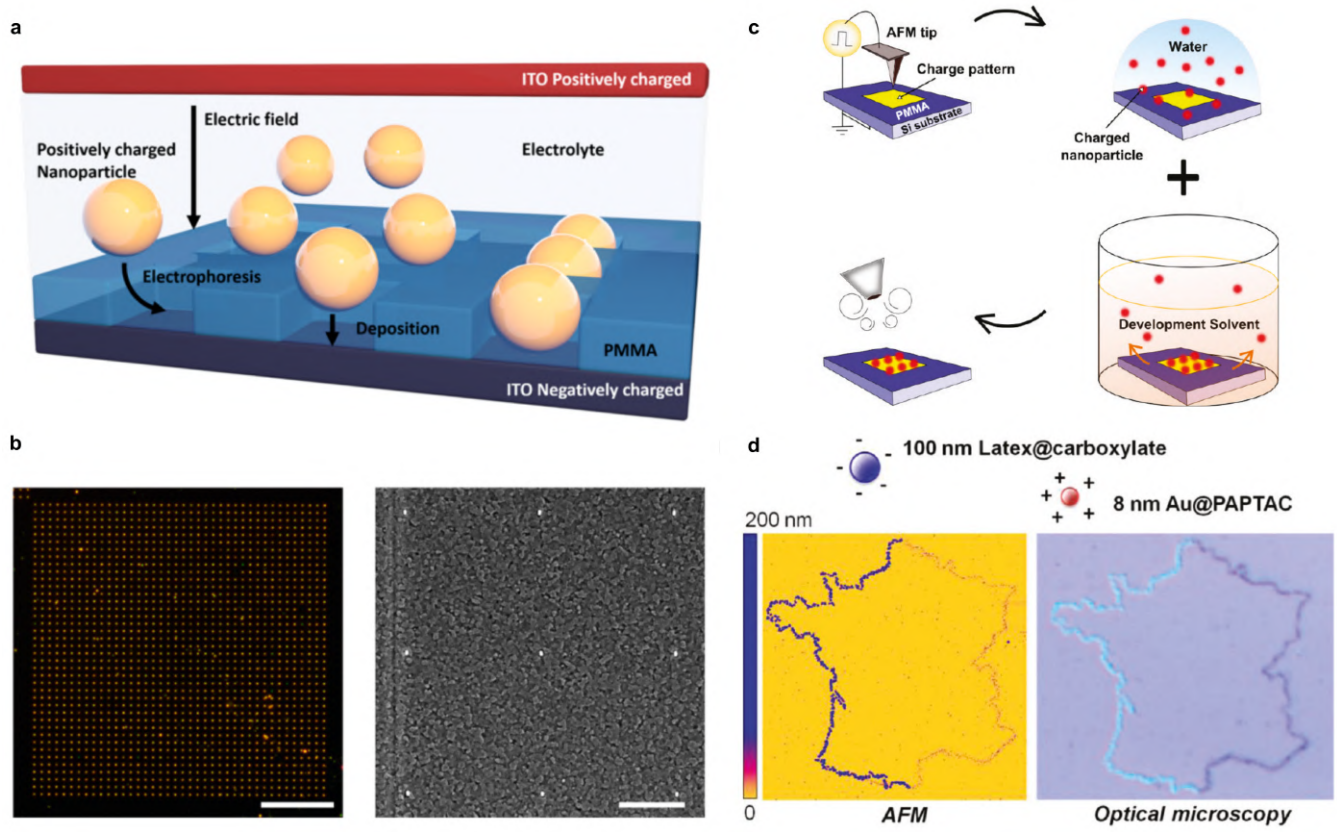

Figure 2.3: a)Scheme of charged gold nanoparticle self-assembly using electrostatic potential created between two electrodes. b) Dark-field and Scanning electron microscopy(SEM) image of single nanospheres reproduced from lattice made by electrostatic templated self-assembly, reproduced with permission from [24], copyright 2018 Americal Chemical Society. c) Scheme of nanoxerography process, charged particles are trapped in the substrate by AFM charge writing. d) AFM and optical microscopy images of self-assembled oppositely charged Latex and gold nanoparticles. By trapping positive or negative charges it is possible to attract differently charged NPs reproduced with permission from [25], copyright 2011 American Chemical Society.

gold NPs and attract gold NPs in nanostructured template through a constant electrostatic potential created between two electrodes (**Figure 2.3**) [24]. This approach leads to the patterned assembly of single gold nanospheres as can be seen in **Figure 2.3 b**. Another approach depicted in **Figure 2.3 c** is to trap locally electrons in a substrate, through AFM writing [25] or micro-contact printing with a nanostructured electrode. This approach, also known as nanoxerography, leads to the attraction and immobilization of nanoparticles by charges trapped in the substrate. Methods based on electrostatic potential as attractive forces, generally fail in

assembling close-packed clusters of NPs because of the repulsive Coulomb force between the charged NPs.

Capillary forces

Nanoparticle assembly through capillary forces is generally done through the use of a nanostructured template [26]. In such an assembly scheme, a meniscus travels through all the wells present on the template, generally by moving a blade. Due to evaporation, nanoparticles are transported to the meniscus through convection flows. At the meniscus, the nanoparticles can either: (i) recirculate towards the bulk volume, (ii) self-assemble into a close-packed film through VdW forces principally. The creation of such a film, known as the accumulation zone, is primordial for capillary self-assembly. In fact, the accumulation zone occupies all the volume available at the meniscus to minimize its free energy, and consequently nanoparticles will fill the holes of the templates. On **Figure 2.4 b** one can see ,on the top right of the image, a microscopy image of an accumulation zone (in light blue), created during a process of capillary self-assembly. In the accumulation zone, one can see two nanoparticles trapped in each hole [27].

When traveling through the template, the meniscus gets pinned at the edges of each wells leading to a deformation of the meniscus as illustrated on **Figure 2.4 a**. This deformation induces a restoring force directed perpendicularly to the meniscus thus acting to keep the NP in the hole. If there is more than one particle in the hole, as depicted in **Figure 2.4 a**, the particle further away from the meniscus is feeling a weaker capillary force from the meniscus and thus can be pushed away by the first NP. This is illustrated in **Figure 2.4 b**, in the accumulation zone, two NPs are trapped in the wells (light blue on top of the image) while down the accumulation zone (i.e where the meniscus has already passed) only one NP is remaining in the hole.

Removal of NPs trapped in the wells of a nanostructured template depends a lot on the depth of the hole, as demonstrated in **Figure 2.4 c and d**. Deep holes favor the anchoring of the NPs in the holes. Capillary-assisted self-assembly is one of the most powerful techniques for self-assembly of nanoparticles as it doesn't depend on the material of the nanoparticles neither the shape of the nanoparticles [28, 29]. Moreover, the assembly setup for capillary-assisted self-assembly is relatively simple and can easily be scalable.

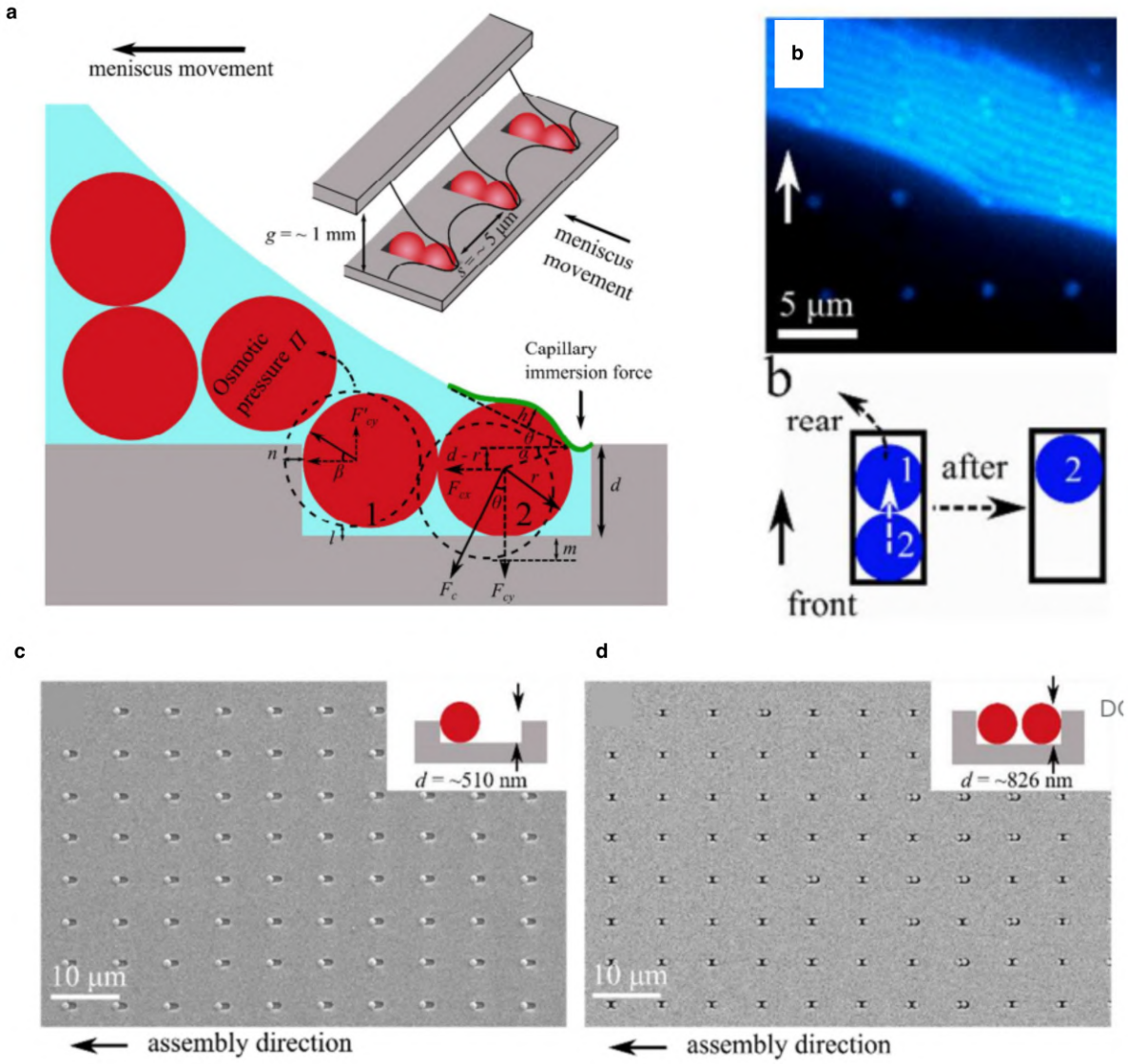

Figure 2.4: a) Forces acting on nanoparticles in capillary assisted self assembly b) Optical images of silica nanoparticles assembled in nanostructured holes, we can see an accumulation zone of NPs in the meniscus. c) and d) SEM images of latex nanoparticles assembled in holes of different depth. Higher depth leads to the assembly of 2 nanoparticles per holes. Reproduced with permission from [27], copyright 2015 Royal Society of Chemistry.

To attract particles into a cavity, it is also possible to functionalize the wells of a nanostructured template with molecules that create a covalent bond with the nanoparticle. Different approaches can be used, the nanoparticle can be functionalized with a ligand that will interact chemically with the molecule bound into the cavity or the molecule in the cavity chemically interacts directly with the nanoparticle. For example, the holes of a patterned PMMA layer

on glass can be functionalized with ThioSilane, the silane group will interact with the available region of glass substrates while the thiol groups are known for binding covalently to gold [30]. When immersed in a gold NPs solution, Thiol groups will react with the gold NPs therefore blocking the NPs in the holes of PMMA layer [31].

Another approach uses DNA functionalized gold NPs, the wells of a patterned template are functionalized with a DNA complementary to the one on the NP such that both react and nanoparticles are immobilized in the wells [32]. Subsequently, it is possible to assemble another layer of NPs on top of the first NPs layer by designing another complementary DNA. Such assembly strategy allows for the fabrication of complex 3D nanostructures [33].

2.3 Plasmonic properties of gold

In 1902 Wood observed a discontinuity in the spectra of a gold grating excited by continuous light [34, 35]: "I was astounded to find that under certain conditions, the drop from maximum illumination to a minimum, a drop certainly of from 10 to 1, occurred within a range of wavelengths not greater than the distance between the sodium lines". Such an experiment can be seen as the birth of modern plasmonics. At the time Wood, had no explanation for the phenomenon he saw, but Rayleigh in 1907 explained one of the anomalies by the excitation of an in-plane diffracted wave, he also proposed a formula to calculate the wavelength of such an anomaly [36]. Then in 1947, Fano explained another type of the anomalies seen by Wood by some "Leaky waves supported by the gratings" [37]. Though this is very close to the definition of surface plasmon, we have to wait until 1957 for the prediction of surface plasmons by Richtie [38]. Up to date, the study of plasmonic phenomena remains very active and fascinating. In this part, the phenomena of surface plasmons and localized surface plasmons (LSPR) will be explained.

2.3.1 Surface plasmon resonance

Metals are characterized by a high number of free electrons as opposed to insulators, which have all of their electrons bound locally to an atom. This means that electrons can travel in metals, under a potential bias for example. Light as an electromagnetic wave can create oscillations of the free electrons of metals. At a certain wavelength depending on the structure of the metal

and its material, a collective oscillation of the free electrons, also known as surface plasmons, can be excited [39]. The interaction of light with metals is dominated by the permittivity function $\epsilon(\omega)$ and linked to the electric field by

$$D = \epsilon_0 \epsilon E \tag{2.8}$$

,

where D is the electric displacement, E the electric field and ϵ_0 is the vacuum permittivity. Permittivity is a measure of the polarizability of a material, in other words it measure how freely electrons move inside a material.

It is easy to calculate the permittivity of free electrons in a metal by considering the Drude-Sommerfeld approximation [40]. In the Drude-Sommerfeld approximation, electrons are treated as free charges, while metal atoms are considered as fixed Ions. The relaxation of the free electrons happens only through collision and the electron-electron interactions are neglected. In this approximation:

$$\epsilon = 1 - \frac{\omega_{\mathrm{p}}^2}{\omega^2 + i\gamma\omega}, \tag{2.9}$$

with

$$\omega_{\mathrm{p}} = \sqrt{\frac{Ne^2}{m\epsilon_0}}. \tag{2.10}$$

In this equation ω_{p} is the bulk plasma frequency and γ is the damping constant. N is the density of free electrons, e the charge of an electron, and m the effective mass of an electron. Optical excitation of metal electrons above the plasma frequency creates positively and negatively charged regions due to the oscillations of the electrons around a positively charged metal core. These oscillations are known as plasmon resonances. For noble metals such as gold and silver, the bulk plasmon frequencies are close to the visible, rendering them interesting to excite plasmon polaritons at visible wavelength. There exist different types of plasmon resonances, bulk plasmons, surface plasmons, and localized surface plasmons. Bulk plasmons are longitudinal waves as opposed to surface plasmons that are transverse waves traveling at the metal-dielectric interface [41]. To understand the excitation of surface plasmons in flat metal

films, it is necessary to resolve Maxwell's equations for transverse magnetic waves and impose a continuity condition at the metal-dielectric interface. By doing so we obtain the dispersion relation of surface plasmons, written

$$k_{\mathrm{sp}} = (\omega/c)\sqrt{(\epsilon_1\epsilon_2)/(\epsilon_1+\epsilon_2)}, \tag{2.11}$$

with k_{sp} the wavevector of surface plasmons, c the speed of light , ϵ_1 the permittivity function of the metal, and ϵ_2 the permittivity of the dielectric. If one plots this dispersion relation along with the dispersion relation of light into air, it can be seen that both curves do not cross (**Figure 2.5**). This means that one cannot couple light to a surface plasmon if light incides from air. For exciting surface plasmons, one needs to modify the dispersion relation of light so that it intersects with the dispersion of surface plasmons. There are different ways of changing the dispersion relation of light, the most common and straightforward is to change the material in which light is propagating.

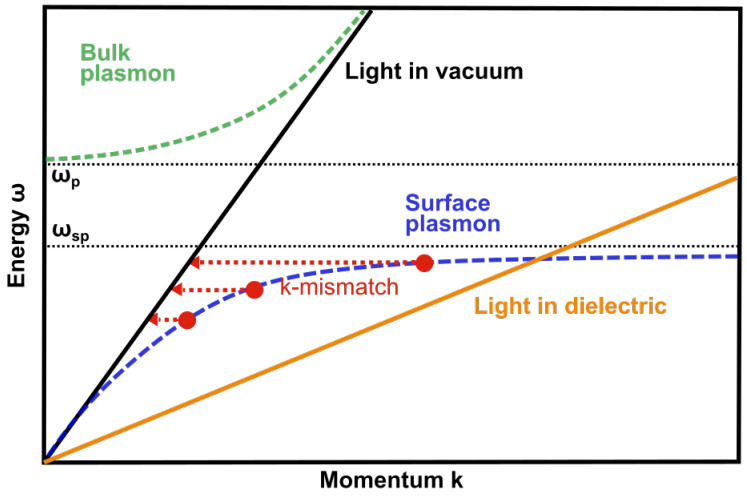

Figure 2.5: Dispersion of light and surface plasmons.

The dispersion of light in a dielectric is plotted in **Figure 2.5**, by replacing air by a dielectric the dispersion line of the incident light and the dispersion relation of surface plasmon overlaps at a specific wavenumber. In other words, surface plasmon resonance can only be excited if light incides from a dielectric material. In Kretcschman configuration, introduced in 1971 [42], a dielectric prism is used to couple light to surface plasmons. Concretely, the k-vector of incident light is tuned to the k-vector of surface plasmons by changing the angle of incidence. In other

words, at a particular angle of incidence, light couples to a surface plasmon resonance resulting in absorption of light by the metal. The incidence angle at which surface plasmon is excited depends strongly on the refractive index surrounding of the metal film. For instance, binding of several molecules on the gold film will change the surrounding refractive index of the metal film and consequently change the angle at which a surface plasmon resonance is excited. For this reason, the Kretcshman configuration is widely used in sensing applications based on refractive index changes [43].

There exist other strategies to modify the k-vector of the incident light, for instance, the use of a grating before the metal or fabricated directly over the metal layer allows to change the k-vector and to couple to surface plasmon modes. Generally, corrugated surfaces allow to change the k-vector of light and couple to surface plasmon. Specifically, the use of nanoparticles to couple to surface plasmons is very appealing as it will be exposed in the next subsection.

2.3.2 Localized surface plasmon resonance

In a metallic nanoparticle, dimension restrictions along all the axis impose a localized oscillation of the surface charge density under light excitation. Metallic nanoparticles generally have a volume substantially smaller than the wavelength of light implying an approximately constant electric field over the whole NP. This approximation is known as the quasi-static approximation regime [44, 45]. In other words, the electron cloud of the nanoparticle is entirely affected by light, creating a net charge separation. As a consequence, the only mode that can be excited in small nanoparticles is of dipolar nature. The bigger the NP is, the larger the net charge separation, affecting absorption and scattering properties of the NP. Also for larger nanoparticles, the quasi-static approximation cannot be totally fulfilled. Using the Laplace equation and the quasi-static approximation regime it is possible to calculate the polarizability of such a nanoparticle by

$$P = \epsilon_0 \epsilon_\mathrm{m} \alpha E_0, \tag{2.12}$$

with

$$\alpha = 4\pi a^3 \frac{\epsilon - \epsilon_\mathrm{m}}{\epsilon + 2\epsilon_\mathrm{m}}. \tag{2.13}$$

α is the polarizability of the nanosphere, a the radius of the nanosphere, ϵ_{m} the permittivity of the metal. Though from **Equation** (2.13) it is seen that the polarizability of a nanosphere undergoes a resonant condition:

$$\epsilon = -2\epsilon_m. \tag{2.14}$$

This resonant condition is known as Frölich condition and using the expression of the dielectric constant for metal in the Drude-Sommerfeld model (**Equation** (2.9)) we find that: $\omega = \omega_{\mathrm{p}}/\sqrt{(3)}$

Thus for small NPs resonant behavior results in the creation of an electric dipole at a specific wavelength determined by the Frölich condition. This resonance results in an increased absorption and scattering of light by the nanosphere.

For the moment, only the case of small NPs was considered. However, it has been observed that an increase in the gold NP size induces a redshift of its plasmon resonance [46], which is not contemplated in the Frölich condition. This can be explained by the fact that the surface density charges in the NPs of opposite charges undergo an electrostatic restoring force. This restoring force is lowered with the separation of charges induced by the higher dimension of bigger NP. This reduced restoring force decreases the frequency of oscillation of the electron cloud in the NP, leading to a redshift of the plasmonic resonances. Moreover, with large nanoparticles, the quasi-static approximation is not true anymore and higher-order modes have to be taken into account.

2.3.3 Shape effect on localized surface plasmon resonance

As it was described in the previous section, nanospheres behave like an electric dipole under plasmon resonance, they absorb and scatter light at wavelength depending on their size. Thanks to the development of colloidal chemistry many different gold nanoparticles shapes can be synthesized such as nanorods [47], nanotriangles [4], nanostars [48]. Due to their different symmetry, anisotropic nanoparticles display different optical properties as compared to nanospheres [49]. This is exemplarily shown in nanorods that display two dipolar resonances: one along the short axis of the axis of the nanorod (transverse plasmon) and the other along

the long axis of the nanorod (longitudinal plasmon). The longitudinal plasmon is far red-shifted compared to the transverse plasmon due to the longer path of the electron movements in the longitudinal axis of the nanorods. Also, the retardation effect is higher in nanorods, as compared to nanospheres, due to a higher charge separation induced by the geometry of the nanorod. In general, the formation of tips induces a higher charge separation due to a higher localization of the surface charges at the tips cause by the increased curvature of the tips. This higher charge separation results in a redshift of the longitudinal plasmon wavelength in gold nanorods with lower width. This explains why not only the length of the nanorod affect the longitudinal plasmon wavelength, but also the aspect ratio has a strong influence on the spectral positions of the plasmonic resonances.

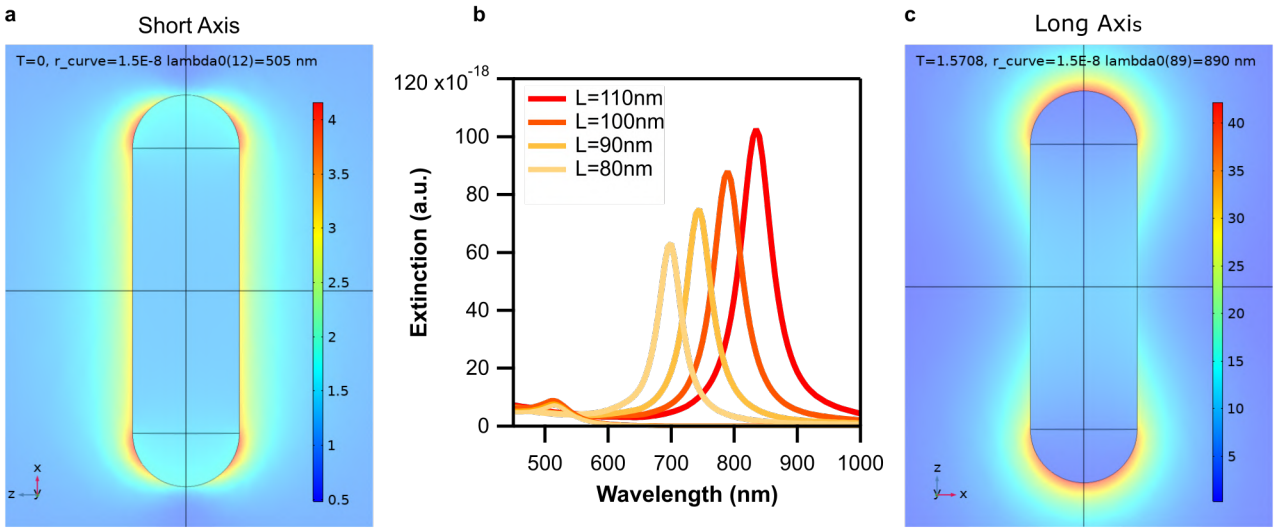

Figure 2.6: Plasmon resonance of gold nanorods simulated by the boundary element method (FEM). a) Simulated near-field of the transversal plasmon resonance from a gold nanorod of 110× 30 nm. b) Simulated extinction of gold nanorods of different length with a fixed thickness of 30 nm. c) Simulated near-field of the longitudinal plasmon resonance from a gold nanorod of 110× 30 nm.

For those complex nanoparticle geometries, it is generally difficult to solve Maxwell equations analytically however it is possible to numerically calculate their optical properties using finite-difference time-domain method, boundary element method, discrete dipole approximation or coupled-wave analysis. Here it is worth mentioning that Gans calculated analytically the optical behavior of ellipsoidal nanoparticles already in 1912 [36]. More recently Garcia De Abajo

proposed an analytical resolution of Maxwell's equations for nanorods [50]. On **Figure 2.6**, Finite element method simulated absorption spectra of nanorods with different lengths and a fixed width can be found. We can see that nanorods have two plasmon modes, the resonance towards the red part of the spectrum is attributed to a longitudinal dipolar mode while the resonance in the blue region is attributed to a transversal dipolar mode. The transversal mode wavelength stays constant at different nanorod lengths while the longitudinal mode redshifts with higher nanorod lengths [51]. More interestingly, the near-field intensities of the two modes are very different, the longitudinal mode has a stronger field enhancement located at the tips compared to the field enhancement of the transversal mode field enhancement located at the side of the rod. Finally, not only do anisotropic nanoparticles present a better tunability of their plasmon resonances through dimension control but they also present dramatic near-field enhancement at their tips.

2.4 Optical properties of gold nanoparticle superlattices

Self-assembly processes allow for the fabrication of nanoparticle clusters. Superlattices, which are periodically arranged clusters of nanoparticles display interesting optical properties due to the near-field and far-field coupling of gold nanoparticles. This part explains the different coupling phenomena taking place in gold nanoparticle superlattices.

2.4.1 Coupling between two gold nanospheres

When the distance between two nanoparticles is in the order of their radius, the electron clouds of each nanoparticle start to interact, which is a well-known plasmonic coupling effect [52, 53]. The detailed theory will not be treated here, however, Nordlander et al made an analogy of plasmonic modes with molecular orbital that is rather easy to understand [54]. In **Section 2.3.2** it was shown that under plasmonic resonance nanoparticles gain the property of an electric dipole. The nature of the plasmonic mode created by nanoparticle coupling strongly depends on the orientation of such dipoles with respect to each other.

In **Figure 2.7** one can see the different dipole orientations possible in the case of dimers of nanospheres. There exist two radiative modes: one where the two dipoles are parallel to

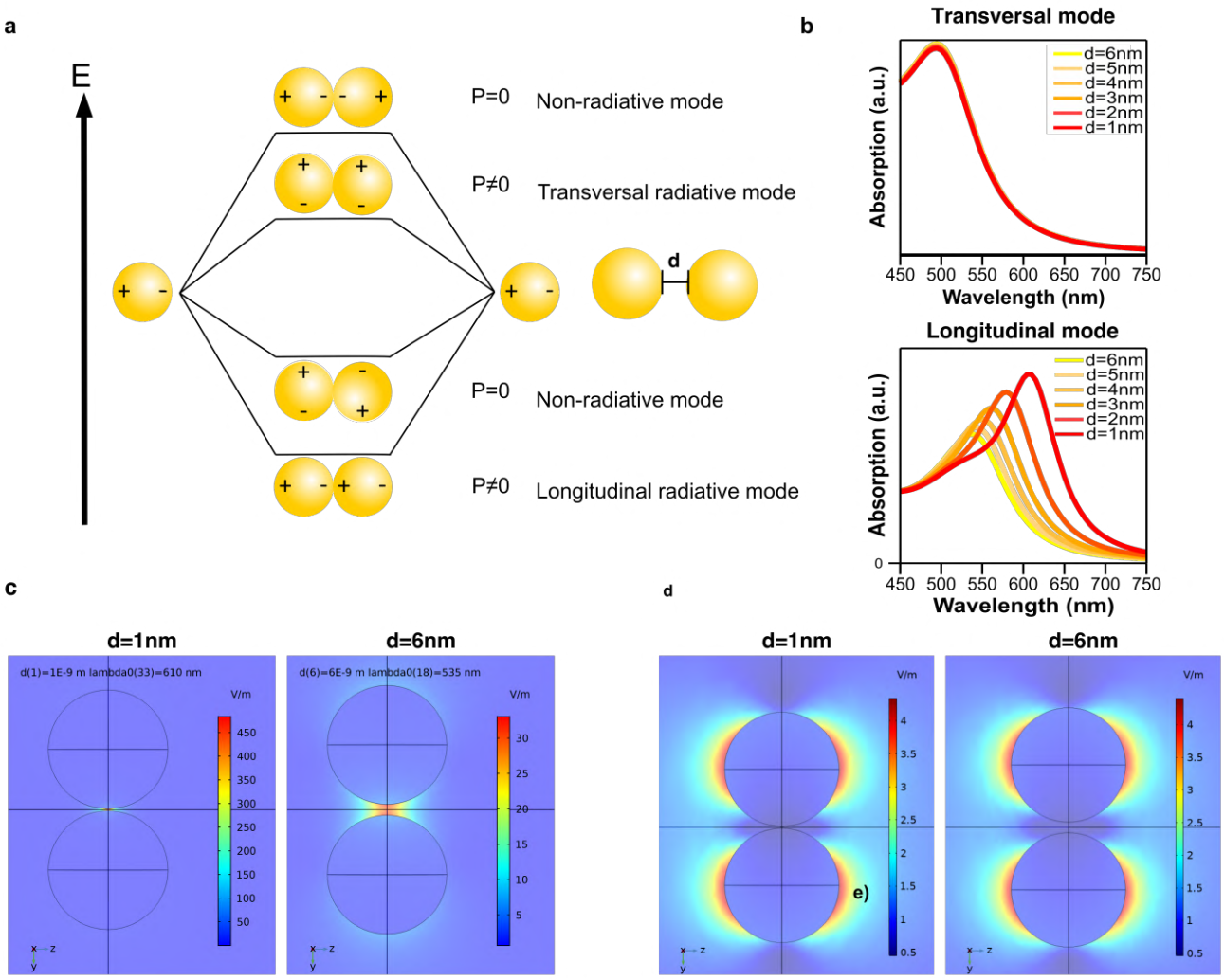

Figure 2.7: Plasmonic coupling between two gold nanospheres. a)Energetic diagram of plasmonic hybridization. b)Near-field plots of the longitudinal mode of nanospheres dimer with different interparticle distances. c) Near-field plots of the transversal mode of nanospheres dimer with different interparticle distances. d) Absorption of the nanosphere dimer longitudinal mode at different interparticle distances. e) Absorption of the nanosphere dimer transversal mode at different interparticle distances.

the longitudinal axis and the other where the dipoles are parallel to the transversal axis. The longitudinal mode leads to a more stable energy mode or a redshift of the resonance while the transversal mode leads to a slightly higher energy mode or slight blueshift of the plasmon resonance. To illustrate such a phenomenon simulated FEM absorption spectra of nanospheres dimers with different interparticle spacing and polarization along the short or long axis of the dimer can be found in **Figure 2.7 b,c**. Polarization along the long axis of the dimer enables for

coupling to the longitudinal resonance while polarization along the short axis enables coupling to the transversal resonance. While the longitudinal resonance wavelength increases with lower interparticle distance, the transversal resonance stays constant, as can be seen in **Figure 2.7 b**. Experimentally, Electron beam lithography fabrication of gold nanoparticles dimers, with defined interparticle distances by El-Sayed, allowed for the measurement of plasmon resonance dependence with interparticle distance, also known as plasmon ruler equation [55].

Even more interesting is the near-field behavior of such dimers: in **Figure 2.7 b,c** we can see near-field plots of a dimer excited along the transversal or the longitudinal axis. The transversal mode behaves similarly to a normal dipole resonance, while the longitudinal mode displays a high near field enhancement at the junction of the two nanoparticles. With lower interparticle distance the electric field gets confined into a smaller volume at the junction of the two nanospheres leading to a higher near-field enhancement. As we will see in **Subsection 2.5.1** such a dramatic near-field enhancement is very important for sensing applications.

2.4.2 Coupling between several gold nanospheres

Nanoparticle chains comprising a higher number of nanoparticles display stronger nanoparticle coupling. In the case more than two nanoparticles are present in the NP chain, new modes arise from plasmonic hybridization [56]. Especially the lowest energy mode, also called subradiant mode, undergoes a gradual redshift until a certain limit. When a certain number of nanoparticles are in a line, the first NP doesn't feel anymore the influence of the last NP on its electron cloud, therefore adding one more NP will not lead to any shift of the plasmonic resonance. This is known as the infinite chain limit [57, 58], which is attained around 10 NPs for different sizes of nanoparticles.

For instance, plasmonic properties of 93 nm nanosphere chains of different lengths can be found in **Figure 2.8**. For a dimer, the subradiant mode is found around 700 nm, while for a longer chain of 10 nanoparticles the subradiant mode redshifts to around 1200 nm. We can see that by adding more NPs to the chain the mode doesn't shift further away. More importantly, NP chains can exhibit higher electric field enhancement than dimers depending on the considered wavelength, the sizes of the NPs, and the number of NPs in the chain [59]

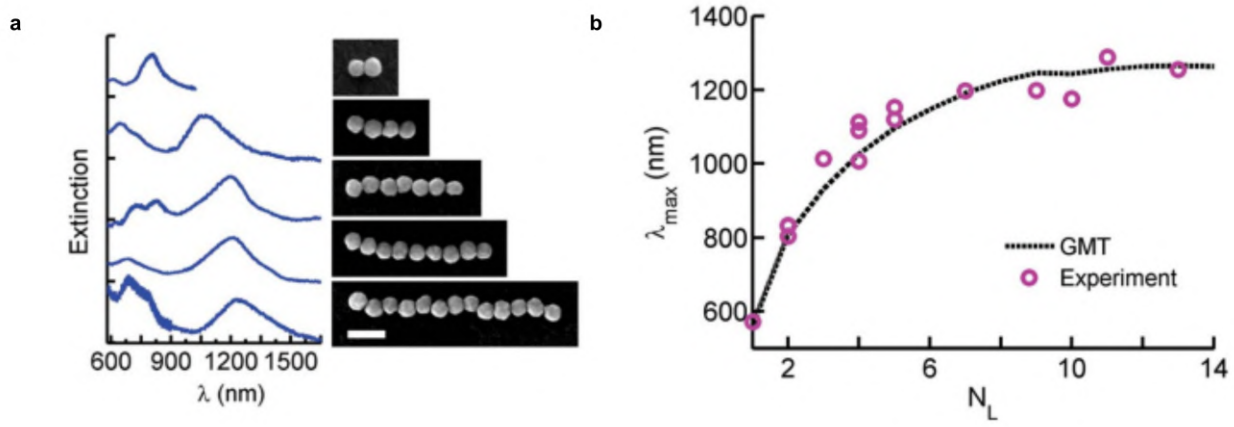

Figure 2.8: Plasmonic coupling between several nanospheres. a) Extinction of nanospheres chains containing different number of nanoparticles and SEM images of the nanoparticle lines b) Evolution of the subradiant plasmon mode in function of the number of nanoparticles. Reproduced with permission from [57], copyright 2014 Royal Society of Chemistry.

2.4.3 Rayleigh-Wood anomaly and surface lattice plasmon resonances

Subsection 2.4.1 and **2.4.2** described the near-field coupling between nanoparticles, however under certain conditions nanoparticles can couple in the far-field as well [60]. Such a far-field coupling can happen when nanoparticles are in a periodical arrangement. This section will review the necessary conditions for far-field coupling and expose the implication of far-field coupling on optical properties.

When arranged into a grating, gold nanoparticles can diffract light in-plane, such an in-plane diffracted order is known as a Rayleigh-Wood anomaly. Due to the in-plane diffracted order, a sudden drop in the reflectivity is observed at a wavelength depending on the period of the structure. This anomaly which was first observed by Wood, was subsequently explained by Rayleigh. The wavelength of the Rayleigh anomaly can be simply calculated by considering the grating equation:

$$n_{\text{substrate}} sin(\theta_{\text{dif}}) = n_{\text{superstrate}} sin(\theta_{\text{inc}}) + m\frac{\lambda_0}{L}. \tag{2.15}$$

For Rayleigh anomaly, θ_{dif} =90° and normal incidence (θ_{inc} =0°) we simplify the grating

equation to

$$\lambda_0 = L n_{\text{substrate}}. \tag{2.16}$$

$n_{\text{substrate}}$ is the refractive index of the substrate, $n_{\text{superstrate}}$ is the refractive index of the superstrate, θ_{inc} is the incident angle, L is the periodicity of the superlattice.

Surface lattice plasmon resonances (SLR) are resonant phenomena arising from the constructive interference of scattered fields from the substructure of the grating. SLR are excited next to Rayleigh anomalies and their wavelength depends on the period of the grating, its materials, and the geometry of the sub-unit. As a rule of thumb, if Rayleigh anomaly's wavelength is matching the grating sub-unit plasmon resonance, it will steer up their absorption resulting in a sharp and intense plasmon resonance [61]. By changing the lattice period, the refractive index of the substrate, or the angle of incidence we can shift the Rayleigh anomaly and thus tune lattice plasmons to different wavelengths [62, 63, 64, 65]. Lattice effects therefore allow to have one more level of control on the plasmonic behavior of the plasmon properties of nanoparticles.

Far-field coupling of nanoparticles enhances the near-field of nanoparticles at a wavelength depending on the lattice period [66]. Thanks to this effect it is possible to increase the near-field at specific wavelengths by designing lattices of gold nanoparticles. Remarkably, the electromagnetic field is enhanced in the close vicinity of the nanoparticles but it is also enhanced in between the cluster [60].

As an interference phenomenon between the scattered field of each grating sub-units, the SLR wavelength also depends on the plasmonic property of the inner structure. Indeed Barnes and coworkers studied the influence of nanoparticle size on the wavelength of lattice plasmon. They found that an increase of the nanoparticle size results in an increase of the lattice plasmon wavelength(of few 10s nm) [43]. Such an effect can be understood by the fact that light scattered by each sub-unit need to be in phase to interfere constructively to create a lattice plasmon. However bigger NPs induce a larger phase-shift due to the retardation effect, therefore leading to a redshift of the lattice plasmon. Lattice plasmon unlike Rayleigh anomaly depends on the size/type of the nanostructure as well as on the material. Lattice plasmons depending

are always shifted towards the red of some nm and the Rayleigh anomaly is only used as an approximation.

Lattice plasmons are highly dependent on the uniformity of the lattice sub-unit. Disorder in a gold NP lattice results in broader lattice plasmon resonances but also in a weaker near-field enhancement. Auguié et al shown that disorder in the placement of NPs and NPs size dispersion lead to weaker and broader lattice plasmon resonances [24]

2.4.4 Plasmonic heating

Plasmonic heating happens thanks to the increased absorption cross-section of metallic nanoparticles at their plasmonic resonance. At resonance, heating by Joule dissipation increases thanks to the amplified movement of conduction electrons. As a result, the heating efficiency of metallic nanostructures increases with the absorption cross-section of nanoparticles, for instance, Kuttner et al shown that core-satellite assemblies of nanospheres on nanorods possess more efficient heating than nanorods at 808 nm excitation [67]. Similarly, dispersed nanorods heat more than dispersed nanospheres in the NIR thanks to their increased absorption in the NIR [68]. Finally, it is also possible to use the properties of plasmonic coupling to increase the absorption cross-section in a broad range of wavelength depending on interparticle distance, size, and shape of the nanoparticles as discussed in the previous sections [69]. In solutions, temperature changes up to 70 °C have been reported however this depends a lot on the power of the laser used and the concentrations of nanoparticles in solution [70, 71].

When working with nanoparticles on a substrate the situation becomes different as the thermal conductivity of the substrate and the superstrate can change drastically the plasmonic heating. Moreover, on a substrate the nanoparticles are fixed which creates a fixed heat source for the surrounding media. Especially, for a substrate with low thermal conductivity like a polymer or glass the temperature attained locally can overcome 100 °C [69, 72]. For instance, by changing the substrate from glass to sapphire, which has a higher thermal conductivity, the heat attained from a single nanosphere fixed on the substrate and covered with water was found to decrease 3 times [73].

Heating using gold nanoparticles has been used already for a long time in the treatment of

tumors by photothermal effects, and the treatment is already under clinical studies [74]. Still, photothermal heating of gold nanoparticles is finding new applications in drug-delivery [75] and thermal lithography [76].

2.5 Surface-enhanced spectroscopies and their application to biosensing

Noble metals have a long history in sensing applications, mainly attributed to their plasmonic properties. Gold and silver are the metals exhibiting the best plasmonic properties due to their low damping. However gold is generally preferred over silver even if silver nanoparticles are said to give rise to higher near-field enhancement. Indeed silver nanoparticles have the tendency to get passivated by oxidation in air [77], are relatively unstable in solution over large period of time, and are cytotoxic [78]. This section will explain how metallic nanoparticles can be used for enhance the Raman scattering of molecules.

2.5.1 Surface-enhanced Raman scattering

When exciting a molecule with light, different phenomena occur: absorption, elastic scattering known as Rayleigh scattering or inelastic scattering through Compton or Raman scattering. Light as an electromagnetic wave can cause vibrations of the chemical bonds composing a molecule. Due to vibrations of the chemical bonds at a specific frequency, the molecule doesn't follow the electric field oscillation of light and scatters light at a different wavelength. This energy difference between incoming and scattered light depends on the frequency of the chemical bond vibration and especially on its polarizability [58]. Therefore each chemical bond has a different Raman scattering wavelength, making Raman a highly specific technique for sensing. However, not all molecules display Raman scattering, and Raman scattering obeys some selection rules that depend on the molecule symmetry. Raman spectra of different molecules can be seen in **Figure 2.9**, in this case, each molecule can be easily distinguished by its most intense Raman peak.

Generally the Raman cross sections of molecules are very low, in the order of 10^{-29} 10^{-30} cm^2,

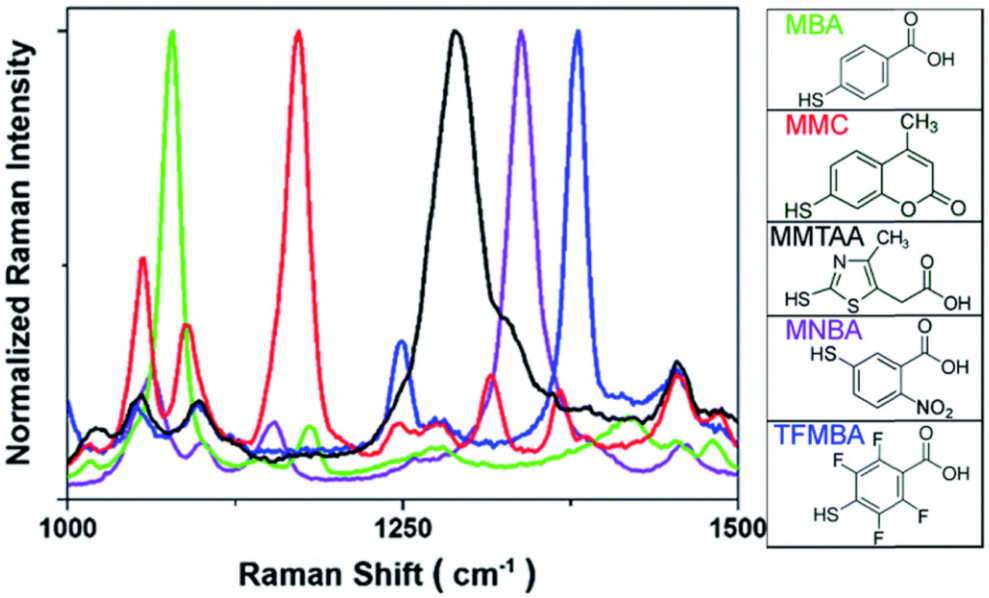

Figure 2.9: Surface-enhanced Raman signal of different molecules attached to gold nanoparticles. The Raman peaks from the different molecules allows for identification of the molecule, reproduced with permission from [7].

making the Raman detection of low concentrations of a molecule difficult without a transducer [79]. For this reason the first Raman spectra of benzene and other liquids, recorded by Venketa Raman using focused sunlight or mercury lamp, required extremely long exposures [80, 81]. Therefore, the implementation of Raman spectroscopy as a widespread analysis technique had to wait for the development of efficient light sources such as lasers. Additionally, the report of high Raman signal from pyridine on silver films in 1973 further increased the interest for Raman scattering [82]. In 1977, two research groups, noting that the high concentration of analyte on the surface could not explain the high Raman signal from Pyridine on silver film, proposes two different theories: Jeanmaire and VanDuyne proposed an electromagnetic theory [83] and Albrecht and Creighton proposed a charge transfer theory [84]. In fact both theories are complementary and widely accepted nowadays. The electromagnetic theory is based on the plasmonic properties of nanometals, the electric field enhancement at the wavelength of excitation enhances the formation of molecular dipole (term $E_{\mathrm{p}}(\omega_{\mathrm{inc}})$ in **Equation 2.17** and the scattered light from the molecules is enhanced by the plasmon resonance (term $E_p(\omega_{\mathrm{inc}} \pm \omega_{\mathrm{vibration}})$). The electromagnetic theory predicts a quadratic dependance of the SERS signal on the local electric field as followed:

$$I_{\mathrm{SERS}} = \alpha_{\mathrm{mol}}^2 \left| E_{\mathrm{p}}(\omega_{\mathrm{inc}})^2 * E_{\mathrm{p}}(\omega_{\mathrm{inc}} \pm \omega_{\mathrm{vibration}})^2 \right| \tag{2.17}$$

I_{SERS} is the intensity of the SERS signal, α_{mol} is the polarizability of the molecule.The plus-minus sign in the SERS equation accounts for the different inelastic scattering processes that can occur, inelastic scattering towards higher energy is known as anti-Stokes Raman shift, and inelastic scattering towards lower energy is known as Stokes Raman shift. Generally, Stokes Raman is used as its excitation is more efficient than anti-Stokes Raman and technically easier to realize.

The dependence of SERS on the fourth power of the local electric field produced by the plasmonic entity explains why increasing the near-field in the vicinity of NPs is so important in applications using SERS. In previous sections, we have seen different strategies for optimizing the near-field enhancement. For instance, changing the shape of nanoparticles from nanospheres to nanostars can result in a high SERS enhancement [85]. Another strategy is to use the junctions between different nanoparticles to create high confinement of the electromagnetic field and therefore a very high SERS enhancement. Gold dimers have been a perfect model to understand the high SERS enhancement coming from plasmonic coupling [86], however clusters with a higher number of NPs can provide even higher SERS signal [87].

Electric field enhancement generally accounts for the biggest part of the SERS enhancement, however, chemical enhancement can also explain a part of the enhancement. The chemical enhancement comes from an increase of the molecule polarizability in an absorbed state, creating a larger electric dipole leading to a higher SERS signal. The adsorbed molecule in its ground state can get excited through charge transfer from the metal to the molecule, resulting in a different Raman cross-section. Moreover, the molecule in the adsorbed state can have different electronic transitions than in "free state", which also affects the Raman signal.

2.5.2 Applications of SERS

Surface-enhanced Raman spectroscopy provides chemical and structural information on molecules, making it an interesting technique for various sensing applications. Moreover, compared to other sensing techniques it is fast, non-invasive, and can detect down to single-molecules in

some cases [88], without the need for sample pretreatment. Especially molecules that have a high Raman cross-section, like molecules with an aromatic ring [89], are easier to detect at very low concentrations due to their high polarizability. In this section, different applications of SERS will be shown.

More and more commonly used chemicals are discovered to be hazardous and toxic to humans and the environment. Pesticides that have been used for decades are now found in soils and river streams in dangerous quantities for biodiversity [90]. In this sense, SERS constitutes a method of choice for the detection of pesticides [91] such as thiabendazole at remarkably low concentrations [92]. Moreover, the design of flexible plasmonic samples makes it possible to sense directly on the skin of fruits [93]. More generally, it is possible to sense several dangerous chemical species, as for example: explosives [94], metal ions [95], toxins [96], estrogens... However, one of the drawbacks of SERS in control and monitoring is that plasmonic substrates are usually for single-use, since molecules and analytes generally bind irreversibly to the gold NPs. Such an effect known as the SERS memory effect, impedes measurement in real-time with a single substrate [97]. This is why reusable substrates are being developed to work in flow and detect analytes in water streams for instance [98].

Due to its versatility and low-cost SERS is of primary interest for biomedical applications. Especially it allows the detection of biomarkers associated with diseases [99], in some cases even in complicated media such as cell media or blood. Generally, label-free detection of analytes in complex media is difficult due to the presence of several molecules and to the low affinity of the analyte of interest to the plasmonic structure. This is why some strategies use functionalization of the plasmonic substrate with aptamers, peptides or antigenes in order to favor binding of the analyte to the plasmonic substrate. In these cases, changes in the Raman signals are detected due to a change in the structural and electronic composition of the selective molecule upon binding of the analyte. For instance, SERS-based immunoassays using Raman reporter functionalized nanoparticles were carried for the detection of cortisol [100].

Rather than sensing analytes indicating for the presence of a particular tumor cell or cancer cell it is possible to image cells using gold nanoparticles decorated with Raman markers. The advantages of SERS to image cells compared to other imaging techniques are different: (i) the Raman signal is not directly prone to bleaching allowing for the study of cell growth and

migration over time, (ii) SERS grant for a very low limit of detection making possible the detection of single cells, (iii) gold nanoparticles are non-cytotoxic allowing for detection even in vivo, (iv) Multiplexing with SERS is easy when appropriate Raman reporters are chosen, as Raman linewidth is in the order of the nm. Using Nanoparticles with Raman reporters and polymer encapsulation, Aberasturi et al have shown the discrimination of different breast cancer cell types through Raman signals of different Raman tags on the surface of the cell. The topography of the cell could also be followed in real-time using Raman maps. Thanks to the low cytotoxicity of gold, such systems could be used in vitro and even in vivo to target tumoral cells. Moreover thanks to the photothermal properties of gold nanoparticles it is possible to monitor the death of tumor cells.

Bibliography

[1] Faraday, M. The Bakerian Lecture : Experimental Relations of Gold (and Other Metals) to Light. *Philos. Trans. Roy. Soc. London* **1857**, *147*, 145–181.

[2] Jana, N. R.; Gearheart, L.; Murphy, C. J. Seed-Mediated Growth Approach for Shape-Controlled Synthesis of Spheroidal and Rod-like Gold Nanoparticles Using a Surfactant Template. *Adv. Mater.* **2001**, *13*, 1389–1393.

[3] Scarabelli, L.; Sánchez-Iglesias, A.; Pérez-Juste, J.; Liz-Marzán, L. M. A "Tips and Tricks" Practical Guide to the Synthesis of Gold Nanorods. *J. Phys. Chem. Lett.* **2015**, *6*, 4270–4279.

[4] Scarabelli, L.; Coronado-Puchau, M.; Giner-Casares, J. J.; Langer, J.; Liz-Marzán, L. M. Monodisperse gold nanotriangles: Size control, large-scale self-assembly, and performance in surface-enhanced raman scattering. *ACS Nano* **2014**, *8*, 5833–5842.

[5] Senthil Kumar, P.; Pastoriza-Santos, I.; Rodríguez-González, B.; Javier García De Abajo, F.; Liz-Marzán, L. M. High-yield synthesis and optical response of gold nanostars. *Nanotechnology* **2008**, *19*, 1–7.

[6] Desantis, C. J.; Skrabalak, S. E. Size-controlled synthesis of Au/Pd octopods with high refractive index sensitivity. *Langmuir* **2012**, *28*, 9055–9062.

[7] Hanske, C.; González-Rubio, G.; Hamon, C.; Formentín, P.; Modin, E.; Chuvilin, A.; Guerrero-Martínez, A.; Marsal, L. F.; Liz-Marzán, L. M. Large-Scale Plasmonic Pyramidal Supercrystals via Templated Self-Assembly of Monodisperse Gold Nanospheres. *J Phys Chem C* **2017**, *121*, 10899–10906.

[8] Carbó-Argibay, E.; Rodríguez-González, B.; Gómez-Graña, S.; Guerrero-Martínez, A.; Pastoriza-Santos, I.; Pérez-Juste, J.; Liz-Marzán, L. M. The crystalline structure of gold nanorods revisited: Evidence for higher-index lateral facets. *Angew. Chem. - Int. Ed.* **2010**, *49*, 9397–9400.

[9] Park, K.; Drummy, L. F.; Wadams, R. C.; Koerner, H.; Nepal, D.; Fabris, L.; Vaia, R. A. Growth mechanism of gold nanorods. *Chem. Mater.* **2013**, *25*, 555–563.

[10] Walsh, M. J.; Barrow, S. J.; Tong, W.; Funston, A. M.; Etheridge, J. Symmetry breaking and silver in gold nanorod growth. *ACS Nano* **2015**, *9*, 715–724.

[11] Pashley, R. M.; Karaman, M. E. *Applied Colloid and Surface Chemistry*; John Wiley & Sons, Ltd: Chichester, UK, 2004.

[12] Ohshima, H. *Electrical Phenomena at Interfaces and Biointerfaces*; John Wiley & Sons, Inc.: Hoboken, NJ, USA, 2012; pp 27–34.

[13] Hamaker, H. C. The London-van der Waals attraction between spherical particles. *Physica* **1937**, *4*, 1058–1072.

[14] Leckband, D.; Israelachvili, J. Intermolecular forces in biology. *Q. Rev. Biophys.* **2001**, *34*, 105–267.

[15] Hückel, P.; Debye, E. The theory of electrolytes. I. Freezing point depression and related phenomena (Translation). *Phys. Z.* **1923**, *24*, 185–206.

[16] Napper, D. H. Polymeric stabilisation of colloidal dispersions. 1983.

[17] Hamaker, H. C. The London-van der Waals attraction between spherical particles. *Physica* **1937**, *4*, 1058–1072.

[18] Mulla, M. A.; Yow, H. N.; Zhang, H.; Cayre, O. J.; Biggs, S. *Fundamentals of Inkjet Printing*; Wiley-VCH Verlag GmbH & Co. KGaA: Weinheim, Germany, 2015; pp 141–168.

[19] Donaldson, S. H.; Lee, C. T.; Chmelka, B. F.; Israelachvili, J. N. General hydrophobic interaction potential for surfactant/lipid bilayers from direct force measurements between light-modulated bilayers. *Proc. Natl. Acad. Sci.* **2011**, *108*, 15699–15704.

[20] Liu, Y.; Han, X.; He, L.; Yin, Y. Thermoresponsive assembly of charged gold nanoparticles and their reversible tuning of plasmon coupling. *Angew. Chem. - Int. Ed.* **2012**, *51*, 6373–6377.

[21] Sánchez-Iglesias, A.; Grzelczak, M.; Altantzis, T.; Goris, B.; Pérez-Juste, J.; Bals, S.; Van Tendeloo, G.; Donaldson, S. H.; Chmelka, B. F.; Israelachvili, J. N.; Liz-Marzán, L. M. Hydrophobic interactions modulate self-assembly of nanoparticles. *ACS Nano* **2012**, *6*, 11059–11065.

[22] Sánchez-Iglesias, A.; Claes, N.; Solís, D. M.; Taboada, J. M.; Bals, S.; Liz-Marzán, L. M.; Grzelczak, M. Reversible Clustering of Gold Nanoparticles under Confinement. *Angew. Chem. - Int. Ed.* **2018**, *130*, 3237–3240.

[23] Taladriz-Blanco, P.; Buurma, N. J.; Rodríguez-Lorenzo, L.; Pérez-Juste, J.; Liz-Marzán, L. M.; Hervés, P. Reversible assembly of metal nanoparticles induced by penicillamine. Dynamic formation of SERS hot spots. *J Mater Chem* **2011**, *21*, 16880–16887.

[24] Zhang, H.; Cadusch, J.; Kinnear, C.; James, T.; Roberts, A.; Mulvaney, P. Direct Assembly of Large Area Nanoparticle Arrays. *ACS Nano* **2018**,

[25] Palleau, E.; Sangeetha, N. M.; Viau, G.; Marty, J. D.; Ressier, L. Coulomb force directed single and binary assembly of nanoparticles from aqueous dispersions by AFM nanoxerography. *ACS Nano* **2011**, *5*, 4228–4235.

[26] Farcau, C.; Sangeetha, N. M.; Moreira, H.; Viallet, B.; Grisolia, J.; Ciuculescu-Pradines, D.; Ressier, L. High-Sensitivity Strain Gauge Based on a Single Wire of Gold Nanoparticles Fabricated by Stop-and-Go Convective Self-Assembly. *ACS Nano* **2011**, *5*, 7137–7143.

[27] Ni, S.; Leemann, J.; Wolf, H.; Isa, L. Insights into mechanisms of capillary assembly. *Faraday Discuss.* **2015**, *181*, 225–242.

[28] Ni, S.; Wolf, H.; Isa, L. Programmable Assembly of Hybrid Nanoclusters. *Langmuir* **2018**, *34*, 2481–2488.

[29] Flauraud, V.; Mastrangeli, M.; Bernasconi, G. D.; Butet, J.; Alexander, D. T.; Shahrabi, E.; Martin, O. J.; Brugger, J. Nanoscale topographical control of capillary assembly of nanoparticles. *Nat. Nanotechnology* **2017**, *12*, 73–80.

[30] Kinnear, C.; Cadusch, J.; Zhang, H.; Lu, J.; James, T.; Roberts, A.; Mulvaney, P. Directed Chemical Assembly of Single and Clustered Nanoparticles with Silanized Templates. *Langmuir* **2018**,

[31] Kinnear, C.; Cadusch, J.; Zhang, H.; Lu, J.; James, T.; Roberts, A.; Mulvaney, P. Directed Chemical Assembly of Single and Clustered Nanoparticles with Silanized Templates. *Langmuir* **2018**,

[32] Lin, Q. Y.; Li, Z.; Brown, K. A.; O'Brien, M. N.; Ross, M. B.; Zhou, Y.; Butun, S.; Chen, P. C.; Schatz, G. C.; Dravid, V. P.; Aydin, K.; Mirkin, C. A. Strong Coupling between Plasmonic Gap Modes and Photonic Lattice Modes in DNA-Assembled Gold Nanocube Arrays. *Nano Lett.* **2015**, *15*, 4699–4703.

[33] Lin, Q.-Y.; Mason, J. A.; Li, Z.; Zhou, W.; O'Brien, M. N.; Brown, K. A.; Jones, M. R.; Butun, S.; Lee, B.; Dravid, V. P.; Aydin, K.; Mirkin, C. A. Building superlattices from individual nanoparticles via template-confined DNA-mediated assembly. *Science* **2018**, *359*, 669–672.

[34] Wood, R. W. On a remarkable case of uneven distribution of light in a diffraction grating spectrum. *Proc. Phys. Soc. London* **1901**, *18*, 269–275.

[35] Enoch, S.; Bonod, N. In *Springer Series in Optical Sciences*; Enoch, S., Bonod, N., Eds.; Springer Series in Optical Sciences; Springer Berlin Heidelberg: Berlin, Heidelberg, 2012; Vol. 167; p 321.

[36] Rayleigh, L. III. Note on the remarkable case of diffraction spectra described by Prof. Wood . *The London, Edinburgh, and Dublin Philosophical Magazine and Journal of Science* **1907**, *14*, 60–65.

[37] Fano, U. The Theory of Anomalous Diffraction Gratings and of Quasi-Stationary Waves on Metallic Surfaces (Sommerfeld's Waves). *J. Opt. Soc. Am.* **1941**, *31*, 213.

[38] R. H. RITCHIE, Plasma Losses by Fast Electrons in Thin Films. *Phys. Rev.* **1956**, *106 N.5*, 8.

[39] Nguyen, H. H.; Park, J.; Kang, S.; Kim, M. Surface plasmon resonance: A versatile technique for biosensor applications. *Sens. Switz.* **2015**, *15*, 10481–10510.

[40] Kociak, M.; Stéphan, O. Mapping plasmons at the nanometer scale in an electron microscope. *Chem. Soc. Rev.* **2014**, *43*, 3865–3883.

[41] Maier, S. A. *Analytica Chimica Acta*; Springer US: New York, NY, 2007; Vol. 677; pp 3–18.

[42] Kretschmann, E. Die Bestimmung optischer Konstanten von Metallen durch Anregung von Oberflächenplasmaschwingungen. *Zeitschrift für Physik* **1971**, *241*, 313–324.

[43] Etxebarria-elezgarai, J.; Mowat, M.; Lopez, E.; Rodr, C.; Olaetxea, I.; Seifert, A. Gaussian Beam Shaping and Multivariate Analysis in Plasmonic Sensing. *Anal. Chem.* **2020**, *92*, 16236–16244.

[44] Bohren, C. F.; Huffman, D. R. *Absorption and Scattering of Light by Small Particles*; Wiley, 1998.

[45] Louis, C.; Pluchery, O. *Angew. Chem. - Int. Ed.*; IMPERIAL COLLEGE PRESS, 2012; Vol. 53; pp 1197–1197.

[46] Müller, M. B.; Kuttner, C.; König, T. A. F.; Tsukruk, V. V.; Förster, S.; Karg, M.; Fery, A. Plasmonic library based on substrate-supported gradiential plasmonic arrays. *ACS Nano* **2014**, *8*, 9410–9421.

[47] Scarabelli, L.; Sánchez-Iglesias, A.; Pérez-Juste, J.; Liz-Marzán, L. M. A "Tips and Tricks" Practical Guide to the Synthesis of Gold Nanorods. *J. Phys. Chem. Lett.* **2015**, *6*, 4270–4279.

[48] Yuan, H.; Khoury, C. G.; Hwang, H.; Wilson, C. M.; Grant, G. A.; Vo-Dinh, T. Gold nanostars: surfactant-free synthesis, 3D modelling, and two-photon photoluminescence imaging. *Nanotechnology* **2012**, *23*, 075102.

[49] Reguera, J.; Langer, J.; Jiménez de Aberasturi, D.; Liz-Marzán, L. M. Anisotropic metal nanoparticles for surface enhanced Raman scattering. *Chem. Soc. Rev.* **2017**, *46*, 3866–3885.

[50] Yu, R.; Liz-Marzán, L. M.; García De Abajo, F. J. Universal analytical modeling of plasmonic nanoparticles. *Chem. Soc. Rev.* **2017**, *46*, 6710–6724.

[51] Reguera, J.; Langer, J.; Jiménez de Aberasturi, D.; Liz-Marzán, L. M. Anisotropic metal nanoparticles for surface enhanced Raman scattering. *Chem. Soc. Rev.* **2017**, *46*, 3866–3885.

[52] Jain, P. K.; Huang, W.; El-Sayed, M. A. On the universal scaling behavior of the distance decay of plasmon coupling in metal nanoparticle pairs: A plasmon ruler equation. *Nano Lett.* **2007**, *7*, 2080–2088.

[53] Zhang, W.; Li, Q.; Qiu, M. A plasmon ruler based on nanoscale photothermal effect. *Opt. Express* **2013**, *21*, 172.

[54] Prodan, E.; Radloff, C.; Halas, N. J.; Nordlander, P. A Hybridization Model for the Plasmon Response of Complex Nanostructures. *Science* **2003**, *302*, 419–422.

[55] Jain, P. K.; Huang, W.; El-Sayed, M. A. On the universal scaling behavior of the distance decay of plasmon coupling in metal nanoparticle pairs: A plasmon ruler equation. *Nano Lett.* **2007**, *7*, 2080–2088.

[56] Hanske, C.; Tebbe, M.; Kuttner, C.; Bieber, V.; Tsukruk, V. V.; Chanana, M.; König, T. A.; Fery, A. Strongly coupled plasmonic modes on macroscopic areas via template-assisted colloidal self-assembly. *Nano Lett.* **2014**, *14*, 6863–6871.

[57] Slaughter, L. S.; Wang, L.-Y.; Willingham, B. A.; Olson, J. M.; Swanglap, P.; Dominguez-Medina, S.; Link, S. Plasmonic polymers unraveled through single particle spectroscopy. *Nanoscale* **2014**, *6*, 11451–11461.

[58] Vandenabeele, P. *Practical Raman Spectroscopy - An Introduction*; John Wiley & Sons, Ltd: Chichester, UK, 2013.

[59] Taylor, R. W.; Esteban, R.; Mahajan, S.; Aizpurua, J.; Baumberg, J. J. Optimizing SERS from Gold Nanoparticle Clusters: Addressing the Near Field by an Embedded Chain Plasmon Model. *J Phys Chem C* **2016**, *120*, 10512–10522.

[60] Kravets, V. G.; Kabashin, A. V.; Barnes, W. L.; Grigorenko, A. N. Plasmonic Surface Lattice Resonances: A Review of Properties and Applications. *Chem. Rev.* **2018**, *118*, 5912–5951.

[61] Brasse, Y.; Gupta, V.; Schollbach, H. C.; Karg, M.; König, T. A.; Fery, A. Mechanotunable Plasmonic Properties of Colloidal Assemblies. *Adv. Mater. Interfaces* **2019**, *1901678*.

[62] Thackray, B. D.; Kravets, V. G.; Schedin, F.; Auton, G.; Thomas, P. A.; Grigorenko, A. N. Narrow Collective Plasmon Resonances in Nanostructure Arrays Observed at Normal Light Incidence for Simplified Sensing in Asymmetric Air and Water Environments. *ACS Photonics* **2014**, *1*, 1116–1126.

[63] Gupta, V.; Probst, P.; Goßler, F.; Steiner, A. M.; Schubert, J.; Brasse, Y.; Koenig, T. A.; Fery, A. Mechanotunable Surface Lattice Resonances in the Visible Optical Range by Soft Lithography Templates and Directed Self-Assembly. *ACS Appl. Mater. Interfaces* **2019**, acsami.9b08871.

[64] Hua, Y.; Fumani, A. K.; Odom, T. W. Tunable Lattice Plasmon Resonances in 1D Nanogratings. *ACS Photonics* **2019**, *6*, 322–326.

[65] Volk, K.; Fitzgerald, J. P.; Ruckdeschel, P.; Retsch, M.; König, T. A.; Karg, M. Reversible Tuning of Visible Wavelength Surface Lattice Resonances in Self-Assembled Hybrid Monolayers. *Adv. Opt. Mater.* **2017**, *5*.

[66] Matricardi, C.; Hanske, C.; Garcia-Pomar, J. L.; Langer, J.; Mihi, A.; Liz-Marzán, L. M. Gold Nanoparticle Plasmonic Superlattices as Surface Enhanced Raman Spectroscopy Substrates. *ACS Nano* **2018**,

[67] Kuttner, C.; Höller, R. P.; Quintanilla, M.; Schnepf, M. J.; Dulle, M.; Fery, A.; Liz-Marzán, L. M. SERS and plasmonic heating efficiency from anisotropic core/satellite superstructures. *Nanoscale* **2019**, *11*, 17655–17663.

[68] Qin, Z.; Wang, Y.; Randrianalisoa, J.; Raeesi, V.; Chan, W. C.; Lipinski, W.; Bischof, J. C. Quantitative comparison of photothermal heat generation between gold nanospheres and nanorods. *Sci. Rep.* **2016**, *6*, 1–13.

[69] Borah, R.; Verbruggen, S. W. Coupled Plasmon Modes in 2D Gold Nanoparticle Clusters and Their Effect on Local Temperature Control. *J Phys Chem C* **2019**, *123*, 30594–30603.

[70] Moustaoui, H.; Saber, J.; Djeddi, I.; Liu, Q.; Diallo, A. T.; Spadavecchia, J.; Lamy De La Chapelle, M.; Djaker, N. Shape and Size Effect on Photothermal Heat Elevation of Gold Nanoparticles: Absorption Coefficient Experimental Measurement of Spherical and Urchin-Shaped Gold Nanoparticles. *J Phys Chem C* **2019**, *123*, 17548–17554.

[71] Jauffred, L.; Samadi, A.; Klingberg, H.; Bendix, P. M.; Oddershede, L. B. Plasmonic Heating of Nanostructures. *Chem. Rev.* **2019**, *119*, 8087–8130.

[72] Jauffred, L.; Samadi, A.; Klingberg, H.; Bendix, P. M.; Oddershede, L. B. Plasmonic Heating of Nanostructures. *Chem. Rev.* **2019**, *119*, 8087–8130.

[73] Gargiulo, J.; Brick, T.; Violi, I. L.; Herrera, F. C.; Shibanuma, T.; Albella, P.; Requejo, F. G.; Cortés, E.; Maier, S. A.; Stefani, F. D. Understanding and Reducing Photothermal Forces for the Fabrication of Au Nanoparticle Dimers by Optical Printing. *Nano Lett.* **2017**, *17*, 5747–5755.

[74] Gargiulo, J.; Brick, T.; Violi, I. L.; Herrera, F. C.; Shibanuma, T.; Albella, P.; Requejo, F. G.; Cortés, E.; Maier, S. A.; Stefani, F. D. Understanding and Reducing Photothermal Forces for the Fabrication of Au Nanoparticle Dimers by Optical Printing. *Nano Lett.* **2017**, *17*, 5747–5755.

[75] Gupta, M. K.; Meng, F.; Johnson, B. N.; Kong, Y. L.; Tian, L.; Yeh, Y. W.; Masters, N.; Singamaneni, S.; McAlpine, M. C. 3D Printed Programmable Release Capsules. *Nano Lett.* **2015**, *15*, 5321–5329.

[76] Fiutowski, J. Mapping of gold nanostructure-enhanced near fields via laser scanning second-harmonic generation and ablation. *J. Nanophoton.* **2012**, *6*, 063515.

[77] Grillet, N.; Manchon, D.; Cottancin, E.; Bertorelle, F.; Bonnet, C.; Broyer, M.; Lermé, J.; Pellarin, M. Photo-oxidation of individual silver nanoparticles: A real-time tracking of optical and morphological changes. *J Phys Chem C* **2013**, *117*, 2274–2282.

[78] Valenti, L. E.; Giacomelli, C. E. Stability of silver nanoparticles: agglomeration and oxidation in biological relevant conditions. *J. Nanoparticle Res. Interdiscip. Forum Nanoscale Sci. Technol.* **2017**, *19*.

[79] Schlücker, S. Surface-Enhanced Raman Spectroscopy: Concepts and Chemical Applications. *Angew. Chem. - Int. Ed.* **2014**, *53*, 4756–4795.

[80] Raman, C.; Krishnan, K. The Optical Analogue of the Compton Effect. *Nature* **1928**, *121*, 3053.

[81] Raman, C.; Krishnan, K. A new type of secondary radiation. *Nature* **1928**, *121*, 501–502.

[82] Albrecht, M. G.; Creighton, J. A. Anomalously intense Raman spectra of pyridine at a silver electrode. *J. Am. Chem. Soc.* **1977**, *99*, 5215–5217.

[83] Jeanmaire, D. L.; Duyne, R. P. V. Surface raman spectroelectrochemistry: Part I. Heterocyclic, aromatic, and aliphatic amines adsorbed on the anodized silver electrode. *J. Electroanal. Chem. Interfacial Electrochem.* **1977**, *84*, 1 – 20.

[84] Fleischmann, M.; Hendra, P.; McQuillan, A. Raman spectra of pyridine adsorbed at a silver electrode. *Chem. Phys. Lett.* **1974**, *26*, 163 – 166.

[85] Tian, F.; Bonnier, F.; Casey, A.; Shanahan, A. E.; Byrne, H. J. Surface enhanced Raman scattering with gold nanoparticles: Effect of particle shape. *Anal. Methods* **2014**, *6*, 9116–9123.

[86] Alexander, K. D.; Hampton, M. J.; Zhang, S.; Dhawan, A.; Xu, H.; Lopez, R. A high-throughput method for controlled hot-spot fabrication in SERS-active gold nanoparticle dimer arrays. *J Raman Spectrosc* **2009**, *40*, 2171–2175.

[87] Pazos-Perez, N.; Wagner, C. S.; Romo-Herrera, J. M.; Liz-Marzán, L. M.; García De Abajo, F. J.; Wittemann, A.; Fery, A.; Alvarez-Puebla, R. A. Organized plasmonic clusters with high coordination number and extraordinary enhancement in surface-enhanced Raman scattering (SERS). *Angew. Chem. - Int. Ed.* **2012**, *51*, 12688–12693.

[88] Chen, H.-y.; Lin, M.-h.; Wang, C.-y.; Chang, Y.-m.; Gwo, S. Large-Scale Hot Spot Engineering for Quantitative SERS at the Single-Molecule Scale. *J. Am. Chem. Soc.* **2015**, *137*, 13698–13705.

[89] Wei, L.; Chen, Z.; Shi, L.; Long, R.; Anzalone, A. V.; Zhang, L.; Hu, F.; Yuste, R.; Cornish, V. W.; Min, W. Super-multiplex vibrational imaging. *Nature* **2017**, *544*, 465–470.

[90] Rodriguez-Mozaz, S.; López De Alda, M. J.; Barceló, D. Monitoring of estrogens, pesticides and bisphenol A in natural waters and drinking water treatment plants by solid-phase extraction-liquid chromatography-mass spectrometry. *J. Chromatogr. A* **2004**, *1045*, 85–92.

[91] Chen, J.; Huang, Y.; Kannan, P.; Zhang, L.; Lin, Z.; Zhang, J.; Chen, T.; Guo, L. Flexible and Adhesive Surface Enhance Raman Scattering Active Tape for Rapid Detection of Pesticide Residues in Fruits and Vegetables. *Anal. Chem.* **2016**, *88*, 2149–2155.

[92] Shiohara, A.; Langer, J.; Polavarapu, L.; Liz-Marzán, L. M. Solution processed poly-

dimethylsiloxane/gold nanostar flexible substrates for plasmonic sensing. *Nanoscale* **2014**, *6*, 9817–9823.

[93] Xu, K.; Zhou, R.; Takei, K.; Hong, M. Toward Flexible Surface-Enhanced Raman Scattering (SERS) Sensors for Point-of-Care Diagnostics. *Adv. Sci.* **2019**, *6*.

[94] Chou, A.; Jaatinen, E.; Buividas, R.; Seniutinas, G.; Juodkazis, S.; Izake, E. L.; Fredericks, P. M. SERS substrate for detection of explosives. *Nanoscale* **2012**, *4*, 7419–7424.

[95] Dugandžić, V.; Kupfer, S.; Jahn, M.; Henkel, T.; Weber, K.; Cialla-May, D.; Popp, J. A SERS-based molecular sensor for selective detection and quantification of copper(II) ions. *Sens. Actuators, B* **2019**, *279*, 230–237.

[96] Kearns, H.; Goodacre, R.; Jamieson, L. E.; Graham, D.; Faulds, K. SERS Detection of Multiple Antimicrobial-Resistant Pathogens Using Nanosensors. *Anal. Chem.* **2017**, *89*, 12666–12673.

[97] Wachter, E. A.; Storey, J. M. E.; Sharp, S. L.; Carron, K. T.; Jiang, Y. Hybrid Substrates for Real-Time SERS-Based Chemical Sensors. *Appl. Spectrosc.* **1995**, *49*, 193–199.

[98] Meier, T. A.; Poehler, E.; Kemper, F.; Pabst, O.; Jahnke, H. G.; Beckert, E.; Robitzki, A.; Belder, D. Fast electrically assisted regeneration of on-chip SERS substrates. *Lab Chip* **2015**, *15*, 2923–2927.

[99] Alvarez-Puebla, R. A.; Agarwal, A.; Manna, P.; Khanal, B. P.; Aldeanueva-Potel, P.; Carbó-Argibay, E.; Pazos-Pérez, N.; Vigderman, L.; Zubarev, E. R.; Kotov, N. A.; Liz-Marzán, L. M. Gold nanorods 3D-supercrystals as surface enhanced Raman scattering spectroscopy substrates for the rapid detection of scrambled prions. *Proc. Natl. Acad. Sci. USA* **2011**, *108*, 8157–8161.

[100] Villa, J. E.; Garcia, I.; Jimenez de Aberasturi, D.; Pavlov, V.; Sotomayor, M. D.; Liz-Marzán, L. M. SERS-based immunoassay for monitoring cortisol-related disorders. *Biosens. Bioelectron.* **2020**, *165*, 112418.

Chapter 3

Homogeneous self-assembly of gold nanospheres into superlattices on a large scale

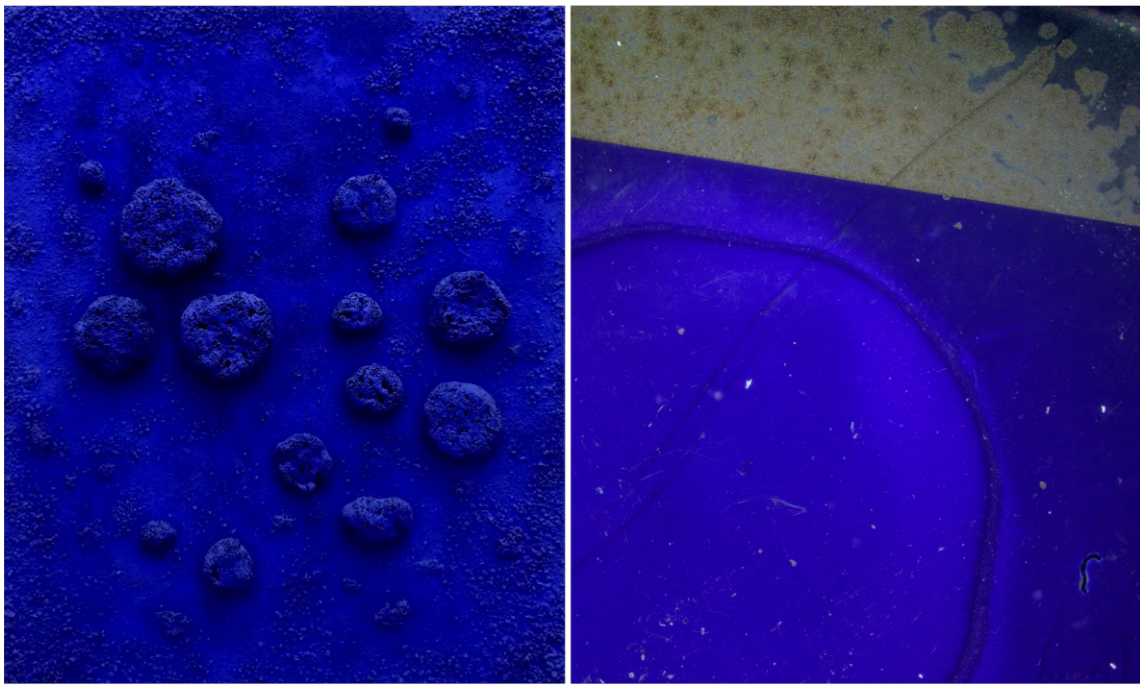

Figure 3.1: On the left: "Photograph of:"L'accord Bleu" by Yves Klein, 1960," by Jaredzimmerman (WMF), under Creative Common BY-SA 4.0 license, on the right:"Le bleu plasmonique" by Mathias Charconnet, 2019, Dark-field microscope image of self-assembled plasmonic superlattice.

Abstract

The SERS enhancement of gold nanoparticle clusters is highly dependent on the number of nanoparticle per cluster due to the hybridization of plasmonic resonances in such clusters. Therefore, the homogeneity of the SERS signal over a plasmonic substrate rely on the regular assembly of nanoparticle clusters with a similar number of particles per cluster. In this sense, periodic arrays of gold nanoparticle clusters seem to be ideal candidates thanks to their high near-field enhancement and their regular organization of gold nanoparticles clusters. However, the large-scale homogeneous self-assembly of periodic arrays of gold nanoparticles can be hampered by the coffee-ring effect. In this chapter, ethanol is added as a co-solvent in the nanoparticle dispersion to foster recirculation flows, known as Marangoni flows, that can reduce the coffee-ring effect and consequently permit the large-scale and homogeneous fabrication of plasmonic superlaticces. Additionally, a systematic study of the surfactant concentration and ethanol ratio is carried-out to find the optimal conditions for the nanoparticle self-assembly. At optimal self-assembly conditions, the resulting plasmonic superlattices exhibited sharp plasmon resonances arising from the coupling of plasmonic cluster modes to an in-plane diffracted mode. This sharp plasmon resonance, was found to be broader and weaker with less homogenous plasmonic lattices. Finally, not only the standard deviation of the SERS signal was significantly reduced in homogeneous superlattices but the increased far-field coupling between the plasmonic clusters induced an increase of the SERS signal of up to an order of magnitude.

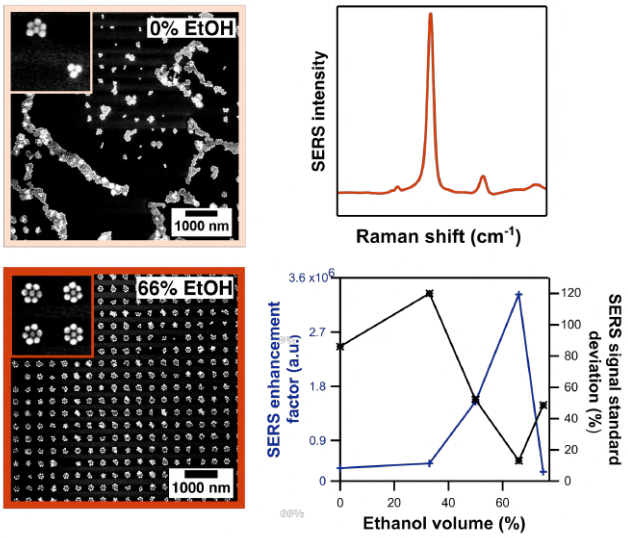

3.1 Introduction

3.1.1 What is templated self-assembly?

In this PhD thesis, the fabrication of gold nanoparticle superlattices was performed by templated self-assembly. Templated self-assembly is a technique that derives from capillary-assisted self-assembly (described in **Section 2.2.2**), which uses the capillary force acting at the meniscus of an evaporating liquid to drive the assembly of nanoparticles into the wells of a 2D periodically nanostructured template [1]. The main difference between capillary assisted self-assembly and templated self-assembly resides in the way the meniscus propagates along the substrate. In capillary self-assembly, the meniscus is dragged along the substrate by a motorized blade (see **Figure 3.2 a and b**). Instead, in templated self-assembly after dropcasting a nanoparticle on top of the nanostructured mold, the droplet is squeezed in between the mold and a substrate (generally made of glass), resulting in the formation of a film of nanoparticles dispersion between the substrate and the template. Upon drying of the nanoparticles film, the meniscus travels over the substrate leading to the periodic assembly of gold nanoparticles (see **Figure 3.2 c**). Such a process yields a readily available plasmonic substrate.

The templated self-assembly process has several advantages: (i) There is no need for subsequent particle transfer from the mold to the substrate after assembly, which could alter the quality of the assembled superlattice due to particle staying trapped in the nanostructured template [2]. By avoiding the transfer step, it is, therefore, possible to obtain higher quality structures. (ii) Templated self-assembly transfer yields a readily available plasmonic substrate. (iii) There is no need for a dedicated motor blade setup for the control of the meniscus movement. Therefore, it is possible to fabricate several substrates at the same time if different molds are available.

However, in templated self-assembly, the meniscus generally dries in an uncontrolled manner, which generally yields non-homogeneous plasmonic structures on the macroscale and the nanoscale. In this chapter, we show how adding ethanol as a co-solvent can help in the formation of homogeneous superlattices. The systematic study of the flows arising in such solvent-mixtures enables the homogeneous self-assembly of gold nanospheres into superlattices with a controlled

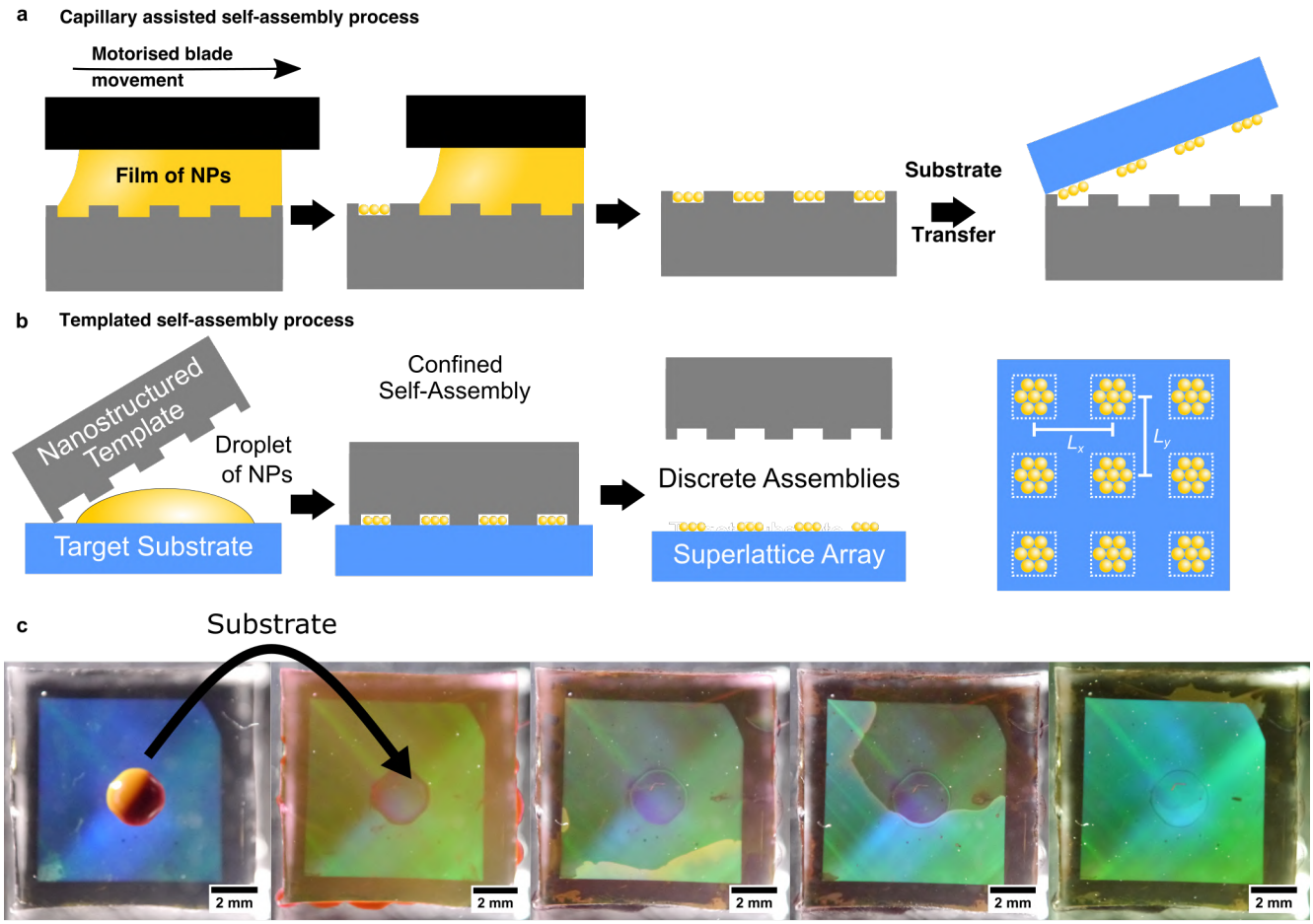

Figure 3.2: Templated self-assembly process. a) Scheme of the capillary assisted self-assembly process. b) Scheme of the templated assisted self-assembly process. c) Macroscopic images of the drying step of the templated self-assembly process. On the top left, we can see a droplet of Gold NPs dispersion in red-orange on top of a nanostructured PDMS template. The droplet is then squeezed between a glass substrate and a patterned PDMS. The NPs film then dries from the bottom right corner to the top left corner of the template.

number of NPs.

3.1.2 Examples of self-assembled gold NP superlattices and their optical properties

Due to their periodical organization, gold NP superlattices have interesting optical properties [3]. Self-assembled superlattices can be composed either of single nanoparticles in a lattice [4] or of nanoparticle clusters arranged in a lattice (as can be seen in **Figure 3.3**) [5]. The

number of nanoparticles in the sub-unit mainly depends on the size of the template wells, but it also depends on the self-assembly parameters such as surface tension [6] of the liquid film and nanoparticle concentration [7]. While the optical properties of single clusters have been studied thoroughly by dark-field spectroscopy [8, 9, 10], plasmonic far-field coupling through lattice effect is getting an increased interest [11, 12, 13]. For far-field coupling to occur, the period of the superlattice has to be chosen so that the cutoff wavelength for Rayleigh anomaly coincides with a plasmon resonance of the grating sub-unit (see **section 2.4.3**) [14]. In general, this means, that for far-field coupling to occur in the visible, the period of the superlattice has to be on the order of 300-600 nm. In **Figure3.3 a** one can see an SEM image of nanosphere clusters in a lattice of 500 nm period. The optical properties of similar plasmonic superlattices comprising different periods are shown in **Figure3.3 b**. An increase of the lattice period yields a shift of the main plasmon resonance attributed to lattice coupling (SLR) [15]. Consequently, such a shift of the surface lattice resonance through period changes, could be used to increase the near-field of plasmonic superlattices at specific wavelength.

3.1.3 Importance of homogeneous self-assembly

On the one hand, dispersed gold nanoparticle solutions provide reproducible SERS signals, however, the enhancement provided by such solutions is generally limited and gold NP solutions are not suited to all sensing strategies [16]. On the other hand, gold nanoparticle assemblies provide remarkable SERS enhancement due to plasmonic coupling, rendering them interesting for sensing applications using SERS (see **Section 2.5.1**). Especially, superlattices of gold nanoparticles provide an additional near-field enhancement thanks to the lattice coupling effect (explained in Section 2.4.3) [17]. Moreover, due to their order on the nanoscale, superlattices display a high density of NPs allowing for remarkable SERS signals.

One of the drawbacks of using NP assemblies for SERS is that they are generally non-homogeneous on the macroscale [18], leading to substrates with very irregular SERS signal [19]. Homogeneous plasmonic substrates would result in more robust SERS substrates. The SERS enhancement of gold NP clusters depends mainly on the number of NPs in the clusters, the size and the shape of the individual NP and their interparticle distance [20, 21, 22]. As a

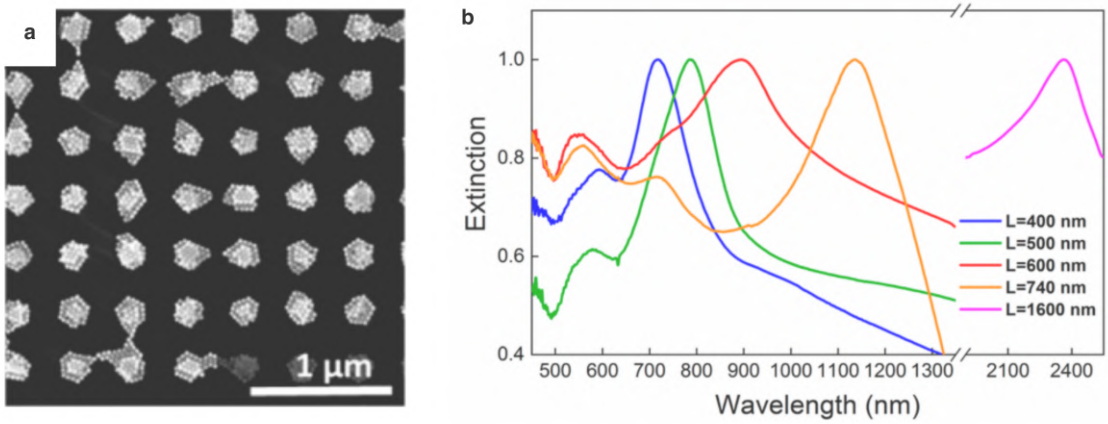

Figure 3.3: Examples of self-assembled gold NP superlattices. SEM images of a) gold nanocubes assembled in a 500 nm lattice, reproduced with permission from [4], copyright 2019 American chemical society. b) Gold nanosphere heptamers assembled into a lattice, reproduced with permission from [9], copyright 2011 American chemical society. c) Gold nanosphere clusters in 500 nm lattice, reproduced with permission from [15], copyright 2018 American chemical society. d) Dark-field scattering spectra of gold nanosphere heptamers under different light polarization, reproduced with permission from [9], copyright 2011 American chemical society. e) UV-VIS-NIR extinction spectra of gold nanosphere clusters in lattice of different periods reproduced with permission from [15], copyright 2018 American chemical society.

consequence, assemblies of nanoparticles with a controlled number of NPs would lead to homogeneous near-field enhancement enabling homogeneous SERS enhancement. Homogeneous near-field enhancement by controlled self-assembly of gold NPs would enable a better quantification of traces of various chemicals by SERS. Different fabrication strategies provided for the fabrication of plasmonic substrates with homogeneous near-field enhancement. However, most of the strategies use lithography processes that are time-consuming [23], or produce substrates with a low SERS enhancement [24].

Furthermore, the fabrication of nanoparticle clusters with a defined particle number is important to understand their optical properties. Different examples of rational study of the optical properties of gold NP clusters were done with different shapes of nanoparticles such as nanospheres and nanorods [25]. Additionally, different geometries of clusters have been studied such as lines and 2D clusters [26, 27]. Such studies, are very important to understand plasmonic

coupling and design more efficient platforms for sensing using SERS [21]. However, far-field coupling by the periodical arrangement of gold nanoparticle clusters has not been investigated thoroughly, mainly because of the fabrication complexity of such systems. Specifically, the homogeneity in the number of particles per cluster in lattices remains challenging. Fabricating lattices with a defined number of nanoparticles per cluster would help in the understanding of lattice plasmons in complex nanoparticle systems.

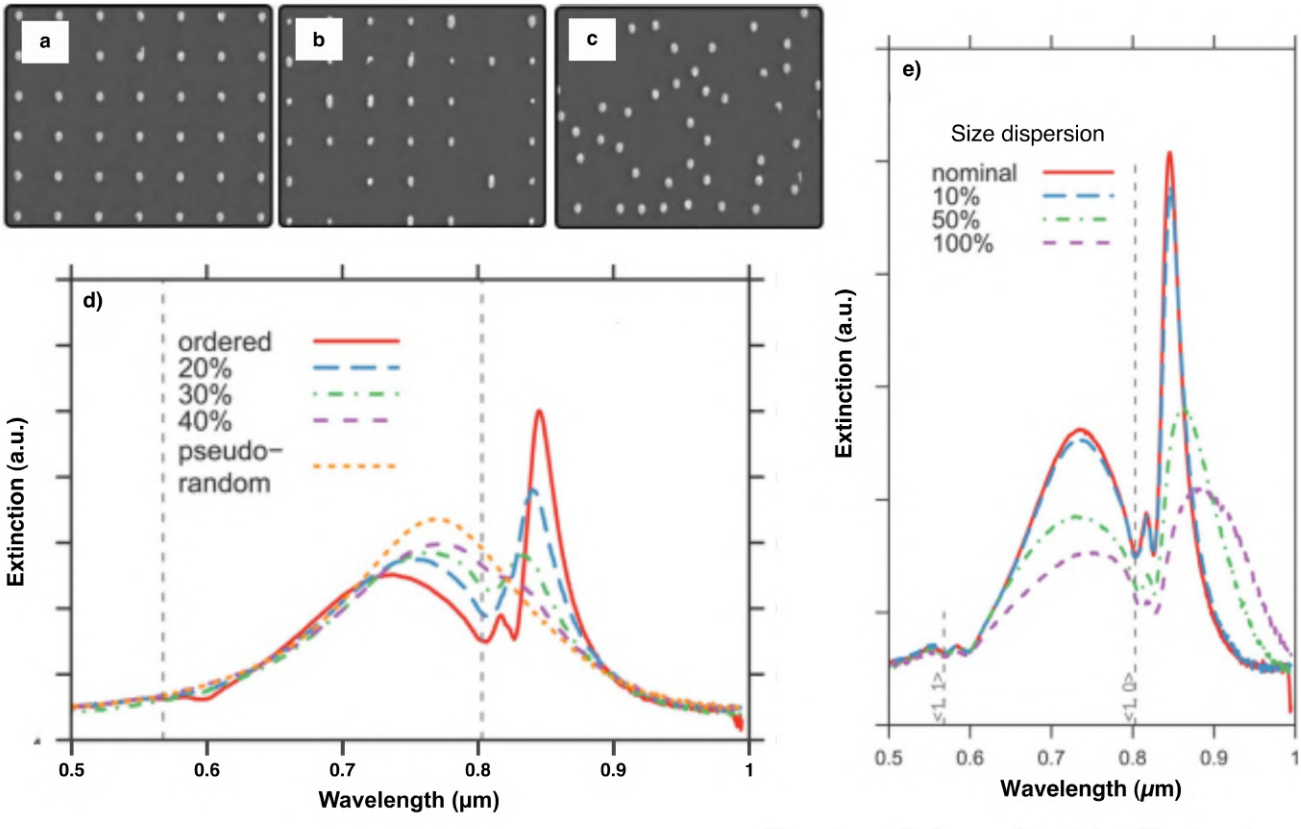

Figure 3.4: Influence of homogeneity on the optical properties of gold NP superlattices. SEM images of a) a perfect superlattice, b) a superlattice with 100% variation in the length of the long-axis of the particles c) a superlattice with pseudo-random particle position. Optical properties of lithographically made plasmonic lattice with d) different placement errors and e) different particle dispersion. Adapted with permission from [14].

Moreover, in the case of nanoparticle superlattices, homogeneity of the nanoparticle size distribution and precision in the placement of nanoparticles in the lattice deeply influence the optical properties of the superlattice [14, 28]. In **Figure 3.4** we can see various gold nanoparticle

lattices created by eBL, some of them display intentionally added disorder. **Figure 3.4 b** shows lattices with a particle placement error of 10 % while **Figure 3.4 c** displays lattice with a variation of the particle size along the long-axis of 100%. The sharp feature around 850 nm in the UV-VIS spectra **Figure 3.4 d**, is present in the case of the ordered lattice and disappears in the case of the pseudo-random lattice, indicating that such a feature arises from a lattice plasmon resonance. Additionally, an increase in the placement disorder and in the nanoparticle size dispersion results in broader lattice plasmon resonances, as can be seen in **Figure 3.4 e**. In other words, the disorder induced either in the placement of the nanoparticles or in the size dispersion of the nanoparticles results in weaker lattice plasmon coupling.

Finally, not only, homogeneous self-assembly of gold nanoparticles should lead to more robust and homogeneous SERS signals but it should also lead to a higher SERS signal thanks to more efficient far-field coupling. The influence of homogeneity on the intensity and standard deviation of the SERS signal motivated our study.

3.2 Results

3.2.1 Flows arising in a droplet of tertiary mixtures

Drying droplets display complicated flow regimes due to the different parameters to be taken into account, such as contact angle, volatility of the solvents, presence of surfactants, temperature of the substrate, humidity. Specifically, tertiary mixtures made of two solvents of different volatility and surfactant molecules are interesting systems to study flow regimes as we will explain in this section. Flows created inside droplets can carry nanoparticles in different regions of the droplet, repartition of the NPs in the droplet is very important as it influences the self-assembly pattern of nanoparticles by templated self-assembly (see **Section 3.2.2**). In this section, the different flows arising in droplets of tertiary mixtures, namely the convection flow resulting in the coffee-ring effect and the Marangoni flows will be explained.

Coffee-ring effect

The coffee-ring effect is named after a famous observation most coffee-drinkers have probably witnessed: dried coffee droplets exhibit donut-like deposition patterns [29]. This deposition pattern is due to an accumulation of particles at the rim of the droplet through convection flows induced by the drying droplet [30]. Higher evaporation occurs at the rim of the droplet, compared to the center of the droplet, due to the higher curvature of the droplet at the rim. This difference in evaporation rate induces a flow towards the rim of the droplet to refill the liquid passing in the form of gas. Colloidal particles are dragged by this flow, and generally get trapped at the edge of the droplet, which explains the formation of a NP ring at the edge of the droplet. The coffee ring can be altered by the creation of recirculating flow at the edge of the droplet, also known as Marangoni flows [31].

Marangoni flows

Unlike coffee droplets, scotch whisky droplets exhibit an almost homogeneous solute deposition under evaporation. Such an observation motivated scientists to study thoroughly flow arising in whisky droplets and to reproduce it artificially in the lab [32]. It was found that the chemical composition of scotch whisky induces recirculation flows at the edge of the droplet, thus reversing the coffee-ring effect [33]. Even if it is tempting to name this effect the whisky drying effect, such recirculation flows are commonly named after Marangoni who discovered this kind of recirculation flows [34].

Marangoni flows are circular flows that occur in liquids or gases due to surface tension gradients, volatility differences in solvent mixtures, or temperature gradients. In this part, we will focus on the case of droplets, and specifically on the solutal Marangoni flow and the surfactant-driven Marangoni flow. Since the temperature-driven Marangoni flow is weaker than the two precedent ones, it will not be taken into account here [32]. Solutal Marangoni flows arise due to volatility differences in solvent mixtures [35]. Surfactant-driven Marangoni flow derives from a surface tension gradient due to a concentration gradient of surfactant molecules at the air-water interface stabilizing the droplet [36, 37].

In tertiary mixtures comprising water, ethanol and surfactants, the solutal Marangoni flow

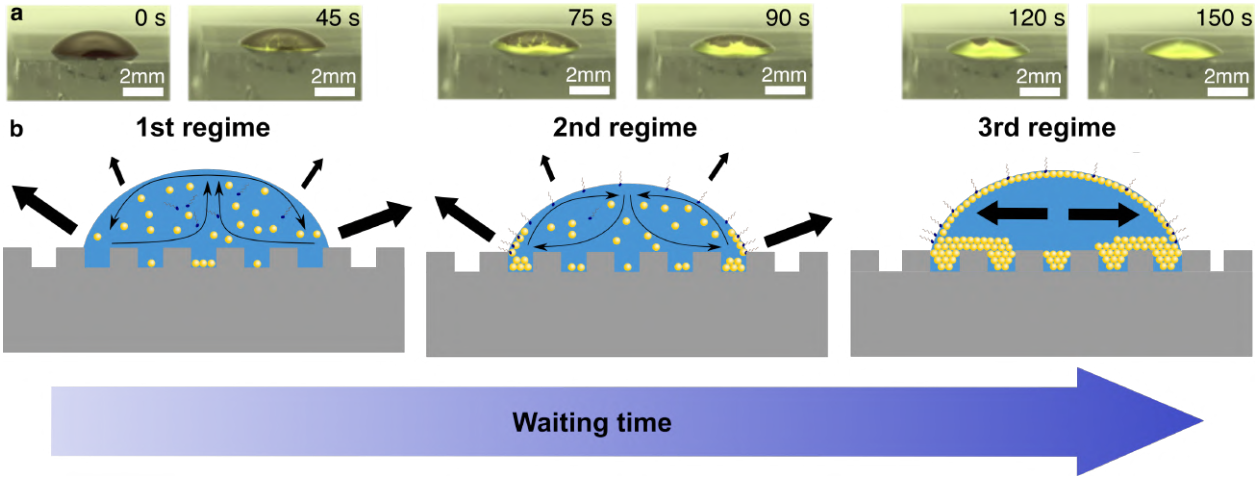

Figure 3.5: Marangoni flows in droplets containing gold NPs, ethanol, water and surfactant. a) Time-evolution of a droplet containing ethanol, water , surfactant and gold NPs. Green-Golden film seen on the droplet is due to close packed arrangement of gold NPs at liquid-air interface. b) Scheme of the flows inside the droplet in different regimes.

and the surfactant-driven Marangoni flow are opposed in directions and their magnitude changes over time [38]. For this reason, such systems have been extensively studied. Here, we will take the case where gold nanoparticles are present in a solution of water, ethanol, and cethyl trimethyl ammonium chloride (CTAC) as a surfactant. Especially, repartition of the gold NPs on the droplet's surface is easily seen in **Figure 3.5** by the appearance of a golden layer, indicating the formation of a close-packed layer of gold NPs at the surface of the droplet.

First, the solutal Marangoni flow is predominant, depicted in **Figure 3.5 b**, first regime; it emerges from the differences in volatility of ethanol and water and creates a circular flow, impeding the NPs to accumulate at the rim of the droplet. After a certain time, surfactant-driven Marangoni flow takes over the solutal Marangoni flow; this step is known as reverse flow and is extensively studied theoretically by various research groups [20]. In this regime, the accumulation of particles at the rim of the droplet starts, as can be seen by the presence of the golden color. Finally, in the third regime, a close-packed layer is formed on the droplet and the shear stress created by the surfactant concentration gradient is canceled by the presence of the NPs. In this last step, we go back to a coffee-ring like scenario with outward flow induced by convection.

3.2.2 Influence of ligand size, surfactant concentration, co-solvent ratio and waiting time on templated self-assembly

Influence of ligand size

The ligand size has a dramatic influence on the forces acting on colloidal nanoparticles. Especially, a longer ligand chain leads to stronger steric repulsion between nanoparticles (see **Section 2.2.1**). Van der Waals (VdW) forces are the main attractive forces keeping nanoparticles in a close-packed organization in the accumulation zone, therefore the balance between steric repulsion and VdW is very important for the formation of the accumulation zone. Higher repulsion forces due to a longer ligand lead to an accumulation zone comprising a lower amount of NPs. The formation of an accumulation zone with a high number of NPs is directly related to a higher assembly yield using capillary assisted self-assembly [39].

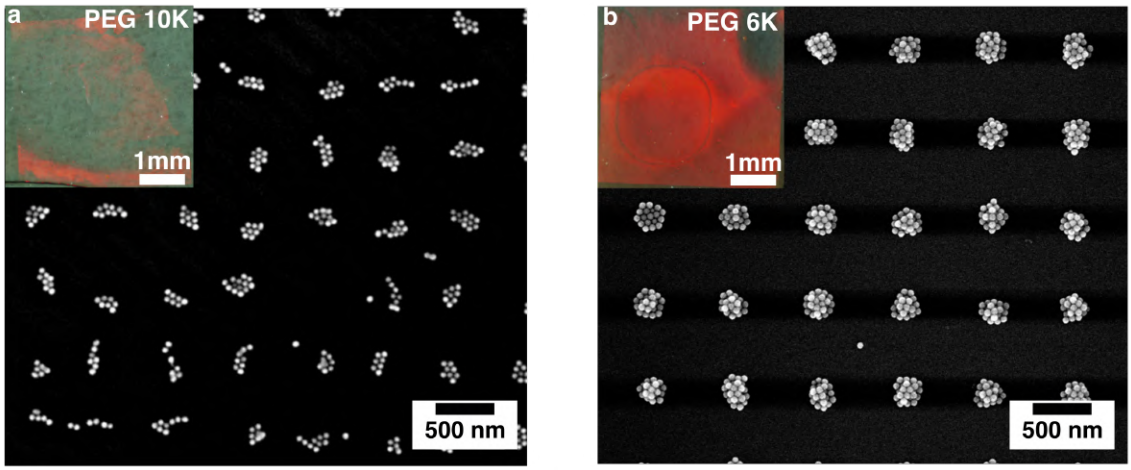

Figure 3.6: Nanoparticle ligand size effect on self-assembly. Images of a superlattice made with a) 10K PEG, b) 6K PEG, with a longer polymer, the steric repulsion is stronger leading to an accumulation zone with fewer NPs and therefore lower assembly yields.

In **Figure 3.6** two superlattices made with 52 nm diameter nanospheres functionalized with 6K polyethylene glycol(PEG) and 10K PEG are shown, the other parameters such as nanoparticle concentration, surfactant concentration, the composition of the solvent were kept constant. The superlattice made with the longer PEG chain displays a lower number of nanoparticles per cluster, but also a lower assembly-yield on the macroscale of nanoparticles as indicated by the

macroscale image in the inset of the SEM images. The lower transfer yield can be explained by the stronger steric repulsion using the longer PEG chain. Finally, the 6k PEG was chosen for the rest of the studies to obtain better assembly yield.

Influence of co-solvent

The influence of co-solvent on the templated self-assembly of gold nanoparticles was studied by assembling 65 nm diameter gold nanospheres coated with 6K PEG and dispersed in solutions comprising different ethanol ratios. For the different assembly, the waiting time between droplet deposition and substrate coverage was fixed to 60 seconds, the surfactant concentration was fixed to 200 µM, and the gold concentration was fixed to 20 mM as measured by the absorption at 400 nm(these parameters will be studied independently in **Section 3.2.2**).

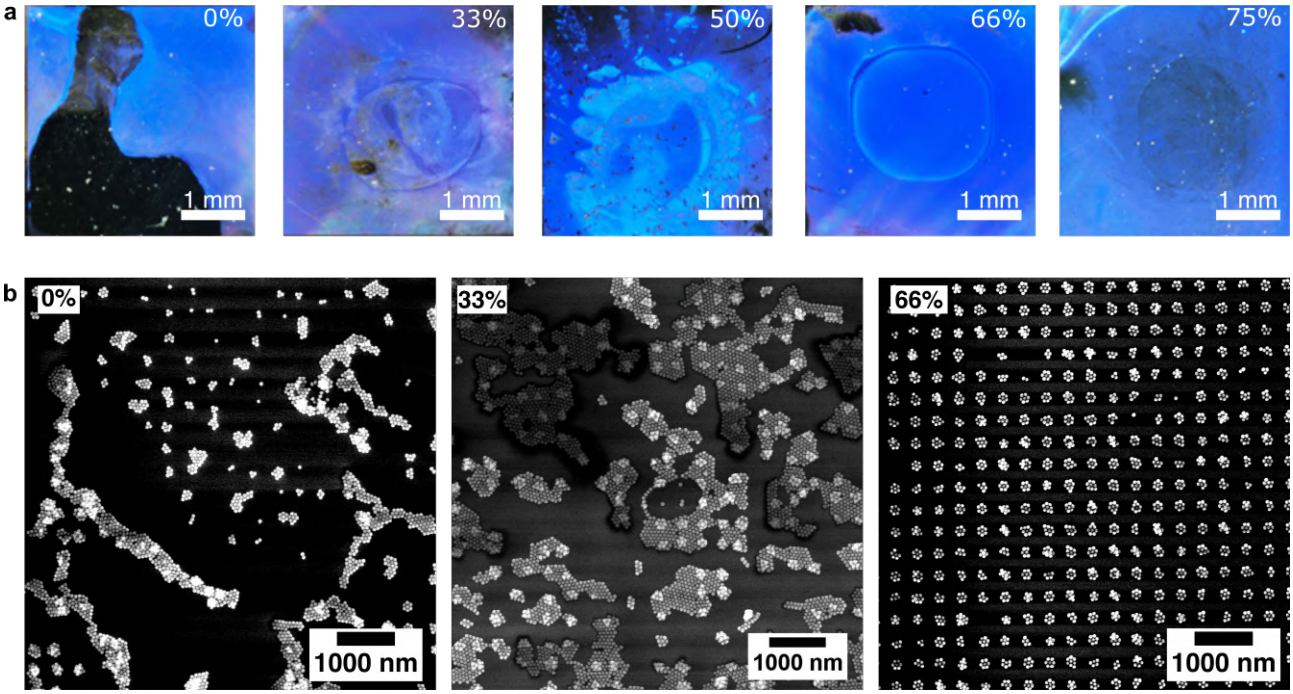

Figure 3.7: Influence of ethanol as a co-solvent on superlattice homogeneity. a) Macroscale images of superlattices made with different ethanol ratios, the blue color indicates the periodic organization of nanoparticles. Lighter blue indicates a higher amount of NPs, the presence of different tints of blue therefore points out the inhomogeneity of the superlattice. b) SEM images of superlattices made with different ethanol ratios.

In **Figure 3.7 a**, we can see macroscale images of samples made with different ethanol ratios,

the blue color indicates for the periodical arrangement of gold nanoparticles. Without ethanol, the templated self-assembly process yields a partial transfer of NPs to the glass substrate while using ethanol the NPs transfer occurs on the whole surface of the glass substrate. The partial transfer of nanoparticles to the glass substrate in absence of ethanol is due to a partial wetting of the glass substrate by the NP solution. By adding ethanol, a superlattice is created on the whole surface of the glass thanks to complete wetting of the glass by the NP film in presence of ethanol. Lighter blue indicates for regions where more NPs are transferred, therefore changes in the tint of the blue in the macroscale images indicate a non-homogeneous sample. By visual inspection, we see that the most homogeneous sample is obtained using 66% of ethanol. Moreover, SEM images on **Figure 3.7 b** reveal that the homogeneity found on the macroscale for the superlattice made with 66% ethanol is also found in the nanoscale in the nanoscale with NP clusters comprising 7 NPs on a large area of the sample. Samples displaying inhomogeneities on the macroscale display a higher dispersion in the number of NPs per cluster in the nanoscale, as exemplified by the SEM images of the superlattices made with 0% and 33% ethanol. Finally, the templated self-assembly process using 66% resulted in the best homogeneity both on the macroscale and the nanoscale, which is why this ratio of ethanol in the nanoparticle dispersion was used in the following studies.

Influence of waiting time and surfactant concentrations

To get a good assembly of NPs, a certain waiting time before putting the substrate on top of the droplet is indispensable. The repartition of NPs in the droplet changes with time, the different flows present in such tertiary droplet mixtures carry the NPs in different regions of the droplet and NPs attract each other through Van der Waals interaction. In **Section 3.2.1**, we have seen the evolution of a droplet of water, ethanol, CTAC and gold NPs at different waiting times, specifically repartition of the particles on the surface of the droplet could be followed by the formation of a golden layer. After 45 s of waiting time, a golden film starts to appear on the rim of the droplet, indicating a high accumulation of NPs at the liquid-air interface in the form of a close-packed layer [40]. After 120 s, the droplet appears totally golden.

Putting the substrate at different stages of waiting time onto the droplet results in different assembly patterns, as depicted in **Figure 3.8** for spherical Au NPs of 65 nm. Visual inspection

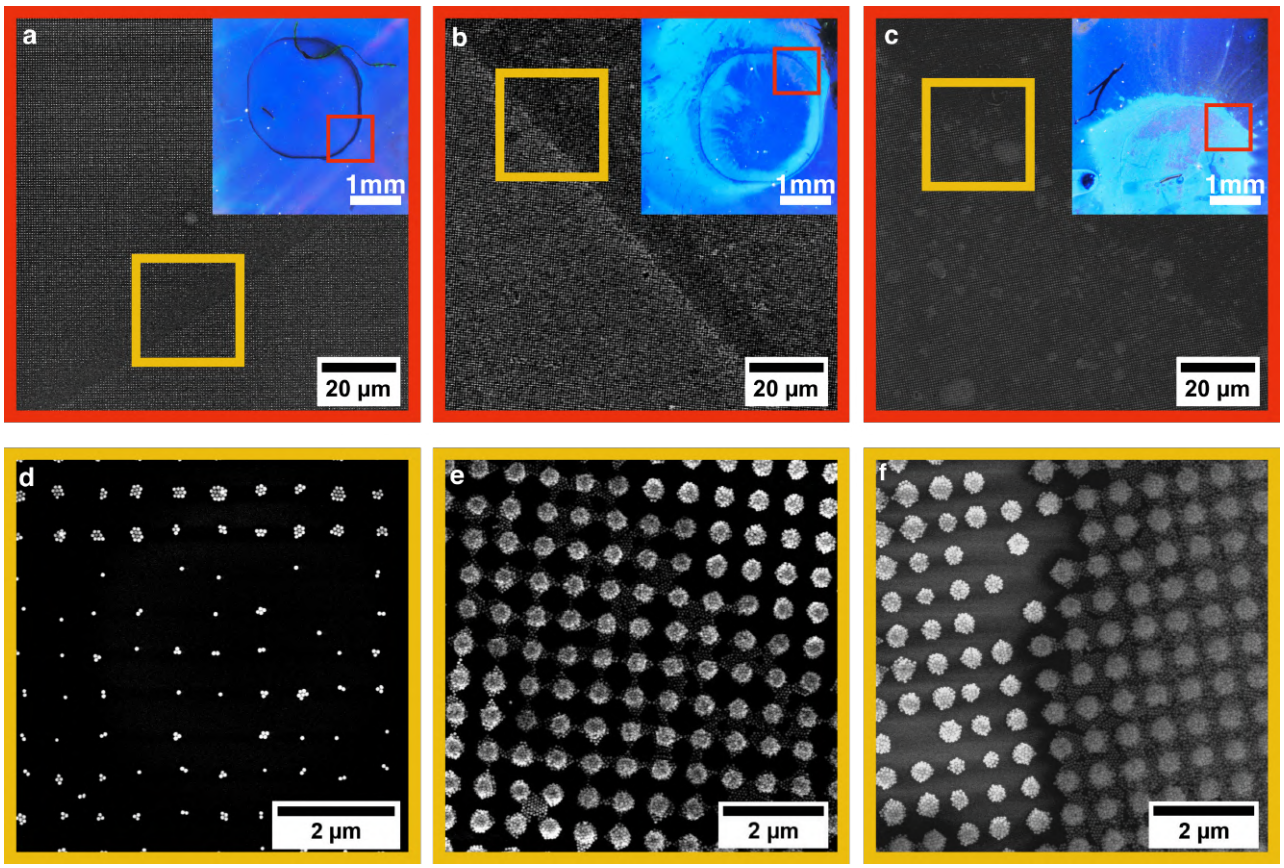

Figure 3.8: SEM images (top) and specific areas zoomed in (bottom) of resulting superlattices of Au nanospheres (65 nm diameter) at different waiting times. The upper insets represent macroscale visual inspection of the samples.

of the samples made at different stages shows a ring indicating the shape of the droplets rim. On these images (insets of **Figure 3.8**) lighter blue denote regions with a higher accumulation of NPs, as confirmed by SEM images. Before 45 s of waiting time, the ring is depleted of NPs; after 45 s, the ring presents an accumulation of NPs; and after 120 s, the whole droplet area is filled with Au NPs, as can be seen in the high magnification SEM images in **Figure 3.8**. The depletion or accumulation of NPs in the ring accounts for the repartition of NPs in the droplet before putting the substrate. Therefore, the transition from a depleted ring to a ring with an accumulation of NPs is a direct consequence of the Marangoni flow reversal.

The effect of surfactant concentration was also studied by fabrication of superlattices with different CTAC concentrations and different waiting times. A detailed kinetic study can be found in **Figure 3.9**, increasing the surfactant concentration and lowering the ethanol fraction in the solution has the same effect: accumulation of NPs in the center of the substrate at lower

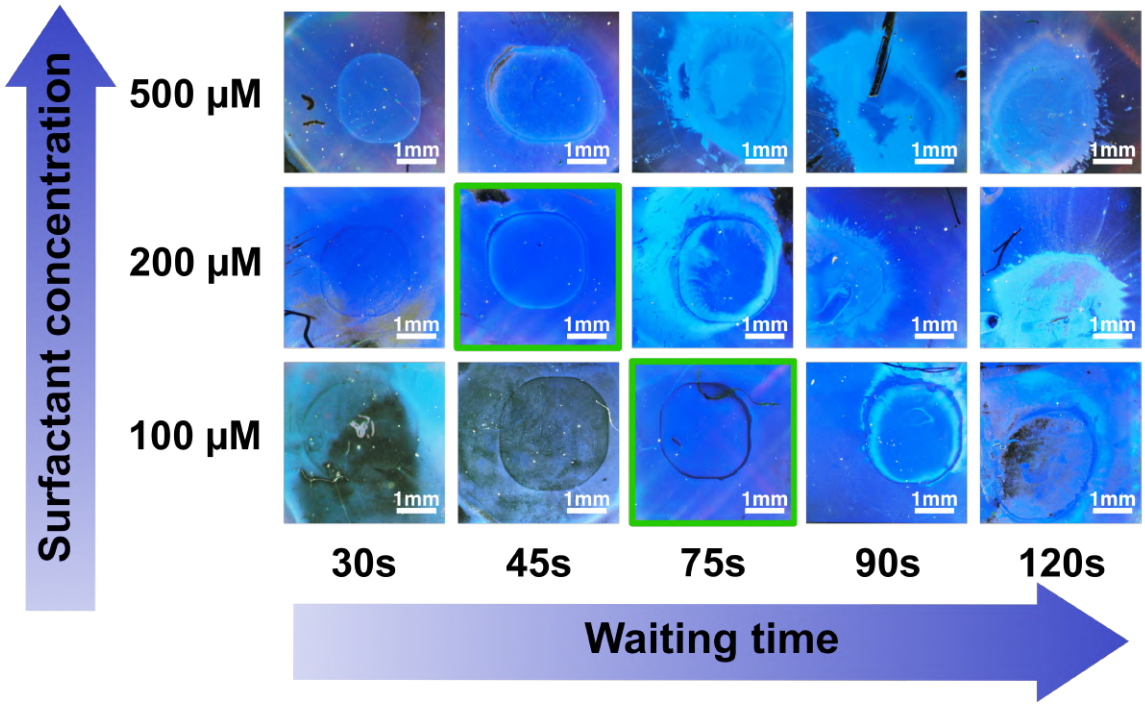

Figure 3.9: Systematic study of the surfactant concentration and waiting time influence on superlattice homogeneity. Blue color indicates for the presence of NPs, lighter blue represents areas with more NPs. The green squares highlight the superlattices with homogeneous repartition of nanoparticles.

waiting times. Indeed, increasing the surfactant concentration will favor the surfactant-driven Marangoni flow, thus, the flow reversal will happen at shorter waiting times, in the same way, lowering the ethanol concentration will disfavor the solutal Marangoni flow resulting in a flow reversal at lower waiting times. Taking this into account, the best parameters for homogeneous self-assembly were found to be 200 µM CTAC as surfactant, 66% ethanol, and 60 s waiting time.

Influence of substrate hydrophilicity

The hydrophilicity of the substrate plays an important role in capillary assisted self-assembly, it favors the transfer of the hydrophilic and hydrophobic NPs to the substrate [2]. In the template-assisted process, increased hydrophilicity of the glass substrate favors the wetting of all its surface by the nanoparticle solution, and therefore hydrophilicity allows for the creation of superlattice on the whole surface of the glass even without using ethanol. The increased hy-

drophilicity of the glass substrates after an oxygen plasma treatment of 2 minutes was confirmed by depositing a 200 µL droplet on top of the glass substrate, the untreated sample was not fully wet by the glass droplet while the plasma treated glass substrate was entirely wet by the water droplet indicating for increased hydrophilicity. On the nanoscale, when using no ethanol and an untreated glass substrate, the superlattice presents ill-defined clusters of nanoparticles and a lot of inhomogeneities (see **Figure 3.10 a**). Using a plasma treated glass substrate and no ethanol, the superlattices present well-defined periodical clusters with a moderate inhomogeneity of the cluster size, as can be seen in the SEM images of **Figure 3.10 b**. However, using 66% ethanol the superlattice quality improves drastically compared to the ones made without ethanol, especially the cluster size is very homogeneous, with mostly 7 NPs per cluster, as can be seen in **Figure 3.10 c**. Ethanol allows for highly homogeneous superlattices Not only does the ethanol enable to get very homogeneous superlattices, but it gives the advantage of avoiding the plasma treatment step of the substrate that can be time-consuming.

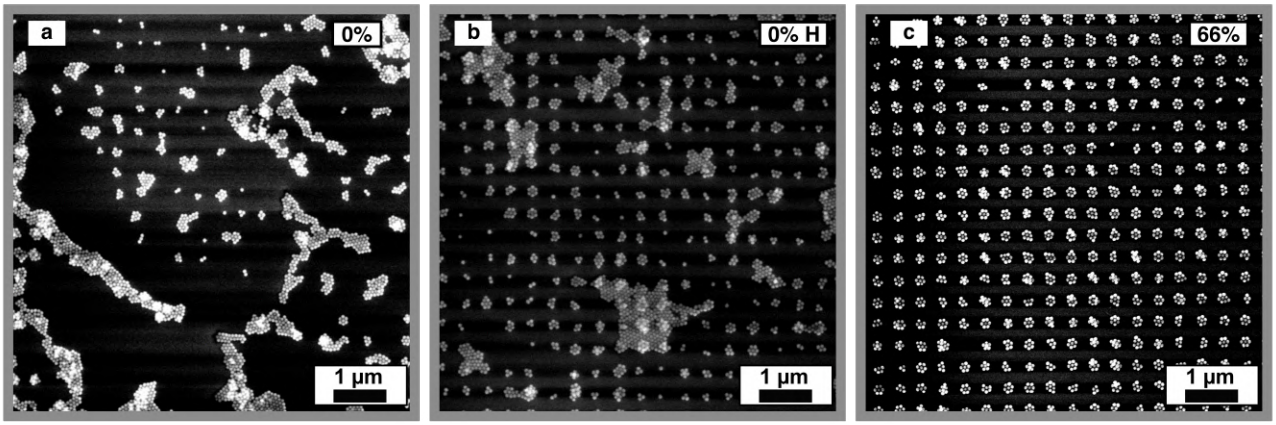

Figure 3.10: Influence of substrate hydrophylisation on superlattice homogeneity. SEM images of superlattices made: a) without ethanol and without hydrophilization, b) without ethanol and with hydrophilization, c) with ethanol and without hydrophilization.

3.2.3 Optical properties of homogeneous self-assembled superlattices

Optical properties of isolated nanosphere clusters and lattices of nanosphere clusters

As we explained in **Section 2.4.3**, organizing nanoparticles into a lattice accounts for an increase of the superlattice optical extinction at a specific wavelength depending on the period. If the period is large, no far-field coupling will occur in the visible region and therefore we can consider the cluster "isolated". Isolated clusters of nanospheres were fabricated by assembling 65 nm nanospheres into a grating of L=1500 nm, images of such a superlattice are found in **Figure 3.11 a**. Comparison of the optical properties of "isolated" clusters and 65 nm nanospheres cluster in a 400 nm lattice are shown in **Figure 3.11 b**.

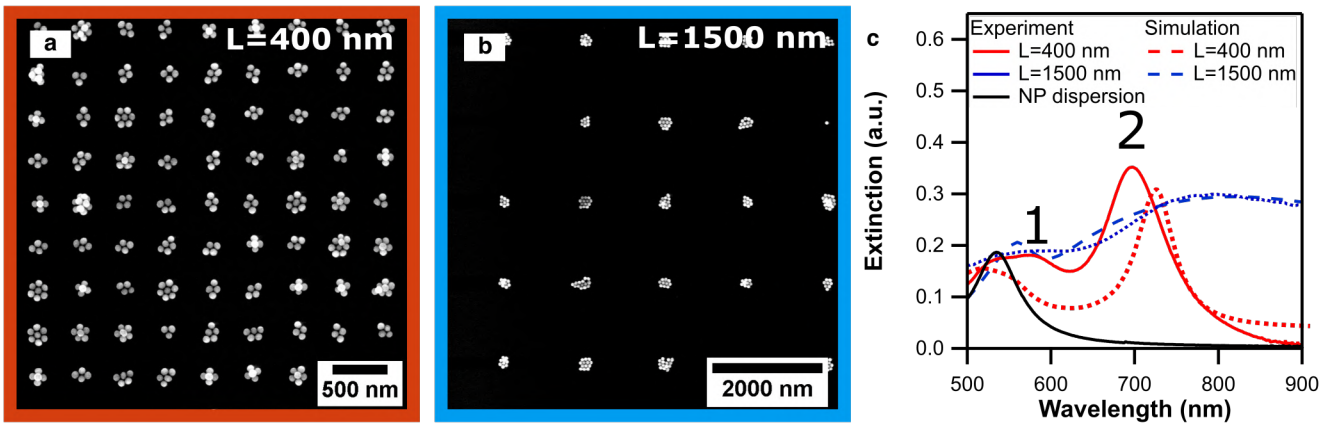

Figure 3.11: Comparison of the optical properties of superlattices of 400 nm (in a lattice) and 1500 nm period ("Isolated"). a) SEM images of 400 nm and 1500 nm period superlattices of 65nm nanospheres b) Experimental and simulated extinction spectra of 65nm nanospheres.

The 'isolated' clusters show a broad extinction spectrum, while the clusters assembled in a lattice show a sharp peak around 700 nm. It is clear that the far-field coupling gained by the periodical organization of the nanospheres clusters induces an increase of the absorption around 700 nm. This phenomenon is also reflected in FEM simulations (see details in materials and methods) and the near-field plots, which confirm the lattice plasmon nature of the resonance at 700 nm (see **Figure Appendix I.1**). The simulated absorption spectra of the 400 nm period superlattice display a lattice plasmon which is slightly sharper than the experimental one.

UV-Vis extinction spectra of superlattices with different homogeneities

Sub-unit homogeneity in lattices (here clusters of NPs) is of particular importance for their optical properties. In gold NP lattices made by EBL, it was shown that the homogeneity of NP size leads to a sharper resonance [14]. The sharpness of lattice plasmons is very relevant for applications in nanolasing, where high Q-factor resonance is needed [41]. The effect of homogeneity on optical properties was studied by fabricating substrates with different ethanol ratios, keeping other parameters constant (surfactant concentration and waiting time).

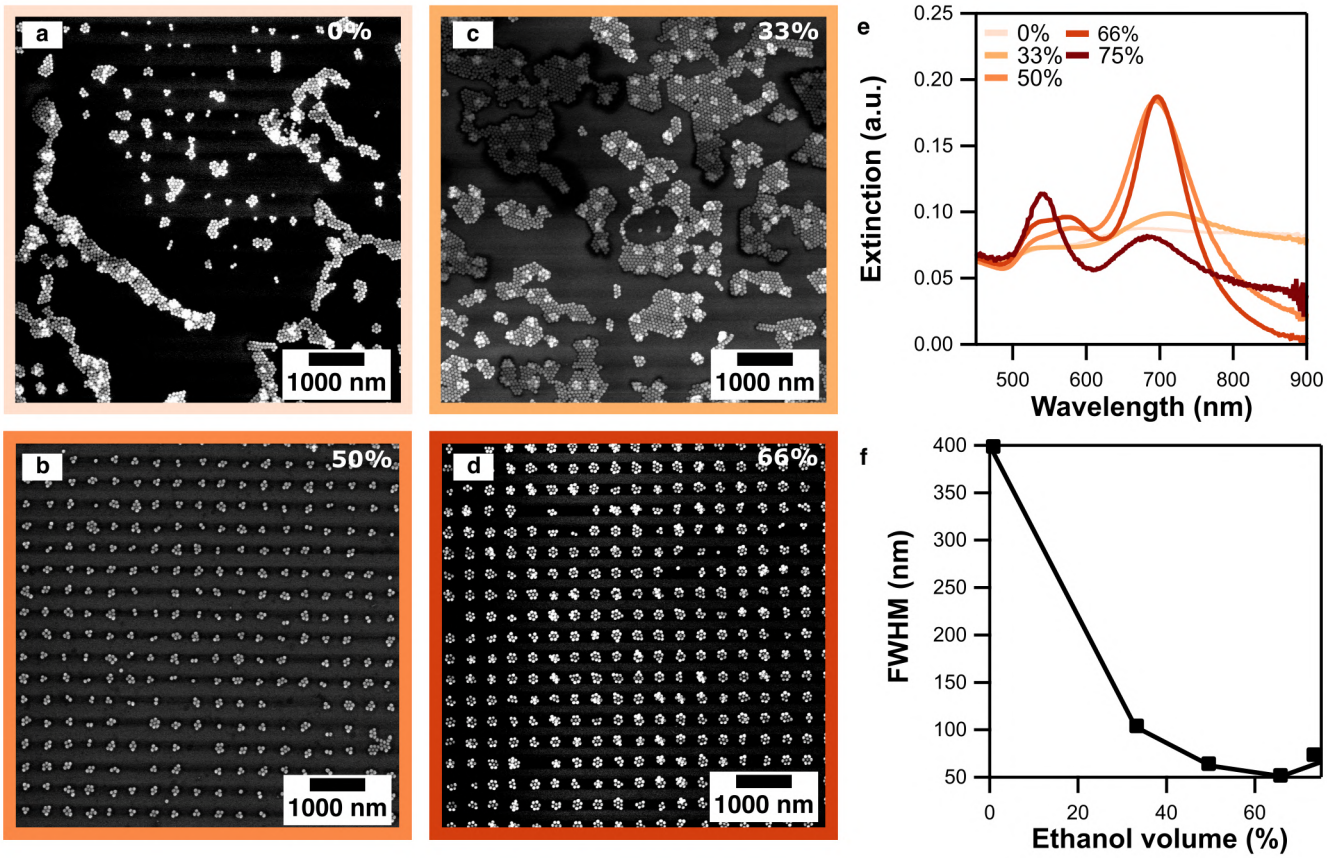

Figure 3.12: Optical properties of superlattices with different homogeneity. a) to d) SEM images of superlattices made with different ethanol ratio. The most homogeneous superlattice is the one made with 66% ethanol ratio. e) Extinction spectra of superlattices from spherical Au NPs (65 nm), fabricated with different concentrations of ethanol. f) FWHM of the peak at 700 nm, which is smallest for samples made with 66% of ethanol.

.

SEM Images of 400 nm period superlattices of 65 nm nanospheres made with different

ethanol ratios can be found in **Figure 3.12 a-d**. For superlattices made with 0 and 33% ethanol ratio, the SEM images depicts high accumulation of NPs and a low organization explaining the broad plasmon peaks. Increasing the ethanol content to 50-66% yields well-organized clusters with a majority of 7 NPs per cluster. A further increase to 75%, results in a lower transfer of NPs to the substrate due to a lower accumulation of NPs in the accumulation zone caused by Marangoni flow reversal at longer times. Optical properties of those superlattices are found in **Figure 3.12 e**. For the samples presenting good periodic organizations, a peak around 700 nm can be observed, this resonance was already attributed to lattice plasmons in the previous **Section 3.12 a**. By increasing the ethanol concentration from 0% to 66%, the FWHM is diminishing from 400 nm to 50 nm; further increase of the ethanol concentration again broadens the peak. The decrease in FWHM of the lattice plasmon peak with increasing ethanol content is explained by the better organization of the superlattice when increasing the ethanol content to 66%. Similar results were obtained using superlattices made with or without hydrophilization (see **Appendix I.2**) Far-field coupling through lattice plasmons is considerably increased by fabricating superlattices with identical sub-units.

SERS enhancement and standard deviation of superlattices with different homogeneity

Extinction properties of nanoparticle superlattices show a significant effect on the sharpness of the lattice plasmon thanks to the homogeneity attained using co-solvent assisted templated self-assembly. The near-field enhancement of plasmonic cluster depends on the size of the NPs, the interparticle distance, the refractive index in close proximity, and the number of NPs per cluster as well as the orientation of the particle in respect to each other. Therefore, having a controlled number of NPs in each cluster on a large scale will have a clear effect on the near-field homogeneity, and hence, sensing performance.

To assess the effect of homogeneity on the near-field enhancement of plasmonic superlattices, SERS signals of 4-MBA (4 Mercaptobenzoic acid) as target were probed. To attain full coverage of the nanostructure, and thus, comparable results between the different structures, the superlattices were incubated in a 100 µM solution of 4 MBA for 2 hours. Due to its thiolated groups, 4-MBA binds covalently to the gold NPs. Plasmonic substrates were then thoroughly

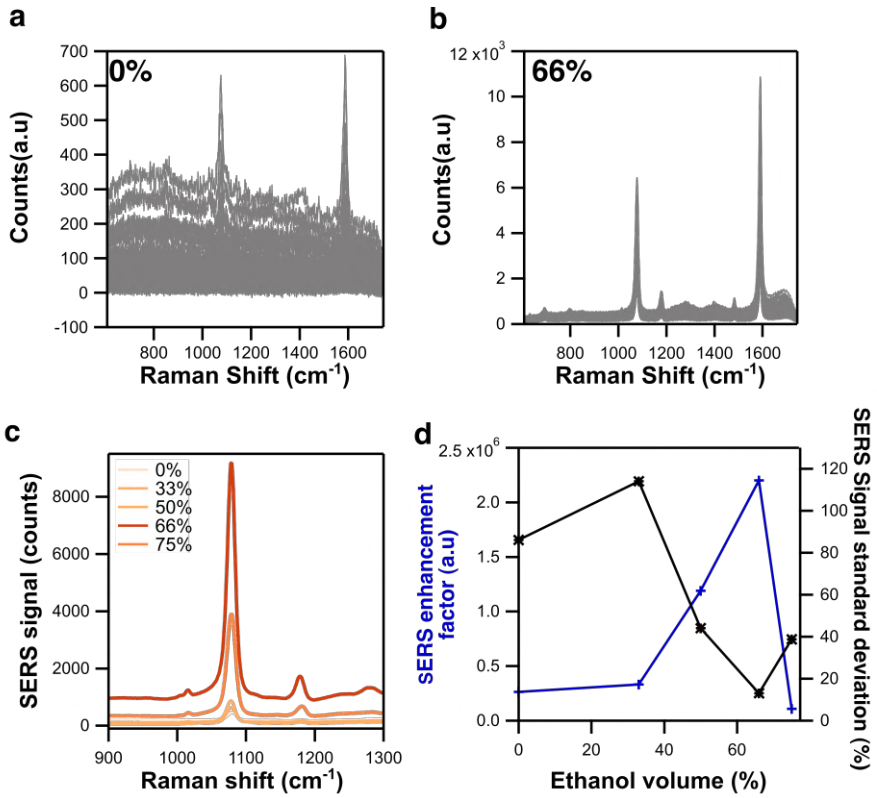

Figure 3.13: SERS signal of superlattices with different homogeneity. Superimposed SERS spectra from 100 random points of superlattices made with a) 0% and b) 66% of ethanol. c)Averaged SERS spectra from 100 randomly chosen points on superlattices made with five different concentrations of ethanol. d) Calculated analytical SERS enhancement factor and standard deviation of the 1600 cm^{-1} 4-MBA SERS peak as a function of the ethanol concentration.

washed with Milli-Q water to remove the excess of 4-MBA that did not covalently bind to gold. To probe the homogeneity of the near-field enhancement, SERS spectra were taken at more than 100 random points over the plasmonic substrates. **Figure 3.13 a** outlines as an example such 100 spectra super-imposed for superlattices made with 0% and 66% ethanol each (spectra for superlattices with made with other ethanol ratio can be seen in **Appendix I.3**). For all ethanol concentrations studied, the SERS spectra were averaged and plotted in **Figure 3.13 d**. The highest signal intensities, are found for the ν_{12} ring stretching vibration at 1080 cm^{-1} and for the ν_{8a} ring stretching vibration at 1600 cm^{-1}, corresponding to the phenyl ring of 4-MBA [16]. The Analytical SERS enhancement factor was calculated using the Raman intensities of the 1600 cm^{-1} and the following equation:

$$\mathrm{AEF} = \frac{I_{\mathrm{SERS}}/C_{\mathrm{SERS}}}{I_{\mathrm{Raman}}/C_{\mathrm{Raman}}}. \tag{3.1}$$

With I_{SERS} the SERS intensity of 4-MBA on the plasmonic superlattices, C_{SERS} the concentration of 4-MBA in the SERS experiment, here 100 µM, I_{Raman} the Raman intensity and C_{Raman} the concentration of 4-MBA in the Raman measurement experiments, here 200 mM. The Raman signal intensity of 4-MBA was recorded using the same measurement conditions as in the SERS measurements.

Figure 3.13d depicts the SERS performance of plasmonic superlattices made with different ethanol ratio, in terms of analytical SERS enhancement factor and standard deviation for the characteristic Raman peak at 1600 cm^{-1} which is assigned to the ν12 aromatic ring vibration of 4-MBA. Standard deviation is calculated from the statistics over the 100 SERS spectra taken at random points of the substrate and represents the deviation from the average value in percentage. Therefore the lower is the value the more homogeneous is the near-field enhancement. Again, the sample with 66% ethanol shows the highest performance, while the sample with 0% ethanol shows poor performance. Using our co-solvent assisted process, the SERS standard deviation of plasmonic superlattices could be reduced from 114% to 13%, and this on a sample of 8×8 mm^2. This value of SERS standard deviation also comforts the fact that the process using 66% ethanol gives the best sample homogeneity as the near-field enhancement depends on the number of NPs we have in a cluster. Moreover, it seems that at the same time that the sample is more homogeneous the analytical SERS enhancement factor is significantly increasing. As a result, the analytical SERS enhancement factor of plasmonic superlattice was improved of an order of magnitude using the co-solvent assisted templated self-assembly process. Such an increase of the SERS enhancement factor in more homogenous superlattices is explained by stronger lattice coupling arising in regular lattices, which is in accordance with the increase in extinction of the surface lattice plasmon resonance with homogenous superlattices.

3.3 Conclusion

The templated self-assembly process was optimized by screening different parameters: the ligand size, the waiting time before adding the substrate, the surfactant concentration and the

ethanol ratio. Especially, Marangoni flows arising in droplets containing water-ethanol and surfactant were taken into account to obtain the best superlattice quality. Homogeneity on the macroscale and the nanoscale was verified thanks to macroscopic images and SEM images. Parameters to get the most homogeneous superlattice were found to be: 200 µM CTAC, 60 s waiting time, and 66% ethanol. Using those parameters superlattices comprising 7 NPs per cluster on average were attained on a macroscale.

The optical properties of superlattices with different homogeneities were studied by UV-VIS. The apparition of a sharp resonance when the clusters are arranged periodically was explained by electromagnetic simulations to arise from lattice effect. Furthermore, the extinction spectra lattices with different qualities shown that more homogeneous lattices display sharper and more intense lattice plasmon. More specifically, the near-field enhancement of homogeneous gold nanoparticle superlattice was measured by SERS. Homogeneity increase in the superlattice yields in more intense SERS signal as well as more homogeneous SERS signal on the whole surface of the plasmonic substrate.

3.4 Materials and methods

3.4.1 Materials

$HAuCl_4 \cdot {}_3H_2O$ (≥99.9%, trace metal basis) was purchased from Alfa Aesar. Sodium borohydride (ReagentPlus©, ≥99%, $NaBH_4$), L-Ascorbic acid (ACS reagents, ≥99%, AA), poly(ethylene glycol) methyl ether thiol average Mn 6000 (PEG-6K), sodium hyprochlorite (6-14% active chlorine, Emplura©), and cetyl-trimethylammonium chloride (≥98%, CTAC) were purchased from Sigma-Aldrich. All solutions, except $HAuCl_4$ and CTAB, were prepared immediately before use. Purified Milli-Q water was used in all experiments (Millipore, 18.2 MΩcm). Glassware was cleaned with aqua regia and rinsed extensively with Milli-Q water before use.

3.4.2 Nanoparticle synthesis and functionnalization

Nanoparticle synthesis

Nanospheres were synthesized by seeded growth as reported recently [30]. First, small seeds of 2 nm were prepared by adding $HAuCl_4$ (50 µL, 0.05 M) to a CTAC solution (5 mL, 100 mM). Subsequently, $NaBH_4$ (200 µL, 0.02 M, i.e., 7.5 mg in 10 mL) was added under vigorous stirring. After 3 min, the mixture was diluted 10 times by a CTAC solution (100 mM). Then, the small seeds were overgrown to 10 nm nanospheres: For this purpose, the small seeds (900 µL) were added to a mixture of AA (40 µL, 0.1 M) and CTAC (10 mL, 25 mM). Next, HAuCl4 (50 µL, 0.05 M) was added under vigorous stirring. The 10 nm seeds showed an LSPR at 520 nm. The dispersion was left undisturbed for at least 1 h. Afterward, the nanospheres were centrifuged (19.300 rcf, 12 cm rotor) and washed at least 3 times with CTAC solution (25 mM). Afterward, the 10 nm-sized nanospheres were overgrown to larger nanospheres: First, the nanospheres (15 µL) were added to a solution AA (40 µL, 0.1 M) and CTAC (10 mL, 25 mM). Subsequently, $HAuCl_4$ (50 µL, 0.05 M) was added. The resulting nanoparticles had rough edges, which were removed by oxidative etching. For this, a diluted solution of sodium hypochlorite (10 µL, 1 to 1.5% of available chlorine) and 10 min later $HAuCl_4$ (10 µL, 0.05 M) was added under continuous stirring. After 30 min, the final nanospheres were centrifuged (1600 rcf,12 cm rotor, 15 min) and redispersed in CTAC solution (500 µM). The final NPs were concentrated to ca. 5 mM Au^0 in a solution of CTAC (500 µM). Functionalization was done by the addition of PEG (1 mg/mL) and stirring overnight at room temperature (RT). Excess unbound PEG was removed by repeated centrifugation (1600 rcf, 12 cm rotor, 15 min) and redispersion of the sedimented NPs in CTAC (500 µM).

Measurement of the gold concentration in the nanoparticle dispersions

The concentration of gold in the nanoparticle dispersions was estimated using the extinction at 400 nm. At this wavelength the extinction of gold nanoparticles doesn't depend on the size or shape of nanoparticles, therefore it constitutes a way for measuring their concentration. Calibration of the 400 nm extinction dependance on gold concentration perfomed by Scarabelli et al [22], shown that 1.2 extinction corresponds to 0.5 mM of gold.

Nanoparticle functionnalization

For functionnalization of the nanoparticles with PEG, the nanoparticles were concentrated by centrifugation and redispersion in 1mM CTAC to have a final concentration of gold between 2 and 10 mM (as measured by the absorption at 400 nm). Then 10 mg/ml of PEG-6K was added to the solution which was left undisturbed overnight. The nanoparticles were then washed by repeating centrifugation and redispersion in CTAC 500 µM at least 4 times. By repeating this operation several times, the PEG that did not bind to the nanoparticles is completely removed. The functionalization step is then repeated by concentrating the nanoparticles to 10 mM in 500 µM and adding 10 mg/mL of PEG-6K. Again the NPs are washed by repeating centrifugation and redispersion in CTAC 500 µM. Finally, the NPs are concentrated to 200 mM in 500 µM CTAC 500 µM, the nanoparticle solutions are stored in the fridge at 8 °C.

3.4.3 Characterisation techniques

Electron Microscopy

Scanning electron microscopy was performed using an environmental SEM (FEI Quanta 250) at an acceleration voltage of 30 kV.

UV-VIS measurements

Extinction spectra of colloidal dispersions were recorded with an Agilent 8453 UV/vis spectrophotometer, using polystyrene cuvettes. Extinction spectra of dry samples were collected using a Carry 5000 UV-vis spectrometer (Agilent).

SERS measurements

For SERS experiments, the samples were cleaned using 10 s of oxygen plasma (Diener pico) at 100 W and 0.4 mbar, followed by 5 minutes of UV-Ozone (bionanoforce). The SERS samples were incubated in an aqueous solution of 4-MBA (100 µM, 2 h), prepared freshly from a stock solution in EtOH (10 mM). After incubation, the samples were thoroughly rinsed with water to remove the excess 4-MBA molecules that did not bind to the AuNPs and dried with N2 flow. SERS Spectra were obtained using a Renishaw inVia reflex equipped with a stigmatic

single-pass spectrometer, a Peltier-cooled CCD detector (1024 x 512 px^2), a 1800 grooves mm^{-1} grating, a HeNe laser as excitation line (633 nm, 0.55 mW), and a 50x lens (LWD, NA 0.5) yielding a spot size of around 20 x 20 μm^2. For each samples more than 100 measurement points were taken in random points.

Bibliography

[1] Hamon, C.; Novikov, S. M.; Scarabelli, L.; Solís, D. M.; Altantzis, T.; Bals, S.; Taboada, J. M.; Obelleiro, F.; Liz-Marzán, L. M. Collective Plasmonic Properties in Few-Layer Gold Nanorod Supercrystals. *ACS Photonics* **2015**, *2*, 1482–1488.

[2] Hanske, C.; Müller, M. B.; Bieber, V.; Tebbe, M.; Jessl, S.; Wittemann, A.; Fery, A. The role of substrate wettability in nanoparticle transfer from wrinkled elastomers: Fundamentals and application toward hierarchical patterning. *Langmuir* **2012**, *28*, 16745–16750.

[3] Kravets, V. G.; Kabashin, A. V.; Barnes, W. L.; Grigorenko, A. N. Plasmonic Surface Lattice Resonances: A Review of Properties and Applications. *Chem. Rev.* **2018**, *118*, 5912–5951.

[4] JuodÄnas, M.; Tamulevičius, T.; Henzie, J.; Erts, D.; Tamulevičius, S. Surface Lattice Resonances in Self-Assembled Arrays of Monodisperse Ag Cuboctahedra. *ACS Nano* **2019**, *13*, 9038–9047.

[5] Yan, B.; Thubagere, A.; Premasiri, W. R.; Ziegler, L. D.; Negro, L. D.; Reinhard, B. Engineered Sers Substrates Employing Nanoparticle Cluster Arrays With Multiscale Signal Enhancement. *ACS Nano* **2011**, *3*, 1190–1202.

[6] Hanske, C.; Hill, E. H.; Vila-Liarte, D.; González-Rubio, G.; Matricardi, C.; Mihi, A.; Liz-Marzán, L. M. Solvent-Assisted Self-Assembly of Gold Nanorods into Hierarchically Organized Plasmonic Mesostructures. *ACS Appl. Mater. Interfaces* **2019**, *11*, 11763–11771.

[7] Ni, S.; Leemann, J.; Wolf, H.; Isa, L. Insights into mechanisms of capillary assembly. *Faraday Discuss.* **2015**, *181*, 225–242.

[8] Fan, J. A.; Wu, C.; Bao, K.; Bao, J.; Bardhan, R.; Halas, N. J.; Manoharan, V. N.; Nordlander, P.; Shvets, G.; Capasso, F. Self-assembled plasmonic nanoparticle clusters. *Science* **2010**, *328*, 1135–1138.

[9] Fan, J. A.; Bao, K.; Sun, L.; Bao, J.; Manoharan, V. N.; Nordlander, P.; Capasso, F. Plasmonic mode engineering with templated self-assembled nanoclusters. *Nano Lett.* **2012**, *12*, 5318–5324.

[10] Yan, B.; Boriskina, S. V.; Reinhard, M. Optimizing Gold Nanoparticle Cluster Configurations (n â¤ 7) for Array Applications. *J Phys Chem C* **2011**, *115*, 4578–4583.

[11] Yadav, R. K.; Otten, M.; Wang, W.; Cortes, C. L.; Gosztola, D. J.; Wiederrecht, G. P.; Gray, S. K.; Odom, T. W.; Basu, J. K. Strongly coupled exciton - surface lattice resonances engineer long-range energy propagation. *Nano Lett. 2020* **2020**, *20*, 5043â5049.

[12] Wang, D.; Bourgeois, M. R.; Lee, W. K.; Li, R.; Trivedi, D.; Knudson, M. P.; Wang, W.; Schatz, G. C.; Odom, T. W. Stretchable Nanolasing from Hybrid Quadrupole Plasmons. *Nano Lett.* **2018**, *18*, 4549–4555.

[13] Cheng, F.; Gao, J.; Luk, S. T.; Yang, X. Structural color printing based on plasmonic metasurfaces of perfect light absorption. *Sci. Rep.* **2015**, *5*, 1–10.

[14] Auguié, B.; Barnes, W. L. Diffractive coupling in gold nanoparticle arrays and the effect of disorder. *Opt. Lett.* **2009**, *34*, 401.

[15] Matricardi, C.; Hanske, C.; Garcia-Pomar, J. L.; Langer, J.; Mihi, A.; Liz-Marzán, L. M. Gold Nanoparticle Plasmonic Superlattices as Surface Enhanced Raman Spectroscopy Substrates. *ACS Nano* **2018**, *12*, 8531–8539.

[16] Konrad, M. P.; Doherty, A. P.; Bell, S. E. Stable and uniform SERS signals from self-assembled two-dimensional interfacial arrays of optically coupled Ag nanoparticles. *Anal. Chem.* **2013**, *85*, 6783–6789.

[17] Khlopin, D.; Laux, F.; Wardley, W. P.; Martin, J.; Wurtz, G. A.; Plain, J.; Bonod, N.; Zayats, A. V.; Dickson, W.; Gérard, D. Lattice modes and plasmonic linewidth engineering in gold and aluminum nanoparticle arrays. *JOSA B* **2017**, *34*, 691.

[18] Xu, Y.; Ye, Z.; Li, C.; McCabe, H.; Kelly, J.; Bell, S. E. Pressing solids directly into sheets of plasmonic nanojunctions enables solvent-free surface-enhanced Raman spectroscopy. *Appl. Mater. Today* **2018**, *13*, 352–358.

[19] Bell, S. E.; Charron, G.; Cortés, E.; Kneipp, J.; de la Chapelle, M. L.; Langer, J.; Procházka, M.; Tran, V.; Schlücker, S. Towards Reliable and Quantitative Surface-Enhanced Raman Scattering (SERS): From Key Parameters to Good Analytical Practice. *Angew. Chem. Int.* **2019**, *59*, 5454–5462.

[20] Taylor, R. W.; Esteban, R.; Mahajan, S.; Aizpurua, J.; Baumberg, J. J. Optimizing SERS from Gold Nanoparticle Clusters: Addressing the Near Field by an Embedded Chain Plasmon Model. *J Phys Chem C* **2016**, *120*, 10512–10522.

[21] Fraire, J. C.; Pérez, L. A.; Coronado, E. A. Cluster size effects in the surface-enhanced raman scattering response of ag and Au nanoparticle aggregates: Experimental and theoretical insight. *J Phys Chem C* **2013**, *117*, 23090–23107.

[22] Pazos-Perez, N.; Wagner, C. S.; Romo-Herrera, J. M.; Liz-Marzán, L. M.; García De Abajo, F. J.; Wittemann, A.; Fery, A.; Alvarez-Puebla, R. A. Organized plasmonic clusters with high coordination number and extraordinary enhancement in surface-enhanced Raman scattering (SERS). *Angew. Chem. Int.* **2012**, *51*, 12688–12693.

[23] Schmidt, M. S.; Hübner, J.; Boisen, A. Large area fabrication of leaning silicon nanopillars for Surface Enhanced Raman Spectroscopy. *Adv. Mater.* **2012**, *24*, 11–18.

[24] Liu, H.; Zhang, X.; Zhai, T.; Sander, T.; Chen, L.; Klar, P. J. Centimeter-scale-homogeneous SERS substrates with seven-order global enhancement through thermally controlled plasmonic nanostructures. *Nanoscale* **2014**, *6*, 5099–5105.

[25] Kuemin, C.; Stutz, R.; Spencer, N. D.; Wolf, H. Precise placement of gold nanorods by capillary assembly. *Langmuir* **2011**, *27*, 6305–6310.

[26] Fan, J. A.; Bao, K.; Wu, C.; Bao, J.; Bardhan, R.; Halas, N. J.; Manoharan, V. N.; Shvets, G.; Nordlander, P.; Capasso, F. Fano-like interference in self-assembled plasmonic quadrumer clusters. *Nano Lett.* **2010**, *10*, 4680–4685.

[27] Hanske, C.; Tebbe, M.; Kuttner, C.; Bieber, V.; Tsukruk, V. V.; Chanana, M.; König, T. A.; Fery, A. Strongly coupled plasmonic modes on macroscopic areas via template-assisted colloidal self-assembly. *Nano Lett.* **2014**, *14*, 6863–6871.

[28] Gupta, V.; Probst, P. T.; Goßler, F. R.; Steiner, A. M.; Schubert, J.; Brasse, Y.; König, T. A.; Fery, A. Mechanotunable Surface Lattice Resonances in the Visible Optical Range by Soft Lithography Templates and Directed Self-Assembly. *ACS Appl. Mater. Interfaces* **2019**, *11*, 28189–28196.

[29] Deegan, R. D. Pattern formation in drying drops. *Phys. Rev. E* **2000**, *61*, 475–485.

[30] Deegan, R. D.; Bakajin, O.; Dupont, T. F.; Huber, G.; Nagel, S. R.; Witten, T. A. Nature1997, Capillary flowas the cause of ring stains fromdried liquid drops.pdf. *Nature* **1997**, *389*, 827–829.

[31] Hu, H.; Larson, R. G. Marangoni effect reverses coffee-ring depositions. *J Phys Chem B* **2006**, *110*, 7090–7094.

[32] Kim, H.; Boulogne, F.; Um, E.; Jacobi, I.; Button, E.; Stone, H. A. Controlled Uniform Coating from the Interplay of Marangoni Flows and Surface-Adsorbed Macromolecules. *Phys. Rev. Lett.* **2016**, *116*, 1–5.

[33] Williams, S.; Brown, M.; Carrithers, A. Poster: Whiskey Webs: Microscale "fingerprints" of bourbon whiskey. 71th Annual Meeting of the APS Division of Fluid Dynamics - Gallery of Fluid Motion. 2018.

[34] Marangoni, C. *Sull'espansione delle goccie d'un liquido galleggianti sulla superfice di altro liquido*; Fratelli Fusi, 1865.

[35] Marin, A.; Karpitschka, S.; Noguera-Marín, D.; Cabrerizo-Vílchez, M. A.; Rossi, M.; Kähler, C. J.; Rodríguez Valverde, M. A. Solutal Marangoni flow as the cause of ring stains from drying salty colloidal drops. *Phys. Rev. Fluids* **2019**, *4*.

[36] Still, T.; Yunker, P. J.; Yodh, A. G. Surfactant-induced Marangoni eddies alter the coffee-rings of evaporating colloidal drops. *Langmuir* **2012**, *28*, 4984–4988.

[37] Marin, A.; Liepelt, R.; Rossi, M.; Kähler, C. J. Surfactant-driven flow transitions in evaporating droplets. *Soft Matter* **2016**, *12*, 1593–1600.

[38] Christy, J. R. E.; Hamamoto, Y.; Sefiane, K. Flow transition within an evaporating binary mixture sessile drop. *Phys. Rev. Lett.* **2011**, *106*, 1–4.

[39] Malaquin, L.; Kraus, T.; Schmid, H.; Delamarche, E.; Wolf, H. Controlled particle placement through convective and capillary assembly. *Langmuir* **2007**, *23*, 11513–11521.

[40] Montelongo, Y.; Sikdar, D.; Ma, Y.; McIntosh, A. J.; Velleman, L.; Kucernak, A. R.; Edel, J. B.; Kornyshev, A. A. Electrotunable nanoplasmonic liquid mirror. *Nat. Mater.* **2017**, *16*, 1127–1135.

[41] Wang, D.; Bourgeois, M. R.; Lee, W. K.; Li, R.; Trivedi, D.; Knudson, M. P.; Wang, W.; Schatz, G. C.; Odom, T. W. Stretchable Nanolasing from Hybrid Quadrupole Plasmons. *Nano Lett.* **2018**, *18*, 4549–4555.

Chapter 4

Self-assembly of differently shaped nanoparticles into superlattices and their optical properties

Figure 4.1: On the left: Photograph of "Van Gogh, 'The starry night', 1889" by Christopher S. Penn, under Creative Comon by 2.0 license. On the right: David Vila-Liarte and Mathias Charconnet, The nanosplasmonics starry night, 2020, photo-montage of various nanoparticle clusters.

Abstract

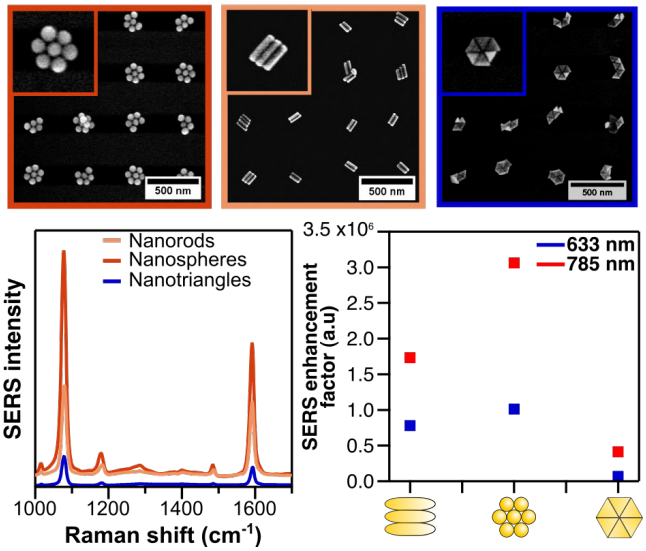

Due to their strong near-field enhancement, anisotropic gold nanoparticles are generally preferred over gold nanospheres for sensing applications using SERS. Therefore, assembling anisotropic gold nanoparticles into periodically arranged clusters, i.e. plasmonic superlattices, appears to be an interesting way of increasing the SERS enhancement of plasmonic superlattices. In this context, nanospheres, nanorods, and nanotriangles were successfully assembled into homogeneous superlattices, using the optimized templated self-assembly process described in **Chapter 3**. The fabrication of superlattices of different periods gives the possibility to tune the surface lattice plasmon resonances towards the standard laser excitation wavelengths (633 nm and 785 nm), which allows for further enhancement of the SERS signal at both wavelengths. As a result, the 400 nm period superlattices yielded higher SERS signals using the 633 nm laser excitation, while the 500 nm period superlattices yielded higher SERS signals using the 785 nm laser excitation. Using the optimal lattice period for each laser excitation wavelength, the SERS enhancement from the differently shaped nanoparticle superlattices was compared, and it was concluded that nanosphere superlattices yielded the highest SERS enhancement factors. Finally, the absorption properties of the differently shaped superlattices were simulated by the finite element method in a collaboration with the University of Southern Denmark, Mads Clausen Institute from the research group of Prof. J. Adam. By considering various cluster morphologies, the simulations reflected satisfactorily the experimental results, and a detailed interpretation of the simulated optical properties was performed to gain insight into the different plasmonic resonances present in the plasmonic superlattices.

4.1 Introduction

4.1.1 SERS enhancement of gold nanostructures

The mechanism of SERS enhancement comprises two components: the chemical enhancement and the electromagnetic enhancement. The chemical enhancement depends on the change of polarizability of the molecule in an adsorbed state, while the electromagnetic enhancement depends on the electric field enhancement provided by the nanostructured substrate (see **Section 2.5.1** for more details). The electromagnetic enhancement constitutes the dominant enhancement in SERS and is responsible for the high sensitivity of SERS [1]. Consequently, the main strategy to increase the SERS enhancement consists of designing nanostructures with high electric field enhancement. In this context, the assembly of gold nanoparticles into close-packed clusters is a very suitable strategy, since plasmonic coupling allows for a dramatic enhancement of the near-field at the junction between nanoparticles. Still, gold nanospheres constitute the simplest nanoparticle morphology, and anisotropic gold nanoparticles exhibit higher electric field enhancement. For this reason, the aim of this chapter is to assemble differently shaped gold nanoparticles into plasmonic superlattices to study their optical properties and SERS enhancement.

4.1.2 Electric field enhancement of anisotropic gold nanoparticles

As explained in **Section 2.3.3**, not only the size of nanoparticles but also their shape deeply influence their optical properties. For nanospheres, an increase in the size leads to a redshift of the plasmon resonance [2], while for nanorods, an increase of the aspect ratio leads to a redshift of the longitudinal plasmon resonance [3, 4]. At their plasmon resonance, anisotropic gold nanoparticles exhibit a higher near-field enhancement than nanospheres [5, 6]. Such a statement is well illustrated by comparing the electric field enhancement of gold nanospheres and gold nanorods. In **Figure 4.2 a,b**, the simulated near-field enhancement plots of a 65 nm sphere and a 110×30 nm nanorod at their plasmon resonance can be seen; the nanorod presents a strong enhancement of the electric field at its tips while the nanosphere presents a lower electric field enhancement. For this reason, gold nanorods are generally preferred over gold nanospheres

in systems that require high near-field enhancement.

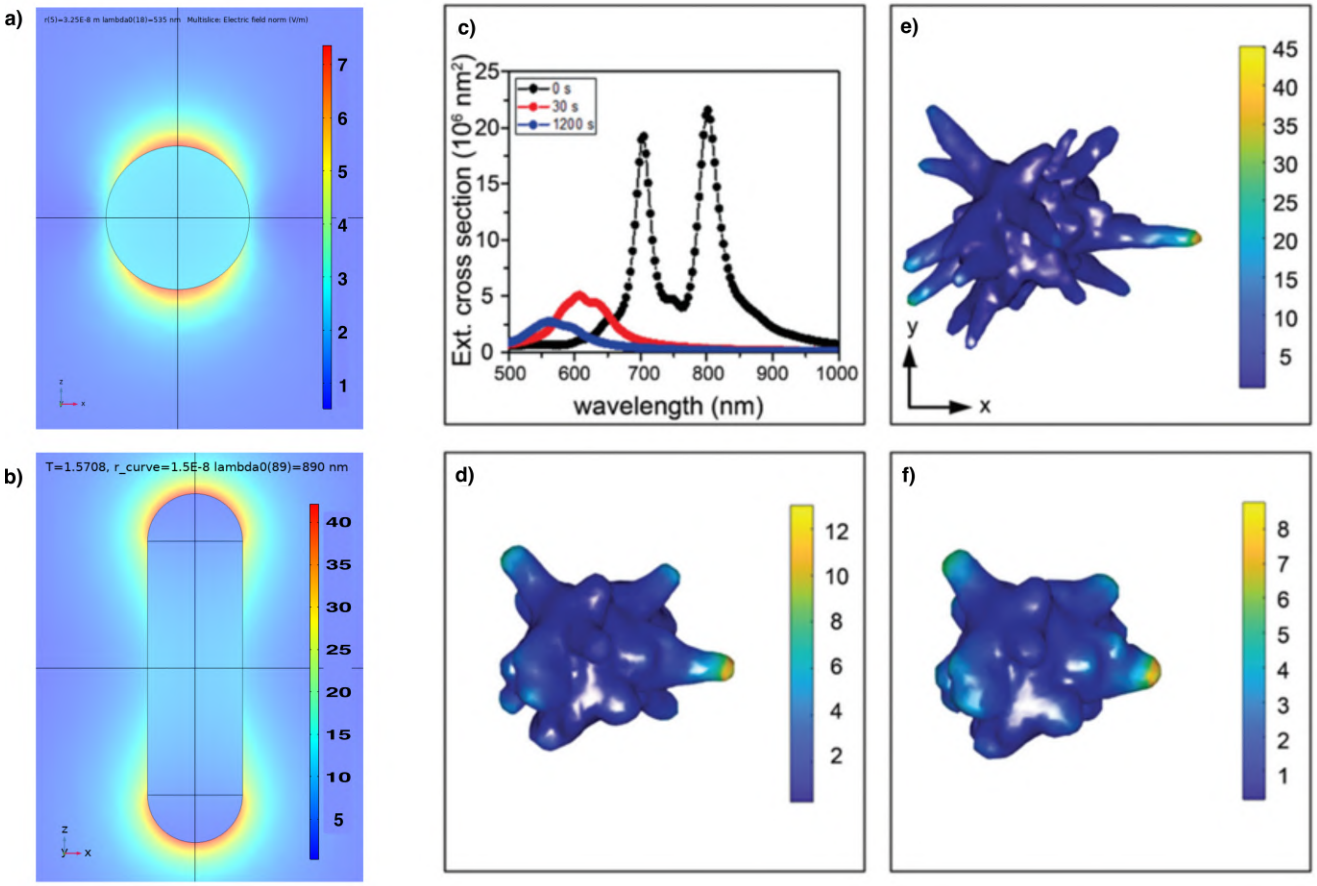

Figure 4.2: FEM simulations of the electric field from a) a 65 nm diameter nanosphere at 535 nm and b) a 110×30 nm nanorod at 890 nm. c) Corresponding simulated optical extinction from the nanostars depicted in d), e) and f). d) to f) Average electric field distribution of nanostars with different tip length and curvature obtained from FEM simulations. c) to f) are reproduced with permission from [7].

In general, the presence of sharp tips allows for a stronger concentration of the electric field leading to high near-field enhancement [8]. Another example presenting the simulated electric field enhancement of nanostars with different tip lengths and curvature is shown in **Figure 4.2 c-f** [7]. A decrease in the electric field enhancement of nanostars is observed with decreasing tip length and curvature. These calculations aimed at explaining the decrease in SERS signal in gold nanostars upon reshaping due to strong thermoplasmonic effects [9, 10]. As a conclusion, anisotropic gold nanoparticles, and particularly gold nanoparticles with sharp tips give rise to strong SERS enhancement, provided that their plasmon resonances match the

laser excitation wavelength.

4.1.3 Self-assembled anisotropic gold nanoparticles for SERS

When nanoparticles are in close proximity to each other (<50 nm), the plasmon resonances of gold nanoparticles can couple, leading to the formation of hotspots (see **Section 2.4.1**) [11, 12]. Confinement of the electric field in the junction of assembled nanoparticles, i.e hotspots, constitutes an attractive way to dramatically enhance the electric field in the vicinity of the nanoparticles.

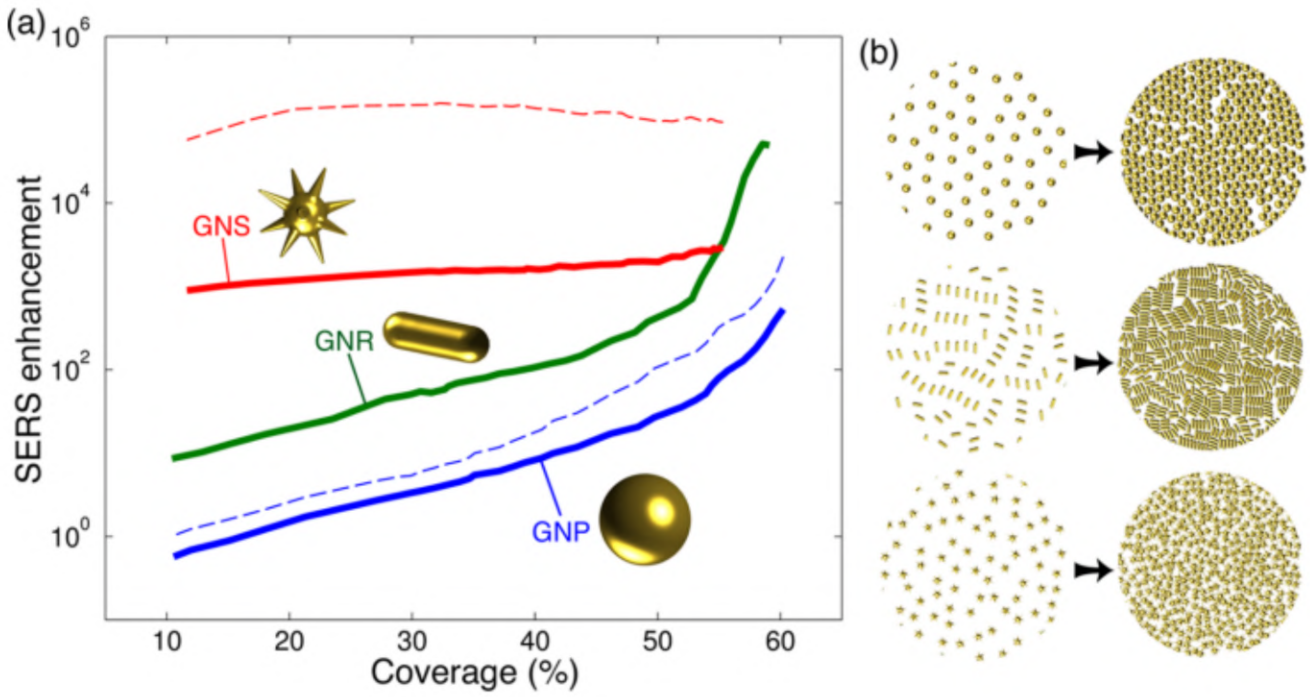

Figure 4.3: Density dependence of the SERS performance in nanoparticle monolayers. (a) Maximum SERS enhancement for planar monolayers of particles with different morphology (see legend). The particle coverage is defined as the fraction of area occupied by the projection of the metal along the plane normal. (b) Sketches showing an increasing density of nanoparticles in the monolayers. All results are averaged over polarizations of the normally incident light. Solid curves are calculated at 785 nm incident wavelength for zero Raman shift, while dashed curves for gold nanospheres and gold nanostars correspond to 633 and 900 nm, respectively. Reproduced with permission from [13], copyright 2017 American Chemical Society.

The formation of hotspots through the self-assembly of spherical gold nanoparticles has

been used for the fabrication of highly efficient SERS substrates [14]. Due to the superior near-field enhancement of anisotropic nanoparticles, one could expect self-assembled anisotropic gold nanoparticles to confer even higher SERS signal than self-assembled gold nanospheres. However, it is not always the case, and the coupling of complex anisotropic gold nanoparticles does not necessarily yield stronger near-field enhancement than those of single nanoparticles [15]. For instance, **Figure 4.3** shows the averaged near-field enhancement of monolayers of differently shaped gold nanoparticles comprising different substrate coverage [13]. Nanostars exhibit a high near-field enhancement in the single-particle limit, however, the aggregation of gold nanostars does not lead to a significant increase of the SERS signal. On the contrary, dilute layers of gold nanospheres and nanorods exhibit a moderate SERS enhancement, while a more compact film of gold nanospheres or nanorods exhibits a boost in their performance at around 50% coverage due to the plasmon coupling of gold nanoparticles. Interestingly, after a certain substrate coverage, the enhancement gained by the nanorods can even surpass the enhancement gained by the assembled nanostars.

Following the idea of improving the SERS signal of plasmonic superlattices through the assembly of anisotropic gold nanoparticles, this chapter shows a comparative study of the SERS enhancement provided by gold nanoparticle superlattices made of different nanoparticle shapes. In the first part, the self-assembly process is extended to nanorods and nanotriangles. The extinction properties of the gold nanoparticle superlattices are then studied by UV-Vis spectroscopy and correlated through FEM simulations to gain an insight on the plasmonic modes involved. Finally, the SERS performance from superlattices of two different periods (400 and 500 nm) and different nanoparticle shapes are analyzed under two laser excitations (633 and 785 nm).

4.2 Results

4.2.1 Self-assembly of differently shaped gold nanoparticles into superlattices

The collective plasmon resonance of plasmonic superlattices mainly depends on its lattice period. As the superlattice period is determined by the period of the nanostructured PDMS molds, the molds were chosen so that the surface lattice resonance of the plasmonic superlattices occurs in the range of the two available laser excitation wavelengths of 633 and 785 nm. The wavelength of surface lattice plasmon resonances can be approximated by the Rayleigh anomaly cutoff wavelength (see **Equation** (2.4.3)). Taking into account the refractive index of the glass substrate of 1.5, 400 nm period superlattices yield a Rayleigh anomaly at 600 nm, i.e close to the 633 nm excitation wavelength, and 500 nm period superlattices yield a Rayleigh anomaly at 750 nm, i.e close to the 785 nm excitation wavelength. Higher periods would lead to Rayleigh anomalies at a higher wavelength than the available laser excitations, which is why the 400 and 500 nm period molds were chosen for this study. The 400 nm period molds display circular wells of 240 nm diameters, while the 500 nm molds display circular wells of 270 nm diameter. Thanks to the small difference in the hole size, a similar number of nanoparticles per cluster can be assembled using both the 400 nm and 500 nm PDMS molds.

The optimized self-assembly process from **Chapter 3** was used to assemble the differently shaped nanoparticles into the wells of the nanostructured molds. Besides, the differently shaped particles were functionalized with the same amount of 6K PEG and the nanoparticle concentration in the droplet was fixed to 20 mM to have a similar amount of gold in the different superlattices (see materials and methods for more details). Remarkably, this process yields well-organized plasmonic superlattices for NPs of different shapes, as can be seen in **Figure 4.4**. Particularly, nanorod-based superlattices comprise around 3-4 nanorods per cluster while nanotriangles-based and nanospheres-based superlattices comprise around 6-7 nanoparticles per cluster. Both for nanorods and nanotriangles, the nanoparticles were found to be mainly assembled side by side.

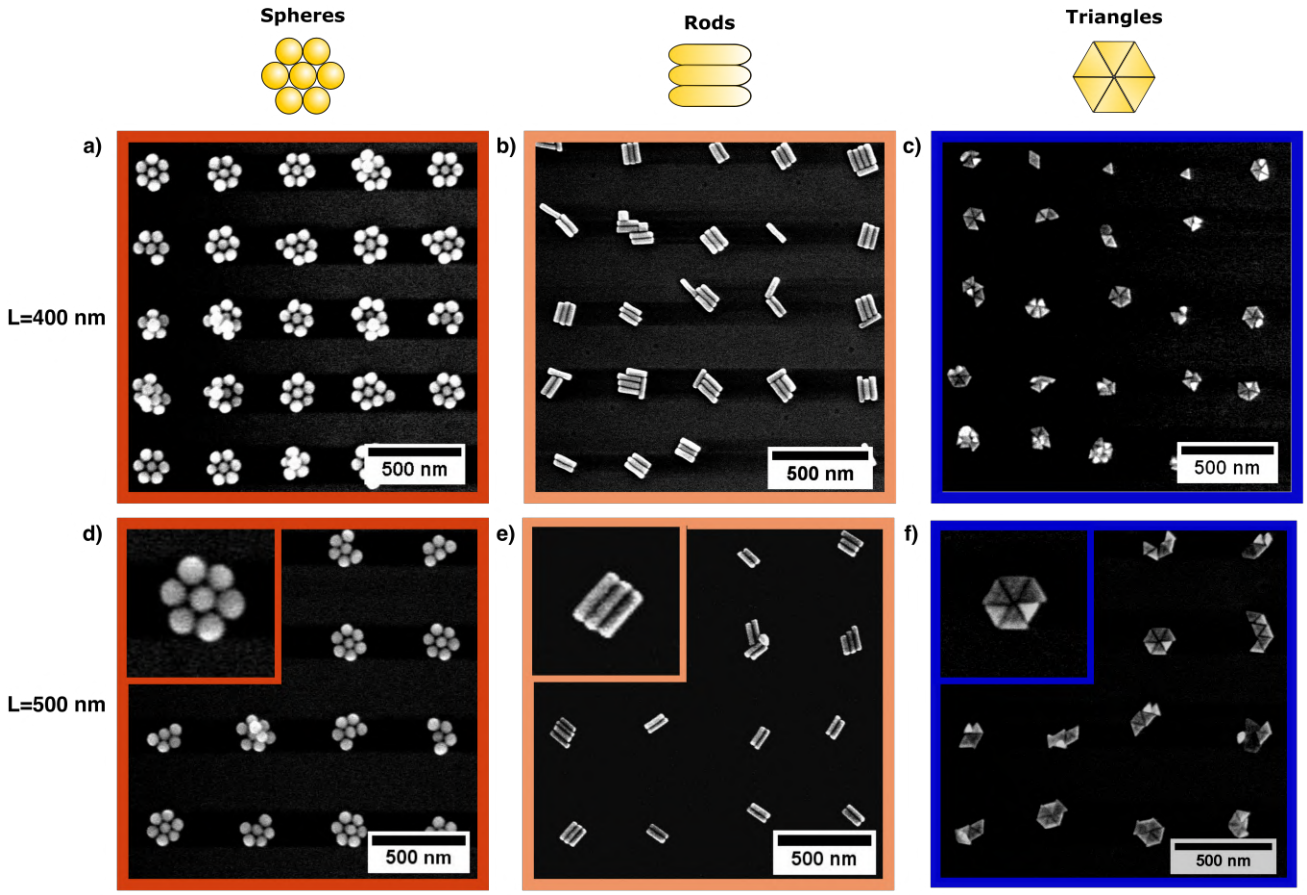

Figure 4.4: SEM images of 400 nm and 500 nm period superlattices made of a) 65 nm nanospheres b) 110× 30 nm nanorods, c) 65 nm edge length nanotriangles.

4.2.2 Optical extinction properties of superlattices made of different shapes

The hybridization between the lattice mode and the cluster-specific plasmon of differently shaped NP clusters was studied by UV-Vis spectroscopy and correlated with FEM electromagnetic simulations. The FEM simulations allow for a distinct understanding of the occurrence of cluster and lattice-specific resonances. Experimental extinction and simulated absorption spectra of plasmonic superlattices of the corresponding nanospheres, nanorods and nanotriangles dispersions can be seen in **Figure 4.5**. Since the superlattices possess sub-units with a different number of particles per cluster, the simulations were carried out with different cluster morphologies to find the nanostructures in best agreement with the experimental data (see **Appendix III.1**). The best results were attained, with the hexamer morphology for the

nanospheres, with the four rods morphology for the nanorods, and finally for the stack of 6 nanotriangles. Given the anisotropy of the nanorods cluster, polarization along the transversal and along the longitudinal axis resulted in very different absorption characteristics (see **Appendix III.3**), which is why the absorption curves for each polarization were averaged to obtain the final absorption curve of the nanorod superlattices. Conversely, for the nanosphere heptamers and hexamers as well as the triangle hexamers, polarization has very little effects on their absorption as can be seen in **Appendix III.4**, thanks to their high symmetry. Therefore, the presented absorption spectra of nanospheres and nanotriangles only show a single polarization. Under these conditions, the simulated spectra reflects relatively well the experimental spectra. However, it has to be highlighted that the experimental UV-Vis data were obtained through the contribution of various cluster morphologies, which explains the discrepancies between the simulated and experimental results. In this sense, the simulated absorption spectra of different cluster morphologies can be averaged to obtain a spectrum that reflects the inhomogeneities present in the plasmonic superlattices (see **Appendix III.5** and **Appendix III.6**). For instance, average spectra of nanosphere hexamers and heptamers in a lattice, shown in **Appendix III.5**, display a broadening of the main plasmon resonance that is also seen in the experimental data.

For a proper understanding of the UV-Vis spectra of plasmonic superlattices , it is necessary to first analyze the extinction properties of dispersed gold nanoparticles displayed in black in **Figure 4.5 a,b,c**. For instance, the nanosphere dispersion displays an extinction peak at 535 nm due to the dipolar resonance of plasmonic nanoparticles, while the nanorods dispersion displays two extinction peaks, one at 520 nm, corresponding to the transversal plasmon mode, and the other around 860 nm corresponding to the longitudinal plasmon mode. The nanotriangles dispersion displays a strong and narrow extinction peak around 650 nm, corresponding to a longitudinal in-plane mode, and a weak shoulder at 530 nm, corresponding to a transversal out-of-plane mode [16].

As a result of plasmonic hybridization, the plasmonic modes present in the extinction spectra of superlattices are different from the extinction spectra of nanoparticle solutions. However, it should be noted that plasmonic resonances at similar wavelengths to the LSPR of single nanoparticles are also found in the optical properties of plasmonic superlattices [17, 18]. Such

modes can be explained by an anti-bonding coupling mode between the assembled nanoparticles, generally leading to a small blueshift of the LSPR of single nanoparticles [19]. For instance, the nanosphere superlattices exhibit an extinction shoulder at around 530 nm, which is slightly blue-shifted compared to the LSPR of dispersed nanoparticles. In the same way, the nanotriangle superlattices exhibit a strong extinction band at 650 nm for the 400 nm lattice and a slight shoulder at 650 nm for the 500 nm period lattice. For the nanorod superlattices, the extinction bands are far shifted from the extinction bands of the nanorods dispersion. For instance, the longitudinal mode of the nanorods seen at 860 nm, in solution, seems to be shifting to 760 nm in the assembled state. Such a blue-shift of the longitudinal resonance in side-by-side assembled nanorods can be explained by a longitudinal anti-bonding coupling mode between the side-by-side assembled nanorods. This phenomenon was already seen in dark-field spectroscopy measurements of single nanorod dimers and led to a blue shift of the main plasmonic resonance of gold nanorods [20, 21]. Additionally, simulated absorption spectra of lattices of three rods side-by-side, displayed in **Appendix III.2**, show a plasmonic resonance at 720 nm, when polarization is along the long axis of the cluster, which is slightly blue-shifted compared to the experimental results. Such a mode corresponds to a side-by-side coupling as exemplified by the near-field plots seen in **Appendix III.2**. For the four rods morphology, the longitudinal coupling resonance redshifted to 760 nm for the 400 nm, due to the coupling of the three rods to the additional rod laying on top, therefore reflecting better the experimental results (see **Figure 4.5 b,e** and **Appendix III.3**).

Additionally to the LSPR modes reminiscing the optical extinction of the nanoparticle dispersions, new plasmonic modes arise under the self-assembled state due to plasmonic coupling. Particularly, in plasmonic superlattices, the plasmonic cluster modes can couple to an in-plane diffracted order, also called Rayleigh anomaly, giving rise to an increase in extinction at a wavelength depending on the lattice period and the refractive index of the substrate [22]. In the nanosphere superlattices, a strong plasmonic mode shifting with the lattice period can be seen experimentally in **Figure 4.5 a**; for the 400 nm period superlattice, this mode is seen at around 705 nm, while for the 500 nm superlattice it is seen at around 760 nm. Similarly, the main peak of the simulated absorption spectra redshifts from 720 nm to 745 nm by changing the lattice period from 400 nm to 500 nm, while the other resonances at 520 nm and 550 nm remain

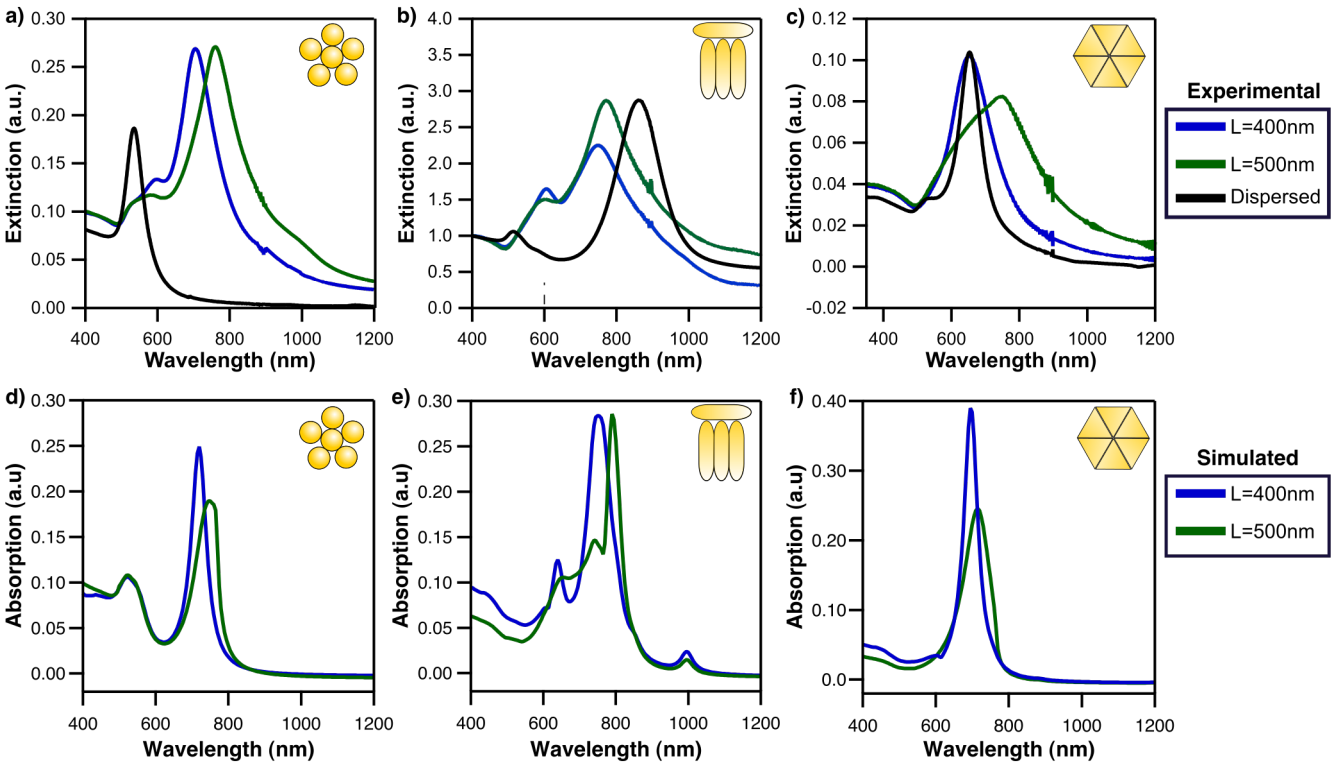

Figure 4.5: Experimental extinction spectra of nanoparticle dispersion, 400 nm and 500 nm period superlattices made of: a) 65 nm diameter gold nanospheres, b) 110×30 nm gold nanorods, c) 65 nm edge length gold nanotriangles. Simulated absorption spectra of 400 nm and 500 nm period superlattices made of d) 65 nm nanospheres hexamers, e) 110×30 nm nanorods in a four rods conformation, f) 65 nm edge length triangle in a stack of 6 triangles.

unaffected (see **Figure 4.5 d**). Such a shift in the simulated spectra supports the assignment of the main plasmonic modes to surface lattice plasmon resonances. Furthermore, the simulated near-field images of the SLR, displayed in **Appendix III.5** show that the mode consists of a cluster plasmonic resonance coupling to a lattice effect. Additionally, nanosphere superlattices present experimentally a coupling mode at a lower wavelength of 600 nm, for both the 400 nm and 500 nm period superlattices. A similar coupling mode was observed in the simulated absorption spectra of hexamers and heptamers around 550− 560 nm, and was more pronounced in the heptamer simulations (see **Appendix III.5**). Such modes were attributed in various studies to higher-order longitudinal bonding coupling modes, which generally appeared at a slightly higher wavelength than the single LSPR of nanospheres [19, 23].

For both the 400 nm and the 500 nm nanorod superlattices, a strong resonance is seen

experimentally at 760 nm and a weaker one at around 600 nm in **Figure 4.5 b**. As it was explained previously, the mode at 760 nm corresponds to an anti-bonding longitudinal plasmonic coupling. Besides, the mode at 640 nm was predominant in the simulations when the polarization was set along the short-axis of the side-by-side nanorods, as can be seen in **Appendix III.3**. Therefore, such a mode is assigned to a transversal bonding mode between the side-by-side assembled nanorods. This coupling mode was also observed at around 600 nm in dark-field scattering measurements of nanorods dimers [24]. Though the number of particles per cluster is similar between the 400 and 500 nm nanorod superlattices, the intensity of the two principal modes is changing; the mode at 600 nm is stronger and more pronounced for the 400 nm period superlattice, while the resonance at 760 nm is stronger for the 500 nm period nanorods-based superlattice. These changes in intensity can be interpreted as a coupling of the plasmonic clusters to a lattice effect. In the case of the 400 nm period superlattice, the Rayleigh anomaly is expected at 600 nm, which justifies the increase in extinction at 600 nm seen in the UV-Vis spectra of the 400 nm period nanorods-based superlattice. Similarly, for the 500 nm superlattice, the Rayleigh anomaly, expected at 750 nm, explains the increase in extinction at 760 nm seen in the UV-Vis spectra of the 500 nm period superlattice. This was further confirmed by the simulated nanorods absorption, where the main plasmon resonance shifted from 760 nm to 790 nm, when increasing the period from 400 nm to 500 nm, indicating a coupling of the cluster plasmon to a lattice effect in the case of the 500 nm period superlattice. Additionally, an increase of intensity from the transversal coupling mode was observed in the simulated absorption of the 400 nm period superlattice, supporting the assignment of this mode to a surface lattice resonance. Interestingly, the choice of the lattice period gave the possibility to couple the lattice effect to the transversal bonding mode or to the longitudinal anti-bonding mode of the nanorods cluster.

For the nanotriangle superlattices, a mode redshifting from 650 nm to 750 nm is seen experimentally in **Figure 4.5 c**, with an increase of the lattice period from 400 nm to 500 nm. The simulated absorption spectra of nanotriangle superlattices, displayed in **Figure 4.5 f**, show the same behavior as in the experiment with a redshift of the main plasmon resonance with a period increase, which supports the assignment of the shifting mode to a surface lattice resonance. Particularly, in the experiment, the plasmon resonances are much broader than in the

simulations. This was explained by simulations through the consideration of a line of triangles in a lattice, such a conformation presents resonances that are both redshifted and blueshifted compared to the triangle hexamers (see **Appendix III.7**). The observation of different plasmonic modes in the line of triangles explains the broadening occurring because of the statistical distribution of nanotriangle morphologies in the experimental measurements.

Overall, the coupling of a specific cluster mode with an in-plane diffracted order results in an increase of the absorption of the superlattices at a wavelength depending on the period of the superlattices but also on the shape of the lattice sub-unit. Particularly, the simulated absorption spectra of the different superlattices gave a thorough understanding of the nature of the plasmonic modes involved in the optical properties of plasmonic superlattices.

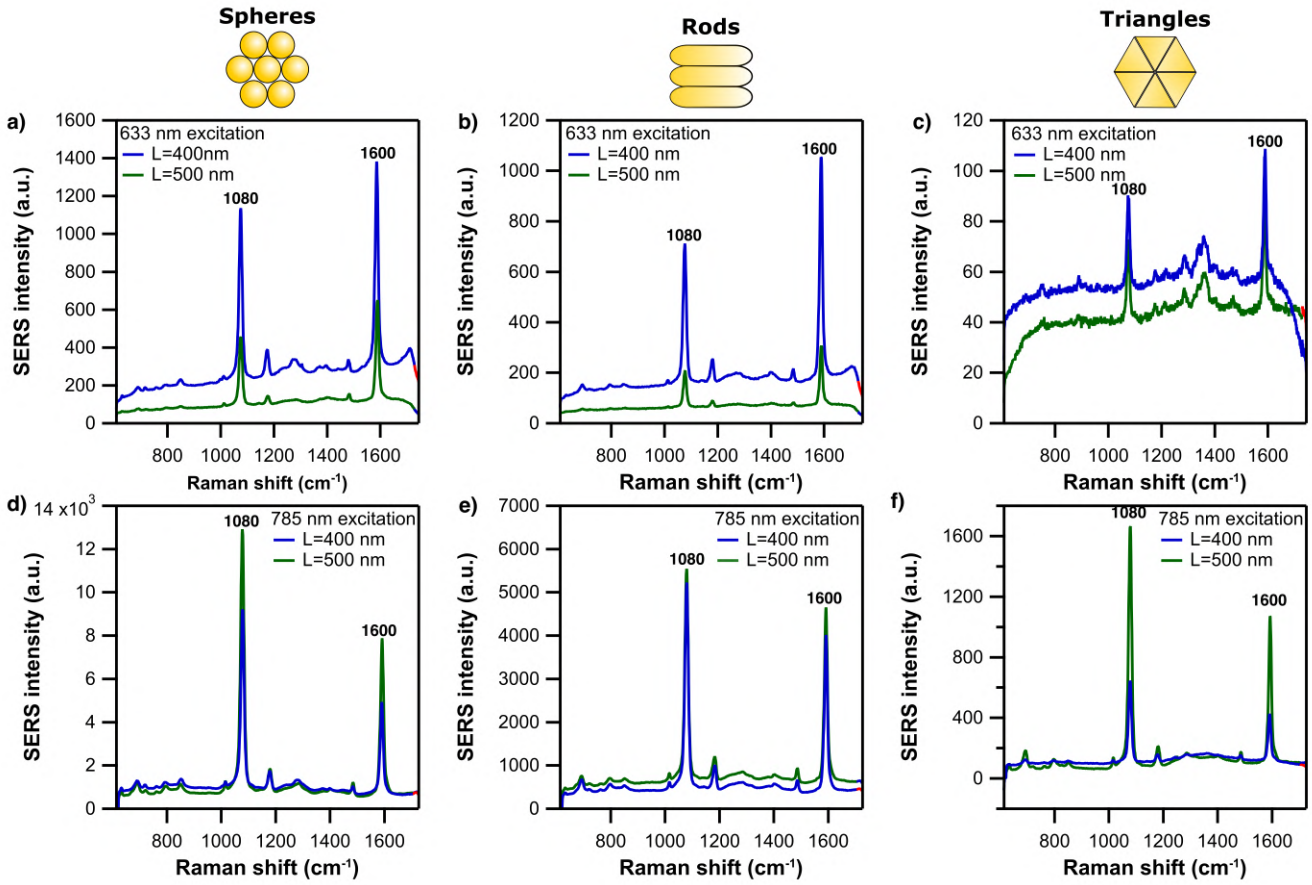

Figure 4.6: Comparison of the experimental SERS efficiency of 400 and 500 nm superlattices made of a), d) nanospheres, b), e) nanorods, c) and f) nanotriangles at a laser excitation of a), b), c) 633 nm and d), e), f) 785 nm with 4-MBA as model analyte.

4.2.3 Effect of the lattice period on the SERS signal

Tailoring of the extinction spectra to the Raman laser excitation wavelength constitutes the principal strategy for improving the SERS properties of a plasmonic substrate [16, 25]. Therefore, the optical extinction spectra of plasmonic superlattices of different periods, seen in the previous section, can serve as an indication of the nanostructure's SERS enhancement. Particularly, superlattices with 500 nm lattice period have shown to absorb light more efficiently at 785 nm compared to 400 nm period superlattices. As a consequence, the 500 nm superlattice is expected to give a higher SERS enhancement than the 400 nm lattice when excited with the 785 nm laser. Conversely, the 400 nm superlattice is expected to give a higher SERS enhancement than the 500 nm lattice when excited with the 633 nm laser.

To compare their SERS efficiency, each superlattice was incubated for 2 hours in a 100 µM 4-MBA solution and then washed with water to remove the excess molecules that did not bind covalently to the gold nanoparticles, SERS spectra were recorded at more than 100 points for each sample. Average SERS spectra of the different superlattices under 633 nm and 785 nm excitations can be seen in **Figure 4.6**. The highest signal intensities are found for the ν_{12} ring stretching vibration at 1080 cm^{-1} and for the ν_{8a} ring stretching vibration at 1600 cm^{-1}, corresponding to the phenyl ring of 4-MBA [26]. Weaker Raman peaks are detected at 692, 726, 800, 850 cm^{-1} due to carboxylic group bending and stretching vibrations and at 1180 and 1480 cm^{-1} due to ν_{9a} and ν_{19b} C-C ring stretching vibrations [27, 28, 29]. Average and standard deviation of the peak intensity at 1080 cm^{-1} for the different superlattices and laser excitation can be seen in **Appendix III.8**. Overall, the standard deviation of the SERS signal remains acceptable (<35%) for the different superlattices, which indicates a reasonable homogeneity of the superlattices over large areas. Especially, nanorod superlattices exhibit standard deviations as low as 8% underlining the quality of the assembled superlattices. Conversely, the nanotriangle superlattices exhibit higher standard deviation (up to 34%), which might be due to a lower control over the number of particles per cluster. For the different shapes of nanoparticles studied here, 500 nm superlattices outperformed the 400 nm period superlattices in SERS intensity using the 785 nm laser excitation. In the same way, the 400 nm superlattices outperformed the 500 nm superlattices in SERS intensity using the 633 nm laser as expected from the UV-Vis extinction

spectra. Furthermore, the SERS enhancement factors calculated from the FEM simulations show a similar influence of the superlattice period on the SERS enhancement using the two available laser excitation wavelengths (see **Appendix III.9**). Thus, the lattice effect can be adjusted to obtain an enhancement of the SERS signal for a specific laser excitation wavelength.

4.2.4 Effect of nanoparticle shape on SERS signal

Taking into account the effect of the lattice period on the SERS signal of superlattices, the SERS signal of superlattices made with different shapes was compared using 633 nm excitation for the 400 nm superlattices and using the 785 nm excitation for the 500 nm period superlattices. The corresponding SERS spectra can be found in **Figure 4.7 a,b**. The analytical SERS enhancement factor (AEF) of such nanostructures was calculated using the following equation [30]:

$$\mathrm{AEF} = \frac{I_{\mathrm{SERS}}/C_{\mathrm{SERS}}}{I_{\mathrm{Raman}}/C_{\mathrm{Raman}}}, \tag{4.1}$$

With I_{SERS} the SERS intensity of 4-MBA on the plasmonic superlattices, C_{SERS} the concentration of 4-MBA in the SERS experiment, here 100 µM, I_{Raman} the Raman intensity and C_{Raman} the concentration of 4-MBA in the Raman measurement experiments, here 200 mM. The Raman signal intensity of 4-MBA was recorded using the same measurement conditions as in the SERS measurement (see **Section 4.4.7** for more details).

Raman spectra of 4-MBA in ethanol are provided in **Appendix III.10**, and exhibit different peaks due to ethanol at 885, 1053, 1099, 1278 and 1458 cm^{-1}, as well as a peak due to the ν_{8a} phenyl ring stretching at 1600 cm^{-1}. Since only the 1600 cm^{-1} was visible in the Raman spectra, its intensity was used to calculate the SERS enhancement factors of the different superlattices. SERS enhancement factors of the superlattices at 633 and 785 nm are shown in **Figure 4.7 c**. The values of the analytical SERS enhancement factors vary between $6.8 \cdot 10^4$ and $3.06 \cdot 10^6$ for plasmonic superlattices of different nanoparticle shapes, which lies within the highest analytical enhancement factors in the literature for assembled colloidal nanoparticles [31, 32]. Interestingly, the gold nanosphere superlattices yielded the highest enhancement factors, which contradicts our first hypothesis that assembling anisotropic gold nanoparticles

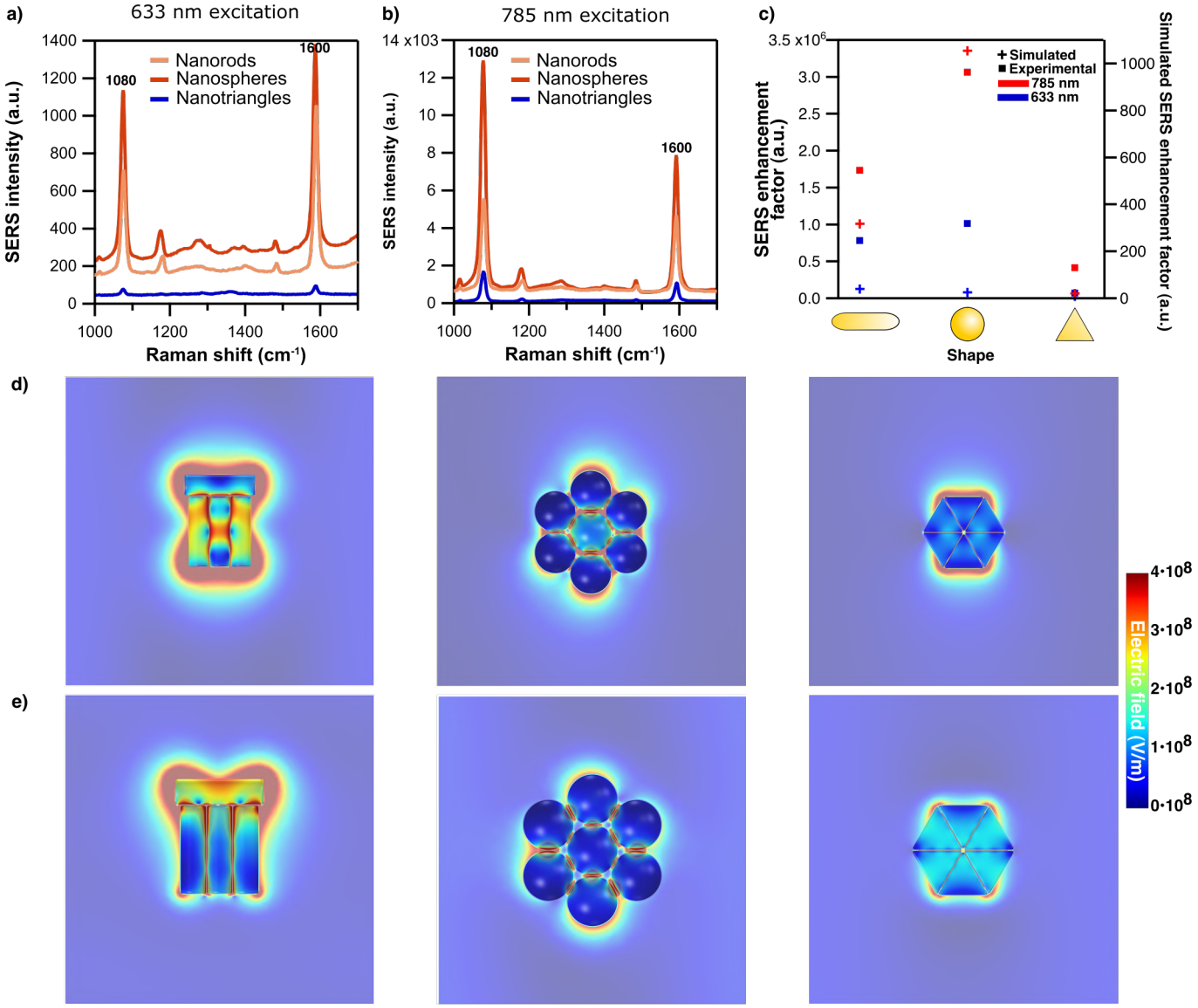

Figure 4.7: Comparison of the SERS efficiency of superlattices made with different nanoparticle shapes: a) 400 nm period superlattices and 633 nm excitation, b) 500 nm period superlattices and 785 nm excitation. c) Calculated experimental analytical SERS enhancement factors and simulated SERS enhancement from differently shaped nanoparticle superlattices of 400 nm under 633 nm laser excitation and 500 nm under 785 nm laser excitation. Electric field distribution for differently shaped superlattices of: d) 400 nm period at 633 nm wavelength and e) 500 nm period at 785 nm wavelength.

would result in a higher enhancement of the SERS signal. To confirm this result, calculations of the SERS enhancement factors were performed through the integration of the simulated electric field over the air domain of the different superlattices. Examples of electric field distribution at

633 nm and 785 nm for differently shaped plasmonic superlattices can be seen in **Figure 4.7**, the high electric field enhancement explains that high SERS signals were recorded using such superlattices. To take into account the different morphologies present in the plasmonic superlattices, the enhancement factors of the different morphologies for each shape and polarizations were averaged. Finally, the average enhancement factors of the different superlattices, shown in **Figure 4.7 c**, display a similar behavior as in the experiment with a lower enhancement at 633 nm than at 785 nm. Particularly, at 785 nm the nanospheres gave the highest simulated SERS enhancement, with an enhancement of more than two times the one of the nanorod superlattices. However, at 633 nm the simulated SERS enhancement predicted that nanorod superlattices should have 2 times higher SERS signals than nanospheres superlattices. Such a discrepancy with the experiment might come from the fact that more than two cluster morphologies are present in the plasmonic superlattices, and that the simulations only consider two different polarization states and a single orientation of the clusters in the lattice. Finally, such a study underlines that clusters of anisotropic nanoparticles do not necessarily yields to a higher SERS enhancement.

4.3 Conclusion

The templated self-assembly process, optimized in **Chapter 3**, could be directly applied to the fabrication of homogenous superlattices of different nanoparticle shapes, with no need for changes in the chemical composition of the nanoparticle dispersion. Thanks to the good control on the nanoparticle self-assembly, the SERS signal from the superlattices displayed a good homogeneity over the whole sample for nanorods and nanospheres, and a moderate homogeneity for the nanotriangles. Tuning of the extinction properties of the differently shaped plasmonic superlattices was achieved by changing their period, thanks to the excitation of surface lattice resonances, confirmed by the simulated absorption spectra. Particularly, the simulated absorption spectra of the different plasmonic superlattices confirmed the assignment of the principal plasmonic modes to surface lattice resonances and enabled a deeper understanding of the nature of the plasmonic resonances. As a result of the lattice effect, the extinction of the superlattices could be increased around the Raman excitation wavelengths. Consequently, the 500 nm pe-

riod superlattices exhibited higher SERS enhancement than the 400 nm period superlattices, using the 785 nm excitation. Conversely, the 400 nm period superlattices exhibited higher SERS enhancement than the 500 nm period superlattice when using the 633 nm excitation. Finally, choosing the optimal lattice period for each excitation wavelength, the nanosphere superlattices provided the highest SERS performance with an analytical enhancement factor of $3.06 \cdot 10^6$, which was further confirmed in the calculations of the simulated SERS enhancement factors. Such a result underlines the fact that self-assembled anisotropic nanoparticles are not always the most suitable to obtain the highest SERS enhancement.

4.4 Materials and methods

4.4.1 Synthesis of nanospheres

Synthesis of nanospheres followed the same procedure as in **Chapter 3** with the difference that the amount of seeds for the final growth was set to 10 µL to obtain a final diameter of 65 nm.

4.4.2 Synthesis of nanorods

Synthesis of nanorods followed a reported seeded-growth synthesis [33]. The initial seeds were prepared by adding $HAuCl_4$ (200 µL, 0.05 M) and ascorbic acid (100 µL, 0.1 M) to 20 mL of a 50 mM CTAB and 13.5 mM n-decanol solution. After 1-2 min, (800 µL, 0.02 M, i.e., 7.5 mg in 10 mL) was added under vigorous stirring at 25-27 °C. The solution was left undisturbed at 25-27 °C for at least 1 hour.

The seeds were then overgrown to 21× 7.5 nm nanorods by adding 300 mL of a 50 mM and 13.5 mM n-decanol solution at exactly 25 °C to a solution of 2.4 mL of 0.01 M $AgNO_3$, 21 mL of 1 M HCl, 3 mL of 0.05 M of $HAuCl_4$ and 3.9 mL of 0.1 M ascorbic acid. Subsequently 18 mL of the seed solution was added under vigorous stirring. The mixture was left undistrubed at 25 °C for at least 4 hours. The solution finally presented a dark brownish gray color and a longitudinal LSPR at 730 nm. The small anisotropic seeds were centrifuged a 14000-15000 rpm for 60 min, the precipitate was redispersed with 10 mM CTAB to obtain a final Au^0 concentration of 4.65 mM.

Finally 110x30 nm nanorods were obtained by adding 10 mL of a 50 mM CTAB and 11 mM n-decanol solution to a solution of 200 µL of 0.01 M $AgNO_3$, 100 µL 0.05 M $HAuCl_4$, 80 µL of a 0.1 M ascorbic acid solution under stirring. Then, 600 µL of 1 M HCl was added to the previous mixture and finally 10 µL of the anisotropic seed solution was added.

4.4.3 Synthesis of nanotriangles

Synthesis of nanotriangles followed a reported seeded-growth synthesis [32]. The initial seeds were prepared by adding $HAuCl_4$ (25 µL, 0.05 M) to a CTAC solution (4.7 mL, 100 mM). Subsequently, $NaBH_4$ (300 µL, 0.01 M, i.e., 7.5 mg in 10 mL) was added under vigorous stirring. The solution was them left at room temperature for 2 hours and was then diluted 10 times into a 0.01 M CTAC solution. For the synthesis of nanotriangles, two growth solutions were prepared:

1. 1.6 mL of a 0.1 M CTAC solution was added to 8 mL of Milli-Q water, followed by 40 µL of 0.05 M $HAuCl_4$ solution, 15 µL of a 0.01 M NaI solution

2. 500 L of a 0.05 M $HAuCl_4$ solution was added to 40 mL of 0.05 M CTAC, followed by 300 µL of a 0.01 M NaI solution

40 and 400 µL of a 0.1 M ascorbic acid solution were added to solution 1 and 2, respectively, and the solution were manually stirred until complete transparency indicating the reduction of Au^{III} to Au^{I}. Subsequently, 800 µL of the seed solution was added to solution 1, and manually stirred for 1 s. Immediately after 3.2 mL of solution 1 was added to solution 2, and manually stirred for 10 s. The solution was left undisturbed for 1 hour. At this point, the solution contains a mixture of nanosphere and nanotriangles. For purification, the concentration of CTAC was set to 0.15 M, and the solution was left undisturbed overnight. Doing so, the nanotriangles flocculate, while the nanospheres stay dispersed, the nanotriangles can then be recovered by removing the supernactant and redisperse them in 5 mL of 0.1 M CTAC solution.

4.4.4 Functionalization of the differently shaped nanoparticles

The concentration of gold in the nanoparticle dispersions was estimated using the extinction at 400 nm. At this wavelength the extinction of gold nanoparticles doesn't depend on the size

or shape of nanoparticles, therefore it constitutes a way for measuring their concentration. Scarabelli et al. performed measurements of the absorption at 400 nm with solutions of gold nanoparticles at different gold concentration [34], and shown that 1.2 extinction corresponds to 0.5 mM of gold. For the functionalization of the nanoparticles with PEG, the nanoparticles were concentrated by centrifugation and redispersion in 1 mM CTAC to have a final concentration of gold between 2 and 10 mM. Then 10 mg/mL of PEG-6K was added to the solution, which was left undisturbed overnight. The nanoparticles were then washed by repeating centrifugation and redispersion in CTAC 500 µM at least 4 times. By repeating this operation several times, the PEG that did not bind to the nanoparticles is completely removed. The functionalization step is then repeated by concentrating the nanoparticles to 10 mM in 500 µM and adding 10 mg/mL of PEG-6K. Again the NPs are washed by repeated centrifugation and redispersion in CTAC 500 µM. Finally, the NPs are concentrated to 200 mM in 500 µM CTAC, and the nanoparticle solutions are stored in the fridge at 8 °C.

4.4.5 Sample preparation for SERS

For SERS experiments, the samples were cleaned using 10 s of oxygen plasma (Diener pico) at 100 W and 0.4 mbar, followed by 5 minutes of UV-Ozone (bionanoforce). The SERS samples were incubated in an aqueous solution of 4-MBA (100 μM, 2 h), prepared freshly from a stock solution in EtOH (10 mM). After incubation, the samples were thoroughly rinsed with water to remove the excess 4-MBA molecules that did not bind to the AuNPs and dried with N_2 flow.

4.4.6 Finite element method simulations

To verify the experimental results, we performed finite-element method (FEM) simulations, using the commercially available software COMSOL Multiphysics. The simulation cell consists of the different particle arrangements in air, on top of a substrate layer, sandwiched between two 100 nm thick perfectly matched layers (PMLs) on the top and the bottom. According to the experiments, the infinite superlattice structure is modeled by setting the lateral cell dimensions to the lattice period and by laterally assigning periodic (Bloch) boundary conditions. The structure is excited by a linearly polarized plane wave of normal incidence, impinging from the

top (air region). Two ports at the PML-air and PML-substrate interfaces register the system reflectance and transmittance response, respectively. For the investigation of plasmonic modes, we subsequently calculate the bulk absorbance by 1-reflectance-transmittance. Parameters such as the dielectric function of gold, the refractive index of the polymer shell around the NPs (PEG-6k), and the radius of the nanosphere were optimized using Mie theory calculations and considering the experimental extinction curve. The best fit was obtained using gold dispersion reported by Olmon et al., together with a radius of 34 nm, 1.2 nm shell thickness, and a refractive index of 1.425 for the polymer shell. Those parameters were transferred to gold nanorods and nanotriangles, except for the dimensions of the nanoparticles which were measured from the SEM images of the plasmonic superlattices.

The enhancement factors were calculated by integrating the fourth power of the electric field over the air domain of the model.

4.4.7 Characterization techniques

Electron microscopy

Scanning electron microscopy was performed using an environmental SEM (FEI Quanta 250) at an acceleration voltage of 30 kV.

UV-Vis spectroscopy

Extinction spectra of colloidal dispersions were recorded with an Agilent 8453 UV-Vis spectrophotometer, using polystyrene cuvettes. Extinction spectra of dry samples were collected using a Carry 5000 UV-vis spectrometer (Agilent).

SERS measurements

SERS Spectra were obtained using a Renishaw inVia reflex equipped with a stigmatic single-pass spectrometer, a Peltier-cooled CCD detector (1024 x 512 px^2), a 1800 grooves mm^{-1} grating, 633 nm and 785 nm excitation wavelengths (0.54 mW for the 633 nm laser and 4.3 mW for the 785 nm excitation line), and a 50× lens (LWD, NA 0.5) yielding a spot size of around 20×20 μm^2. For each samples more than 100 measurement points were taken in random points using 0,5 s

integration time.

For the Raman measurements, 4-MBA was dissolved in ethanol to obtain a 200 mM solution. The Raman spectra of the 4-MBA solution were acquired using the same conditions than the SERS measurement, i.e 50× objective, 0.5 s integration time, 0.53 mW and 4.3 mW for the 633 and 785 nm laser excitation respectively. 50 spectra were recorded and averaged to obtain the Raman spectra.

Bibliography

[1] Schlücker, S. Surface-Enhanced Raman Spectroscopy: Concepts and Chemical Applications. *Angew. Chem. - Int. Ed.* **2014**, *53*, 4756–4795.

[2] Bastús, N. G.; Comenge, J.; Puntes, V. Kinetically controlled seeded growth synthesis of citrate-stabilized gold nanoparticles of up to 200 nm: Size focusing versus ostwald ripening. *Langmuir* **2011**, *27*, 11098–11105.

[3] Huang, X.; El-Sayed, M. A. Gold nanoparticles: Optical properties and implementations in cancer diagnosis and photothermal therapy. *J. Adv. Res.* **2010**, *1*, 13–28.

[4] Qin, Z.; Wang, Y.; Randrianalisoa, J.; Raeesi, V.; Chan, W. C.; Lipinski, W.; Bischof, J. C. Quantitative comparison of photothermal heat generation between gold nanospheres and nanorods. *Sci. Rep.* **2016**, *6*, 1–13.

[5] Kuttner, C.; Höller, R. P.; Quintanilla, M.; Schnepf, M. J.; Dulle, M.; Fery, A.; Liz-Marzán, L. M. SERS and plasmonic heating efficiency from anisotropic core/satellite superstructures. *Nanoscale* **2019**, *11*, 17655–17663.

[6] Reguera, J.; Langer, J.; Jiménez de Aberasturi, D.; Liz-Marzán, L. M. Anisotropic metal nanoparticles for surface enhanced Raman scattering. *Chem. Soc. Rev.* **2017**, *46*, 3866–3885.

[7] Vanrompay, H.; Bladt, E.; Albrecht, W.; Béché, A.; Zakhozheva, M.; Sánchez-Iglesias, A.; Liz-Marzán, L. M.; Bals, S. 3D characterization of heat-induced morphological changes of Au nanostars by fast: In situ electron tomography. *Nanoscale* **2018**, *10*, 22792–22801.

[8] Tran, V.; Thiel, C.; Svejda, J. T.; Jalali, M.; Walkenfort, B.; Erni, D.; Schlücker, S. Probing the SERS brightness of individual Au nanoparticles, hollow Au/Ag nanoshells, Au nanostars and Au core/Au satellite particles: single-particle experiments and computer simulations. *Nanoscale* **2018**, *10*, 21721–21731.

[9] González-Rubio, G.; Guerrero-Martínez, A.; Liz-Marzán, L. M. Reshaping, Fragmentation, and Assembly of Gold Nanoparticles Assisted by Pulse Lasers. *Acc. Chem. Res.* **2016**, *49*, 678–686.

[10] Vanrompay, H.; Bladt, E.; Albrecht, W.; Béché, A.; Zakhozheva, M.; Sánchez-Iglesias, A.; Liz-Marzán, L. M.; Bals, S. 3D characterization of heat-induced morphological changes of Au nanostars by fast: In situ electron tomography. *Nanoscale* **2018**, *10*, 22792–22801.

[11] Yoon, J. H.; Selbach, F.; Langolf, L.; Schlücker, S. Ideal Dimers of Gold Nanospheres for Precision Plasmonics: Synthesis and Characterization at the Single-Particle Level for Identification of Higher Order Modes. *Small* **2018**, *14*, 1–5.

[12] Fraire, J. C.; Pérez, L. A.; Coronado, E. A. Cluster size effects in the surface-enhanced raman scattering response of ag and Au nanoparticle aggregates: Experimental and theoretical insight. *J Phys Chem C* **2013**, *117*, 23090–23107.

[13] Solís, D. M.; Taboada, J. M.; Obelleiro, F.; Liz-Marzán, L. M.; García De Abajo, F. J. Optimization of Nanoparticle-Based SERS Substrates through Large-Scale Realistic Simulations. *ACS Photonics* **2017**, *4*, 329–337.

[14] Matricardi, C.; Hanske, C.; Garcia-Pomar, J. L.; Langer, J.; Mihi, A.; Liz-Marzán, L. M. Gold Nanoparticle Plasmonic Superlattices as Surface-Enhanced Raman Spectroscopy Substrates. *ACS Nano* **2018**, *12*, 8531–8539.

[15] Shiohara, A.; Langer, J.; Polavarapu, L.; Liz-Marzán, L. M. Solution processed polydimethylsiloxane/gold nanostar flexible substrates for plasmonic sensing. *Nanoscale* **2014**, *6*, 9817–9823.

[16] Kuttner, C.; Mayer, M.; Dulle, M.; Moscoso, A.; López-Romero, J. M.; Förster, S.; Fery, A.; Pérez-Juste, J.; Contreras-Cáceres, R. Seeded Growth Synthesis of Gold Nanotriangles:

Size Control, SAXS Analysis, and SERS Performance. *ACS Appl. Mater. Interfaces* **2018**, *10*, 11152–11163.

[17] Taylor, R. W.; Esteban, R.; Mahajan, S.; Aizpurua, J.; Baumberg, J. J. Optimizing SERS from Gold Nanoparticle Clusters: Addressing the Near Field by an Embedded Chain Plasmon Model. *J Phys Chem C* **2016**, *120*, 10512–10522.

[18] Yan, B.; Boriskina, S. V.; Reinhard, B. M. Optimizing Gold Nanoparticle Cluster Configurations ($n \geq 7$) for array applications. *J Phys Chem C* **2011**, *115*, 4578–4583.

[19] Yoon, J. H.; Selbach, F.; Langolf, L.; Schlücker, S. Ideal Dimers of Gold Nanospheres for Precision Plasmonics: Synthesis and Characterization at the Single-Particle Level for Identification of Higher Order Modes. *Small* **2018**, *14*, 1–5.

[20] Halas, N. J.; Lal, S.; Chang, W.-S.; Link, S.; Nordlander, P. Plasmons in Strongly Coupled Metallic Nanostructures. *Chem. Rev.* **2011**, *111*, 3913–3961.

[21] Wang, G.; Akiyama, Y.; Kanayama, N.; Takarada, T.; Maeda, M. Directed Assembly of Gold Nanorods by Terminal-Base Pairing of Surface-Grafted DNA. *Small* **2017**, *13*, 1–8.

[22] Kravets, V. G.; Kabashin, A. V.; Barnes, W. L.; Grigorenko, A. N. Plasmonic Surface Lattice Resonances: A Review of Properties and Applications. *Chem. Rev.* **2018**, *118*, 5912–5951.

[23] Greybush, N. J.; Liberal, I.; Malassis, L.; Kikkawa, J. M.; Engheta, N.; Murray, C. B.; Kagan, C. R. Plasmon Resonances in Self-Assembled Two-Dimensional Au Nanocrystal Metamolecules. *ACS Nano* **2017**, *11*, 2917–2927.

[24] Funston, A. M.; Novo, C.; Davis, T. J.; Mulvaney, P. Plasmon Coupling of Gold Nanorods at Short Distances and in Different Geometries 2009. *Nano Lett.* **2009**, *9*, 1651–1658.

[25] Khlebtsov, B. N.; Khanadeev, V. A.; Burov, A. M.; Le Ru, E. C.; Khlebtsov, N. G. Reexamination of Surface-Enhanced Raman Scattering from Gold Nanorods as a Function of Aspect Ratio and Shape. *J Phys Chem C* **2020**, *124*, 10647–10658.

[26] Michota, A.; Bukowska, J. Surface-enhanced Raman scattering (SERS) of 4-mercaptobenzoic acid on silver and gold substrates. *J Raman Spectrosc* **2003**, *34*, 21–25.

[27] Bishnoi, S. W.; Rozell, C. J.; Levin, C. S.; Gheith, M. K.; Johnson, B. R.; Johnson, D. H.; Halas, N. J. All-Optical Nanoscale pH Meter. *Nano letters* **2006**, *6*, 1687–1692.

[28] Lee, S. B.; Kim, K.; Kim, M. S. Surface-Enhanced Raman Scattering of o-Mercaptobenzoic Acid in Silver Solution. *J Raman Spectrosc* **1991**, *22*, 811–817.

[29] Ma, C.; Harris, J. M. Surface-Enhanced Raman Spectroscopy Investigation of the Potential-Dependent Acid - Base Chemistry of Silver-Immobilized 2-Mercaptobenzoic Acid. *Langmuir* **2011**, *27*, 3527–3533.

[30] Ru, E. C. L.; Blackie, E.; Meyer, M.; Etchegoin, P. G. Surface Enhanced Raman Scattering Enhancement Factors : A Comprehensive Study. *J Phys Chem C* **2007**, *111*, 13794–13803.

[31] Bodelón, G.; Montes-García, V.; López-Puente, V.; Hill, E. H.; Hamon, C.; Sanz-Ortiz, M. N.; Rodal-Cedeira, S.; Costas, C.; Celiksoy, S.; Pérez-Juste, I.; Scarabelli, L.; La Porta, A.; Pérez-Juste, J.; Pastoriza-Santos, I.; Liz-Marzán, L. M. Detection and imaging of quorum sensing in Pseudomonas aeruginosa biofilm communities by surface-enhanced resonance Raman scattering. *Nat. Mater.* **2016**, *15*, 1203–1211.

[32] Scarabelli, L.; Coronado-Puchau, M.; Giner-Casares, J. J.; Langer, J.; Liz-Marzán, L. M. Monodisperse gold nanotriangles: Size control, large-scale self-assembly, and performance in surface-enhanced raman scattering. *ACS Nano* **2014**, *8*, 5833–5842.

[33] González-Rubio, G.; Kumar, V.; Llombart, P.; Díaz-Nuúñez, P.; Bladt, E.; Altantzis, T.; Bals, S.; Pen, O.; Noya, E. G.; Macdowell, L. G.; Liz-Marzán, L. M. Disconnecting Symmetry Breaking from Seeded Growth for the Reproducible Synthesis of High Quality Gold Nanorods. *ACS Nano* **2019**, *13*, 4424–4435.

[34] Scarabelli, L.; Grzelczak, M.; Liz-Marzán, L. M. Tuning Gold Nanorod Synthesis through Prereduction with Salicylic Acid. *Chem. Mater.* **2013**, *25*, 4332–4338.

Chapter 5

Mechanically Tunable Lattice-Plasmon Resonances by Self-Assembled Superlattices for Surface-Enhanced Raman Spectroscopy

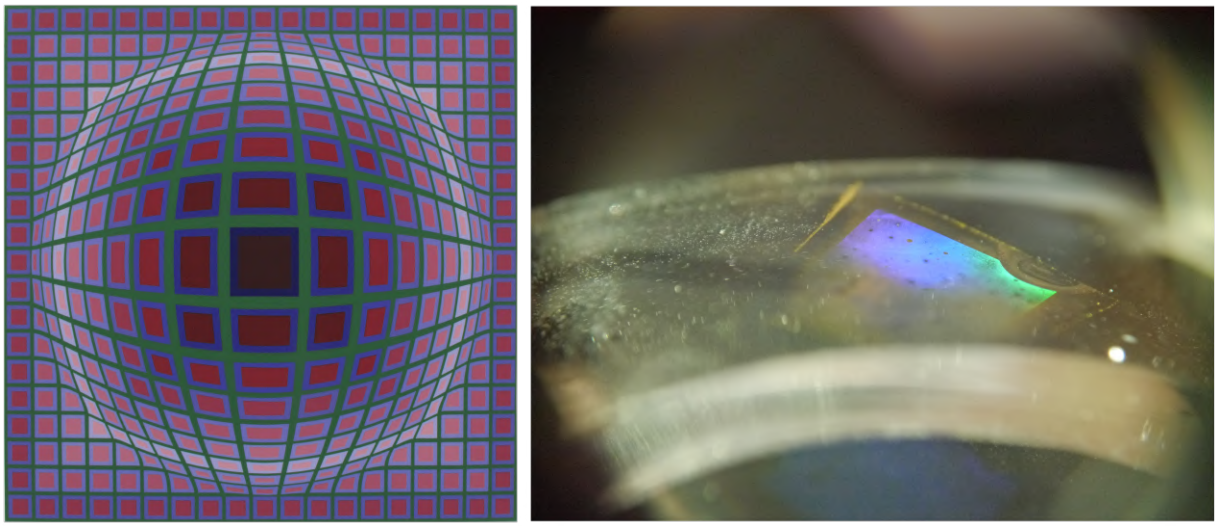

Figure 5.1: On the left: Photograph of "Victor Vasarely - Titan [1985]" by Gandalf's Gallery, licensed under Creative Common BY-NC-SA 2.0 , on the right: Photograph of a bended flexible superlattice under white light. The colors appearing of the surface of the sample are due to diffraction.

Abstract

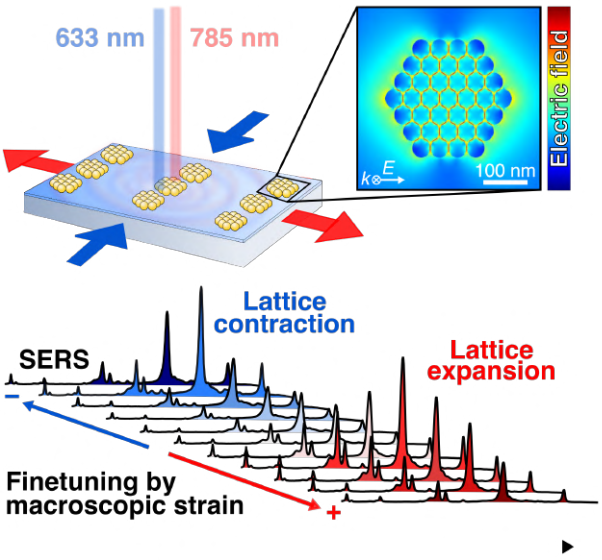

While the two previous chapters focused on increasing the surface-enhanced Raman spectroscopy (SERS) signal of superlattice by improving the homogeneity of superlattices and varying the shapes of nanoparticles, the aim of this chapter is to find the optimal lattice parameters for SERS. Indeed, lattice plasmon resonances can be employed for ultra sensitive SERS provided they are spectrally matched to the excitation wavelength. The spectral positions of lattice plasmon modes critically depend on the lattice period, therefore screening of the lattice parameters constitutes a strategy to find the optimal lattice period for SERS. Instead of fabricating superlattices with different periods, nanoparticle superlattices were assembled on flexible supports to enable tuning of the lattice parameters by mechanical deformation. The highest SERS performance was achieved through matching the lattice plasmon mode to the excitation wavelength, by post-assembly fine-tuning of long-range structural parameters. Both unidirectional and bidirectional lattice deformations can be used to tune an initial lattice structure to both red-shifted and blue-shifted excitation lines, as exemplified by lattice expansion and contraction, respectively. This proof-of-principle study represents a basis for alternative designs of adaptive functional nanostructures with mechanically tunable lattice resonances using strain as a macroscopic control parameter. This chapter is inspired from a publication that was submitted in December 2020 to advance functional materials [1].

5.1 Introduction

5.1.1 Enhancement of SERS signal by plasmonic tuning

Tuning of plasmon resonances to a specific wavelength is probably one of the most studied characteristics of plasmonic systems. Plasmon resonances can be engineered through the nanostructure's composition, morphology, and environmental refractive index [2, 3]. High and efficient SERS signal enhancement typically demands a close match between the plasmon resonance wavelength and the excitation source [4]. This is why fine and reversible tuning of plasmon resonance is interesting to understand the relationship between plasmon resonance wavelength and SERS intensity. Matching of the plasmon resonance to the laser wavelength constitutes the main strategy to increase the SERS signal.

5.1.2 Reversible self-assembly in colloidal systems

Upon assembly, the optical behavior of single gold nanoparticles changes. In a close packed assembly of gold nanoparticles, the plasmon resonance from single NP hybridize thanks to plasmonic coupling leading to a redshift of the nanoparticles extinction (see **Section 2.4.1**). Therefore varying the assembly state, or to another extent the distance between assembled nanoparticles, constitutes a strategy for tuning the optical properties of gold nanoparticles. In colloidal solutions, the reversible assembly of gold NPs using an external trigger such as pH [5], temperature [6] or solvent change [7] renders plasmonic tuning possible over a wide wavelength range. As an example, **Figure 5.2 a** shows that the optical properties of penicillamine coated colloidal NPs can be tailored through the solution pH.The observed shift of the absorption band is explained by a controlled aggregation of the NPs at low pH values, due to changes in the H-bonding dominated interparticle forces, as demonstrated by the TEM images in **Figure 5.2 b**.

Controlled and reversible aggregation of NPs in liquid gives access to the on-demand creation of hotspots, which facilitate high SERS signals. In **Figure 5.2**, the SERS signal of penicillamine coated nanoparticles upon subsequent changes of pH between 7 and 3 can be seen, SERS peaks at $1187\,\mathrm{cm}^{-1}$ and $888\,\mathrm{cm}^{-1}$ are only seen when the nanoparticles are in an aggregated state at pH 3 and represent the SERS signal of penicillamine. Upon disassembly of the nanoparticles,

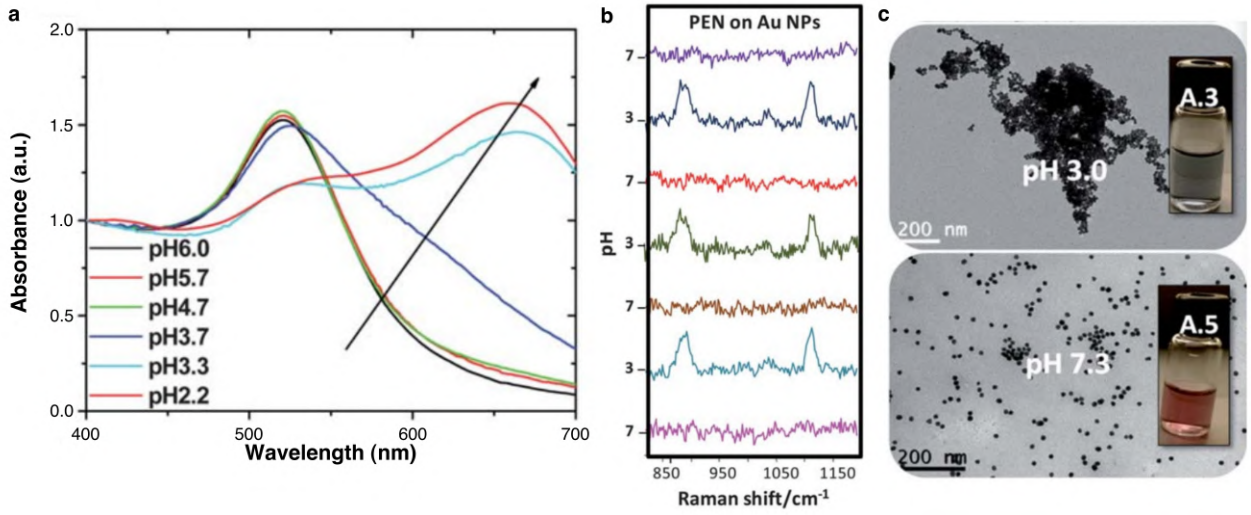

Figure 5.2: Plasmonic tuning by reversible aggregation of colloidal nanoparticles in solution. a) UV-Vis extinction spectra of penicillamine-coated gold NPs at different pH. b) SERS spectra of the penicillamine-coated gold NPs at different pH. c) TEM images of samples prepared using a solution with aggregated NPs or non-aggregated NPs. Adaptated with permission from [5], copyright 2011 Royal Society of Chemistry.

by switching to pH 7, the SERS signal is lost. Such an example shows how dynamically tuned plasmon resonances can be interesting for use in sensing applications by SERS.

5.1.3 Flexible substrates for plasmonic tuning

In most cases, the mechanisms proposed for plasmon tunability in colloidal solutions are not applicable to nanoparticles that are fixed on a substrate. Alternatively, the substrate on which the nanostructure is supported provides access to further tunability by using elastomeric materials [8] or through conformational changes of the supporting polymer under an external stimuli [9, 10]. Several studies have been reported on the manipulation of plasmonic modes of substrate-supported nanostructures by tuning near-field interactions between NPs [11, 12]. For instance, Baumberg and coworkers used dark-field spectroscopy to demonstrate the controlled detuning of a single plasmonic dimer under mechanical strain [8]. Mechanical tuning of far-field coupling through lattice plasmons has been applied to both all-dielectric [13] and plasmonic [14] lattice structures on stretchable supports. Expectations are high and numerous applications would benefit from the ability to implement active mechanical tuning, opening new avenues

toward structural coloration with full-spectrum response [15], mechano-chromic materials [16], nano-lasing [14], and programmable plasmon-mode engineering [17].

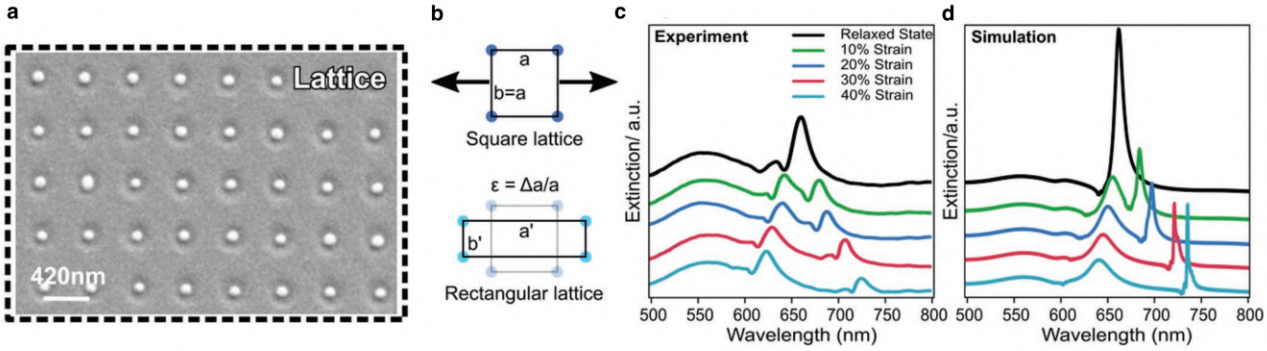

Figure 5.3: Plasmonic tunability of stretchable plasmonic lattices. a) SEM image of a self-assembled plasmonic lattice on a flexible substrate. b) Scheme of a square lattice upon unidirectionnal stretching. c) Experimental UV-Vis extinction spectra of a 420 nm plasmonic lattice upon mechanical deformation. d) Simulated extinction spectra of a 420 nm plasmonic lattice upon mechanical deformation, adaptated with permission from [18], copyright 2019 American Chemical Society.

As an example, **Figure 5.3** shows the optical properties of a stretchable plasmonic lattice composed of single nanospheres upon mechanical deformation. Upon elongation to a rectangular lattice, the lattice plasmon mode initially present at 670 nm splits into two modes, one shifting towards the blue and the other shifting toward the red. The appearance of two modes that shifts with elongation, corresponds to an elongation of the lattice in the x-axis and a contraction of the lattice in the y-axis due to the unidirectional stress applied on the flexible lattice.

5.1.4 Flexible plasmonic superlattices as SERS substrates

As is was exposed in the previous section, the optical properties of plasmonic superlattices is tailored through their lattice period. Fabrication of superlattices with different periods is usually achieved by self-assembly with molds comprising wells in square lattices of different periods. High and efficient SERS signal enhancement typically demands a close match between the plasmon resonance wavelength and the excitation source [19, 20]. In the case of resonant

excitation, lattice plasmons can generate intense electromagnetic fields, as required for ultra sensitive SERS spectroscopy [21, 22, 23]. Hanske et al demonstrated that plasmonic superlattices gave the highest SERS enhancement at the best match between lattice plasmon and laser excitation [24]. However, tuning both the lattice period and the size of the substructures requires iterative remodeling of the template structure and its repeated fabrication by electron-beam lithography (EBL), which is time-consuming and costly. This issue makes mode matching a complex and tedious task that generally results in a trade-off between excitation efficiency and signal enhancement.

A key issue during the fabrication of superlattices with different periods is the rigid template that predetermines the plasmonic structure through the assembly procedure. This chapter introduces a more practical solution that allows for the subsequent modification of the lattice structure by a mechanical stimulus. Ideally, continuous and reversible tuning of the lattice periodicity would allow for a precise adjustment of the lattice resonance to the excitation wavelength of the laser, thus enabling a versatile screening for the most efficient SERS performance. While the precedent chapters aimed at optimizing the templated self-assembly process and finding the most appropriate nanoparticles for SERS sensing, this chapter aims at optimizing the lattice period for best SERS signal using mechanical deformation of stretchable superlattices.

5.2 Results

5.2.1 Self-assembly of stretchable superlattices

The fabrication of highly regular supercrystal arrays follows the template-assisted self-assembly process described in **Chapter 3** with the difference that the substrate is now made of PDMS. Because the template and the target substrate were made of PDMS, it was necessary to apply a thin layer of polyethyleneimine (PEI), acting as an adhesive layer, to promote particle transfer and adhesion onto the target substrate [25]. Gold nanospheres of different sizes, ranging from 30 to 105 nm in diameter, were assembled into superlattices of 500 nm period (see **Figure 5.4 a,b,c**). Nanospheres of 40 nm diameter were found to yield the most suitable clusters, with high packing density and uniform cluster size.

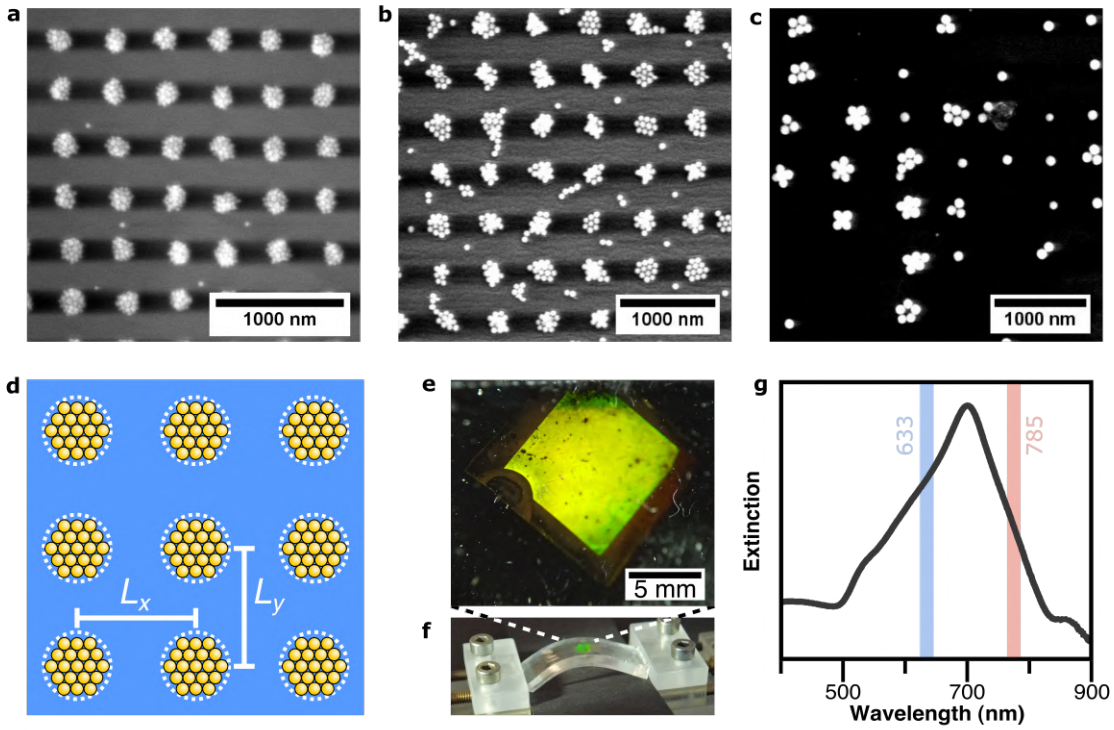

Figure 5.4: Templated self-assembly on PDMS substrate. SEM images of PDMS-supported superlattices made of: a) 40 nm nanospheres, b) 65 nm nanospheres, c) 105 nm nanospheres. d) Schematic representation of the superlattice design with indicated lattice periods in horizontal Lx and vertical direction Ly. Superlattice under white-light illumination in relaxed e) and bent f) states. The green iridescent color arises from light diffraction. g) Extinction of transmitted light in the relaxed state.

As an example, **Figure 5.4 e** shows a macroscale photograph of a superlattice under white light illumination. At specific angles, an intense iridescent color can be observed due to a diffraction order going back to the camera. Limited only by the size of the template, macroscale periodic arrangements of gold NPs were obtained over areas as large as one square centimeter. Due to the elastic nature of the PDMS substrate, it can be readily stretched or bent by mechanical deformation (see **Figure 5.4 f**).

In this chapter, pre-patterned templates containing circular holes of 270 nm diameter, in a square grid with a period of 500 nm were used as templates for the self-assembly (**Figure 5.4 d**). The 500 nm periodicity was specifically chosen because the lattice plasmon resulting from this period is located at around 700 nm, which is in between the two targeted excitation wavelengths

of 633 and 785 nm, as shown in **Figure 5.4 g**.

5.2.2 Superlattice expansion and compression

PDMS is a rubber-like elastic material with a Poisson's ratio near 0.5 [26], which is why it contracts in the directions transversal to the direction of strain. Such a feature can be used to expand and compress superlattices post-assembly. By stretching the PDMS-supported superlattice, a gradual color change of the illuminated superlattice can be observed by the eye (**Figure 5.5 a**), which indicates a change of the period and thus of the diffracted wavelengths.

Nonetheless, this visual indication gives no information about the state of the cluster substructures nor about the precise change of the lattice period. Indeed, different scenarios could take place under applied stress, such as detachment and slipping of the clusters on the substrate; changes in the interparticle gaps; or fragmentation [25] of the clusters into smaller units. Especially the latter two would induce dramatical changes in the resulting optical properties [27]. The balance between cohesive (particle-to-particle) and adhesive (particle-to-substrate) forces plays a critical role in the different possible scenarios. If the cohesion between PEG-coated NPs were much larger than their adhesion to PEI-coated PDMS, the clusters would detach during stretching. In the reverse case, the applied stress could break up the clusters, as was recently evidenced by mechanical simulations using the lattice spring model [25]. Both extreme cases must thus be avoided. Any structural changes of the cluster, including the number of NPs [28] and their interparticle distances [29], could have detrimental effects on lattice plasmons and SERS enhancement.

Therefore, environmental scanning electron microscopy (e-SEM) was performed, to study the structural changes of the superlattice upon mechanical deformation. **Figure 5.5 b and c** compare the superlattice in the pristine/relaxed state and at 30% elongation. Please note, the observed dark vertical lines are artifacts due to charging during scanning (see **Appendix III.1**). The lateral resolution of e-SEM imaging does not allow for direct quantification of interparticle distances within a cluster. Nevertheless, statistical evaluation of the data obtained from image analysis yields reliable data for the relative change in interparticle distance when strain is applied. **Appendix III.2** demonstrates that the interparticle gaps do not expand with the

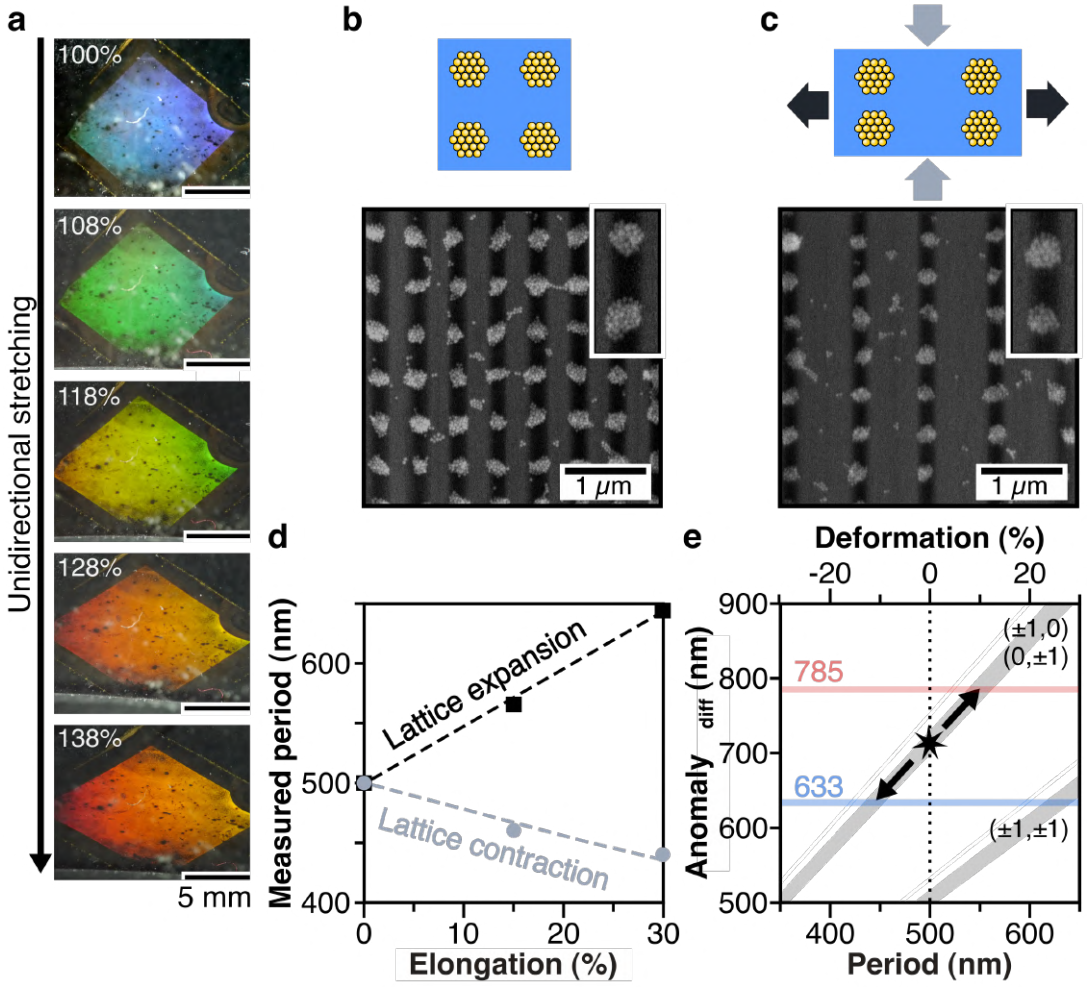

Figure 5.5: Tuning of lattice period: (a) Digital photographs of a superlattice on PDMS under unidirectional stretching and white-light illumination, due to changes in the diffracted wavelength. A gradual color change is observed upon stretching. (b,c) Schematic drawings and environmental SEM images of a 500 nm superlattice in the pristine state (b) and elongated by 30% (c). (d) Changes in horizontal (black square) and vertical period (grey cricle) under unidirectional strain, evaluated from SEM images. Dashed lines are guides to the eye. (e) Spectral position of diffraction anomalies (grey) at normal incidence as a function of lattice period, predicted by lattice theory (Eq. 1).

mechanical deformation of the substrate. Neither a fragmentation, break-up, nor any other significant conformational changes could be observed, even after repeated stretching cycles. Therefore, it is assumed that the clusters are robust against the applied mechanical stress and that the balance between cohesion and adhesion is appropriate for tuning the lattice period. In addition, the lattice periods of the superlattice under stretching were determined from e-SEM

images taken at different uniaxial elongations (see **Appendix III.3**). At 30% elongation, the lattice periods in the horizontal and vertical directions changed from 500 nm to 645 nm and 440 nm, respectively (see **Figure 5.5 d**). The magnitude of the horizontal expansion is almost twice the vertical contraction, as expected for an incompressible rubber-like material with a Poisson's ratio near 0.5, such as PDMS.

5.2.3 Asymmetric optical tuning by unidirectional strain

Once the conformational changes upon unidirectional strain have been exposed, the corresponding optical effects can be studied. Lattice plasmons rely on the constructive interference of scattered fields produced by the periodically arranged clusters [30, 31]. The lattice plasmon wavelength of a square array can be estimated from the wavelength of in-plane diffracted orders λ_{diff}, also known as Rayleigh cutoff wavelengths, describing specific lattice effects, in analogy to so-called Wood's and Rayleigh's anomalies (see **Section 2.4.3**) [32, 33]. The spectral position of this lattice resonance effect is determined by the period of the grating L, the refractive indices of interfacing media (substrate $n_{\mathrm{sub}} \approx 1.40 - 1.45$ for PDMS and superstrate $n_{\mathrm{top}} = 1$ for air), and the angle of incidence θ [34]. Thus, a square lattice with a period of 500 nm on a PDMS substrate corresponds to a diffraction mode [35] at 700 nm (asterisk in **Figure 5.5 e**). To match the diffraction mode with the excitation lines at 633 and 785 nm, the grating period has to be reduced to ≈ 440 nm or extended to ≈ 550 nm, respectively. However, for efficient transfer of energy from the incident light into the lattice plasmon, this anomaly must also energetically overlap with the plasmon resonance of the substructure [30], i.e., the self-assembled clusters [18]. **Appendix III.4** shows the results of numerical calculations by the finite-difference time-domain (FDTD) method for the absorption cross-section of an isolated cluster and the resulting broad resonance modes in the corresponding spectra (for details on modeling see **Section 5.4.10**). Only in the case of mutual resonance, there is an additional gain in the local near-fields within the lattice [24, 21], as required for SERS (see **Appendix III.5**). For that reason, the design of suitable lattice structures for efficient SERS excitation by mode matching is challenging, since several structural and optical parameters must be adjusted to each other at the same time.

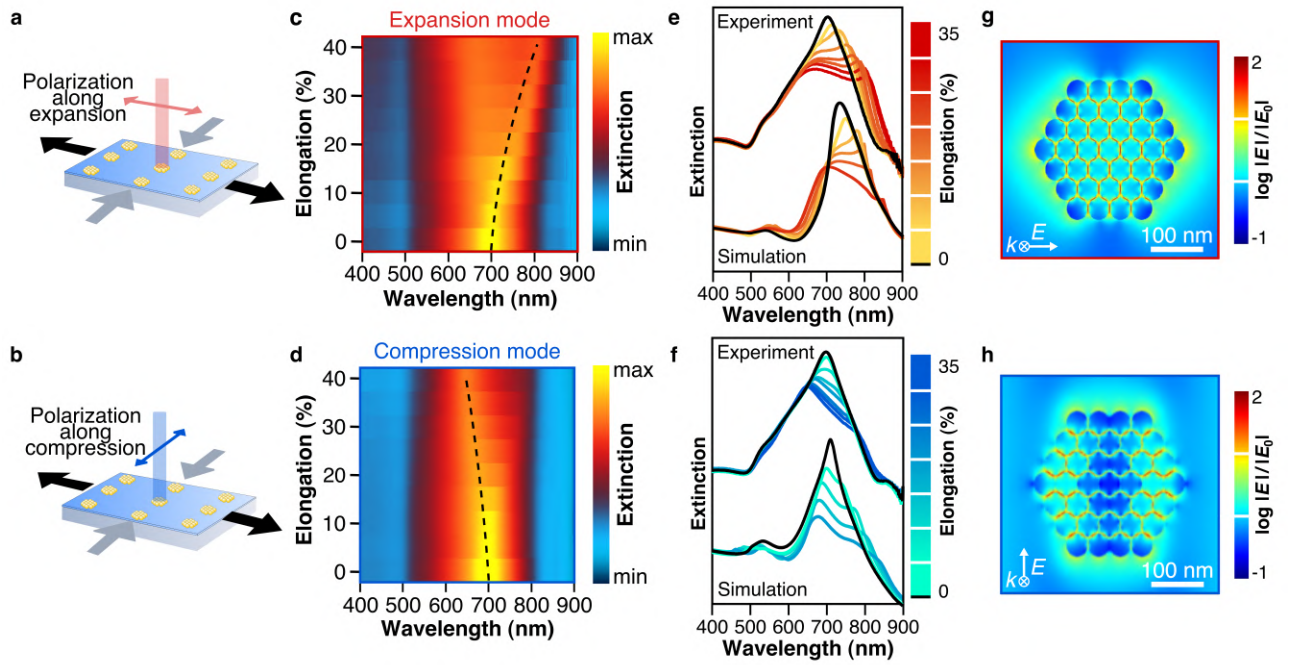

Figure 5.6: Optical changes for lattice expansion and compression during asymmetric unidirectional mechanical deformation for a pristine lattice with 500 nm period: scheme of stretched superlattice and light polarization, along the direction of either expansion (a) or compression (b). (c,d) Extinction spectra for various elongation states, according to the provided color scale. Comparison of experimental and simulated extinction spectra upon unidirectional strain and light polarized along the direction of expansion (e) and contraction (f), in stacked representation. Black curves represent the optical properties of the superlattice in pristine conditions. Electric field maps for the expansion (g) and compression (h) modes for an array with 15% of elongation at the wavelength of the resonance peaks.

One can assume that asymmetric lattice deformations would result in optical anisotropy, with the coexistence of two separate grating anomalies in orthogonal directions. Each anomaly should be located at a distinct wavelength, either blue-shifted for lattice compression or red-shifted for lattice expansion (cf. **Figure 5.5** e). Control over the optical properties is important because they represent the basis for the excitation of electromagnetic hotspots and SERS in plasmonic nanostructures [36, 37]. To better understand the influence of lattice variations on SERS measurements, the optical properties need to be correlated with unidirectional deformations of the lattice. For this purpose, UV-Vis extinction spectroscopy was performed in

transmission geometry with a custom-made stretching device to study the changes in optical properties at a fixed sample position while applying unidirectional strain.

Figure 5.6 shows a UV-Vis spectroscopic analysis under linearly polarized light, so that the influence on the optical spectra of both lattice modifications could be studied separately. Polarization was adjusted along the direction of either expansion (**Figure 5.6 c,e**) or compression (**Figure 5.6 d,f**). For clarity, a simplified notation of expansion and compression mode was used below. The lattice plasmon of the superlattice in pristine/relaxed state builds on a grating anomaly (first-order diffractive mode), giving rise to a sharp extinction band around 710 nm, together with a shoulder at 530 nm. This peak is assigned mainly to a mixture of the plasmon mode for individual nanoparticles [38], with high-order longitudinal modes of the cluster, as shown in **Appendix III.4**.

Using light polarized along the axis of elongation, the lattice plasmon was found to redshift from 710 to 805 nm, for a lattice elongation of 35% (expansion mode, **Figure 5.6 c,e**). If the incident light is polarized along the axis of compression, a lattice plasmon blueshift from 710 to 623 nm is observed instead (compression mode, **Figure 5.6 d,f**). Hence, the polarization direction acts as a switch between both lattice plasmons. The evolution of the expansion and compression modes could also be reproduced by FDTD simulations, as shown in **Figure 5.6 e,f**. Considering the multitude of parameters in this system (see **Section 5.4.10**) and irregularities of the self-assembled clusters, the agreement between experimental and theoretical data is remarkable. Minor discrepancies can be attributed to the presence of more than a single cluster configuration in real samples, which is likely to influence the coupling efficiency to the lattice plasmon. In addition, for the sake of simplicity, the interparticle spacing in the simulations was fixed to 1 nm, set by a shell of refractive index of 1.46 to emulate PEG. Nevertheless, the evolution of the lattice modes upon lattice deformation is consistent with the experimental results. **Figure 5.6 g** illustrates that the expansion mode is supported by the entire cluster, while the compression mode presents a mode profile that enhances mainly the field in the lateral part of the cluster (**Figure 5.6 h**). The spectral position of the diffraction modes matches well with the position of the cluster modes in isolated state (**Appendix III.4**). The lattice mode thus hybridizes with the different cluster modes to form lattice plasmons depending on their spectral overlap.

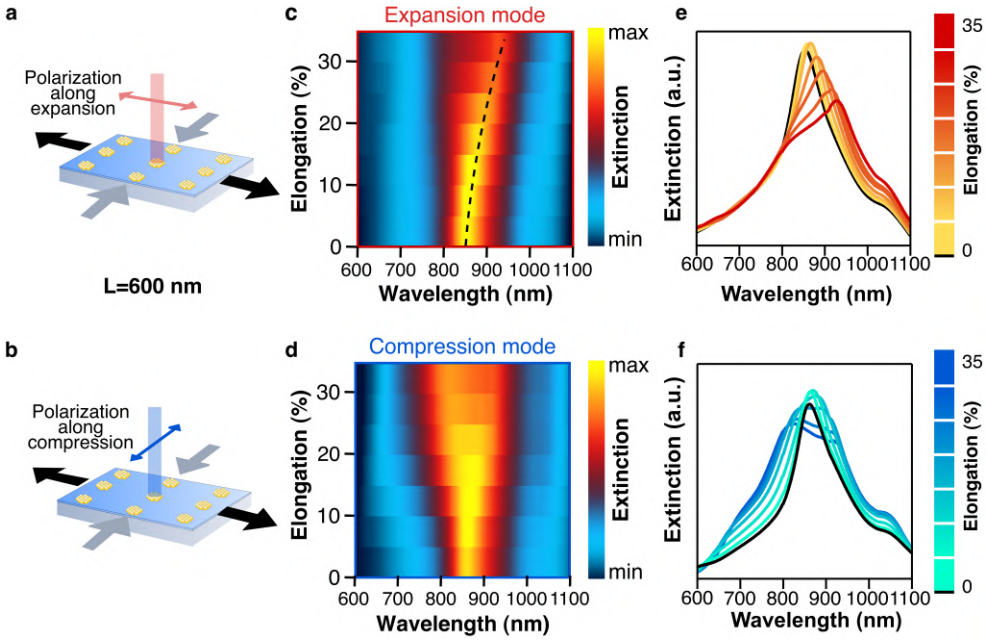

Figure 5.7: Optical changes for lattice expansion and compression during asymetric unidirectional mechanical deformation for a pristine lattice with 600 nm period: scheme of stretched superlattice and light polarization, along the direction of either expansion (a) or compression (b). (c,d) Extinction spectra for various elongation states, according to the provided color scale. Experimental extinction spectra upon unidirectional strain and light polarized along the direction of expansion (e) and contraction (f). Black curves represent the optical properties of the superlattice in pristine conditions.

It should be noted that, next to the expansion mode, a broad peak can be observed between 650 and 700 nm, likely due to plasmon modes of the cluster substructures, that do not couple to the lattice. In other words, the progressive tuning of the grating anomaly (diffractive mode) toward the red leads to a decoupling of the clusters from the lattice. This observation is supported by FDTD simulations, which predict a similar contribution for an isolated cluster of nanoparticles (**Appendix III.4**), with a broad band between 650 and 800 nm.

To further support our understanding of the mode evolution, extinction measurements with polarization along the elongation and contraction direction were repeated with a pristine superlattice of 600 nm period (**Figure 5.7**). In this case, the pristine lattice plasmon was located at 840 nm, the expansion mode shifted up to 930 nm at 30% elongation and the compression mode shifted to 810 nm at 30% elongation. The evolution of the modes observed during strain

is fully consistent with our understanding, as detailed above. Changing the initial period of the superlattice enables to screen lattice plasmons at a different wavelength range. However, the plasmon modes of the 600 nm period superlattice under stretching overlap neither with the 633 nm excitation nor with the 785 nm excitation. Considering that contraction and elongation modes for the 500 nm pristine lattice overlap with 633 and 785 nm, this model system is ideal for use under both SERS laser line excitations.

5.2.4 Symmetric optical tuning through bidirectional strain

A clear understanding of the anisotropic optical response of unidirectionally deformed lattices was gained in the previous section. Since the plasmonic response strongly depends on the polarization state of the incoming light, the competition between transversal lattice plasmon modes may hinder the formation of efficient hotspots. Consequently, it would be advantageous to avoid symmetry breaking by applying a uniform strain in both directions. For this purpose, a custom-made two-dimensional stretching device was used. Here, the sample was clamped at all four sides, so that strain can be applied symmetrically. Because this device can only apply positive strain, the experiments were limited to the (bidirectional) optical tuning of the expansion mode.

Figure 5.8 compares the mode evolution for unidirectional (**Figure 5.8 a,b**) and bidirectional lattice deformations (**Figure 5.8 b,d**). By performing optical measurements with unpolarized light, it was observed that the asymmetric deformation mainly leads to a blueshift of the compression mode toward 633 nm. Though observable, the red-shifting expansion mode appears much weaker, which may be partly caused by the contribution of the cluster plasmon under non-resonant conditions to the lattice, as explained above. In addition, the imbalance between the number of compressed and extended cluster gaps within the measurement spot favors the compression mode. Because of the finite size of the illuminated area, lattice expansion is accompanied by a decrease in the number of sub-units with extended periods. On the contrary, lattice compression increases the number of sub-units with shorter periods within the probed area. To further support our understanding of the mode evolution, the same experiments were also carried out with a superlattice of 600 nm period and showed a similar behavior(**Appendix**

III.6).

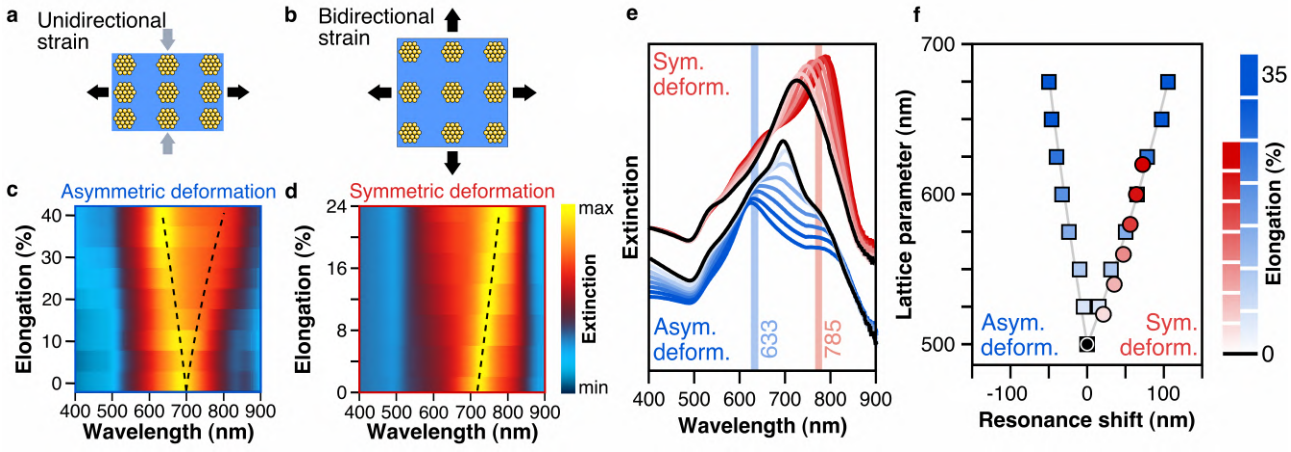

Figure 5.8: Optical effects of asymmetric (unidirectional) versus symmetric (bidirectional) lattice deformation: (a,b) Schematic depiction of lattice deformations. Extinction maps for a 500 nm superlattice under asymmetic (c) and symmetric (d) strain. Dashed lines indicate mode shifts. (e) Corresponding extinction spectra. (f) Comparison of the resonance shifts under asymmetric (blue squares) and symmetric deformations (red circles).

Upon bidirectional bidirectional stretching ($L_x = L_y$), a completely different optical behavior was observed. **Figure 5.8 d** shows a pronounced expansion mode that progressively red-shifts (800 nm at 20% elongation). A second spectral feature develops around 600 - 650 nm, which could be attributed to lattice plasmons formed by the (±1, ±1) diffractive mode (**Figure 5.8 e**). The red-shift and the secondary feature are corroborated by FDTD simulations as shown in **Appendix III.7**. Upon bidirectional strain, the intensity of the expansion mode is much higher than that under unidirectional strain. This effect is in agreement with the understanding of the lattice plasmon, because coupling occurs more efficiently in a symmetric lattice, where both lattice parameters can diffract the excitation light efficiently.

In the light of the optical properties of superlattices under bidirectional stretching, it can be concluded that bidirectional stretching is the method of choice to obtain an intense expansion mode, as exemplified here for square superlattices. Most of the experiments reported in the literature used unidirectional strain and thus considered asymmetric mechanical deformations [17, 18]. Performing stretching experiments with bidirectional strain control allows us to avoid contraction of the sample and better-controlled strain distribution. Independent

control for the periods in both axes allows for geometries that are not achievable with simple unidirectional stretching. To investigate the effect of symmetry on the optical properties of superlattices in more detail, a custom-made stretching device with separate control over both stretching axes was used. This allowed us to perform two-step stretching experiments: first, a square lattice was expanded into a rectangular lattice with a fixed vertical axis; the vertical axis was then gradually elongated to obtain a stretched square lattice. By stretching a square lattice into a rectangular one, a redshift of the lattice plasmon was observed, as expected. However, a significant broadening of the lattice mode was also observed (**Appendix III.8**). By stretching from a rectangular lattice into a stretched square lattice, an additional redshift of the expansion mode could be observed, but this time, the band became significantly sharper. A higher symmetry in superlattices leads to more intense and sharper lattice plasmon resonances, especially in the case of non-ideally aligned exciting fields or depolarized light, which is appealing for applications relying on high Q factors, such as nanolasing [14]. It is worth mentioning that a refractive-index matching layer [39, 40] on top of the plasmonic superlattices further decreases the spectral linewidth (**Appendix III.9**), which is however not an option regarding SERS applications.

Figure 5.8 f compares the evolution of the lattice plasmons for asymmetric (blue squares) and symmetric deformations (red circles). For both methods of deformation, the expansion modes follow a linear trend with the elongation of the substrate. This behavior could be expected considering the linear relationship of the spectral position of the Rayleigh cutoff wavelength with the lattice period (**Figure 5.5 e**). The fact that both deformation methods yield almost identical plasmonic wavelengths further supports the proposed concept of mechano-plasmonic tuning.

5.2.5 SERS performance of strain-deformed superlattices

Finally, the impact of lattice tuning on SERS performance was investigated. Starting from the hypothesis that the best SERS performance relies on mode matching to the excitation laser [24], resonance states can be expected for asymmetric elongation of 30 - 40% for 633 nm excitation, and symmetric elongation of 10 - 20% for 785 nm excitation. To probe SERS enhancement, a

low-molecular-weight model analyte, 4-Nitrothiophenol (NTP), with a high affinity to adsorb onto gold surfaces was used. To avoid detrimental effects on the PDMS substrate, such as reduced elasticity, no additional cleaning steps, such as oxygen plasma, were applied. It is well known that oxidized PDMS exhibits a brittle interface, which would undergo irreversible cracking when stretched. Labeling with NTP was carried out by drop-casting a freshly prepared 1 µM analyte solution, followed by washing with ethanol (**Section 5.4.10**). NTP is a widely used performance marker in SERS spectroscopy, due to its intense stretching vibration of the NO_2 group at 1330 cm^{-1}.

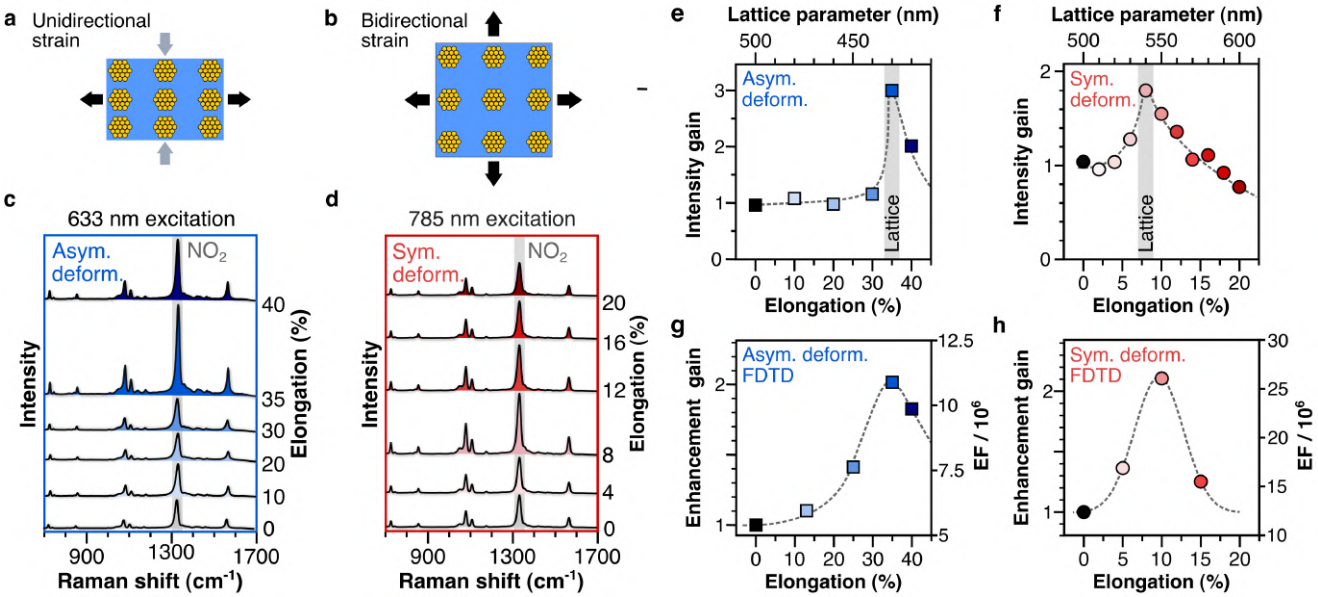

Figure 5.9: Mechanical tuning of SERS performance as a function of mode-matching: Schematic drawings of unidirectionally a) or bidirectionally b) deformed superlattices. Stacked SERS spectra of an NTP-labeled superlattice under unidirectional stretching at 633 nm excitation c), and under bidirectional stretching at 785 nm excitation d). e,f) SERS enhancement as a function of lattice elongation, obtained from the intensity of the NO_2 stretching vibration (gray highlighted area in c,d) and normalized to the intensity in unstretched state. Enhancement was found to peak at resonant conditions between lattice plasmons and excitation lines. Dashed lines serve as guide to the eye. Gray highlighted areas indicate a spectral matching of the lattice modes with the corresponding excitation lines (cf. **Figure 5.5**). g,h) Gain in enhancement predicted by FDTD modeling.

Figure 5.9 provides a summary of SERS experiments performed with both 633 and 785 nm

excitation lasers, so as to investigate the effects of mode-matching by tuning the lattice parameters. The experiments were performed without an additional linear polarizer so that it can be expected that the excitation light is partially depolarized by the Raman microscope optics. In principle, substrate stretching is accompanied by a decrease in the number of SERS emitters in the finite excitation volume (**Appendix III.10**) and thus a decrease in signal intensity could be expected. However, in the case of 633 nm excitation and unidirectional asymmetric stretching (**Figure 5.9 c**), the Raman fingerprint remains almost constant up to an elongation of 30%. At 35%, when the lattice plasmon and the excitation laser are in resonance, the intensity increases significantly by 1.8 times by symmetric stretching and 3 times by asymmetric stretching (**Figure 5.9 e**) â normalized to the intensity in the unstretched state. Further stretching, however, causes a new loss of signal intensity, which confirms that SERS generated by the compression mode is highly sensitive to changes in lattice period of ±25 nm (equivalent to ±5%). This is corroborated by numerical calculations of the dipole enhancement E^2/E_0^2 by the local electric field E_{loc} in the twofold amplification process, i.e., the augmented excitation of a molecular dipole by an incident photon ($_{\mathrm{exc}}$) and the stimulated emission of a scattered photon λ_{sca} [19, 41].

$$EF = \frac{|E_{\mathrm{loc}}(\lambda_{\mathrm{exc}})|^2}{|E_0(\lambda_{\mathrm{exc}})|^2} \cdot \frac{|E_{\mathrm{sca}}(\lambda_{\mathrm{sca}})|^2}{|E_0(\lambda_{\mathrm{sca}})|^2} \tag{5.1}$$

This first-order approximation of the change in enhancement factors (EFs of 10^6 â 10^7, **Figure 5.9 g**, right axis) upon unidirectional strain is in excellent agreement with our experimental observations.

In the case of bidirectional symmetric stretching and 785 nm excitation (**Figure 5.9 d**), a similar trend was also observed. After an initial damping up to 4% elongation, the signal intensity increased ca. 2-fold, with a maximum at 8-9% elongation, followed by a gradual decrease (**Figure 5.9 f**). This behavior resembles the response curve of a resonance phenomenon, as one might expect for an excitation matching effect, also theoretically corroborated by FDTD simulations (**Figure 5.9 h**). To test the repeatability of the plasmon tunability, extinction and SERS measurement cycles between different stretching states were performed (**5.10**). Excellent repeatability of the plasmon resonance wavelength and the SERS enhancement was found.

To illustrate the importance of the lattice mode for increased SERS efficiency, a substrate

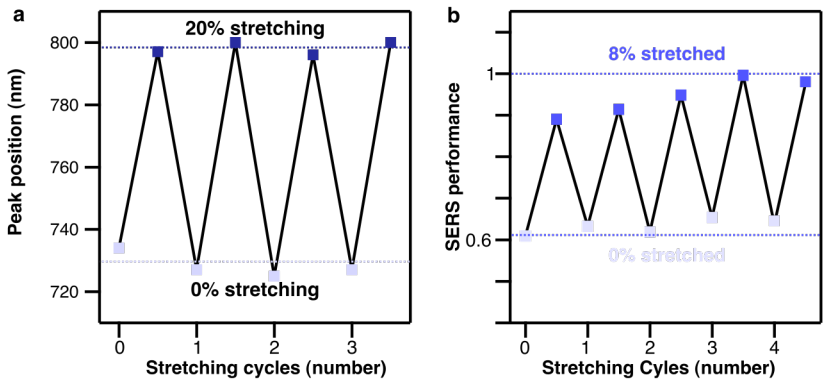

Figure 5.10: Repeatability of the optical properties of a stretchable superlattice. a) Evolution of the lattice plasmon peak position for successive switching between 0% and 20% elongation states. b) Evolution of the SERS performance for sucessive switching between 0% and 20% elongation states

without any structural order was prepared for comparison. For this purpose, a drop of a colloidal dispersion of Au nanospheres was drop-cast on PEI-coated PDMS without the spatial confinement of the nanostructured template. The resulting nanostructures consist of random domains (**Appendix III.11**) so that any influence from periodic order can be excluded. During stretching, the SERS signal was found to dramatically decrease using 785 nm excitation and stayed almost constant using 633 nm excitation (**Appendix III.12**). This behavior is attributed to a combination of the poorly excitable nanostructures as well as a decrease in the number of Raman marker molecules in the excitation volume upon stretching (Figure S13). For structured samples, the latter is compensated by the gain in enhancement upon excitation matching, which does not occur in the unorganized sample. Indeed, the optical properties of the unorganized sample (**Appendix III.11**) indicate a poorly defined plasmonic band, which did not show any significant changes upon stretching. It is thus concluded that the hierarchical organization of the cluster into a periodic superstructure is the key to the observed SERS amplification. In both deformation scenarios, the highest gain in SERS performance was found by matching the lattice plasmon mode to the excitation wavelength, through fine-tuning of the lattice plasmon by post-assembly adjustment of long-range structural parameters.

Apart from the direct application of superlattices on flexible supports, the presented technology can be used for screening of structural parameters and identifying the most-suitable

SERS conditions, i.e., a contracted lattice of 450 nm for 633 nm excitation and an expanded lattice of 530 nm for 785 nm excitation.

5.3 Conclusion

Mechanical tuning of lattice plasmon resonances was demonstrated using a model system of self-assembled nanoparticle superlattices on a flexible substrate. This model system allows for a modulation of the lattice periods using strain as a macroscopic control parameter. In this way, the structural parameters of the superstructures could be reversibly readjusted while keeping the plasmonic substructures intact. The deformation of the lattice was assumed to have a major effect on the inter-cluster distances as inferred from the optical spectra. Intra-cluster distances might be affected as well, but to a much lesser extent for the elongation rates considered. This hypothesis is supported by the fact that elongated superlattices showed intense SERS signals emanating from the cluster substructures, indicating that such hotspots are still active upon deformation. We investigated the optical changes caused by expansion and contraction of the lattice, as a means for active mechanical tuning of plasmonic properties such as the control over the spectral position of the lattice plasmon. Here, we revealed the inherent differences between asymmetric and symmetric lattice deformations by a correlation of optical and structural parameters, which was faithfully reproduced by electromagnetic simulations. Rectangular lattice geometries were found to exhibit competition between compression and expansion modes. As a proof of concept, lattice expansions and contractions were shown to adapt a single lattice structure to either red-shifted or blue-shifted excitation lines, respectively. An additional gain in SERS performance was observed when the lattice was tuned in resonance with the excitation, as initially hypothesized. Finally, the most suitable periods for SERS were found to be 450 nm for the 633 nm excitation and 530 nm for the 785 nm excitation.

5.4 Materials and methods

5.4.1 Materials

$HAuCl_4 \cdot {}_3H_2O$ (≥99.9%, trace metal basis) and 4-nitrothiophenol (96%, NTP) were purchased from Alfa Aesar. Sodium borohydride (ReagentPlus©, ≥99%, $NaBH_4$), cetyltrimethylammonium chloride (≥98%, CTAC), L-ascorbic acid (ACS reagents, ≥99%, AA), poly(ethylene glycol) methyl ether thiol average (Mn 6 kg mol^{-1}, PEG-6K), polydimethylsiloxane (Sylgard© 184, PDMS), polyethyleneimine (Mw 25 kg mol^{-1}, PEI, highly branched), and sodium hypochlorite (6 - 14% active chlorine, Emplura©, NaOCl) were purchased from Sigma-Aldrich. All solutions, except $HAuCl_4$ and CTAC, were prepared immediately before use. Purified Milli-Q water was used in all experiments (Millipore, 18.2 M cm). Glassware was cleaned with aqua regia and rinsed extensively with Milli-Q water before use.

5.4.2 Nanoparticle synthesis

Nanospheres were synthesized by seeded growth as reported recently [22]. First, small seeds of 2 nm were prepared by adding $HAuCl_4$ (50 µL, 0.05 M) to a CTAC solution (5 mL, 100 mM). Subsequently, $NaBH_4$ (200 µL, 0.02 M, i.e., 7.5 mg in 10 mL) was added under vigorous stirring. After 3 min, the mixture was diluted 10 times by a CTAC solution (100 mM). Then, the small seeds were overgrown to 10 nm nanospheres: For this purpose, the small seeds (900 µL) were added to a mixture of AA (40 µL, 0.1 M) and CTAC (10 mL, 25 mM). Next, HAuCl4 (50 µL, 0.05 M) was added under vigorous stirring. The 10 nm seeds showed an LSPR at 520 nm. The dispersion was left undisturbed for at least 1 h. Afterward, the nanospheres were centrifuged (19.300 rcf, 12 cm rotor) and washed at least 3 times with CTAC solution (25 mM). Afterward, the 10 nm-sized nanospheres were overgrown to larger nanospheres: First, the nanospheres (125 µL) were added to a solution AA (40 µL, 0.1 M) and CTAC (10 mL, 25 mM). Subsequently, $HAuCl_4$ (50 µL, 0.05 M) was added. The resulting nanoparticles had rough edges, which were removed by oxidative etching. For this, a diluted solution of sodium hypochlorite (10 µL, 1 to 1.5% of available chlorine) and 10 min later $HAuCl_4$ (5 µL, 0.05 M) was added under continuous stirring. After 30 min, the final nanospheres were centrifuged (3100 rcf,12 cm rotor, 15 min) and

redispersed in CTAC solution (500 µM). The final NPs were concentrated to ca. 5 mM Au^0 in a solution of CTAC (500 µM). Functionalization was done by the addition of PEG (1 mg/mL) and stirring overnight at room temperature (RT). Excess unbound PEG was removed by repeated centrifugation (3100 rcf, 12 cm rotor, 15 min) and redispersion of the sedimented NPs in CTAC (500 µM).

5.4.3 Preparation of PDMS target substrates

PDMS was prepared by casting of a cross-linker/prepolymer mixture (1:15, 25 g) in a leveled polystyrene dish (10 cm diameter) and degassing in a vacuum. The PDMS mixture was cross-linked in two steps: 24 h at RT and then 5 h at 80 °C. The cured PDMS was cut into 1x4.5 cm^2 strips and incubated in a fresh PEI solution (10 mg/mL), to promote the adhesion between nanoparticles and PDMS substrate. After 3 h, the strips were removed, washed with water, dried under a N_2 stream, and directly used as target substrates.

5.4.4 Preparation of PDMS soft templates

Soft PDMS templates were fabricated by pouring a cross-linker/prepolymer mixture (1:10) onto patterned silicon masters or their negative replicas with OrmoStamp© (Microresist Technology) [42]. The mixtures were degassed for 2 h to increase the percolation of the polymer inside the nanostructures and then cured (45 min, 100 °C).

5.4.5 Templated self-assembly of superlattices

A 2 µL droplet of nanoparticle dispersion (30 mM Au^0) calculated from the extinction at 400 nm, 66% EtOH, 200 µM CTAC) is cast on a PDMS target substrate. After 40 s of waiting time, a nanostructured PDMS stamp was added on top of the droplet. This template featured a square lattice of holes of 270 nm with a spacing of 500 nm. After 2 h and complete evaporation of the liquid, the PDMS template was carefully lifted off the flexible PDMS substrate. The resulting dried and nanostructured film consists of a nanoparticle superlattice representing the inverse structure of the template.

5.4.6 Fabrication of disorganized sample

To fabricate disorganized samples of disordered Au nanoparticles, Au^0 dispersion (100 µL, 4 mM, 40 nm-sized PEG-coated nanospheres) was drop-cast on a PDMS target substrate and allowed to dry (3 h, RT).

5.4.7 UV-Vis spectroscopy

Extinction spectra of colloidal dispersions were recorded with an Agilent 8453 UV-Vis spectrophotometer, using polystyrene cuvettes. Extinction spectra of dry samples were collected using a Carry 5000 UV-Vis spectrometer (Agilent). Samples were mounted on custom-made stretching devices and measured under normal incidence. The measurements were performed in such a way that the same surface area was probed during strain experiments.

5.4.8 Electron microscopy

Scanning electron microscopy was performed using an environmental SEM (FEI Quanta 250). Extra precaution was necessary to image the flexible superlattices because of an accumulation of charges at the surface even at low voltages. Already, at 20 kV (15,000x magnification), deformations of the superlattice structure were visible owing to charging (**Appendix III.3**). For that reason, overview images were recorded at an acceleration voltage of 10 kV with an integration time of 1 µs per line at a magnification of 16,000x. Detail images, resolving the NPs within the clusters, were taken at 20 kV with an integration time of 10 µs per line at a magnification of 30,000x.

5.4.9 SERS measurements

For SERS experiments, the samples were incubated in an aqueous solution of NTP (1 µM, 2 h), prepared freshly from a stock solution in EtOH (10 mM). After incubation, the samples were thoroughly rinsed with water to remove the excess NTP molecules that did not bind to the AuNPs and dried with N2 flow. Spectra with 633 nm excitation were obtained using a Renishaw inVia reflex equipped with a stigmatic single-pass spectrometer, a Peltier-cooled CCD

detector (1024 x 512 px^2), a 1800 grooves mm^{-1} grating, a HeNe laser as excitation line (633 nm, 0.55 mW), and a 50x lens (LWD, NA 0.5) yielding a spot size of around 20X20 μm^2. Spectra with 785 nm excitation (Ondax SureLock mini-benchtop stabilized laser, 10 mW) were obtained using a custom-made portable Raman system with a lens (10 mm focal length,) and spot size of ca. 150 x 150 μm^2. For both excitations, the same spot measurements were performed to provide quantitative data for the change in SERS performance during stretching experiments and at defined elongation states. To obtain statistically relevant data, data for extended sample areas of 200 x 200 μm^2 were collected by surface mapping. During stretching experiments, the focus was readjusted after each elongation step. The focus plane was defined as the z-height yielding maximum signal intensity.

5.4.10 Electromagnetic simulations

Numerical calculations were performed using Lumerical FDTD Solutions (version 2020a R7). Clusters of NPs with a diameter of 40 nm were modeled with interparticle distances of 1 nm, using a non-uniform mesh. Each particle was enclosed in a shell of 0.5 nm thickness with a refractive index of 1.46 to emulate PEG. The PDMS substrate was modeled as a smooth surface with a refractive index of 1.4. For gold, tabulated data by Johnson and Christy was used [43]. For the calculation of extinction cross-sections, a polarized plane-wave source was injected at normal incidence in a range of 400 to 900 nm. Two orientations of the cluster (0° and 90° rotation) have been considered and averaged. The enhancement factor (EF) of SERS was defined as the product of the enhancements of the field intensity $|E|^2/|E_0|^2$ at the incident wavelength of excitation and at the corresponding Stokes-shifted frequency of the vibrational mode of interest (Equation (5.1)). The electric-field enhancements have been calculated from the surface integral of the intensity enhancement on the surface of the NPs and normalized by the total number of particles per μm^2. The surface-averaged electric field $|E|^2/|E_0|^2$ was defined as

$$\left\langle \frac{|E|^2}{|E_0|^2} \right\rangle = \frac{\int\int \frac{|E|^2}{|E_0|^2} dS}{dS}. \tag{5.2}$$

Since the experimental light source is a partially depolarized beam, an average of different

polarizations and their respective cluster rotations was considered in this case. For the isolated cluster, a total-field scattered-field (TFSF) source with the same intensity by unit area was used for the periodic system to calculate the absorption cross-section.

$$EF = \frac{|E_{\mathrm{loc}}(\lambda_{\mathrm{exc}})|^2}{|E_0(\lambda_{\mathrm{exc}})|^2} . \frac{|E_{\mathrm{sca}}(\lambda_{\mathrm{sca}})|^2}{|E_0(\lambda_{\mathrm{sca}})|^2} \tag{5.3}$$

5.4.11 Measurement of the interparticle distance

The interparticle distance (IPD) was evaluated from e-SEM images. Direct measurement of the gaps is highly challenging owing to the resolution limit of the environmental SEM and the sampleâs susceptibility to accumulate charges. For this reason, we evaluated the gap sizes indirectly by measuring linear oligomers within clusters, i.e., lines/chains of particles. By preferentially measuring the length of particle lines oriented along the direction of stretching, we studied the impact of substrate deformation (by unidirectional stretching) on the average interparticle distances within clusters (e.g., sample at 30% elongation, **Appendix III.2**). Each line corresponds to a separate determination of the gap size IPD with its respective uncertainty. The description implies equal distributed gap sizes within each measured line as calculated by

$$IPD = (k-1)^{-1}(L - \sum_{L=1}^{k} D_j)(k-1)^{-1}(L - k\langle D\rangle), \tag{5.4}$$

where L is the total measured length of the respective line, composed of k particles of diameters D_j. The gap sizes per line are determined by the sum over all gaps per line, this is the difference of each line length L and the presumed length contribution by k particles $\sum D_j \approx k\langle D\rangle$, divided by the number of gaps $k-1$. Averaging the gap sizes of all lines with the same number of particles, consisting of $(k1)m_k$ gaps, yields

$$\langle IPD_k\rangle = ((k-1)m_k)^{-1} \sum_{j=1}^{m_k} (L_{\mathrm{kj}} - k\langle D\rangle), \tag{5.5}$$

with $L_{\mathrm{k}}j$ being the length of the m_k individual chains with k particles. The uncertainty of $\langle IPD_k\rangle$ from (5.5) can be calculated by error propagation as

$$\Delta\langle IPD_k\rangle = ((k-1)m_k)^{-1}\sqrt{(}m_k(\Delta L)^2 + km_k(\Delta)^2). \tag{5.6}$$

Equation S4 considers $\langle D \rangle$ as a statistical quantity with the variation $\Delta\langle D \rangle = \Delta D/\sqrt{k}$ and that the error of chain length determination ΔL is the same for all chains. ΔL is mostly driven by the resolution of e-SEM, and we assume a realistic value of $\Delta L = 1$ nm for all lines. The uncertainty of the particle size derived from TEM imaging was determined to $\Delta D = 2.4$ nm (cf. **Appendix III.2**). The ratio between the term corresponding to D and the one corresponding to L under the square root in (5.6) ranges from 17 to 35 for chain lengths between 3 and 6 particles, as in the present case. The contribution of the length error can thus be neglected, resulting in

$$\Delta\langle IPD_k \rangle = (k-1)^{-1}\sqrt{(\frac{k}{m_k})}\Delta D. \tag{5.7}$$

(5.5) leads to the averaged interparticle distance over all gaps and all chains

$$\langle IPD \rangle = Ng^{-1}\sum_k (k-1)m_k\langle IPD_k \rangle, \tag{5.8}$$

thereby taking into account the total number of gaps $N_g = \Delta_k(k1)m_k$. Error propagation delivers the final uncertainty of the averaged gaps from the complete sample.

$$\Delta\langle IPD \rangle = N_g^{-1}\sqrt{\sum_k ((k-1)m_k)^2\Delta\langle IPD_k \rangle^2} \tag{5.9}$$

Inserting Equation (5.6) into (5.8) yields the uncertainty of the total averaged interparticle distance $\langle IPD \rangle$ just by the error ΔD of the particle size and represents a weighted standard error of ΔD,

$$\Delta\langle IPD \rangle = N_g^{-1}\Delta D\sqrt{\sum_k km_k}, \tag{5.10}$$

where the summation again is over all chain lengths (number of particles k). The obtained results are plotted in **Appendix III.2**.

Bibliography

[1] Mathias Charconnet, J. L.-M. L. M., Christian Kuttner Mechanically Tunable Lattice-Plasmon Resonances by Self-Assembled Superlattices for Surface-Enhanced Raman Spectroscopy. *Adv. Funct. Mater.* **Submitted, December 2020**,

[2] Müller, M. B.; Kuttner, C.; König, T. A. F.; Tsukruk, V. V.; Förster, S.; Karg, M.; Fery, A. Plasmonic library based on substrate-supported gradiential plasmonic arrays. *ACS Nano* **2014**, *8*, 9410–9421.

[3] Volk, K.; Fitzgerald, J. P.; Ruckdeschel, P.; Retsch, M.; König, T. A.; Karg, M. Reversible Tuning of Visible Wavelength Surface Lattice Resonances in Self-Assembled Hybrid Monolayers. *Adv. Opt. Mater.* **2017**, *5*.

[4] Kuttner, C.; Mayer, M.; Dulle, M.; Moscoso, A.; López-Romero, J. M.; Förster, S.; Fery, A.; Pérez-Juste, J.; Contreras-Cáceres, R. Seeded Growth Synthesis of Gold Nanotriangles: Size Control, SAXS Analysis, and SERS Performance. *ACS Applied Materials and Interfaces* **2018**, *10*, 11152–11163.

[5] Sánchez-Iglesias, A.; Grzelczak, M.; Altantzis, T.; Goris, B.; Pérez-Juste, J.; Bals, S.; Van Tendeloo, G.; Donaldson, S. H.; Chmelka, B. F.; Israelachvili, J. N.; Liz-Marzán, L. M. Hydrophobic interactions modulate self-assembly of nanoparticles. *ACS Nano* **2012**, *6*, 11059–11065.

[6] Taladriz-Blanco, P.; Buurma, N. J.; Rodríguez-Lorenzo, L.; Pérez-Juste, J.; Liz-Marzán, L. M.; Hervés, P. Reversible assembly of metal nanoparticles induced by penicillamine. Dynamic formation of SERS hot spots. *J Mater Chem* **2011**, *21*, 16880–16887.

[7] Kruse, J.; Merkens, S.; Chuvilin, A.; Grzelczak, M. Kinetic and Thermodynamic Hysteresis in Clustering of Gold Nanoparticles: Implications for Nanotransducers and Information Storage in Dynamic Systems. *ACS Appl. Nano Mater.* **2020**, *3*, 9520–9527.

[8] Cole, R. M.; Mahajan, S.; Baumberg, J. J. Stretchable metal-elastomer nanovoids for tunable plasmons. *Appl. Phys. Lett.* **2009**, *95*, 1–4.

[9] Peng, J.; Jeong, H. H.; Lin, Q.; Cormier, S.; Liang, H. L.; De Volder, M. F.; Vignolini, S.; Baumberg, J. J. Scalable electrochromic nanopixels using plasmonics. *Sci. Adv.* **2019**, *5*, 1–9.

[10] Tokareva, I.; Minko, S.; Fendler, J. H.; Hutter, E. Nanosensors based on responsive polymer brushes and gold nanoparticle enhanced transmission surface plasmon resonance spectroscopy. *J. Am. Chem. Soc.* **2004**, *126*, 15950–15951.

[11] Kang, H.; Heo, C. J.; Jeon, H. C.; Lee, S. Y.; Yang, S. M. Durable plasmonic cap arrays on flexible substrate with real-time optical tunability for high-fidelity SERS devices. *ACS Applied Materials and Interfaces* **2013**, *5*, 4569–4574.

[12] Aksu, S.; Huang, M.; Artar, A.; Yanik, A. A.; Selvarasah, S.; Dokmeci, M. R.; Altug, H. Flexible plasmonics on unconventional and nonplanar substrates. *Adv. Mater.* **2011**, *23*, 4422–4430.

[13] Zhang, C.; Jing, J.; Wu, Y.; Fan, Y.; Yang, W.; Wang, S.; Song, Q.; Xiao, S. Stretchable All-Dielectric Metasurfaces with Polarization-Insensitive and Full-Spectrum Response. *ACS Nano* **2020**, *14*, 1418–1426.

[14] Wang, D.; Bourgeois, M. R.; Lee, W. K.; Li, R.; Trivedi, D.; Knudson, M. P.; Wang, W.; Schatz, G. C.; Odom, T. W. Stretchable Nanolasing from Hybrid Quadrupole Plasmons. *Nano Lett.* **2018**, *18*, 4549–4555.

[15] Tseng, M. L.; Yang, J.; Semmlinger, M.; Zhang, C.; Nordlander, P.; Halas, N. J. Two-Dimensional Active Tuning of an Aluminum Plasmonic Array for Full-Spectrum Response. *Nano Lett.* **2017**, *17*, 6034–6039.

[16] Minati, L.; Chiappini, A.; Armellini, C.; Carpentiero, A.; Maniglio, D.; Vaccari, A.; Zur, L.; Lukowiak, A.; Ferrari, M.; Speranza, G. Gold nanoparticles 1D array as mechanochromic strain sensor. *Mater Chem Phys* **2017**, *192*, 94–99.

[17] Yang, A.; Hryn, A. J.; Bourgeois, M. R.; Lee, W.-K.; Hu, J.; Schatz, G. C.; Odom, T. W. Programmable and reversible plasmon mode engineering. *Proc. Natl. Acad. Sci.* **2016**, *113*, 14201–14206.

[18] Brasse, Y.; Gupta, V.; Schollbach, H. C.; Karg, M.; König, T. A.; Fery, A. Mechanotunable Plasmonic Properties of Colloidal Assemblies. *Adv. Mater. Interfaces* **2019**, *1901678*.

[19] Kuttner, C. Plasmonics in Sensing: From Colorimetry to SERS Analytics. *Plasmonics* **2018**,

[20] Graham, D. et al. Theory of SERS enhancement: General discussion. *Faraday Discuss.* **2017**, *205*, 173–211.

[21] Černigoj, J.; Silvestri, F.; Stoevelaar, L. P.; Berzinš, J.; Gerini, G. Lattice Resonances and Local Field Enhancement in Array of Dielectric Dimers for Surface Enhanced Raman Spectroscopy. *Sci. Rep.* **2018**, *8*, 1–7.

[22] Hanske, C.; González-Rubio, G.; Hamon, C.; Formentín, P.; Modin, E.; Chuvilin, A.; Guerrero-Martínez, A.; Marsal, L. F.; Liz-Marzán, L. M. Large-Scale Plasmonic Pyramidal Supercrystals via Templated Self-Assembly of Monodisperse Gold Nanospheres. *J Phys Chem C* **2017**, *121*, 10899–10906.

[23] Hanske, C.; Hill, E. H.; Vila-Liarte, D.; González-Rubio, G.; Matricardi, C.; Mihi, A.; Liz-Marzán, L. M. Solvent-Assisted Self-Assembly of Gold Nanorods into Hierarchically Organized Plasmonic Mesostructures. *ACS Applied Materials & Interfaces* **2019**, *11*, 11763–11771.

[24] Matricardi, C.; Hanske, C.; Garcia-Pomar, J. L.; Langer, J.; Mihi, A.; Liz-Marzán, L. M. Gold Nanoparticle Plasmonic Superlattices as Surface Enhanced Raman Spectroscopy Substrates. *ACS Nano* **2018**, *12*, 8531–8539.

[25] Steiner, A. M.; Mayer, M.; Seuss, M.; Nikolov, S.; Harris, K. D.; Alexeev, A.; Kuttner, C.; König, T. A.; Fery, A. Macroscopic Strain-Induced Transition from Quasi-infinite Gold Nanoparticle Chains to Defined Plasmonic Oligomers. *ACS Nano* **2017**, *11*, 8871–8880.

[26] Dogru, S.; Aksoy, B.; Bayraktar, H.; Alaca, B. E. Poisson's ratio of PDMS thin films. *Polym Test* **2018**, *69*, 375–384.

[27] Mitomo, H.; Horie, K.; Matsuo, Y.; Niikura, K.; Tani, T.; Naya, M.; Ijiro, K. Active Gap SERS for the Sensitive Detection of Biomacromolecules with Plasmonic Nanostructures on Hydrogels. *Adv. Opt. Mater.* **2016**, *4*, 259–263.

[28] Fan, J. A.; Bao, K.; Sun, L.; Bao, J.; Manoharan, V. N.; Nordlander, P.; Capasso, F. Plasmonic mode engineering with templated self-assembled nanoclusters. *Nano Lett.* **2012**, *12*, 5318–5324.

[29] Jain, P. K.; Huang, W.; El-Sayed, M. A. On the universal scaling behavior of the distance decay of plasmon coupling in metal nanoparticle pairs: A plasmon ruler equation. *Nano Lett.* **2007**, *7*, 2080–2088.

[30] Kravets, V. G.; Kabashin, A. V.; Barnes, W. L.; Grigorenko, A. N. Plasmonic Surface Lattice Resonances: A Review of Properties and Applications. *Chem. Rev.* **2018**, *118*, 5912–5951.

[31] Ross, M. B.; Mirkin, C. A.; Schatz, G. C. Optical Properties of One-, Two-, and Three-Dimensional Arrays of Plasmonic Nanostructures. *J Phys Chem C* **2016**, *120*, 816–830.

[32] Hessel, A.; Oliner, A. A. A New Theory of Wood's Anomalies on Optical Gratings. *Appl. Opt.* **1965**, *4*, 1275.

[33] Humphrey, A. D.; Barnes, W. L. Plasmonic surface lattice resonances in arrays of metallic nanoparticle dimers. *Journal of Optics (United Kingdom)* **2016**, *18*, 35005.

[34] Gupta, V.; Probst, P. T.; Goßler, F. R.; Steiner, A. M.; Schubert, J.; Brasse, Y.; König, T. A.; Fery, A. Mechanotunable Surface Lattice Resonances in the Visible Optical Range by Soft Lithography Templates and Directed Self-Assembly. *ACS Applied Materials and Interfaces* **2019**, *11*, 28189–28196.

[35] Kravets, V. G.; Schedin, F.; Grigorenko, A. N. Extremely narrow plasmon resonances based on diffraction coupling of localized plasmons in arrays of metallic nanoparticles. *Phys. Rev. Lett.* **2008**, *101*, 1–4.

[36] Höller, R. P. M.; Kuttner, C.; Mayer, M.; Wang, R.; Dulle, M.; Contreras-Cáceres, R.; Fery, A.; Liz-Marzán, L. M. Colloidal Superstructures with Triangular Cores: Size Effects on SERS Efficiency. *ACS Photonics* **2020**, *7*, 1839–1848.

[37] Tran, V.; Thiel, C.; Svejda, J. T.; Jalali, M.; Walkenfort, B.; Erni, D.; Schlücker, S. Probing the SERS brightness of individual Au nanoparticles, hollow Au/Ag nanoshells, Au nanostars and Au core/Au satellite particles: Single-particle experiments and computer simulations. *Nanoscale* **2018**, *10*, 21721–21731.

[38] Dregely, D.; Hentschel, M.; Giessen, H. Excitation and tuning of higher-order fano resonances in plasmonic oligomer clusters. *ACS Nano* **2011**, *5*, 8202–8211.

[39] Thackray, B. D.; Kravets, V. G.; Schedin, F.; Auton, G.; Thomas, P. A.; Grigorenko, A. N. Narrow Collective Plasmon Resonances in Nanostructure Arrays Observed at Normal Light Incidence for Simplified Sensing in Asymmetric Air and Water Environments. *ACS Photonics* **2014**, *1*, 1116–1126.

[40] Ponomareva, E.; Volk, K.; Mulvaney, P.; Karg, M. Surface Lattice Resonances in Self-Assembled Gold Nanoparticle Arrays: Impact of Lattice Period, Structural Disorder, and Refractive Index on Resonance Quality. *Langmuir* **2020**, *36*, 13601â13612.

[41] Fraire, J. C.; Pérez, L. A.; Coronado, E. A. Cluster size effects in the surface-enhanced raman scattering response of ag and Au nanoparticle aggregates: Experimental and theoretical insight. *J Phys Chem C* **2013**, *117*, 23090–23107.

[42] Qin, D.; Xia, Y.; Whitesides, G. M. Soft lithography for micro- and nanoscale patterning. *Nat Protoc* **2010**, *5*, 491–502.

[43] Johnson, P. B.; Christy, R. W. Optical Constants of the Noble Metals. *Phys. Rev. B* **1972**, *6*, 4370–4379.

Chapter 6

Real-time SERS sensing by polymer coating of plasmonic substrates and removal through thermoplasmonic effects

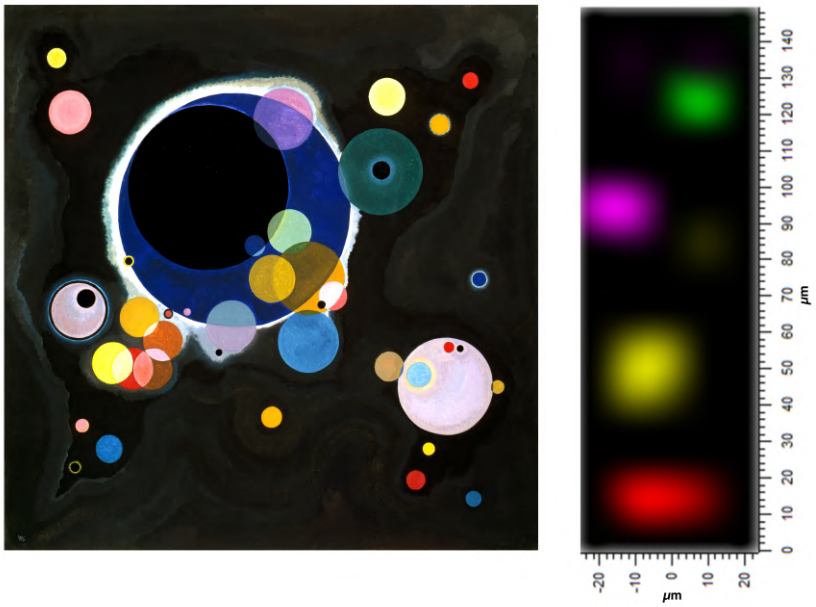

Figure 6.1: On the left: "Wassily Kandinsky (1866-1944), Several Circles, 1926" by Tulip Hysteria / Go to albums, under Creative Common public domain mark 1.0. On the right: SERS map of a plasmonic substrate functionalized with different molecules, each color represents the detection of a different analyte.

Abstract

The need for continuous monitoring systems requires the development of sensing devices capable of screening multiple chemical species directly at the point of care. As a technique for the non-invasive detection of chemicals at low concentrations, Raman spectroscopy appears as a technique of choice for resolving in situ chemical or biological processes. Thanks to the use of a plasmonic substrate, SERS allows for the detection of chemicals up to the single-molecule limit. However, in the context of real-time monitoring, SERS suffers from the irreversible adsorption of molecules on the plasmonic surface, which hinders the subsequent detection of other molecules. This so-called memory effect leads to inaccuracies in the monitoring of dynamic processes. In this chapter, a solution to the memory effect, based on the protection of the plasmonic material by a laser-removable polymer, is presented. In this regard, a PLGA thin layer is deposited on top of a plasmonic substrate, and thanks to the thermal degradability of PLGA, it can be removed by laser irradiation, mediated by the thermoplasmonic properties of the plasmonic substrate. This approach, which leaves a hole in the polymer layer upon laser irradiation, allows for the unveiling of the NPs and therefore enables SERS measurement through the created hole. Notably, thanks to the spatial resolution of the hole generation, it is possible to perform more than 10000 measurements using a single substrate and to monitor changes in a solution over time by the PLGA-SERS method. The content of this chapter was filed as patent application the 21st of December 2020, entitled Layered substrate and uses thereof (EP20383131.8).

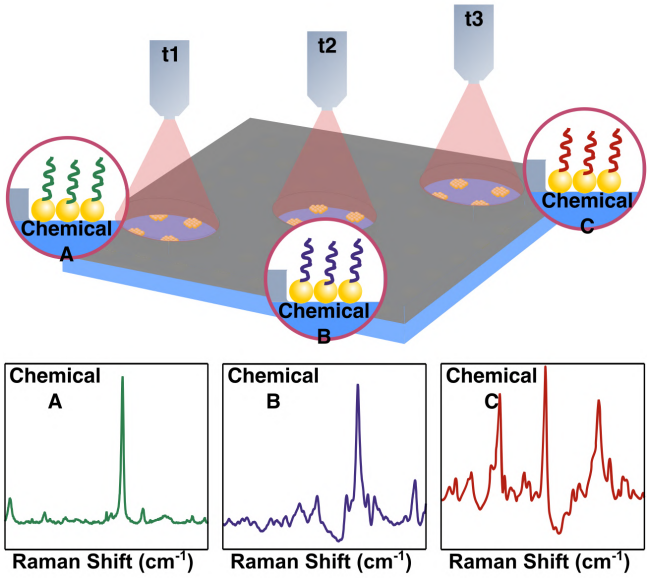

6.1 Introduction

6.1.1 Real-time SERS sensing and SERS memory effect

SERS has proven to be a technique of choice for the multiplexed detection of trace analytes in different applications going from medical diagnosis to environmental monitoring [1, 2]. Furthermore, as a non-invasive and label-free monitoring method, SERS is an ideal candidate for in situ sensing. However, real-time SERS detection constitutes a complex yet very rewarding challenge that would grant access to chemical information of a solution at a given time [3, 4]. Consequently, real-time SERS measurements in flows would allow for better water quality control, for instance by detecting the presence of pesticides or estrogens in tap water [5, 6, 7]. Still, for real-time SERS sensing one of the main limitations comes from the irreversible adsorption of analytes on the surface of nanoparticles: by the time molecules adsorb on the surface of the plasmonic particles, their desorption becomes difficult [8, 9]. As a consequence, the Raman signal of such molecules is still visible even at later stages after incubation, interfering in subsequent measurements. Such an effect, known as the memory effect, hinders real-time detection with the standard SERS strategy, where the analyte solution is continuously in contact with the plasmonic substrate. Using this standard strategy, the main approach to monitor changes in a solution consists of using a virgin substrate to detect the analytes at a given time. Yet, this strategy is not satisfactory enough as it does not allow for continuous SERS measurements and demands the use of a new substrate for each measurement point.

6.1.2 Solution to the SERS memory effect

Different solutions have been proposed to render SERS substrates re-usable and therefore eligible for real-time sensing. The main strategy consists of cleaning the substrate from molecular adsorbates, after cleaning the substrate is in a pristine state and can be re-used for new measurements. For instance, in the case of sulfur-gold bonds, the use of oxidative species such as sodium hypochlorite has shown to be efficient for breaking gold-sulfur bonds responsible for covalent binding of thiolated analytes to gold nanoparticles [10]. Other approaches involve the incubation of the plasmonic substrate in a solvent that alters electrostatic interactions, so

that the analytes adsorbed through electrostatic interactions desorb and the plasmonic system can be recycled [11]. Though interesting, such techniques do not allow for in-situ measurements, as the substrates need to be removed from the solution of interest prior to cleaning by suitable chemicals. Other innovative examples use photocatalytic materials such as ZnO or TiO_2 coatings on plasmonic substrates, to degrade covalent bonds created between the SERS substrate and the analyte through photocatalytic processes [12, 13]. Though photocatalysis based methods enable real-time sensing, the time required to clean the substrate of adsorbed molecules is in the order of 10 minutes, therefore dynamic processes cannot be properly resolved using these methods. Using a similar concept, Belder and coworkers have shown in situ real-time SERS measurements in a microfluidic channel by electrical regeneration of a silver wire [14, 15]. Finally, the strategy followed by Gao et al. consists in the in situ synthesis of the nanoparticles directly in the microfluidic channel where the SERS measurement takes place. Consequently, for each measurement a new synthesis is carried out in the microfluidic channel. This approach enables real-time sensing by SERS in microfluidic channels, however, it requires high consumption of material and the contamination of the microfluidic channels by remaining nanoparticles can cause a memory effect interfering with subsequent measurements [16, 17].

6.1.3 Plasmonic heating for the degradation of polymers

There exist a lot of thermodegradable polymers, indisputably one of the most studied ones is poly-lactic-co-glycolic acid (PLGA). The degradation of PLGA by hydrolysis is accelerated at high temperature and leaves lactic and glycolic acid as side products [18, 19]. In **Section 2.4.4**, it has been shown that plasmonic nanoparticles can generate heat when excited by a laser at their plasmon resonance. Therefore, plasmonic nanoparticles can be used as a heat source for the degradation of polymers, for instance. Gupta et al. have demonstrated the laser-induced PLGA degradation by incorporating gold nanorods within the polymeric material. The stimuli-responsive PLGA erosion occurred because of the photothermal response of the Au NRs when irradiated with a resonant laser [20, 21].

In this chapter, a PLGA thin-layer is applied to gold nanoparticle superlattices, protecting the gold nanoparticles from analyte absorption. Irradiation of the PLGA-coated superlattices

by a focused laser beam enables the formation of a hole in the layer due to the thermoplasmonic effect, rendering the nanoparticles available to the exterior environment and particularly to analytes. As a consequence, the presence of analytes can be monitored by SERS after the generation of a hole in the PLGA layer. Measurements at arbitrary times can then be done by the subsequent generation of new holes. The PLGA-SERS method renders real-time SERS sensing possible with any SERS substrate available, as will be shown throughout the chapter.

6.2 Results

6.2.1 SERS memory effect

As an illustration of the SERS memory effect, SERS spectra from a pristine plasmonic superlattice were recorded after incubation in 4-MBA, then in nicotinamide, and finally in a 50:50 mixture of both 4-MBA and nicotinamide (see **Figure 6.2**). During the initial incubation with a 4-MBA solution, a characteristic 4-MBA vibration at 1078 cm^{-1}, assigned as a $\nu 12$ aromatic ring vibration (red highlighted region), was unequivocally detected. However, such plasmonic superlattices could not be reused, even after rinsing the same substrate with water and incubating it with nicotinamide, the peak from 4-MBA was still present in the SERS spectrum, while no peak associated to nicotinamide was observed (normally expected at the position marked in orange color in the spectra of **Figure 6.2**). In the same way, adding a mixture of 4-MBA + nicotinamide, posterior to the 4-MBA incubation, did not allow for nicotinamide detection. From these data, it could be concluded that molecules cannot be efficiently removed by rinsing the sample with water, and on this account, the irreversible adsorption of 4-MBA impedes the molecules of nicotinamide to interact with the NPs present on the plasmonic substrate. This experiment reflects what happens in most attempts for real-time sensing and constitutes the unwanted SERS memory effect.

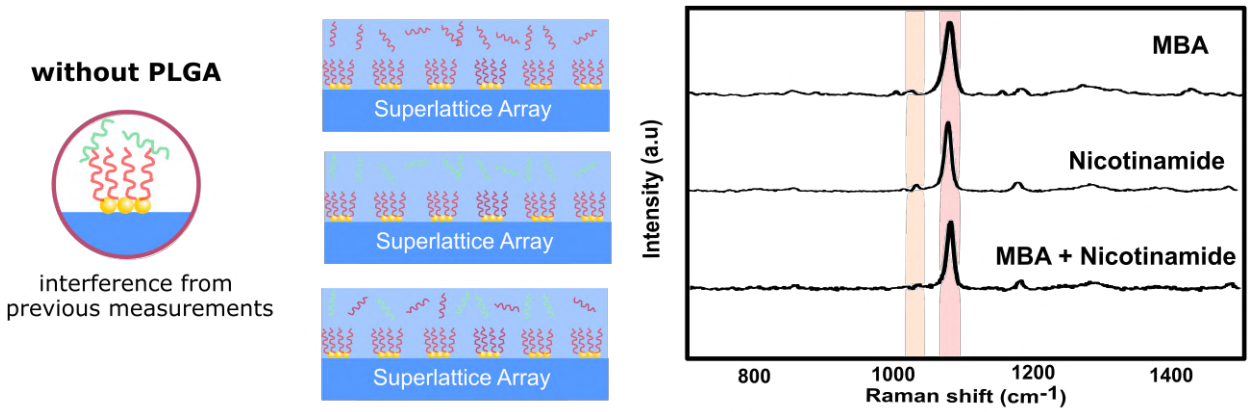

Figure 6.2: Sequential SERS measurements of different analytes with a gold nanosphere superlattice as SERS substrate without PLGA layer. On the left: Sketch of molecules interacting with the superlattice, first the sample is incubated with a 4-MBA solution, nicotinamide is subsequently added, however, nicotinamide molecules are blocked by 4-MBA previously absorbed on the NPs, the same happens with a 50:50 mixture of 4-MBA and nicotinamide. On the right: SERS spectra after adding the different analytes on the SERS substrate.

6.2.2 Resolution of the SERS memory effect by the PLGA-SERS method

As a solution to the unwanted SERS memory effect, and in general, to single-use SERS substrates, a polymer protecting gold NPs and readily removable by laser exposition is added on top of the gold NP superlattice. Removal of the polymer layer renders NPs available for interaction with the incubation solution, and therefore removal of the polymer constitutes an active stimulus for SERS measurement. Especially, temporal control of the polymer removal would enable real-time SERS measurements. Poly-Lactic-co-Glycolic acid has been chosen as a polymer coating the plasmonic substrate for its thermodegradable properties, low-cost and biocompatibility. To create a thin film of PLGA on top of the gold NPs superlattice, PLGA was dissolved in acetone or ethyl acetate, to obtain a 12 wt% solution, and spin-coated at 1500 rpm on top of the superlattice (more details are provided in materials and methods section). The choice of an appropriate solvent is essential to get a perfect coverage of the plasmonic superlattice, indeed using acetone only a partial coverage was achieved, whereas when PLGA was dissolved in ethyl acetate and spin-coated, the whole substrate was covered with a thin layer of

around 1.5 µm as measured by SEM cross-sections (**Appendix III.1 a,b)**). Perfect coverage of the plasmonic superlattice is necessary so that the whole substrate is impermeable to the analyte solution, as displayed by the absence of analytes detections by SERS using the sample with perfect PLGA coverage (**Appendix III.1 c,d**).

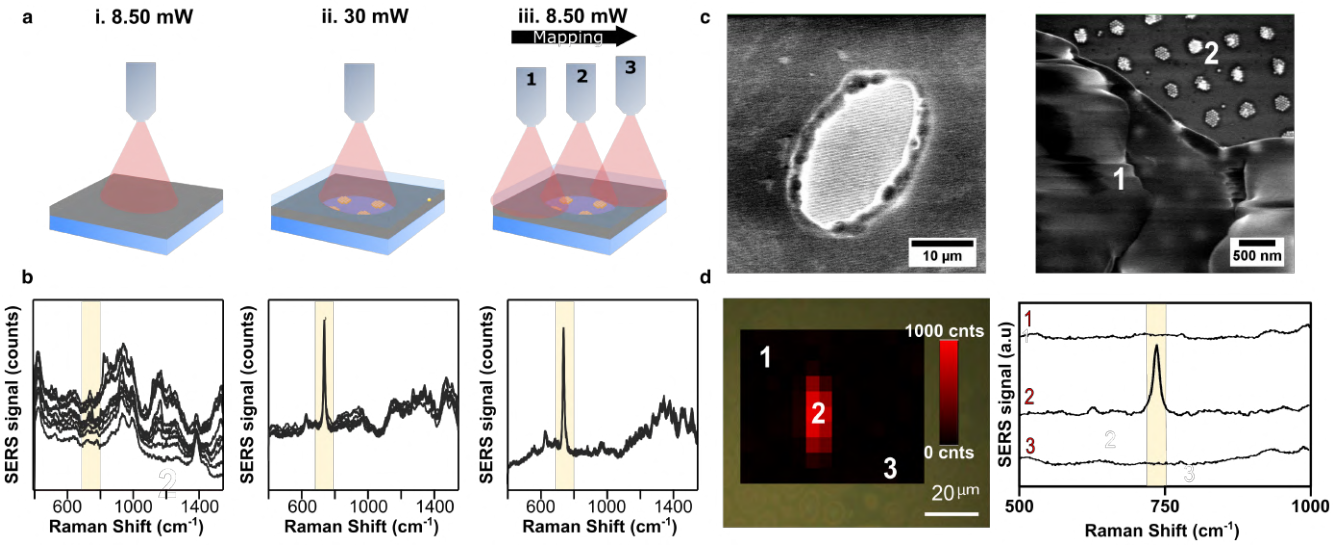

Figure 6.3: a) Scheme of the sensing route using the PLGA-coated plasmonic substrate, 0.03 mW/µm^2 doesnt́ harm the PLGA layer. First, the superlattice is irradiated with a 785 nm laser at a laser irradiance of 0.11 mW/µm^2 generating a hole in the PLGA layer, then 0.03 mW/µm^2 laser irradiance can be used to make a SERS map of the previously created hole. b) SERS spectra of adenosine after each step of the sensing route, SERS signal of adenosine is only seen after the generation of a hole. c) SEM images of a hole created in the PLGA layer using a 785 nm laser at 0.11 mW/µm^2 irradiance. d) SERS map after hole creation, in the presence of an adenosine solution. Scalebar accounts for the signal at 735 cm^{-1}. On the right, we can see SERS spectra in regions 1 and 3 (where PLGA remains) and in region 2 (where PLGA was degraded).

To alter the impermeability of the PLGA coated SERS substrate, the strategy consists of creating a hole in the PLGA layer. Generation of a hole in the PLGA layer takes advantage of the thermodegradable property of PLGA, which implies that PLGA can be degraded by heat into lactic acid and glycolic acid [18]. The creation of a hole results in the uncovering of the gold nanoparticles and therefore enables the interaction of molecules with the plasmonic component.

In our setup, the heat generated by plasmonic nanoparticles through light absorption is used as a heat source for the degradation of PLGA [22, 23]. The degradation of polymers by the thermoplasmonic properties of gold nanoparticles was also shown with other polymers such as PMMA, PET, or polycarbonate [24, 25]. Consequently, by using a laser excitation with a spot size of 20 x 10 µm, a local temperature increase can be generated to degrade the PLGA selectively in the irradiated area. Such localized plasmonic heating was validated by infrared thermal images, the obtained results showed a local temperature increase from 30 to 38 °C on the surface of the plasmonic superlattice excited with a 785 nm laser excitation at an irradiance of 0.11 mW/µm^2 (see **Appendix III.2**). No temperature increase was observed when the laser light was focused outside of the plasmonic superlattice, validating that heat comes from the gold nanoparticles and not from the laser alone. However, even though infrared images are significant to sense a temperature increase, such measurements do not reflect the exact temperature next to the NPs at the nanoscale, which is likely to be considerably higher [26, 27]. For instance, Käll and collaborators using anti-stokes thermometry, have shown that bowtie antennas can increase the local temperature of more than 100 °C resulting in the formation of nanobubbles when the bow-ties are in water [28].

Figure 6.3 a depicts the strategy to use PLGA-coated superlattices for SERS measurements. The approach consists of using the 785 nm laser excitation at two laser irradiance:

- First, an 'openning 'irradiance, which gives rise to a temperature increase sufficient to degrade locally the PLGA layer, is applied.
- Second, a 'reading'laser irradiance, which allows to perform the SERS measurement is applied. The laser irradiance should be high enough to perform the SERS measurement, however it should not be high enough to cause damage to the PLGA layer.

Generation of a hole in the PLGA layer favors the analyte molecules to diffuse towards the SERS substrate and therefore allows their detection by SERS. Identification of the 'opening irradiance was carried out by irradiating a PLGA-coated SERS substrate at different laser irradiance for 1 s, in the presence of an adenosine solution on top of the PLGA-coated plasmonic substrate. The presence of a SERS signal around 735 cm^{-1} after the laser irradiation will indicate the degradation of the polymer layer. At a laser irradiance of 0.03 mW/µm^2, no

SERS signal was detected (see **Figure 6.3 b**, indicating no degradation of the PLGA layer, consequently 0.03 mW/µm^2 was chosen as 'reading'irradiance. From this experiment, it can be concluded that the 'reading'laser irradiance is not intense enough to give rise to the generation of an efficient plasmonic heating to break the polymeric chains and create a hole in the PLGA layer. Subsequently, the sample was irradiated at a higher laser irradiance of 0.11 mW/µm^2 for 1s, leaving a hole in the PLGA layer due to degradation of the polymeric chains through plasmonic heating, as evidenced by the presence of a SERS signal at 735 cm^{-1} (see **Figure 6.3 b**). Generation of a hole in the PLGA layer by laser irradiation was further confirmed by SEM images, the hole was found to have an elliptical shape of 20 µm × 10 µm (see **Figure 6.3 c**). By the time of the hole creation, SERS signal from adenosine was detected (**Figure 6.3 b**) on account of the diffusion adenosine molecules through the recently generated hole, to the gold nanoparticles. Finally, the 'reading'laser irradiance was used to perform SERS mapping of the opened hole. A SERS map of the region taken in the SEM images revealed that the Raman signal due to adenosine was only visible in zone 2, where the hole was created in the PLGA layer, while zones 1 and 3, corresponding to parts of the substrate coated with PLGA, did not provide any signal (**Figure 6.3 d**). Here, the reading laser fluence was used during the SERS scanning to avoid the unnecessary degradation of the PLGA layer. Importantly, the time needed to generate a hole is very short (1 s), allowing for a rapid hole generation in different places of the substrate. Such a feature will be important for real-time sensing as will be shown in the next section.

Finally, the same sequential measurement as with the bare plasmonic sample was applied to the PLGA-coated plasmonic sample. In Brief, the PLGA-coated substrate was sequentially incubated in 4-MBA, nicotinamide, and 50:50 mixture solution of 4-MBA and nicotinamide. For each analyte, the laser focus was moved to a virgin region thanks to a piezoelectric controller, and a new hole was generated in the PLGA-coated substrate to perform a new SERS measurement. All the changes in solutions could be detected by the PLGA-SERS method. As shown in **Figure 6.4**, not only the characteristic peak of 4-MBA molecule around 1078 cm^{-1}, was detected, but also during the subsequent nicotinamide incubations, the nicotinamide peak at 1032 cm^{-1}, assigned to a δ_{12} ring vibration, could be monitored. Furthermore, 4-MBA and nicotinamide were also detected using a 50:50 mixture of both analytes. This experiment un-

derlines the efficiency of the PLGA-SERS method to overcome the SERS memory effect.

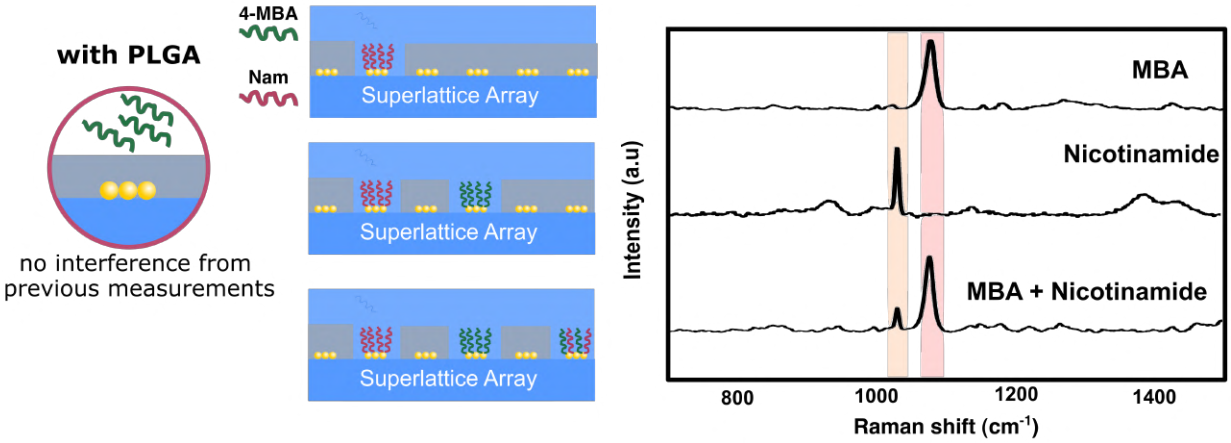

Figure 6.4: Sequential SERS measurements of different analytes with a PLGA-coated plasmonic superlattice. On the left: sketch of molecules interacting with the superlattice. First, 4-MBA molecules are introduced and bind to gold NPs, nicotinamide molecules are then added, but nicotinamide is blocked by 4-MBA absorbed on the NPs, the same happens with a mixture of 4-MBA and nicotinamide (Nam). After each analyte addition, a hole is created in the PLGA layer to allow interaction of the solution with the revealed area. On the right: SERS spectra after adding different analytes on the SERS substrate.

6.2.3 Transferability of the PLGA-SERS method to other samples

Until now, the PLGA-SERS method was only implemented with plasmonic superlattices, which are ideal SERS sensing platforms, but their fabrication is not straightforward. In this section, the use of the PLGA-SERS method is extended to dried droplets of a gold nanoparticle solution, to show the versatility of the method. Such samples were chosen because they feature a very simple fabrication process that can be easily reproduced in any chemistry laboratory without special equipment. SEM images of the dried droplet of gold nanoparticles, found in **Appendix III.3**, display randomly organized clusters of gold nanoparticles.

The applicability of the PLGA-SERS method to a disorganized sample was tested by following the same strategy as in the previous section. Thus, the SERS maps before and after application of the laser at the 'opening'irradiance were recorded. Remarkably, the obtained maps, shown in **Figure 6.5 a,b**, only display SERS signal of methylene blue after the irradi-

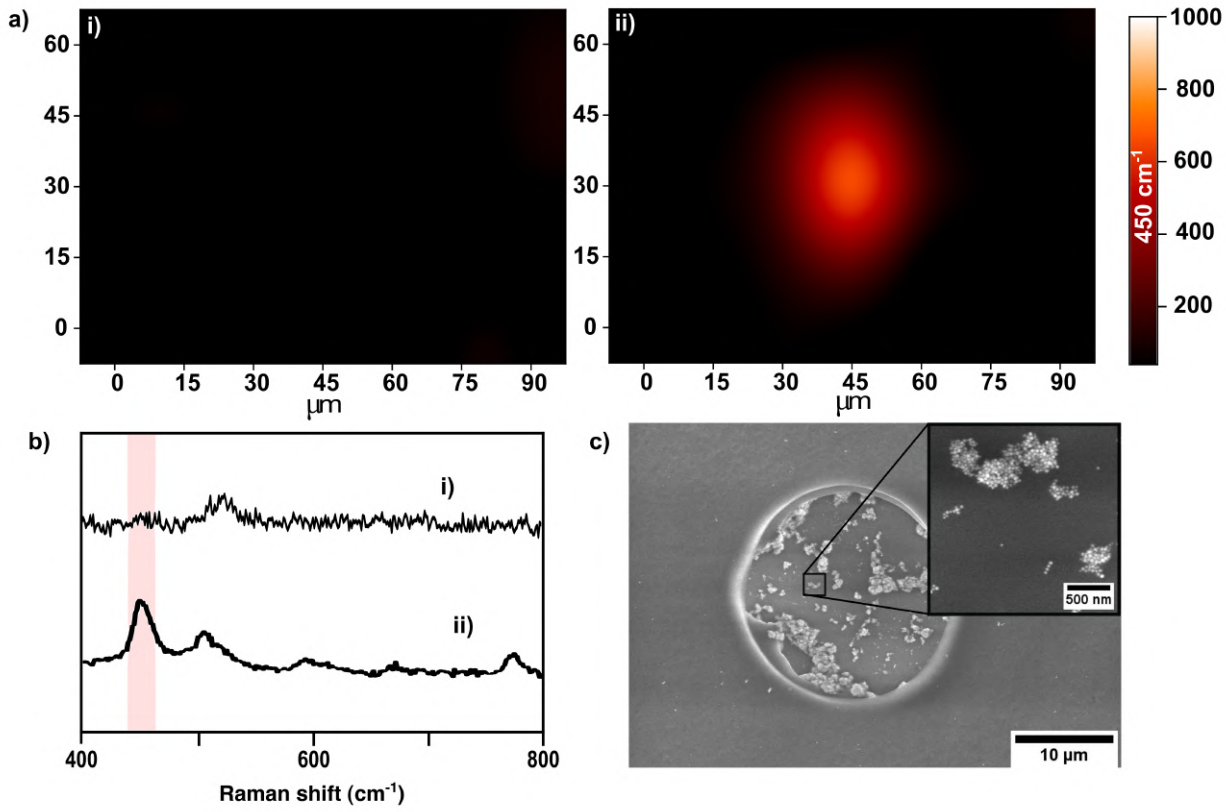

Figure 6.5: PLGA-SERS method application to a dried gold NPs droplet. SERS maps of a PLGA-coated dried droplet sample in the presence of methylene blue a) before and b) after the generation of a hole in the PLGA layer. c) SERS spectra corresponsing to the SERS maps. d) SEM images of a hole in the PLGA layer on top of a dried droplet sample.

ation at the hole generation irradiance. Accordingly, the SERS spectra corresponding to the two maps can be seen in **Figure 6.5 b**. The formation of a hole in the PLGA layer was further confirmed by SEM images in **Figure 6.5 c**. The fact that the PLGA-SERS method is transferable to simple plasmonic samples such as dried droplets of gold nanoparticles underlines the universality of the process. Along with the facile modification step of the substrate by spin coating of PLGA, it can be envisioned that such a method will open new sensing capabilities to a wide variety of SERS substrates.

6.2.4 Spatial resolution of the hole generation

For real-time SERS measurements, the PLGA-SERS strategy rely on the creation a hole at a virgin position of the coating at a defined time, to monitor the analytes present in the solution

at this specific time. To that end, the desired position of the hole is changed by moving the sample with a piezoelectric stage. Accordingly, the spatial resolution between the created holes must be small to be able to carry out several measurements at different times with one substrate. **Figure 6.6 a** displays a SERS map of a PLGA coated superlattices with two holes created 20 µm apart and in the presence of a nicotinamide solution. SERS signal of nicotinamide is only seen in the two created holes (see **Figure 6.6 b**). The good spatial resolution of the hole generation is attributed to the small size of the laser beam, as well as the precision of the piezoelectric stage from the Raman microscope.

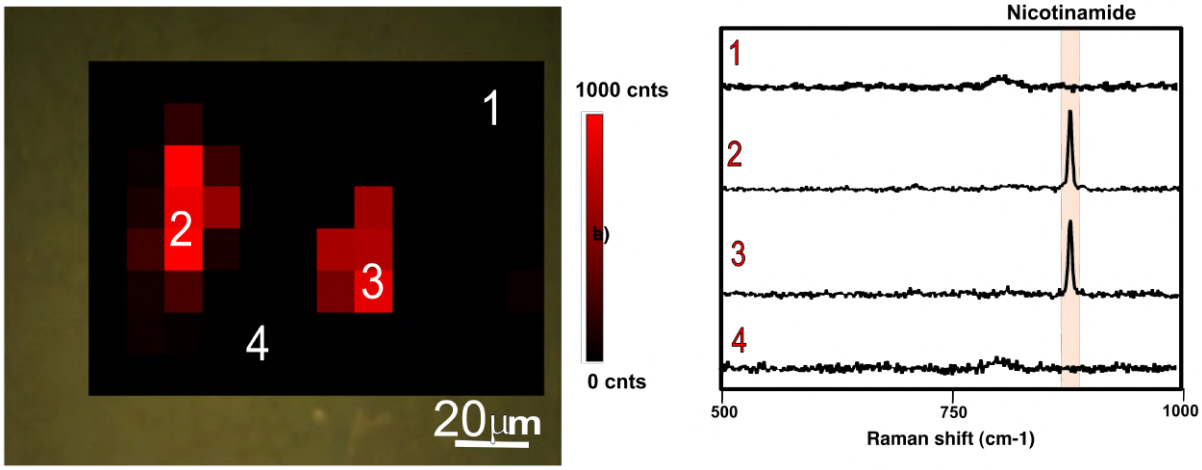

Figure 6.6: Spatial control of the hole formation on the PLGA layer. a) SERS map of a PLGA-coated superlattice with two holes created by laser irradiation, red colour represents the presence of nicotinamide. High resolution on the hole formation can be appreciated. b) SERS spectra taken at different position of the map. SERS signal of adenosine is only found in the region of the holes.

The micron-scale control on the hole formation can be used to create a new hole at a defined position each time a SERS measurement is needed. This idea is illustrated in **Figure 6.7**, for the multiplex SERS detection of different analytes. To that end, the analytes were chosen so that their Raman peaks are not overlapping, to dissociate them easily using their Raman components. The chosen analytes are 4-MBA with a vibrational fingerprint at 1084 cm^{-1}, assigned to the ν_{12} ring stretching, crystal violet with a vibrational fingerprint at 1183 cm^{-1}, assigned to C-H in plane deformation in the aromatic ring [29], thiabendazole with a vibrational fingerprint at 1015 cm^{-1}, assigned to a C-N stretching in the aromatic ring [30, 31], and nicotinamide wih

a Raman peak at 1032 cm^{-1}, assigned to the δ_9 aromatic ring bending [32].

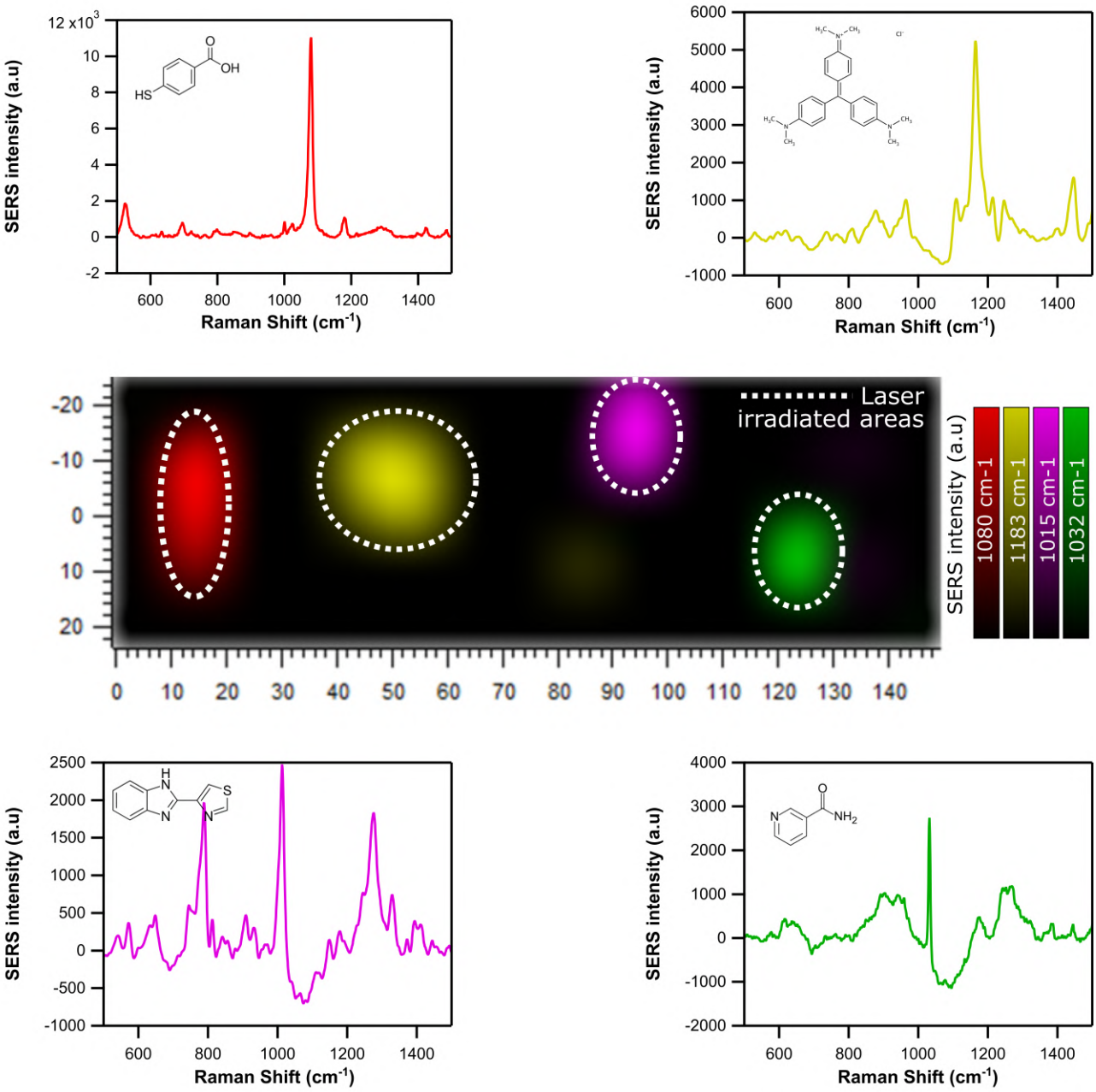

Figure 6.7: Multiplex SERS detection with high spatial resolution. SERS map of a superlattice with 4 holes created by laser irradiation (see text for details). The map was generated by integration of characteristic vibrational modes of 4-MBA at 1084 cm^{-1} (1), crystal violet at 1183 cm^{-1} (2), thiabendazole at 1015 cm^{-1} (3) and nicotinamide at 1032 cm^{-1} (4). The map was recorded using the "r"eading'laser irradiance with 1s integration time and a 50× objective.

The PLGA-coated plasmonic sample was incubated with analytes one by one; after the addition of an analyte solution a hole was generated using the 'opening'irradiance; after the

hole generation, the analyte solution was removed and the sample cleaned by flushing water over its surface. Once the sample was cleaned, a new analyte solution was added and a hole was created at a virgin position of the substrate. Such a process was repeated until the superlattice was incubated with all the analytes. In the end, the sample was left with 4 holes that were incubated in different solutions. The irradiated area was then mapped by SERS using the 'reading'laser irradiance. The resulting SERS map, shown in **Figure 6.7**, was generated by using the SERS intensities at the wavenumbers of the respective characteristic peaks for each analyte.

Only the laser-irradiated areas show a SERS signal, moreover, each hole presents the characteristic Raman spectra from the analyte present at the time of the hole generation. Thus, such a method allows for the perfect identification of the different analytes introduced on top of the PLGA-coated substrate. Remarkably, on 120 x 40 µm area 4 SERS measurements could be made. Given the size of the plasmonic substrate (1 x 1 cm^2) and the spatial resolution shown in the multiplexing experiment, it is theoretically possible to make around 20000 SERS measurements on one single sample. Moreover, with bigger plasmonic substrates and smaller laser spots it should be possible to make even more measurements on a single substrate.

6.2.5 Real-time sensing in microfluidic channels by the PLGA-SERS method

The short time needed to create a hole (1 s) along with the high spatial resolution of hole generation provided by the PLGA-SERS opens the possibility for the monitoring of dynamic processes by SERS without interferences from previous measurements. As a proof of concept, a PLGA-SERS substrate was implemented with a microfluidic device attached on top of the PLGA layer. The whole microfluidic plasmonic device was mounted along with a syringe pump system, in order to control the flow of analytes in the chip, as described in material and methods. A scheme of the experiment can be found in **Figure 6.8 a**.

For each new SERS measurement, the position of the sample is changed thanks to a piezoelectric stage to find a pristine region of the sample, a new hole is then created at this place for sensing the analyte in the solution at this precise time. Consequently the changes of analytes in

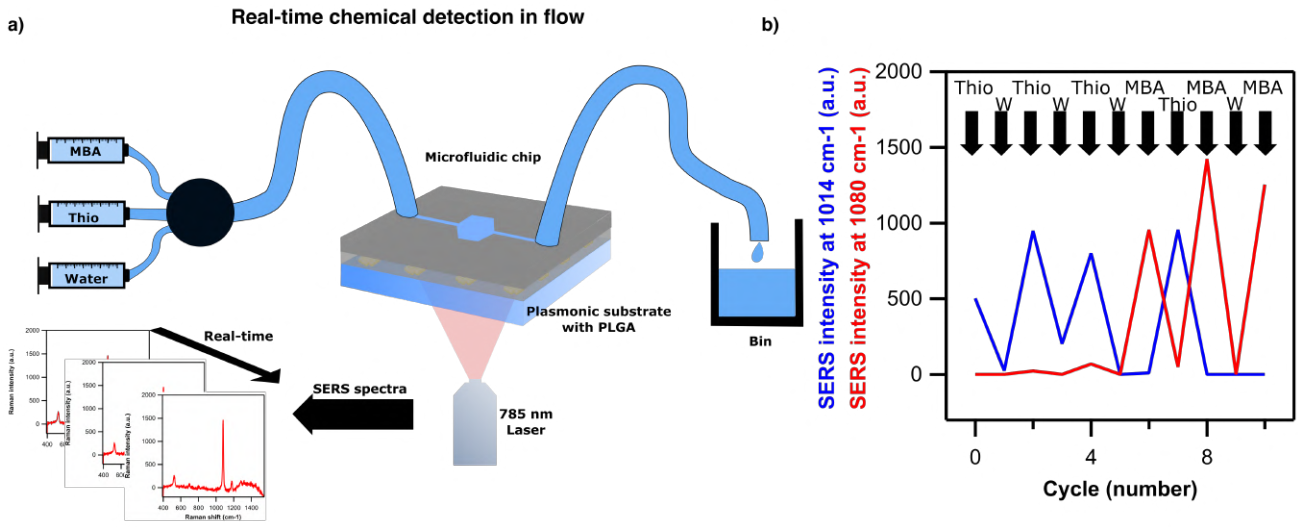

Figure 6.8: Real-time SERS monitoring in the channel of a microfluidic chip. a) Schematic view of the setup for SERS measurement in the microfluidic channel. b)SERS intensity of the characteristic mode of thiabendazole at 1014 cm^{-1} in red and 4-MBA at 1080 cm^{-1} in blue, as a function of the introduction cycles by the syringe pump, for a plasmonic superlattice coated with a PLGA sheathing layer. The black arrows on top of each graph represent the introduction of a different analyte solution (water, thiabendazole or 4-MBA) in the microfluidic channel at the indicated introduction cycle.

the microfluidic channel were followed using the PLGA-SERS method. As a result, it was found that the presence of analytes could be monitored in real-time within the microfluidic channel, on the basis of the most intense SERS peak from 4-MBA (at 1080 cm^{-1}) and thiabendazole (at 1014 cm^{-1}). Conversely, we used an uncoated plasmonic sample as control, again without using the PLGA layer, and the signal of the first molecule attached to the substrate is persistent (here MBA), even under water or thiabendazole flowing (see **Appendix III.4**). Using the PLGA layer, perfect identification of the analyte in the channel is achieved through the Raman measurement. This experiment constitutes a significant example of how SERS substrates could be used, for instance, for in situ detection of hazardous molecules in wastewater treatment plants.

6.2.6 Conclusion

The impossibility to make real-time SERS measurements using bare plasmonic substrates was clearly demonstrated in this chapter. As a solution to the memory effect, the plasmonic sub-

strates were modified with a PLGA coating layer that could be locally removed upon laser irradiation thanks to the thermoplasmonic properties of the plasmonic substrates. Due to the outstanding temporal and spatial resolution of the hole generation in the PLGA layer, the PLGA-SERS method proved to be an efficient method for real-time SERS sensing. Especially, the in-situ sensing of analytes flowing in a microfluidic channel was achieved using the PLGA-SERS method. Such an example might serve as a basis for the fabrication of a pesticide sensor in tap water for instance. Moreover, the great simplicity of the method along with the transferability to different plasmonic substrates will allow others to adopt this technology even with other plasmonic substrates. The different advantages of the PLGA-SERS methods show the great potential for its use to future real-time sensing applications.

6.3 Materials and methods

6.3.1 Chemicals

For the synthesis of gold nanoparticles $HAuCl_4 \cdot {}_3H_2O$ (≥99.9%, trace metal basis) was purchased from Alfa Aesar. Sodium borohydride (ReagentPlus©, ≥99%, $NaBH_4$), cetyl-trimethylammonium chloride (≥98%, CTAC), L-Ascorbic acid (ACS reagents, ≥99%, AA), poly(ethylene glycol) methyl ether thiol average Mn 6000 (PEG-6K), sodium hyprochlorite (6-14% active chlorine, Emplura©) were purchased from Sigma-Aldrich. All solutions, except $HAuCl_4$ and CTAB, were prepared directly before use. Purified Milli-Q water was used in all experiments (Millipore, 18.2 MΩ cm). Glassware was cleaned with aqua regia and rinsed extensively with Milli-Q water before use. Poly-lactic co-glycolic 75:25 (LA:GA) 25 000 Mn Acid endcap, Poly lactide co-glycolide 95:5 25 000 mn Acid endcap was purchased from Polysciences. Poly lactide co-glycolide 85:15 esther endcap was purchased from Sigma Aldrich.

6.3.2 Raman analytes

4-Nitrothiophenol (96%, NTP) was purchased from Alfa Aesar, Adenosine (suitable for cell culture), 4-Mercaptobenzoic acid (90%, 4-MBA), Thiabendazole (≥99% powder), Cristal Violet (dye content ≥ 90%) and Nicotinamide (≥98%,powder) was purchased from Sigma-Aldrich.

6.3.3 Synthesis, functionalization and self-assembly of gold nanoparticles

The synthesis and functionalization of gold nanospheres followed the method described in **Section 5.4.2**. The templated self-assembly of the gold nanospheres followed a similar process as described in **Section 5.4.5**. Briefly, a 2 µL droplet of a gold nanosphere solution (50 mM Au^0 35 nm gold nanospheres, 66% EtOH, 200 µM) was casted on top of a nanostructured PDMS mold. After 45 s waiting time, a glass substrate was added on top of the stamp. After 2 h and complete evaporation of the liquid, the PDMS template was carefully lifted off the flexible PDMS substrate. The resulting dried and nanostructured film consists of a nanoparticle superlattice representing the inverse structure of the template.

6.3.4 Fabrication of the disorganized sample

To fabricate disorganized samples of disordered Au nanoparticles, Au^0 dispersion (100 µL, 4 mM, 35 nm sized PEG-coated nanospheres) was drop-cast on a PDMS target substrate and allowed to dry for 3 hours at room temperature.

6.3.5 Fabrication of the PLGA coating

PLGA coatings were fabricated by spin coating a solution of PLGA on top of the nanoparticle superlattice. For this, the PLGA pellets were dissolved in ethanol or acetone to obtain a 12 wt% solution. After adding the pellets to the solvent, the solutions were mechanically stirred for 2 h. Subsequently, a 300 µL droplet was deposited on top of the plasmonic substrate such that it wetted the whole surface of the sample. The spin coating process was then started at a speed of 1500 rpm.

6.3.6 Microfluidic chip and synringe pump flow

PDMS Sylgard© 184 was purchased from Sigma-Aldrich, Microdevices were used according to the fabrication method described by Shin et al. Accordingly, soft lithography was used to develop positive SU8 240 µm relief patterns with the desired geometry on a silicon wafer.

Polydimethylsiloxane (PDMS, Sylgard 184, Dow Corning GmbH) was mixed at a 10:1 weight ratio of base to curing agent. The mixed solution was poured into the SU8 master and then degassed to remove air bubbles. Once the solution was cured, the replica-molded layer was trimmed, perforated, and autoclaved. The PDMS devices were then exposed to a plasma cleaning treatment (2 min) and subsequently bound to the PLGA-plasmonic substrate. The flow in the microfluidic channel was generated using a Cetoni Nemesys syringe pump using the low-pressure module. The flow was set at 10 000 µL/h and the outlet was connected to another syringe pump at the same flow rate of 10 000 µL/h

6.3.7 Characterization

Scanning electron microscopy was performed using an environmental SEM (FEI Quanta 250). The acceleration voltage of the electron beam was varied between 5 and 20 kV to obtain the images. Extra precaution was necessary to image the PLGA coated substrate because of an accumulation of charges at the surface even at low voltages. Already, at 20 kV (15000x magnification), degradation of the PLGA layer by the electron could be seen. For that reason, overview images were recorded at an acceleration voltage of 10 kV with an integration time of 1s per line at a magnification of 2500x. Detail images, resolving the NPs within the clusters, were taken at 20 kV with an integration time of 10 µs per line at a magnification of 30000x.

SERS spectra were collected with a confocal Raman microscope (Renishaw inVia) equipped with a 1024 x 512 CCD detector, and using a 785 nm laser excitation source.

Bibliography

[1] Gao, R.; Choi, N.; Chang, S. I.; Lee, E. K.; Choo, J. Real-time analysis of diaquat dibromide monohydrate in water with a SERS-based integrated microdroplet sensor. *Nanoscale* **2014**, *6*, 8781–8786.

[2] Alvarez-Puebla, R. A.; Agarwal, A.; Manna, P.; Khanal, B. P.; Aldeanueva-Potel, P.; Carbó-Argibay, E.; Pazos-Pérez, N.; Vigderman, L.; Zubarev, E. R.; Kotov, N. A.; Liz-Marzán, L. M. Gold nanorods 3D-supercrystals as surface enhanced Raman scattering

spectroscopy substrates for the rapid detection of scrambled prions. *Proc. Natl. Acad. Sci. USA* **2011**, *108*, 8157–8161.

[3] Lafuente, M.; Pellejero, I.; Clemente, A.; Urbiztondo, M. A.; Mallada, R.; Reinoso, S.; Pina, M. P.; Gandía, L. M. In Situ Synthesis of SERS-Active Au@POM Nanostructures in a Microfluidic Device for Real-Time Detection of Water Pollutants. *ACS Appl. Mater. Interfaces* **2020**, *12*, 36458–36467.

[4] Langer, J. et al. Present and Future of Surface-Enhanced Raman Scattering. *ACS Nano* **2019**, *14*, 28–117.

[5] Chen, J.; Huang, Y.; Kannan, P.; Zhang, L.; Lin, Z.; Zhang, J.; Chen, T.; Guo, L. Flexible and Adhesive Surface Enhance Raman Scattering Active Tape for Rapid Detection of Pesticide Residues in Fruits and Vegetables. *Anal. Chem.* **2016**, *88*, 2149–2155.

[6] Plou, J.; García, I.; Charconnet, M.; Astobiza, I.; GarcíaâAstrain, C.; Matricardi, C.; Mihi, A.; Carracedo, A.; LizâMarzán, L. M. Multiplex SERS Detection of Metabolic Alterations in Tumor Extracellular Media. *Adv. Funct. Mater.* **2020**, *30*, 1910335.

[7] Chen, J.; Huang, Y.; Kannan, P.; Zhang, L.; Lin, Z.; Zhang, J.; Chen, T.; Guo, L. Flexible and Adhesive Surface Enhance Raman Scattering Active Tape for Rapid Detection of Pesticide Residues in Fruits and Vegetables. *Anal. Chem.* **2016**, *88*, 2149–2155.

[8] Lin, P. Y.; Hsieh, C. W.; Hsieh, S. Rapid and Sensitive SERS Detection of Bisphenol A Using Self-assembled Graphitic Substrates. *Sci. Rep.* **2017**, *7*, 1–6.

[9] Wachter, E. A.; Storey, J. M. E.; Sharp, S. L.; Carron, K. T.; Jiang, Y. Hybrid Substrates for Real-Time SERS-Based Chemical Sensors. *Appl. Spectrosc.* **1995**, *49*, 193–199.

[10] Ansar, S. M.; Ameer, F. S.; Hu, W.; Zou, S.; Pittman, C. U.; Zhang, D. Removal of molecular adsorbates on gold nanoparticles using sodium borohydride in water. *Nano Lett.* **2013**, *13*, 1226–1229.

[11] Shin, Y.; Jeon, I.; You, Y.; Song, G.; Lee, T. K.; Oh, J.; Son, C.; Baek, D.; Kim, D.; Cho, H.; Hwang, H.; Kim, T.; Kwak, S. K.; Kim, J.; Lee, J. Facile Microfluidic Fab-

rication of 3D Hydrogel SERS Substrate with High Reusability and Reproducibility via Programmable Maskless Flow Microlithography. *Adv. Opt. Mater.* **2020**, *8*, 1–10.

[12] Sinha, G.; Depero, L. E.; Alessandri, I. Recyclable SERS substrates based on Au-Coated ZnO nanorods. *ACS Appl. Mater. Interfaces* **2011**, *3*, 2557–2563.

[13] Guselnikova, O.; Samant, R.; Postnikov, P.; Trelin, A.; Svorcik, V.; Lyutakov, O. Plasmon-assisted self-cleaning sensor for the detection of organosulfur compounds in fuels. *J. Mater. Chem. C* **2019**, *7*, 14181–14187.

[14] Höhn, E. M.; Panneerselvam, R.; Das, A.; Belder, D. Raman spectroscopic detection in continuous microflow using a chip-integrated silver electrode as an electrically regenerable surface-enhanced raman spectroscopy substrate. *Anal. Chem.* **2019**, *91*, 9844–9851.

[15] Meier, T. A.; Poehler, E.; Kemper, F.; Pabst, O.; Jahnke, H. G.; Beckert, E.; Robitzki, A.; Belder, D. Fast electrically assisted regeneration of on-chip SERS substrates. *Lab Chip* **2015**, *15*, 2923–2927.

[16] Strehle, K. R.; Cialla, D.; Rösch, P.; Henkel, T.; Köhler, M.; Popp, J. A reproducible surface-enhanced Raman spectroscopy approach. Online SERS measurements in a segmented microfluidic system. *Anal. Chem.* **2007**, *79*, 1542–1547.

[17] Dugandžić, V.; Hidi, I. J.; Weber, K.; Cialla-May, D.; Popp, J. In situ hydrazine reduced silver colloid synthesis â Enhancing SERS reproducibility. *Anal. Chim. Acta* **2016**, *946*, 73–79.

[18] Hirenkumar, M.; Steven, S. Poly Lactic-co-Glycolic Acid (PLGA) as Biodegradable Controlled Drug Delivery Carrier. *Polymers* **2012**, *3*, 1–19.

[19] Agrawal, C. M.; Huang, D.; Schmitz, J. P.; Athanasiou, K. A. Elevated temperature degradation of a 50:50 copolymer of PLA-PGA. *Tissue Eng.* **1997**, *3*, 345–352.

[20] Gupta, M. K.; Meng, F.; Johnson, B. N.; Kong, Y. L.; Tian, L.; Yeh, Y. W.; Masters, N.; Singamaneni, S.; McAlpine, M. C. 3D Printed Programmable Release Capsules. *Nano Lett.* **2015**, *15*, 5321–5329.

[21] Chuang, C. C.; Cheng, C. C.; Chen, P. Y.; Lo, C.; Chen, Y. N.; Shih, M. H.; Chang, C. W. Gold nanorod-encapsulated biodegradable polymeric matrix for combined photothermal and chemo-cancer therapy. *Int. J. Nanomed.* **2019**, *14*, 181–193.

[22] Brongersma, M. L.; Halas, N. J.; Nordlander, P. Plasmon-induced hot carrier science and technology. *Nat. Nanotechnology* **2015**, *10*, 25–34.

[23] Quintanilla, M.; Kuttner, C.; Smith, J. D.; Seifert, A.; Skrabalak, S. E.; Liz-Marzán, L. M. Heat generation by branched Au/Pd nanocrystals: Influence of morphology and composition. *Nanoscale* **2019**, *11*, 19561–19570.

[24] Fiutowski, J. Mapping of gold nanostructure-enhanced near fields via laser scanning second-harmonic generation and ablation. *J. Nanophoton.* **2012**, *6*, 063515.

[25] Haas, K. M.; Lear, B. J. Degradation of polypropylene carbonate through plasmonic heating. *Nanoscale* **2013**, *5*, 5247–5251.

[26] Borah, R.; Verbruggen, S. W. Coupled Plasmon Modes in 2D Gold Nanoparticle Clusters and Their Effect on Local Temperature Control. *J Phys Chem C* **2019**, *123*, 30594–30603.

[27] Baffou, G.; Berto, P.; Bermúdez Ureña, E.; Quidant, R.; Monneret, S.; Polleux, J.; Rigneault, H. Photoinduced heating of nanoparticle arrays. *ACS Nano* **2013**, *7*, 6478–6488.

[28] Jones, S.; Andrén, D.; Karpinski, P.; Käll, M. Photothermal Heating of Plasmonic Nanoantennas: Influence on Trapped Particle Dynamics and Colloid Distribution. *ACS Photonics* **2018**, *5*, 2878–2887.

[29] Reguera, J.; Jiménez De Aberasturi, D.; Winckelmans, N.; Langer, J.; Bals, S.; Liz-Marzán, L. M. Synthesis of Janus plasmonic-magnetic, star-sphere nanoparticles, and their application in SERS detection. *Faraday Discuss.* **2016**, *191*, 47–59.

[30] Polavarapu, L.; Porta, A. L.; Novikov, S. M.; Coronado-Puchau, M.; Liz-Marzán, L. M. Pen-on-paper approach toward the design of universal surface enhanced Raman scattering substrates. *Small* **2014**, *10*, 3065–3071.

[31] Luo, H.; Huang, Y.; Lai, K.; Rasco, B. A.; Fan, Y. Surface-enhanced Raman spectroscopy coupled with gold nanoparticles for rapid detection of phosmet and thiabendazole residues in apples. *Food Control* **2016**, *68*, 229–235.

[32] Castro, J. L.; Arenas, J. F.; Lopez-Ramirez, M. R.; Soto, J.; Otero, J. C. Surface-enhanced Raman scattering of picolinamide, nicotinamide, and isonicotinamide: Unusual carboxamide deprotonation under adsorption on silver nanoparticles. *J. Colloid Interface Sci.* **2013**, *396*, 95–100.

Chapter 7

Conclusion and outlook

The fabrication of novel plasmonic nanostructures with defined optical properties has led to a huge improvement in various fields including catalysis [1], cancer therapy [2] and biosensing [3]. Particularly, in the field of biosensing, surface-enhanced Raman spectroscopy has proven to be a technique of choice for the detection of biomarkers, and improvement in the SERS enhancement of plasmonic substrates is still needed to attain better sensing capabilities. In this PhD thesis, the surface-enhanced Raman scattering performance of plasmonic superlattices were improved through the rational design and the study of the optical properties of self-assembled gold nanoparticles. Particularly, the optical properties of the fabricated superlattices were correlated with SERS enhancement.

In **Chapter 3**, the templated self-assembly process was optimized using ethanol as a co-solvent to obtain more homogeneous gold nanosphere superlattices. The systematic study of the ethanol ratio and surfactant concentration on the quality of the assembly resulted in the fabrication of high-quality arrays of nanosphere heptamers, which improved the SERS enhancement by an order of magnitude compared to the structures that were made without ethanol. Additionally, the gain in homogeneity resulted in sharper and stronger plasmon resonances as well as a much lower statistical uncertainty, where the standard deviation of the SERS signal could be decreased to 15%.

Following the optimized self-assembly process of **Chapter 3**, gold nanoparticles of different shapes (nanospheres, nanorods and nanotriangles) could be assembled into homogeneous superlattices of two different lattice periods using the chemical conditions determined for the

homogeneous assembly of nanospheres. Coupling of the lattice effect to different cluster plasmon modes allowed for the optimization of the SERS enhancement at two laser excitations wavelengths depending on the lattice period. Using 633 nm laser excitation, the 400 nm period superlattices outperformed the 500 nm period superlattices, while the 500 nm period superlattices outperformed the 400 nm period superlattices at 785 nm excitation. Interestingly, out of the differently shaped nanoparticle superlattices, the nanosphere superlattices exhibited the highest SERS signal, with an analytical SERS enhancement factor of $3 \cdot 10^6$.

The period of the nanostructured mold defines the fixed period of the assembled superlattice, and consequently of the surface lattice resonance, therefore tailoring of the surface lattice resonance towards a precise wavelength requires iterative fabrication of nanostructures with different periods. To overcome this lengthy process, the templated self-assembly process was transferred to flexible PDMS substrates in **Chapter 5**. Tuning of the flexible superlattice period by post-assembly mechanical deformation provided continuous and reversible adjustment of the surface lattice plasmon resonances towards pre-defined wavelengths. Both unidirectional and bidirectional lattice deformations were used to adapt a single lattice structure to both red-shifted and blue-shifted excitation lines, which allowed to increase the SERS signal by a factor of 3 when the surface lattice resonance matched precisely the excitation wavelength.

Finally, a process for real-time sensing of hazardous chemicals in microfluidic channels was presented in **Chapter 6**. Such a process relies on the coating of the plasmonic substrate with PLGA as a thermolabile polymer. Taking advantage of the efficient light-to-heat conversion of plasmonic nanostructures, a hole that served as a measurement window for SERS recording could be generated in the PLGA layer by laser irradiation of the PLGA-coated plasmonic superlattice. While bare plasmonic substrates are prone to the SERS memory effect which hampers the successive reuse of a plasmonic substrate for multiple SERS detections, PLGA coatings impeded analytes molecules to bind irreversibly to the gold nanoparticles and enabled to make several SERS measurements with a single substrate. Thanks to the generation of small holes into the PLGA layer (20×10 µm), and to the high spatial resolution in the hole generation, 4 measurement windows could be created in an area of 120×40 µm for the measurement of different analytes. Accordingly, PLGA-coated SERS samples could be used for real-time detection of thiabendazole, a toxic pesticide, in microfluidic channels. Along with the shown transfer-

ability of the PLGA-SERS method to simple plasmonic samples, such as dried droplets of gold nanoparticles, this proof-of-concept experiment exhibits the great potential of PLGA-coated plasmonic substrates for the monitoring of in situ chemical or biological processes.

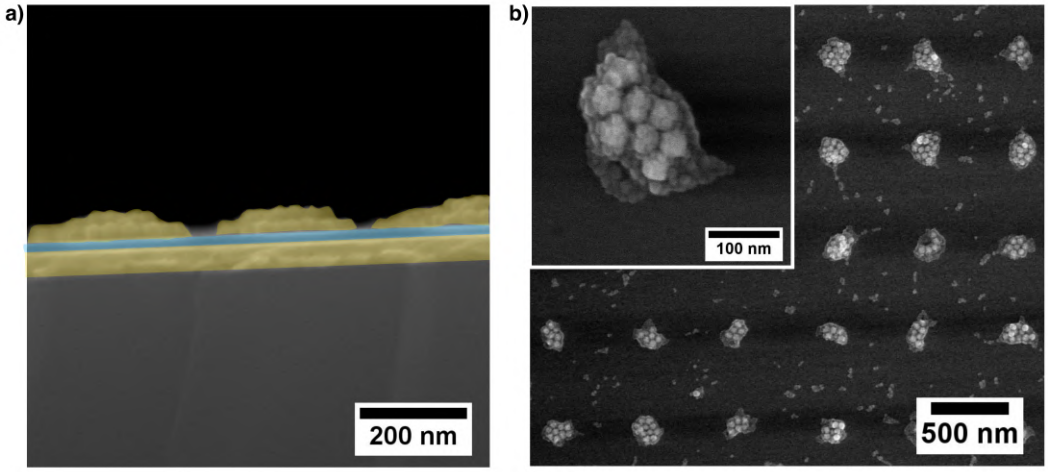

Figure 7.1: a) SEM image of superlattice on mirror architecture, gold is depicted in yellow and Al_2O_3 in blue. The assembled gold nanospheres stands on a substrate comprising a 50 nm-thick gold layer and a 20 nm-thick Al_2O_3 layer made by atomic layer deposition. b) SEM image of 40 nm nanospheres and 10 nm CaF_2:Y_3^+,Nd_3^+ nanoparticles assembled in a superlattice of 500 nm period.

While different strategies for improving the performance of plasmonic superlattices have been exposed in this PhD thesis, the SERS enhancement of gold on mirror architectures seen on **Figure 7.1 a** is still under investigation. Such structures are expected to further enhance the SERS signal of plasmonic superlattices thanks to an out-of-plane coupling between the superlattice and the gold layer [4, 5]. Additionally, the optical properties of the different superlattices studied throughout this thesis might serve as the basis for other applications. For instance, surface lattice resonances possess interesting properties that have been applied to structural color generation [6] or light emission and harvesting [7]. As an example, plasmonic lattices have been coupled to light emitters to create nano-lasing phenomena [8], in this sense the direct assembly of gold nanoparticles with photoluminescent nanoparticles into superlattices presented in **Figure 7.1 b** could lead to interesting plasmon-exciton coupling.

Bibliography

[1] De Barros, H. R.; García, I.; Kuttner, C.; Zeballos, N.; Camargo, P. H.; De Torresi, S. I. C.; López-Gallego, F.; Liz-Marzán, L. M. Mechanistic Insights into the Light-Driven Catalysis of an Immobilized Lipase on Plasmonic Nanomaterials. *ACS Catal.* **2021**, *11*, 414–423.

[2] Rastinehad, A. R. et al. Gold nanoshell-localized photothermal ablation of prostate tumors in a clinical pilot device study. *Proc. Natl. Acad. Sci. USA* **2019**, *116*, 18590–18596.

[3] Zhang, Y.; Jimenez de Aberasturi, D.; Henriksen-Lacey, M.; Langer, J.; Liz-Marzán, L. M. Live-Cell Surface-Enhanced Raman Spectroscopy Imaging of Intracellular pH: From Two Dimensions to Three Dimensions. *ACS sensors* **2020**, *5*, 3194–3206.

[4] Huang, Y.; Ma, L.; Hou, M.; Li, J.; Xie, Z.; Zhang, Z. Hybridized plasmon modes and near-field enhancement of metallic nanoparticle-dimer on a mirror. *Sci. Rep.* **2016**, *6*, 1–9.

[5] Benz, F.; Chikkaraddy, R.; Salmon, A.; Ohadi, H.; De Nijs, B.; Mertens, J.; Carnegie, C.; Bowman, R. W.; Baumberg, J. J. SERS of Individual Nanoparticles on a Mirror: Size Does Matter, but so Does Shape. *J. Phys. Chem. Lett.* **2016**, *7*, 2264–2269.

[6] Cheng, F.; Gao, J.; Luk, S. T.; Yang, X. Structural color printing based on plasmonic metasurfaces of perfect light absorption. *Sci. Rep.* **2015**, *5*, 1–10.

[7] Mubeen, S.; Lee, J.; Lee, W. R.; Singh, N.; Stucky, G. D.; Moskovits, M. On the plasmonic photovoltaic. *ACS Nano* **2014**, *8*, 6066–6073.

[8] Wang, D.; Bourgeois, M. R.; Lee, W. K.; Li, R.; Trivedi, D.; Knudson, M. P.; Wang, W.; Schatz, G. C.; Odom, T. W. Stretchable Nanolasing from Hybrid Quadrupole Plasmons. *Nano Lett.* **2018**, *18*, 4549–4555.

Appendices

Appendix A

Homogeneous self-assembly of gold nanospheres into superlattices on a large scale

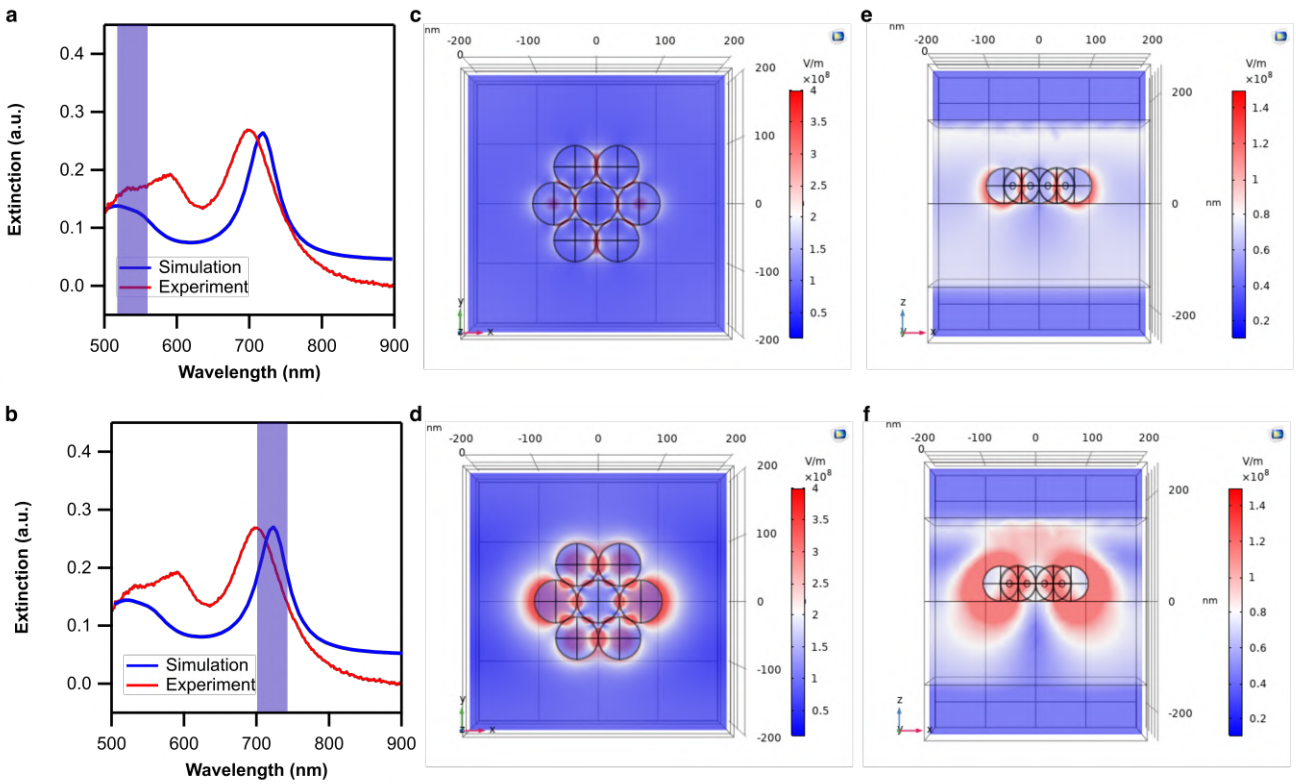

Figure Appendix I.1: Extinction spectra of 400 nm period superlattice of 65 nm spheres heptamers with a) 600 nm resonance underlined, b) 700 nm resonance underlined. Top view of the simulated near-field of 400 nm superlattices at: c) 600 nm, d) 700 nm. Cross-section view of the simulated near-field of 400 nm superlattice at: e) 600 nm, d) 700 nm.

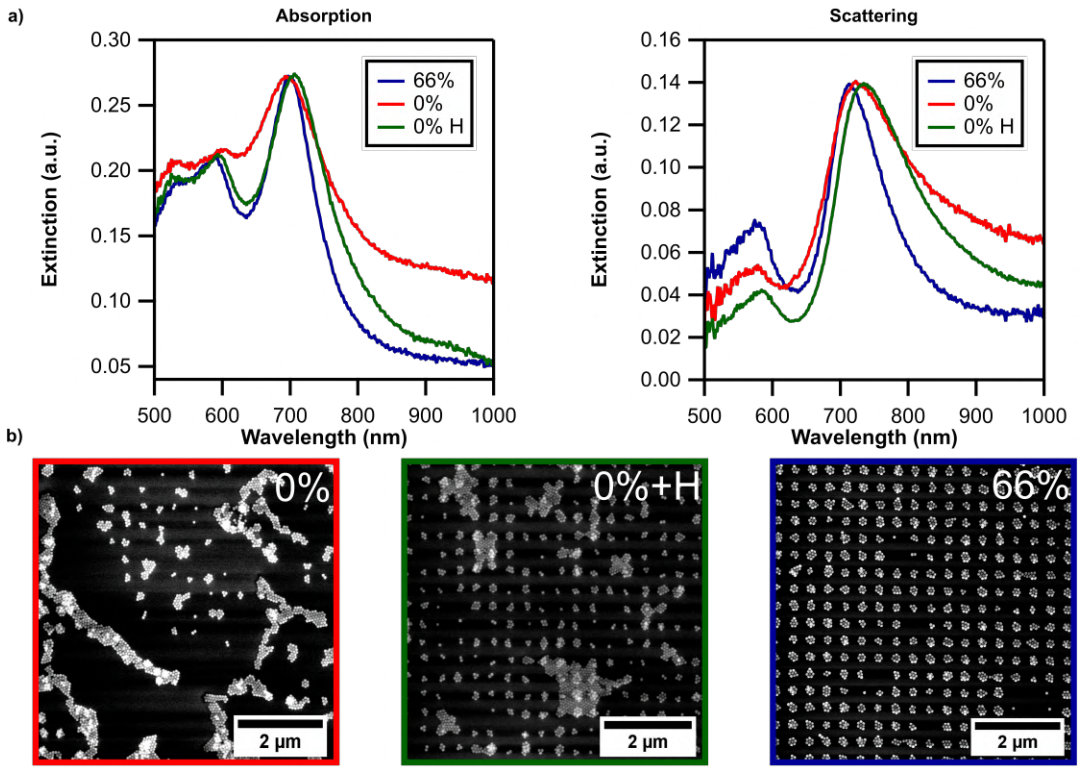

Figure Appendix I.2: a) Absorption and scattering spectra of superlattices made with or without ethanol. b) SEM images of superlattices made with or without ethanol.

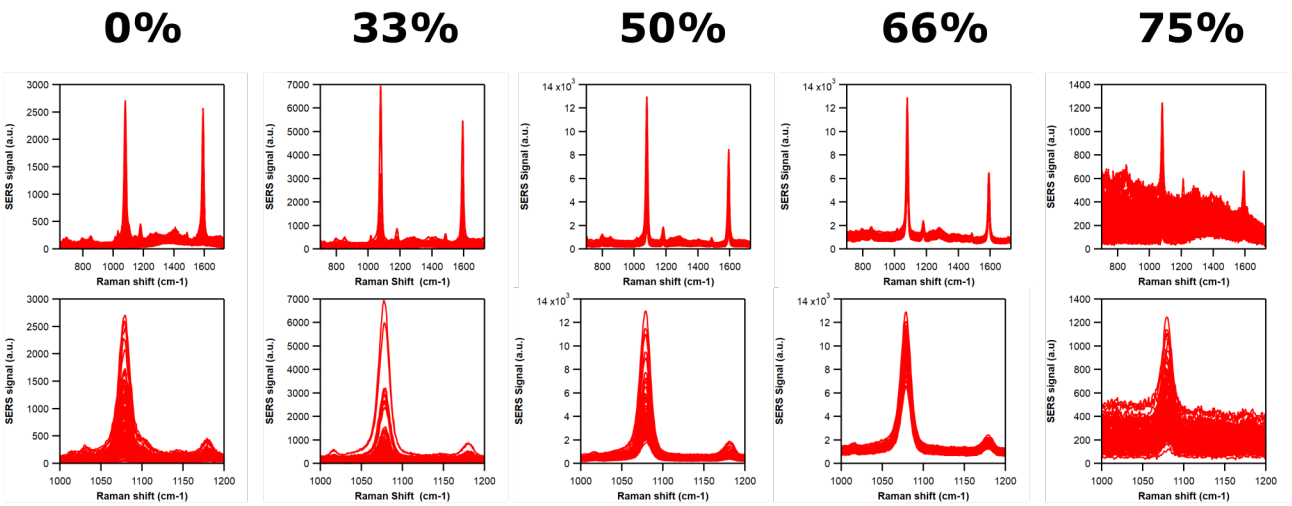

Figure Appendix I.3: Superimposed SERS spectra of randomly taken measurements on superlattice made with different ethanol ratio.

Appendix B

Self-assembly of differently shaped nanoparticles into superlattices and their optical properties

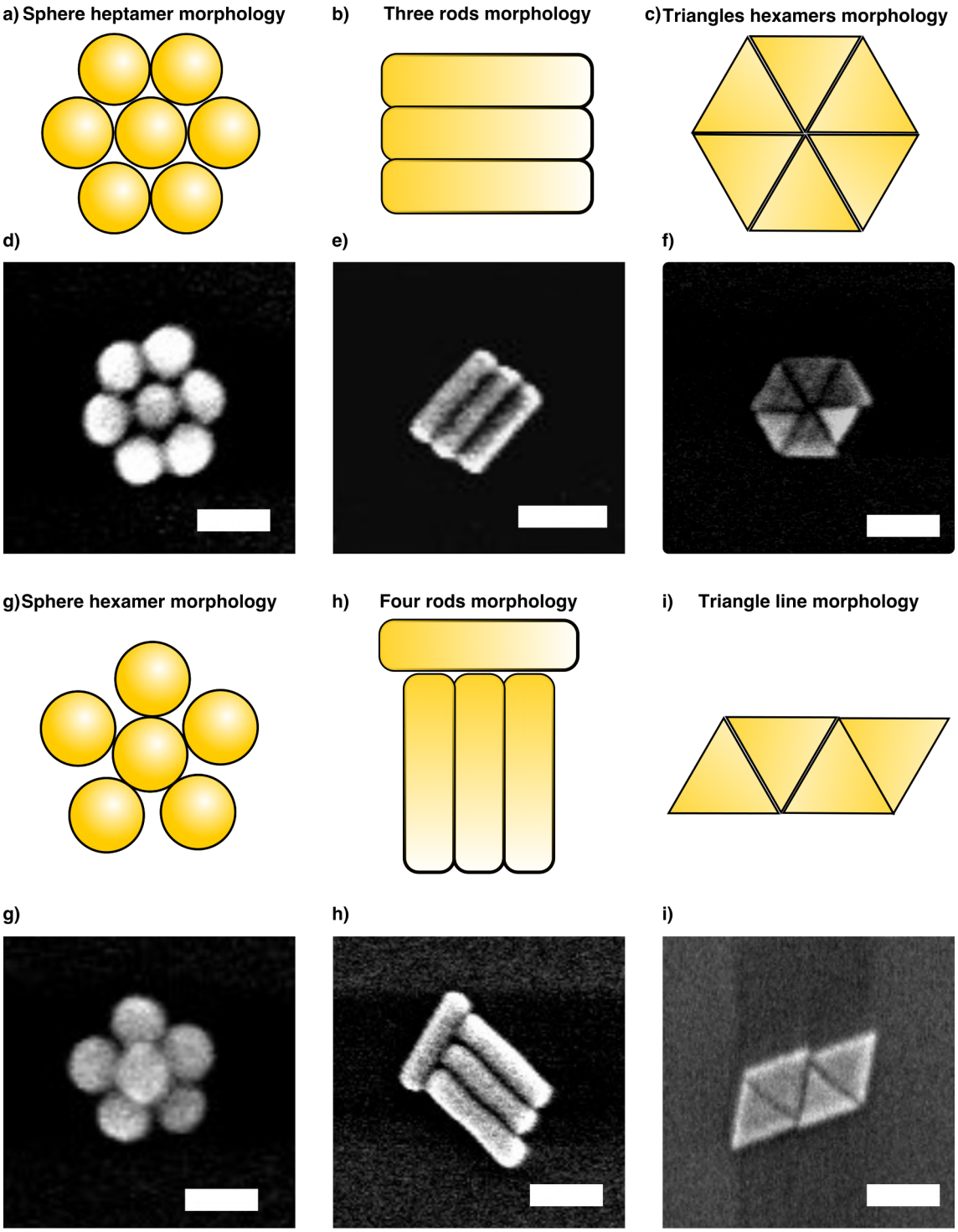

Figure Appendix III.1: Different cluster morphologies considered in the FEM simulations. a,b,c) Scheme of the heptamer, three rods and triangle hexamers morphologies. d,e,f) SEM images of single clusters with the heptamer, three rods, and triangle hexamers morphology. g,h,i) scheme of the hexamer, four rods, and triangle line morphologies. j,k,l) SEM images of single cluster with the hexamer, four rods and line of triangle morphologies.

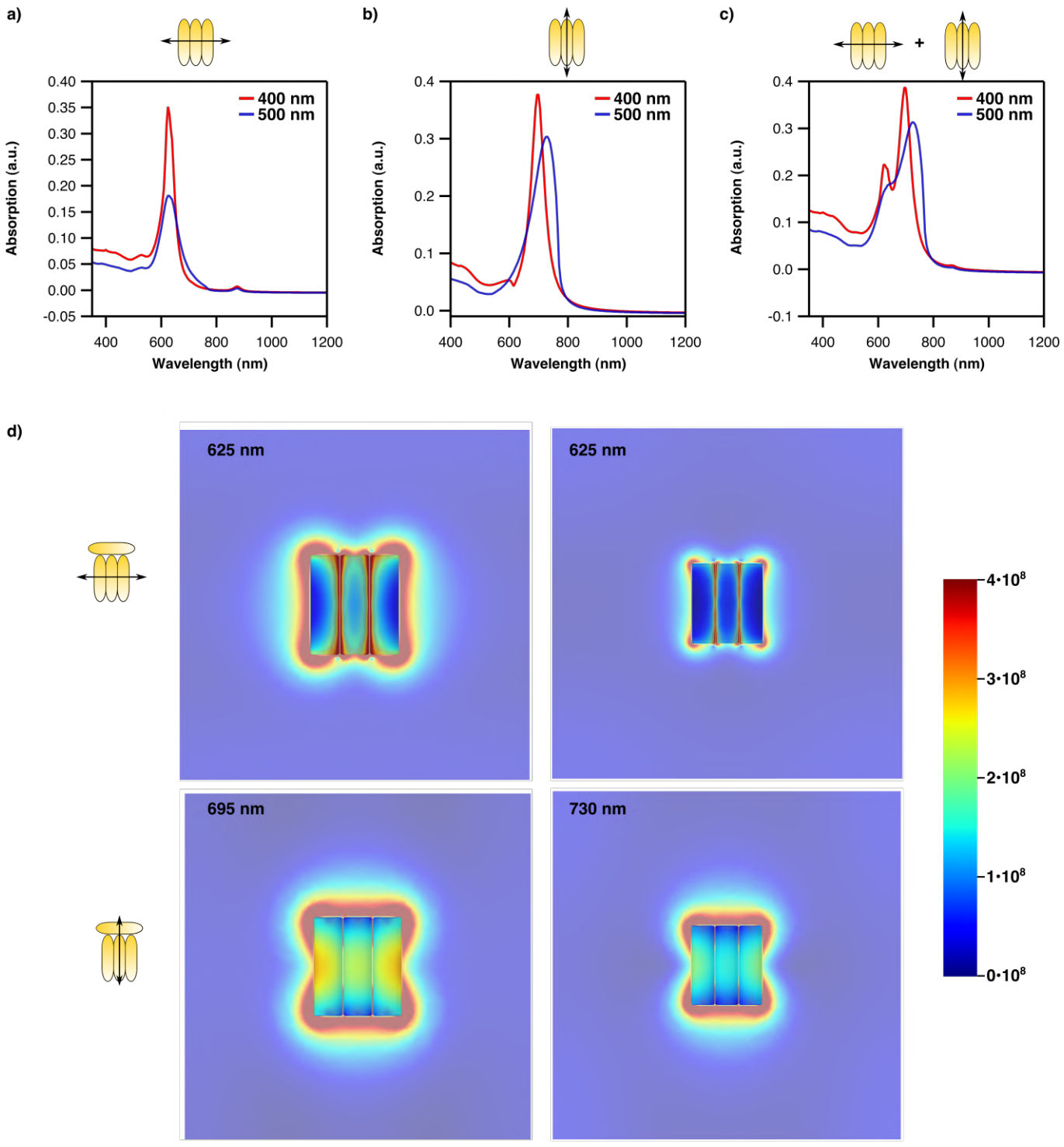

Figure Appendix III.2: Simulated absorption spectra of three rods clusters in a lattice of 400 nm and 500 nm under a) polarization along the short axis and b) long axis of the side-by-side assembled nanorods. c) Average of the absorption spectra of four rods cluster in a lattice of 400 nm and 500 nm under both polarizations. d) Electric field distribution of the principal plasmonic resonances present in the simulated absorption spectra of the three rods morphology.

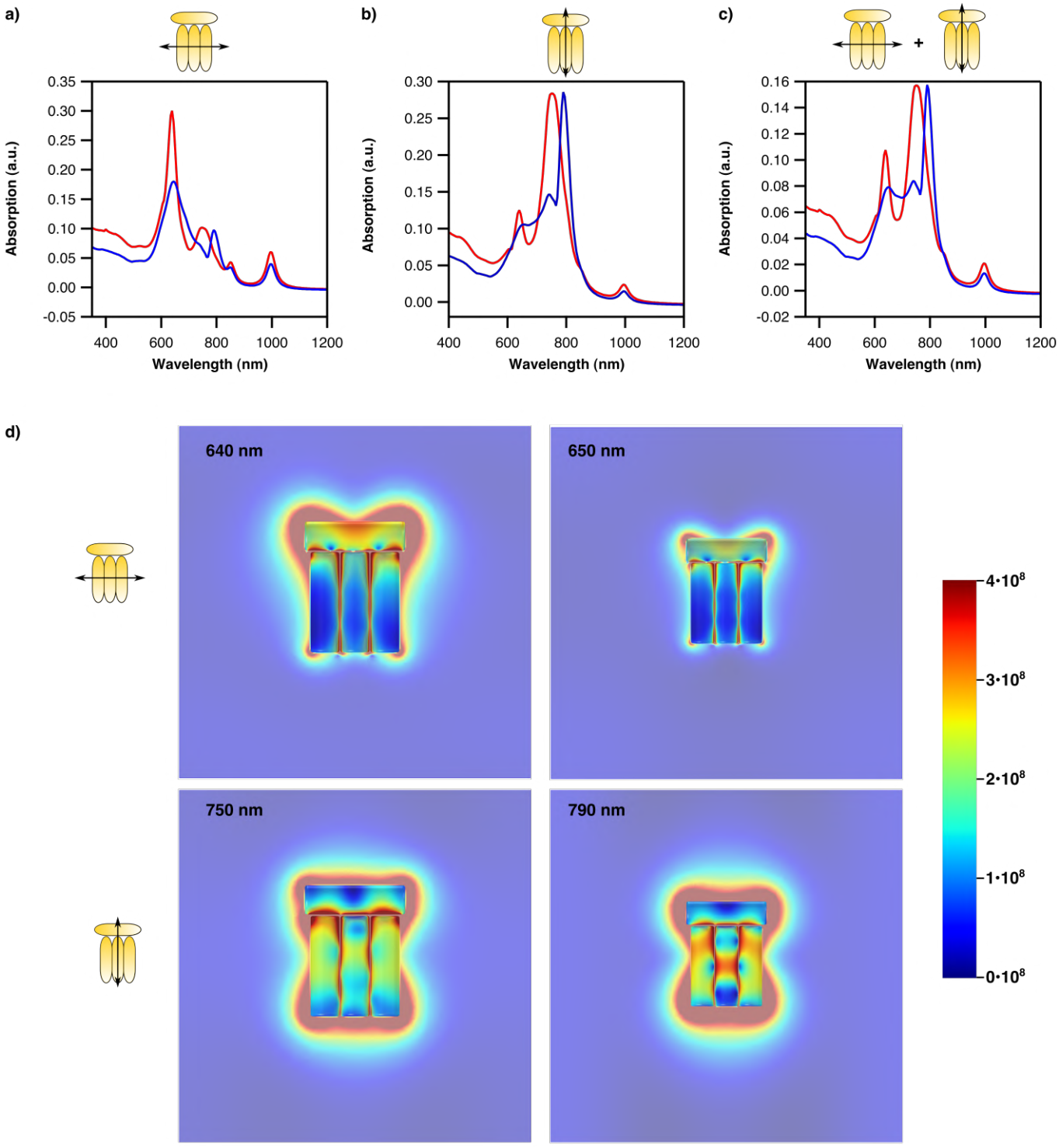

Figure Appendix III.3: Simulated absorption spectra of four rods clusters in a lattice of 400 nm and 500 nm under a) polarization along the short axis and b) long axis of the side-by-side assembled nanorods. c) Average of the absorption spectra of four rods cluster in a lattice of 400 nm and 500 nm under both polarizations. d) Electric field distribution of the principal plasmonic resonances present in the simulated absorption spectra of the four rods morphology.

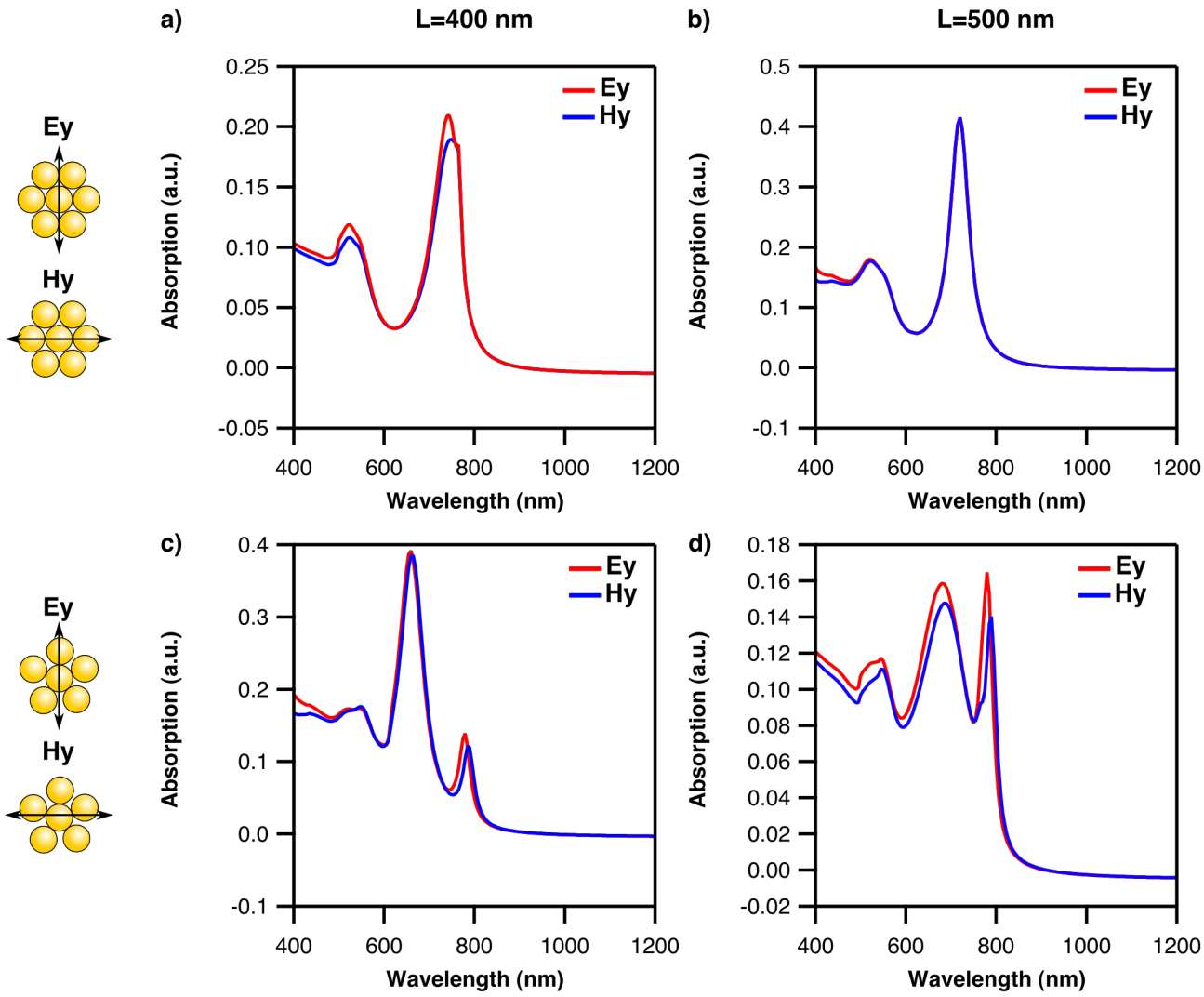

Figure Appendix III.4: Simulated absorption spectra of nanosphere heptamers and hexamers in superlattices of 400 and 500 nm under different polarizations: heptamers in a) a 400 nm lattice and b) a 500 nm lattice; hexamers in c) a 400 nm lattice and d) a 500 nm lattice.

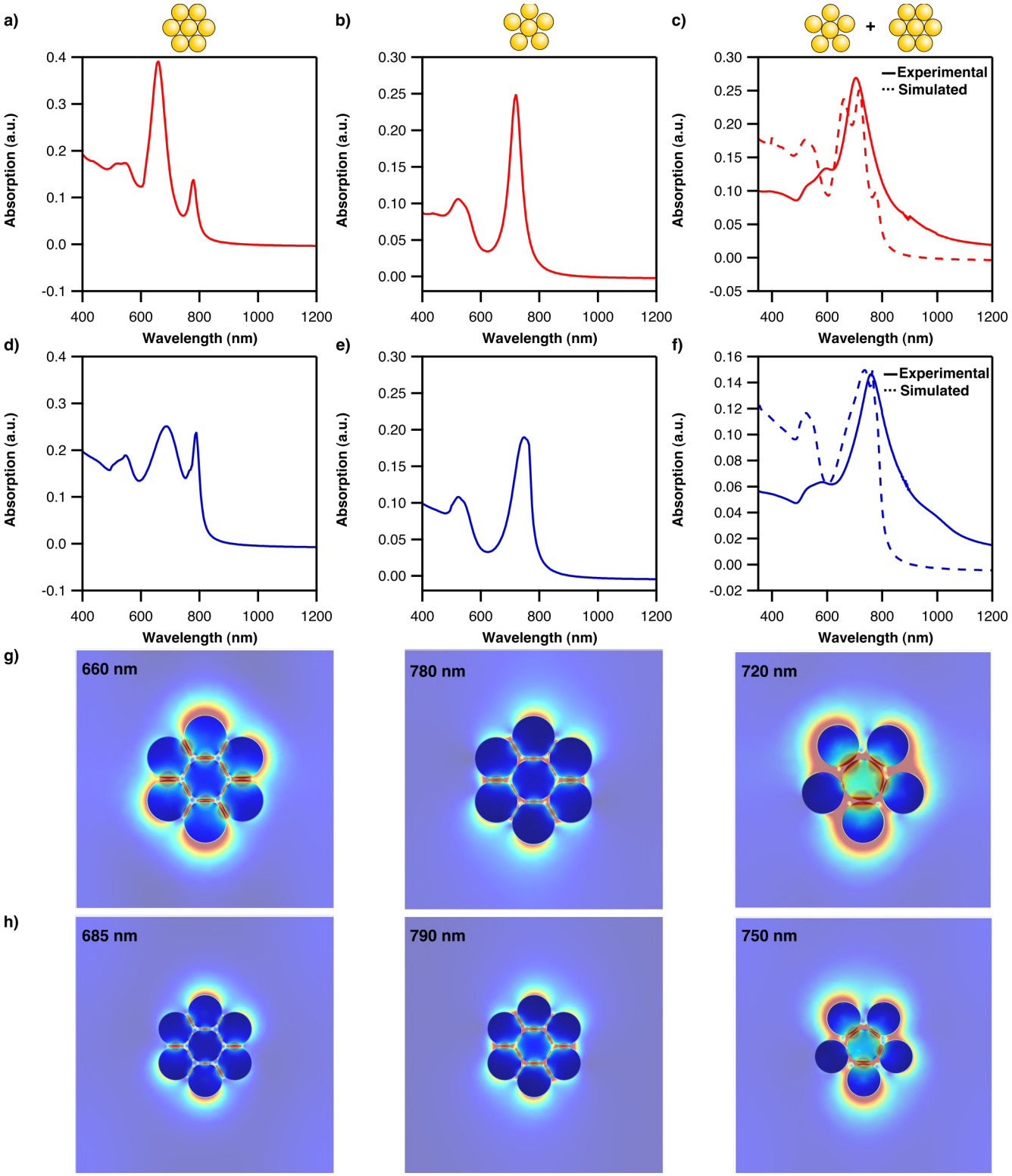

Figure Appendix III.5: Simulated absorption spectra of nanosphere superlattices made of different sub-units. a) Heptamers, b) hexamers in a 400 nm period superlattice and c) average absorption spectra of the heptamers and hexamers in a 400 nm period superlattice. d) Heptamers, e)hexamers in a 500 nm period superlattice and f) average absorption spectra of the heptamers and hexamers in a 500 nm period superlattice. Simulated near-field images of the main plasmonic resonances present in the heptamer and hexamer conformation in a: g) 400 nm lattice and h) 500 nm lattice.

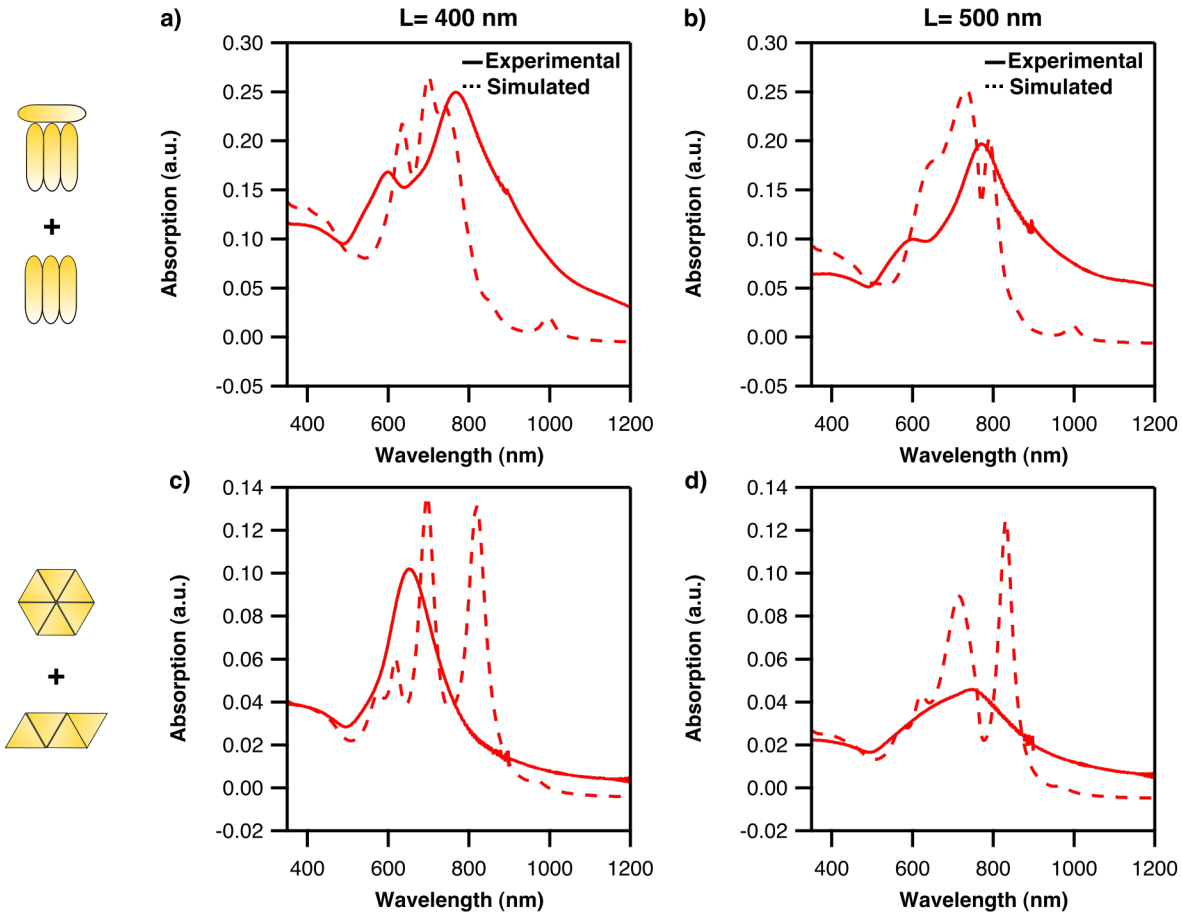

Figure Appendix III.6: Average simulated absorption spectra of nanorod and nanotriangle superlattices of different cluster morphologies and under two orthogonal polarizations. Averaged simulated absorption spectra of four nanorods and three nanorods morphologies in: a) a 400 nm lattice, and under two polarizations, b) in 500 nm lattice and under two polarizations. Averaged simulated absorption spectra of triangle hexamers and line of triangles morphologies in: c) a 400 nm lattice, and under two polarizations, d) in 500 nm lattice and under two polarizations.

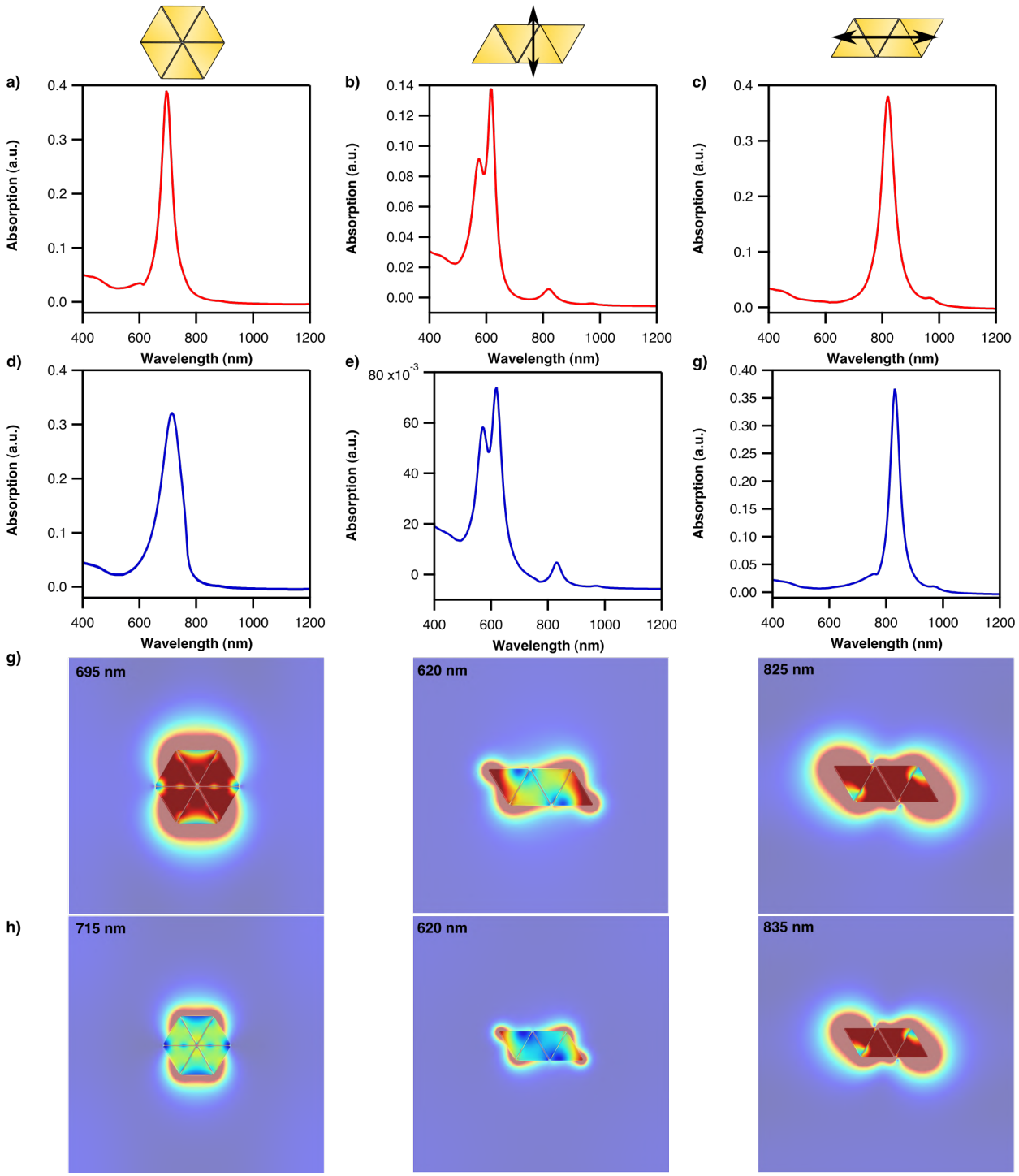

Figure Appendix III.7: Simulated absorption spectra of triangles supperlattices with different sub-unit morphologies. a) Triangle hexamers in a 400 nm lattice, Line of triangles in a 400 nm lattice with b) polarization along the short axis of the line, c) polarization along the long axis of the line. d) Triangle hexamers in a 500 nm lattice, Line of triangles in a 500 nm lattice with e) polarization along the short axis of the line, f) polarization along the long axis of the line. g) Simulated near-field images of the main plasmonic resonances present in the triangle hexamers and line of triangles conformation in a: g) 400 nm lattice and h) 500 nm lattice.

Table Appendix III.8: Comparison of the SERS intensity at 1080 cm^{-1} for the 400 and 500 nm period superlattices made of nanospheres, nanorods, nanotriangles at a laser excitation of 633 nm and 785 nm with 4-MBA as model analyte.

785 nm excitation	400 nm	500 nm
Spheres	8800 ± 1200 (13%)	12500 ± 1900 (15%)
Rods	4700 ± 1200 (25%)	5390 ± 460 (8.6%)
Triangles	620 ± 220 (34%)	1650 ± 560 (33%)

633 nm excitation	400 nm	500 nm
Spheres	1070 ± 320 (29%)	440 ± 150 (34%)
Rods	620 ± 150 (24%)	208 ± 32 (15%)
Triangles	94 ± 20 (24%)	58 ± 14 (24%)

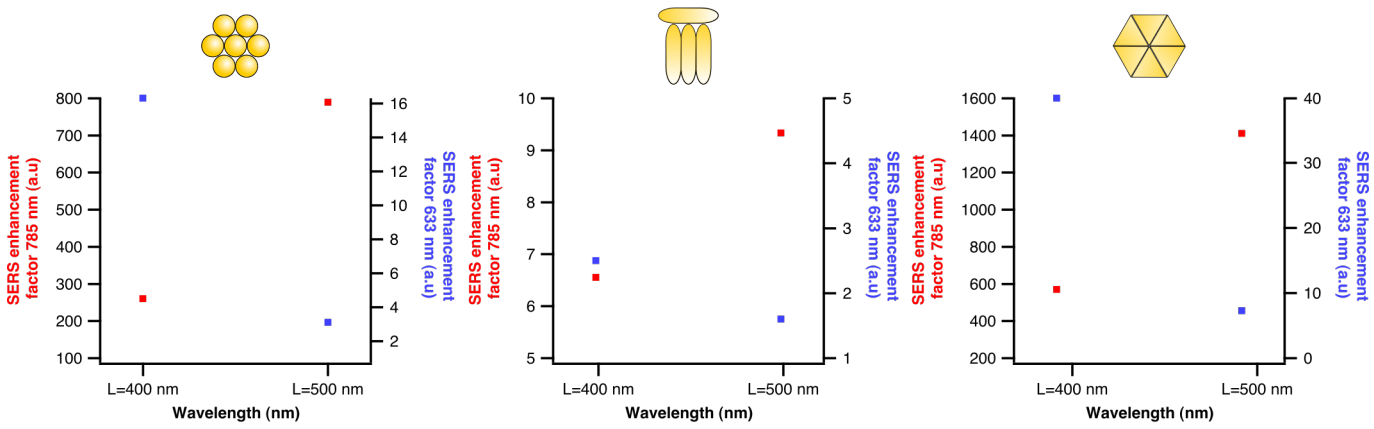

Figure Appendix III.9: Comparison of the simulated SERS enhancement factors for superlattices of different periods and shapes.

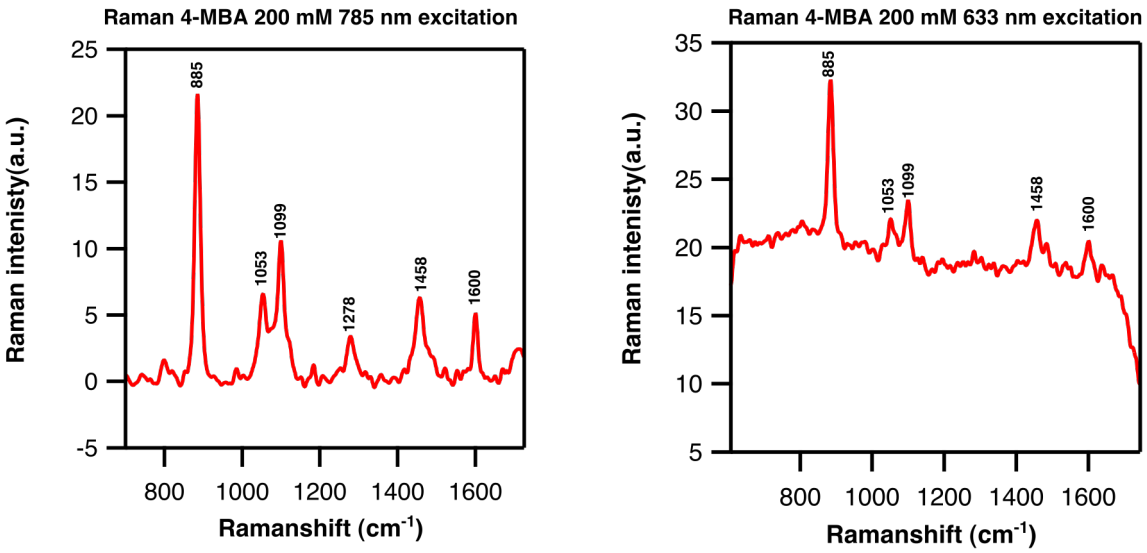

Figure Appendix III.10: Raman spectra from 200 mM 4-MBA in ethanol at a) 785 nm laser excitation and b) 633 nm laser excitation.

Appendix C

Mechanically Tunable Lattice-Plasmon Resonances by Self-Assembled Superlattices for Surface-Enhanced Raman Spectroscopy

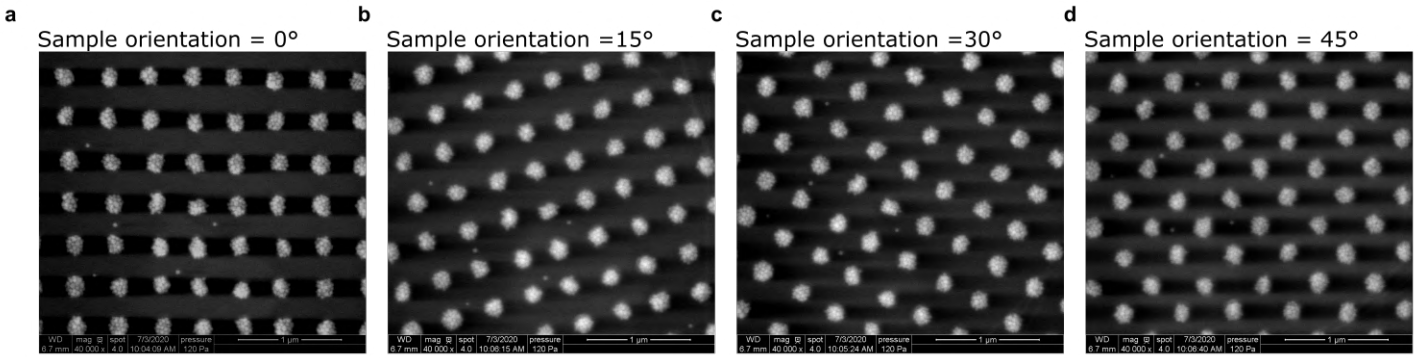

Figure Appendix III.1: Examples of SEM images of a superlattice with period of 500 nm for different orientations of the sample. The effect of surface charging can be observed as dark shadows along the scanning direction. By changing the sample orientation, it can be clearly shown that these are merely imaging artifacts that do not indicate changes in the structures or the sample surface.

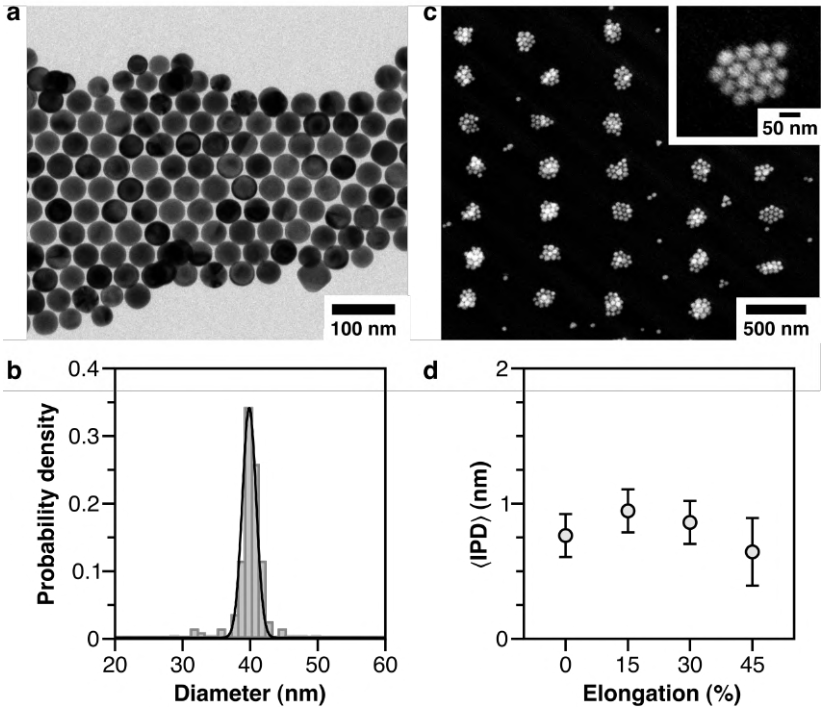

Figure Appendix III.2: Examples of SEM images of a 500 nm superlattice under unidirectional stretching. a) The overview image at 20 kV shows a deformation of the sample surface, indicated in blue, owing to charging effects. b-f) Detail images taken at 10 kV allow for quantification of the period of the superlattice at different elongation states.

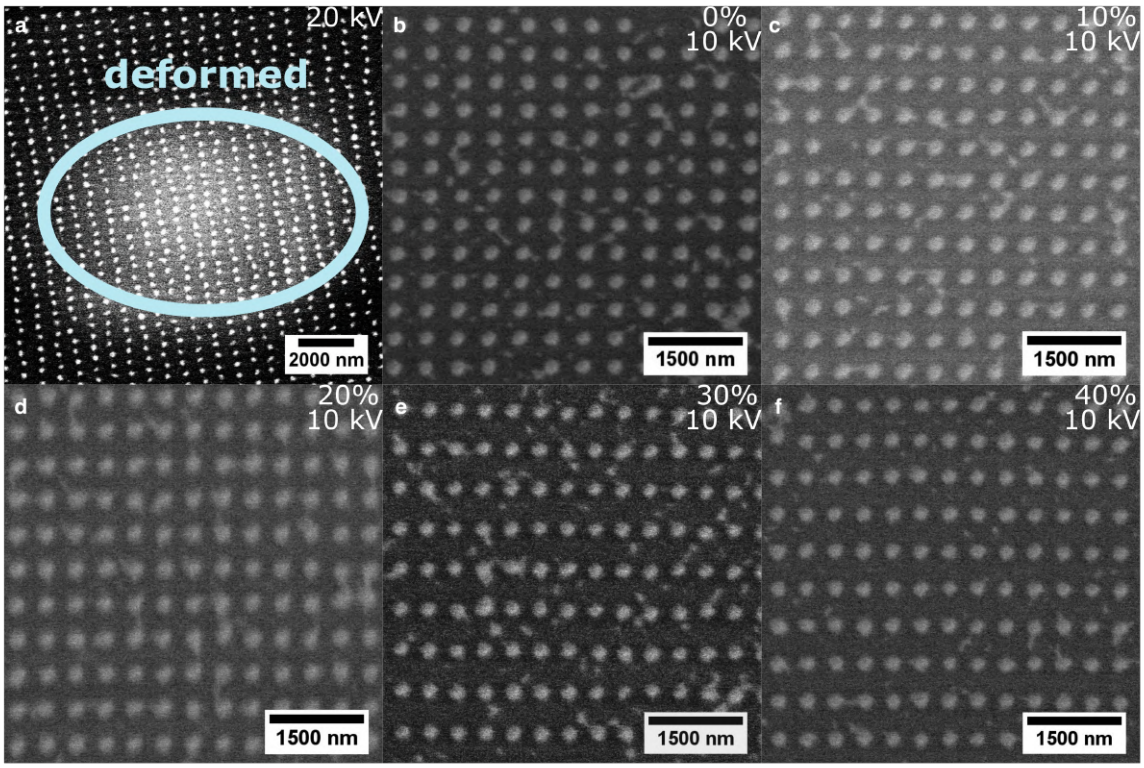

Figure Appendix III.3: Examples of SEM images of a 500 nm superlattice under unidirectional stretching. a) The overview image at 20 kV shows a deformation of the sample surface, indicated in blue, owing to charging effects. b-f) Detail images taken at 10 kV allow for quantification of the period of the superlattice at different elongation states.

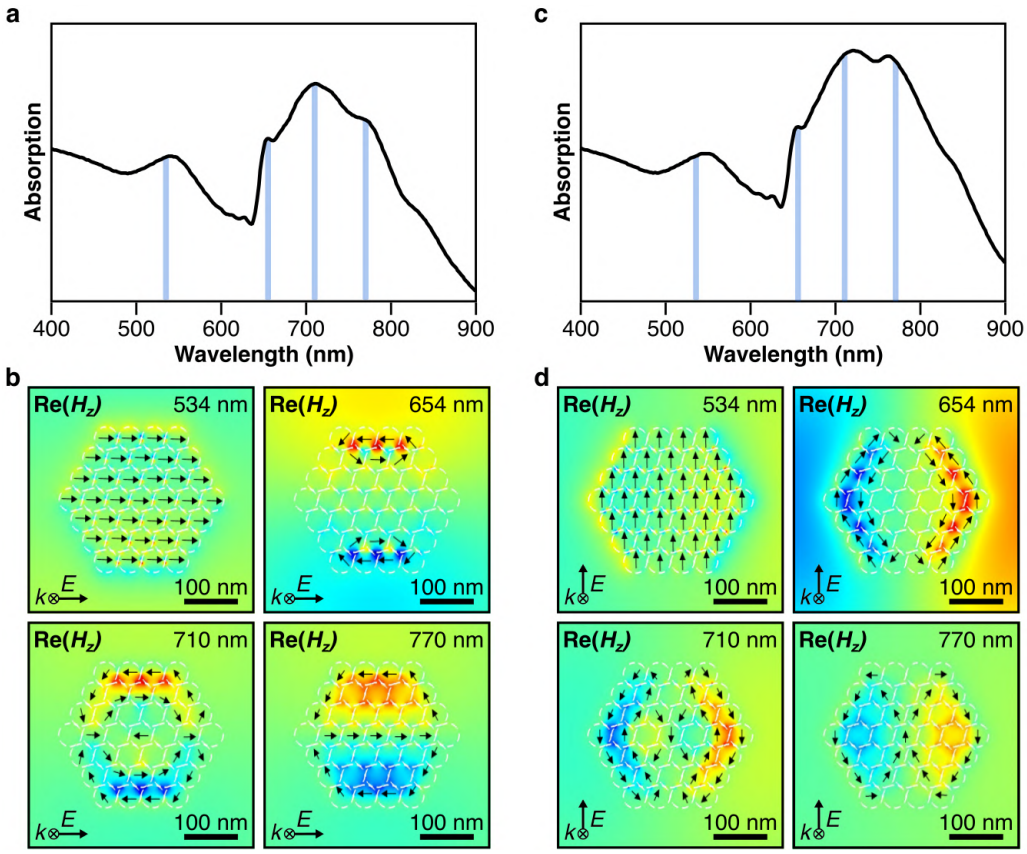

Figure Appendix III.4: Electromagnetic simulations of an isolated cluster for polarization along a,b) x and c,d) y direction: a,c) absorption cross sections and (b,d) snapshots of different resonance modes illustrated by the real part of the vertical magnetic field Hz. The black arrows indicate the direction of the electric current.

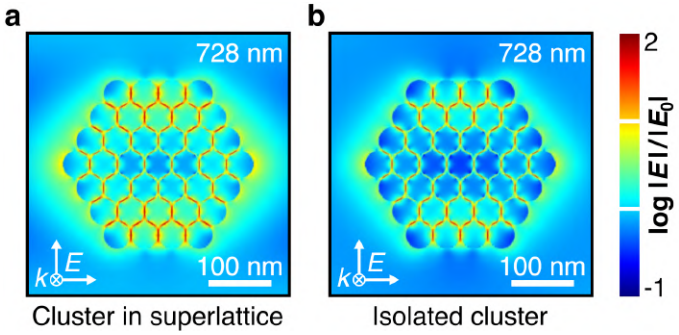

Figure Appendix III.5: Comparison of the near-field enhancement of a cluster in a periodic arrangement (left) with a lattice parameter of 500 nm compared to an isolated cluster (right); excited at 728 nm using a light source with an intensity normalized by area. In periodic arrangement the field enhancement within the gaps is much more pronounced (red areas).

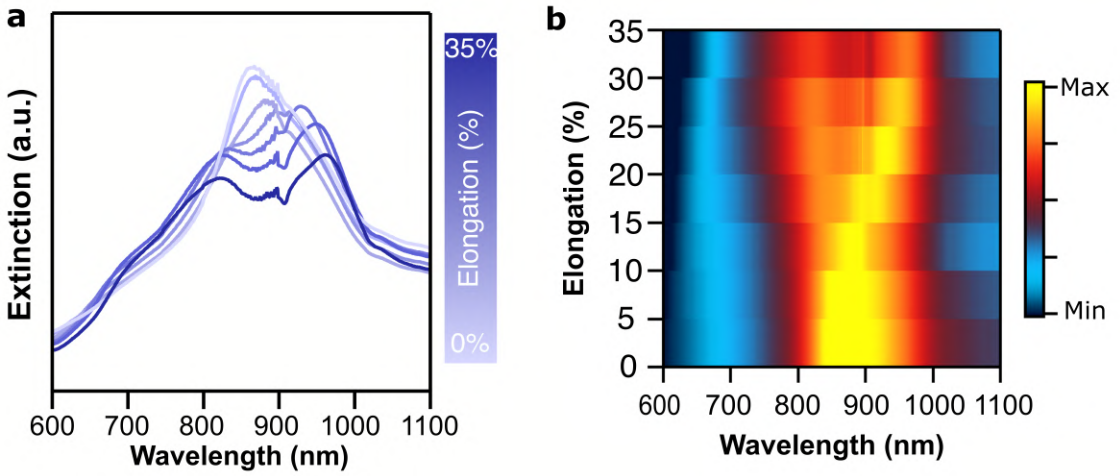

Figure Appendix III.6: Extinction spectra of a superlattice with a period of 600 nm at different elongation states using a) unpolarized light (this is without using a linear polarizer), b) light polarized along the contraction axis c) along the elongation axis. Corresponding extinction maps for d) unpolarized light, e) light polarized along the contraction axis, f) light polarized along the elongation axis.

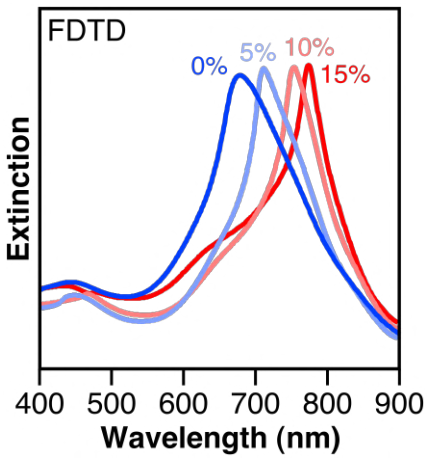

Figure Appendix III.7: Simulated extinction spectra of a superlattice with an initial periodicity of 500 nm, which is deformed bidirectionally by 5%, 10% and 15% giving lattice parameters of 525 nm, 550 nm, and 600 nm, respectively.

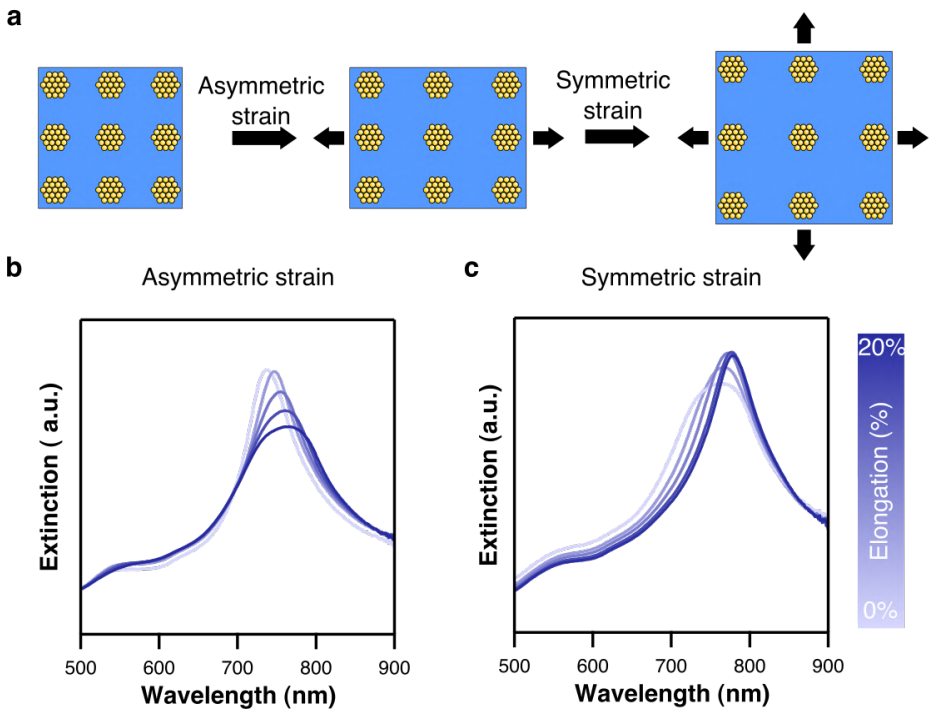

Figure Appendix III.8: a) Two-step stretching process: First, the sample is stretched (in x-direction) to a rectangular lattice, without contraction in y-direction, by using a 2D stretching device. Then, the sample is stretched in y-direction to form a square lattice. Extinction spectra of a 500 nm superlattice b) stretched to a rectangular lattice without contraction and c) stretched from a rectangular lattice to a square lattice.

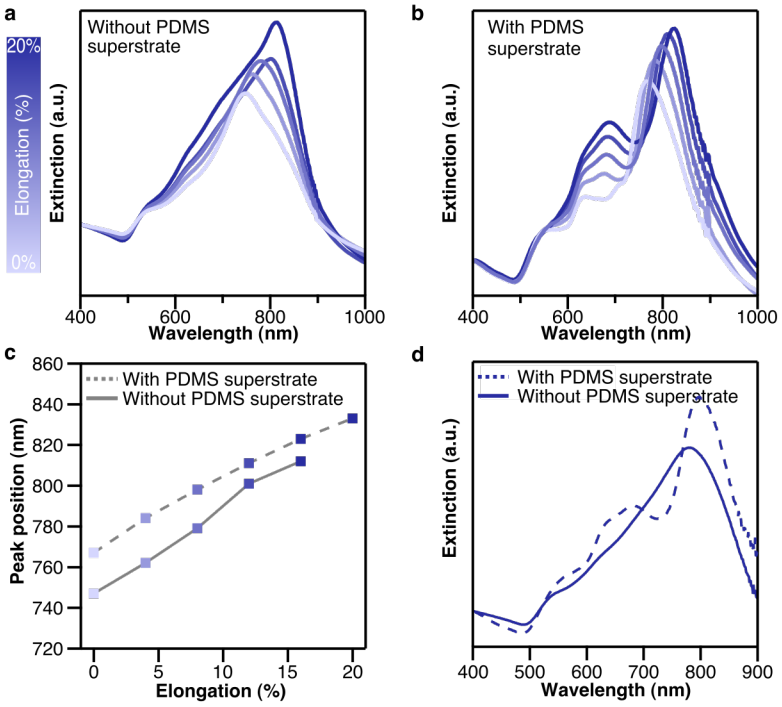

Figure Appendix III.9: Extinction properties of superlattice with a period of 500 nm a) with and b) without an additional layer of PDMS (as superstrate) cast on top of the sample to provide a homogenous refractive index environment. c) Evolution of the lattice plasmon peaks under stretching with and without the PDMS superstrate. d) Comparison of extinction spectra between a sample with and without PDMS superstrate at 8% elongation. The secondary peak at around 650 nm could be attributed to plasmonic contributions of higher order.

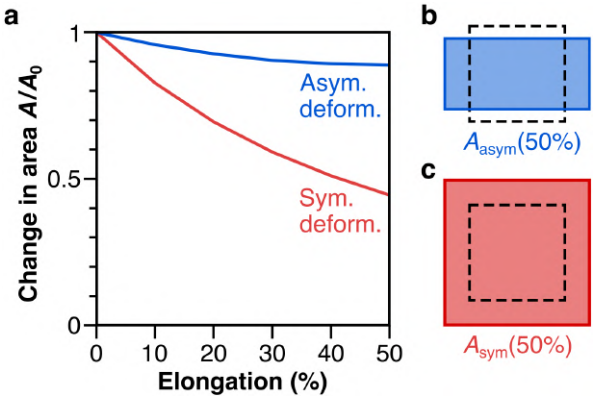

singlelinecheck=off

Figure Appendix III.10: a) Change in surface area upon asymmetric (blue) and symmetric stretching (red) of a material with a Poisson's ratio of 0.5, estimated by Equation C.3 and C.4, respectively; b,c) illustration of the effect of elongation on a schematic substrate surface with an exemplary elongation of 50% (colored area) versus 0% (black dashed line).

The change of surface area A at elongation $\Delta L/L$in reference to the area in unstretched state A_0 can be geometrically estimated. In the case of asymmetric deformation (Aasym/A0), this is for uniaxial strain, Poisson's ratio needs to be considered:

$$A_{asym}(\Delta L/L)/A_0 = (1 + \Delta L/L)(1 - \Delta L/L) \tag{C.3}$$

In case of a symmetrical deformation (A_{sym}/A_0) it is assumed that the substrate deforms equally both vertically and horizontally.

$$A_{sym}(\Delta L/L)/A_0 = (1 + \Delta L/L)^2 \tag{C.4}$$

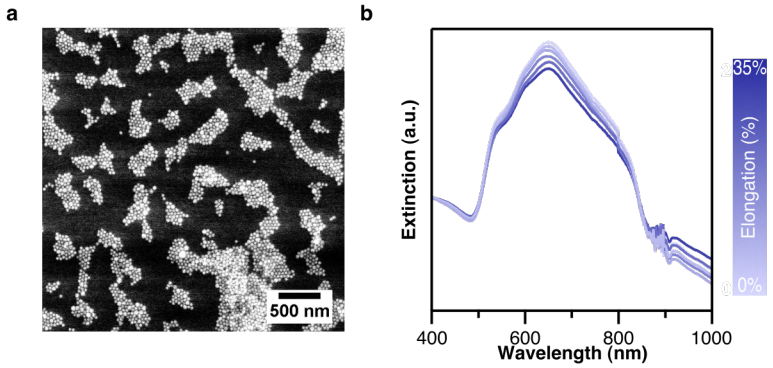

Figure Appendix III.11: Reference sample of disorganized NPs: a) e-SEM image and b) optical properties for different elongation states. The extinction spectra remain almost unaffected by the stretching, which indicates the absence of any lattice effect, as expected.

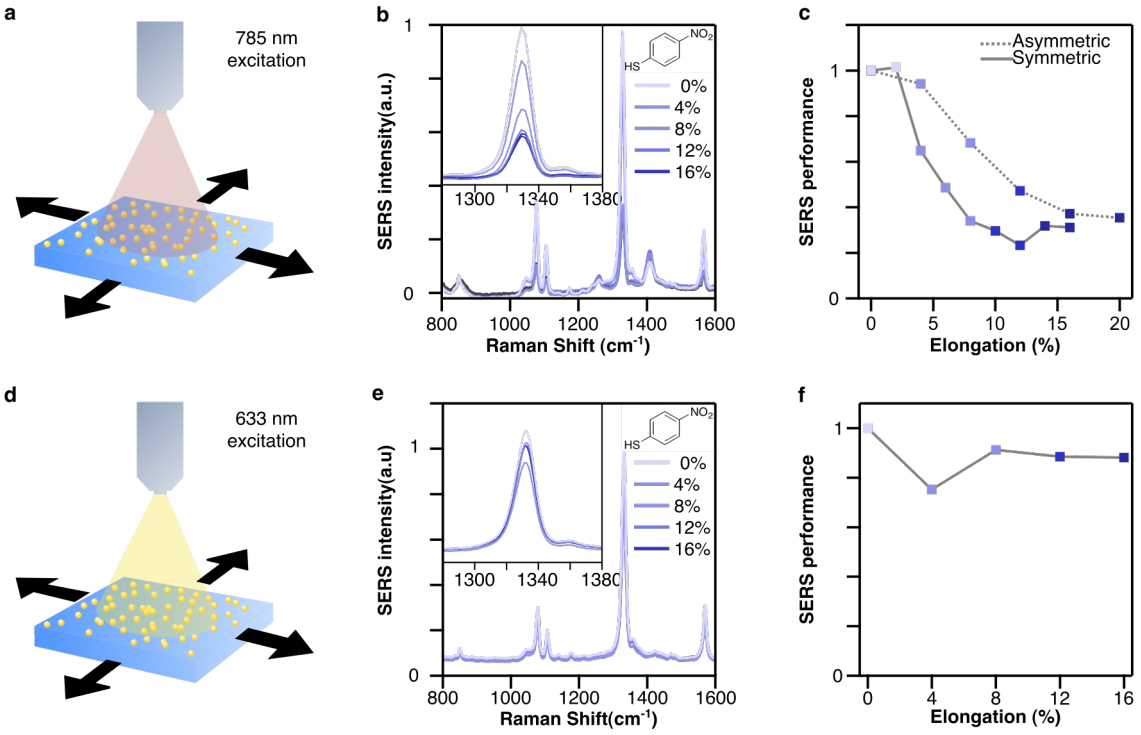

Figure Appendix III.12: SERS signal of the sample of disorganized NPs at 633 and 785 nm excitation: a) Schematic of the disorganized sample symmetrically stretched under 785 nm excitation; b) SERS spectra and c) signal intensity at 1330 cm^{-1} corresponding to the NO2 signal of NTP at different elongation states under 785 nm excitation. d) Schematic of the disorganized sample symmetrically stretched under 633 nm excitation; e) SERS spectra and f) signal intensity at 1330 cm^{-1} corresponding to the NO_2 signal of NTP at different elongation states under 633 nm excitation.

Appendix D

Real-time SERS sensing by polymer coating of plasmonic substrates and removal through thermoplasmonic effects

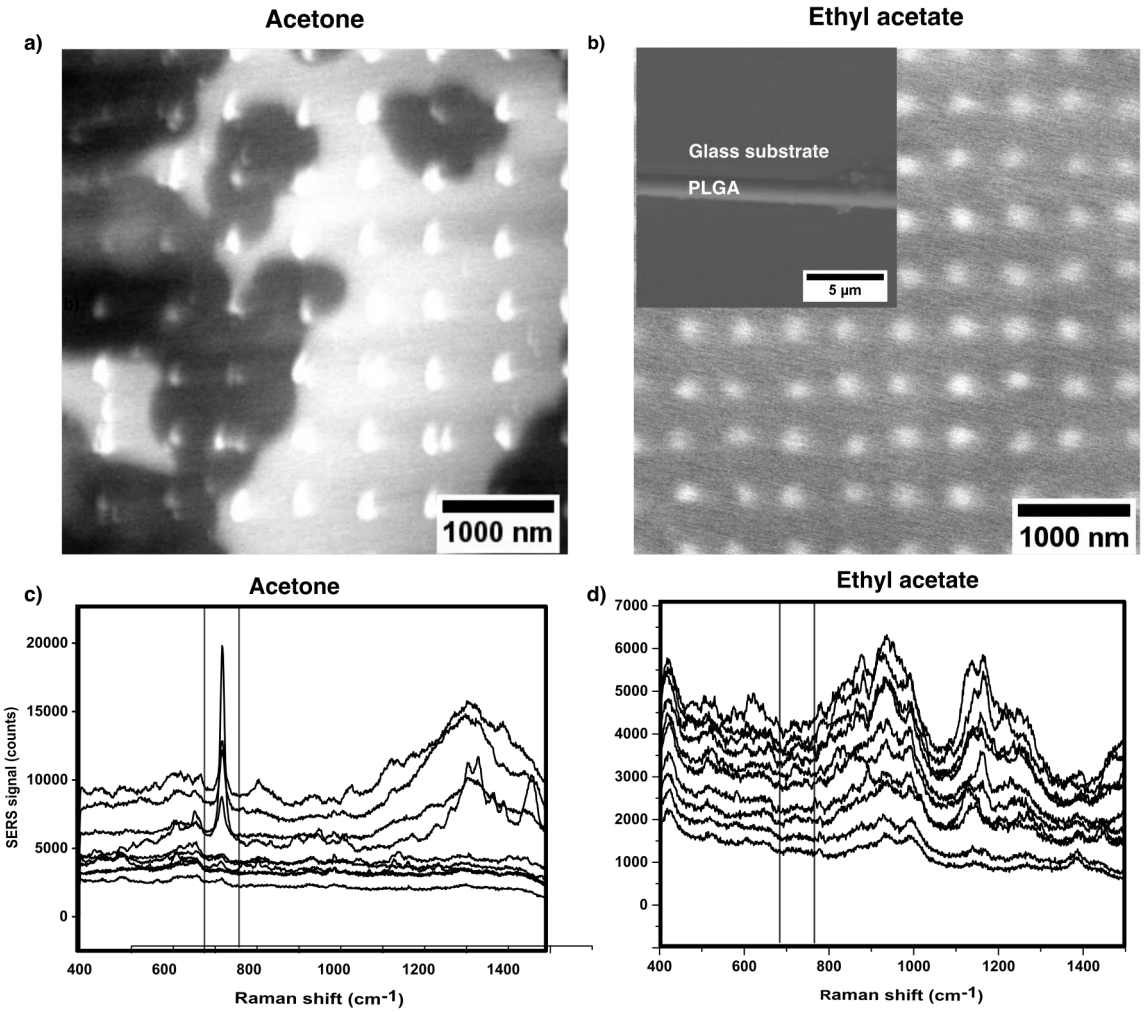

Figure Appendix III.1: SEM images of PLGA coatings made from dissolved PLGA in a) acetone, b) ethyl acetate. SERS spectra, at a low laser fluence of 0.08 mJ/m^2, of PLGA coated superlattices made from dissolved PLGA in c) acetone, d) ethyl acetate. Signal is observed with the superlattices made from PLGA dissolved in acetone due to the uncomplete coverage of the superlattice by spin coating.

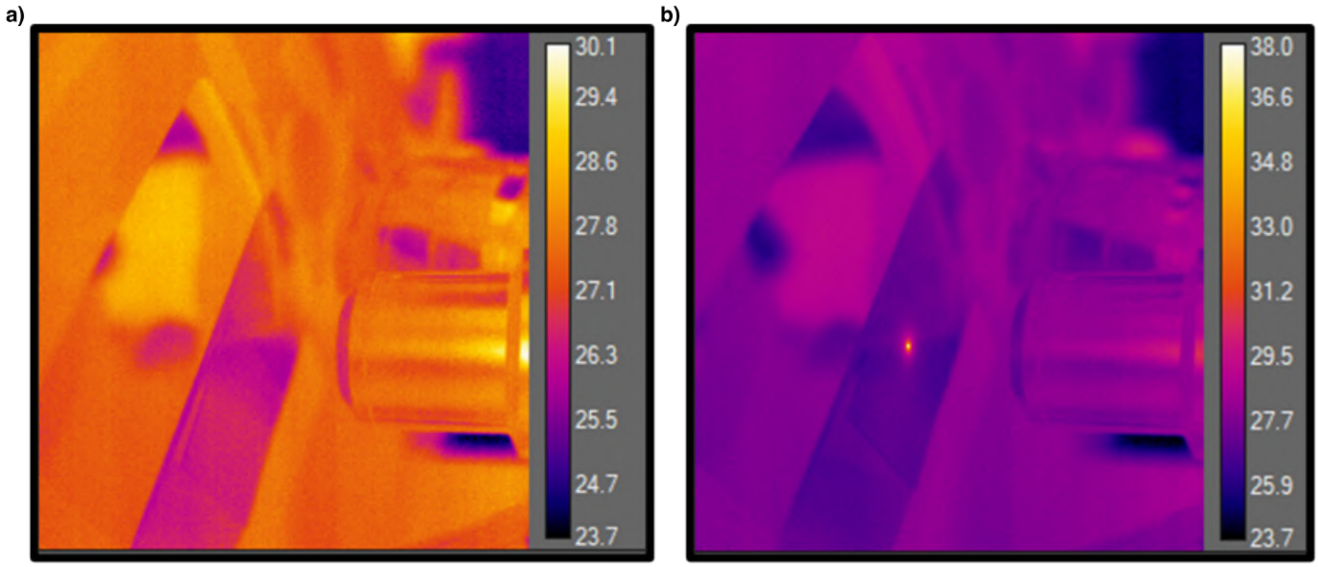

Figure Appendix III.2: Thermal infrared image of a superlattice under a) no laser irradiation, b) 785 nm laser irradiation at an irradiance of $0.32\,\mathrm{mW/\mu m^2}$

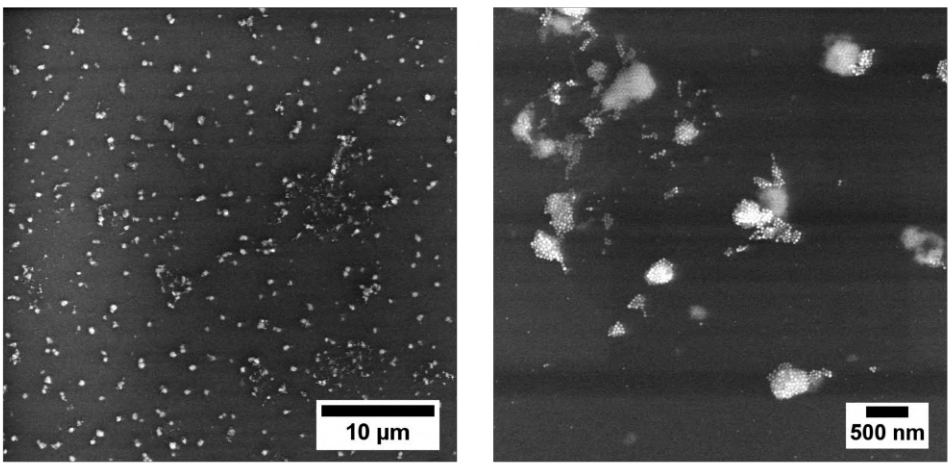

Figure Appendix III.3: SEM images of an unorganized sample made by drying a $200\,\mu$L droplet of nanoparticle solution.

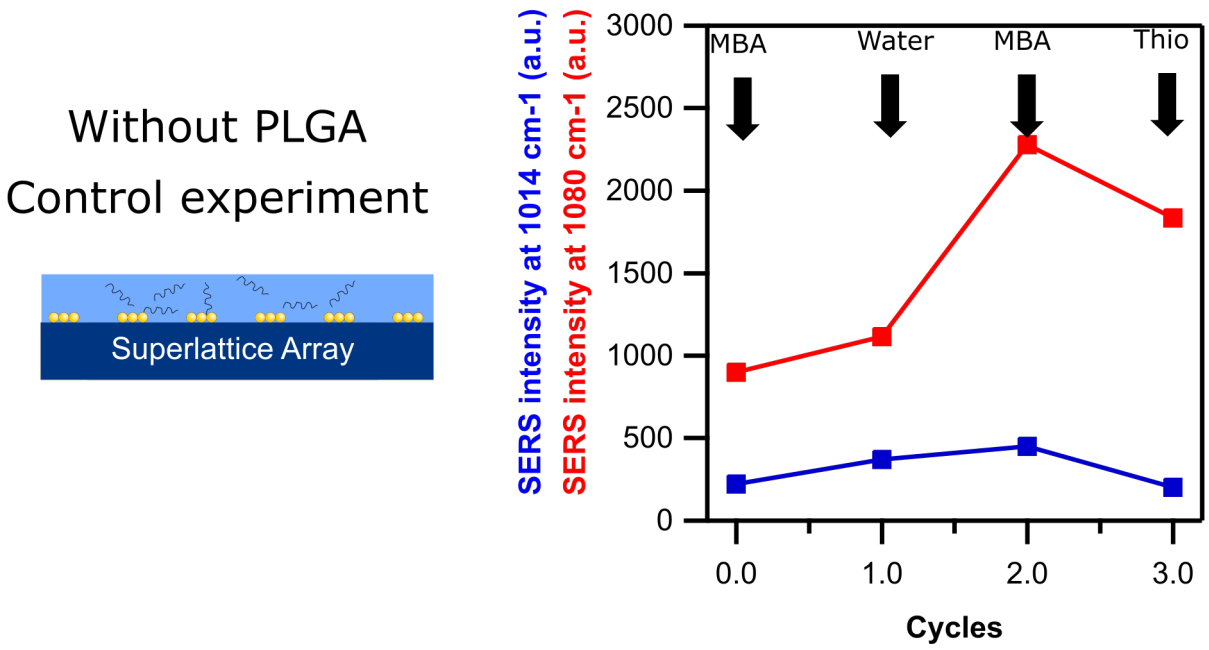

Figure Appendix III.4: SERS control experiment of the microfluidic flow measurement using a superlattice without PLGA layer. SERS intensity of the characteristic mode of thiabendazole at 1014 cm^{-1} in red and 4-MBA at 1080 cm^{-1} in blue, as a function of the introduction cycles (n) by the syringe pump, for a plasmonic superlattice coated without the PLGA sheathing layer. The black arrows on top of each graph represent the introduction of a different analyte solution (W, T or M) in the microfluidic channel at the indicated introduction cycle.

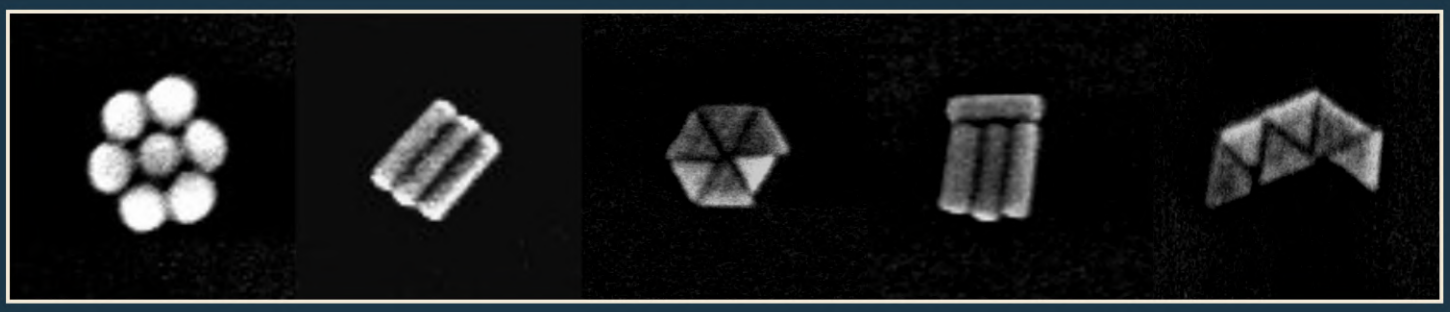

This thesis is oriented towards the fabrication and optical characterization of ordered clusters of gold nanoparticles, i.e. plasmonic superlattices, as substrates for surface-enhanced spectroscopy. Due to their remarkable ability to confine light to the nanoscale, plasmonic nanostructures are ideal platforms for ultrasensitive spectroscopy techniques, such as surface-enhanced Raman scattering (SERS) spectroscopy. SERS has emerged as a technique of choice for the monitoring of low concentrations of chemicals and biological markers. Therefore, the fabrication of new optimized plasmonic substrates for SERS is essential for the detection of even lower concentrations of molecules. High and ecient SERS signals typically demands a match between the plasmon resonance wavelength and the Raman laser excitation wavelength. Plasmon resonances can be tailored through the nanostructure's shape or material. Particularly, in periodically arranged nanoparticles, i.e. plasmonic superlattices, the plasmon resonance can be tuned through changes in the lattice period. In this context, the overall goal of this thesis is to fabricate and study the plasmonic properties of highly regular gold nanoparticle superlattices made through self-assembly, with the aim of optimizing their SERS performance.